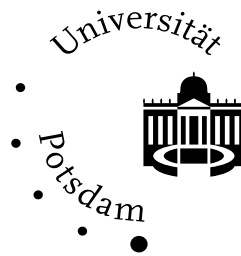


Institut für Chemie  
Physikalische Chemie

---

# Experimental and Theoretical Investigations of Molecular Ions by Spectroscopy as well as Ion Mobility and Mass Spectrometry



## Dissertation

zur Erlangung des akademischen Grades

"doctor rerum naturalium"

(Dr. rer. nat.)

in der Wissenschaftsdisziplin "Physikalische Chemie"

eingereicht an der  
Mathematisch-Naturwissenschaftlichen Fakultät  
der Universität Potsdam

von

Daniel Riebe

Potsdam, den 25.04.2016

1. Gutachter: Herr Prof. Dr. Hans-Gerd Löhmannsröben, Universität Potsdam
2. Gutachter: Herr Prof. Dr. Bernd Abel, Universität Leipzig
3. Gutachter: Herr Prof. Dr. Kevin Pagel, Freie Universität Berlin

Published online at the  
Institutional Repository of the University of Potsdam:  
URN urn:nbn:de:kobv:517-opus4-94632  
<http://nbn-resolving.de/urn:nbn:de:kobv:517-opus4-94632>

## PUBLICATIONS

Zühlke, M.; **Riebe, D.**; Beitz, T.; Löhmannsröben, H.-G.; Zenichowski, K.; Diener, M.; Linscheid, M. An electrospray ionization-ion mobility spectrometer as detector for high-performance liquid chromatography. *Eur. J. Mass Spectrom.* **2015**, *21* (3), 391.

Brendler, C.; **Riebe, D.**; Zenichowski, K.; Beitz, T.; Löhmannsröben, H.-G. Laser-based ion mobility spectrometer for the direct analysis of aromatic compounds in liquids. *Int. J. Ion Mobil. Spectrom.* **2014**, *17* (3-4), 105–115.

**Riebe, D.**; Beitz, T.; Dosche, C.; Löhmannsröben, H.-G.; Raab, V.; Raab, C.; Unverzagt, M. High-Resolution Spectrometer Using Combined Dispersive and Interferometric Wavelength Separation for Raman and Laser-Induced Breakdown Spectroscopy (LIBS). *Appl. Spectrosc.* **2014**, *68* (9), 1030–1038.

**Riebe, D.**; Laudien, R.; Brendler, C.; Beitz, T.; Löhmannsröben, H.-G. Laser ionization of H<sub>2</sub>S and ion-molecule reactions of H<sub>3</sub>S<sup>+</sup> in laser-based ion mobility spectrometry and drift cell time-of-flight mass spectrometry. *Anal. Bioanal. Chem.* **2013**, *405* (22), 7031–7039.

Brendler, C.; **Riebe, D.**; Ritschel, T.; Beitz, T.; Löhmannsröben, H. G. Investigation of neuroleptics and other aromatic compounds by laser-based ion mobility mass spectrometry. *Anal. Bioanal. Chem.* **2013**, *405* (22), 7019–7029.

**Riebe, D.**; Zühlke, M.; Zenichowski, K.; Beitz, T.; Dosche, C.; Löhmannsröben, H.-G. Characterization of Rhodamine 6G Release in Electrospray Ionization by Means of Spatially Resolved Fluorescence Spectroscopy. *Z. Phys. Chem.* **2011**, *225* (9-10), 1055–1072.

Laudien, R.; **Riebe, D.**; Beitz, T.; Löhmannsröben, H.-G. Detection of explosive related nitroaromatic compounds (ERNC) by laser-based ion mobility spectrometry. In *Optically Based Biological and Chemical Detection for Defence IV*; Carrano, J. C., Zukauskas, A., Eds.; SPIE Europe Security and Defence. International Society for Optics and Photonics, 2008; Vol. 7116, p 71160T.

## TALKS

IMS-Anwendertreffen 2016 (meeting of German IMS users), Hannover

Bunsentagung 2014 (conference of the German society for physical chemistry), Hamburg

IMS-Anwendertreffen 2014, Essen

ISIMS 2013 (conference of the International Society of Ion Mobility Spectrometry), Boppard

INN mass spec 2013 (Innovations in MS Instrumentation Conference), St Petersburg (talk)

IMS-Anwendertreffen 2012, Berlin (talk)

## ZUSAMMENFASSUNG

Ziel dieser Arbeit war die Aufklärung unterschiedlicher Ionisationsmethoden (Resonanzverstärkte Mehrphotonenionisation – REMPI, Elektrosprayionisation – ESI, chemische Ionisation bei Atmosphärendruck – APCI) in der Ionenmobilitäts (IM)-Spektrometrie. Um ein besseres Verständnis der Ionisationsprozesse zu erhalten, wurden zusätzlich verschiedene spektroskopische, massenspektrometrische und theoretische Methoden eingesetzt. Ein weiterer Schwerpunkt war die Entwicklung neuer experimenteller Techniken, darunter ein hochauflösender Spektrograph und verschiedene Kombinationen von IM- und Massenspektrometern.

Der neuartige, hochauflösende 2D Spektrograph ermöglicht spektroskopische Auflösungen im Bereich kommerzieller Echelle-Spektrographen. Die geringste erreichte Halbwertsbreite eines Peaks betrug 25 pm. Der 2D Spektrograph beruht auf der Wellenlängenseparation von Licht durch eine Kombination aus einem Prisma und einem Gitter in der einen Dimension und einem Etalon in der zweiten Dimension. Das Instrument wurde erfolgreich zur Aufnahme von Raman- und laserinduzierten Plasmaspektren eingesetzt.

Verschiedene spektroskopische Methoden (Lichtstreuung und Fluoreszenzspektroskopie), die sowohl eine räumliche, als auch eine spektrale Auflösung erlauben, wurden zur Untersuchung der Freisetzung der Ionen im Elektrospray angewandt. Die Untersuchung beruht auf der Verschiebung der Fluoreszenzbande von Rhodamin 6G-Ionen um 50 nm beim Übergang aus den Elektrospray-Tropfen in die Gasphase.

Eine neuentwickelte Ionisationskammer bei reduziertem Druck (0,5 mbar) wurde an ein Flugzeit-Massenspektrometer gekoppelt. Darin wurde nach REMPI von  $\text{H}_2\text{S}$  eine zum  $\text{H}_2\text{O}$  analoge Ionisationschemie beobachtet. Neben  $\text{H}_2\text{S}^+$  und seinen Fragmenten wurden als Ergebnis von Protonen-Transferreaktionen  $\text{H}_3\text{S}^+$  und protonierte Analytionen beobachtet.

Zur Aufklärung der Peaks in IM-Spektren wurde eine Kopplung von IM-Spektrometer und linearem Quadrupol-Ionenfallen-Massenspektrometer entwickelt. Die Kopplung kann mit verschiedenen Ionisationsquellen (ESI, REMPI, APCI) ausgestattet werden und wurde zur Charakterisierung des Peptids Bradykinin und des Neuroleptikums Promazin angewendet.

Die Ionisation von Sprengstoffen in einer APCI-Quelle, die auf weicher Röntgenstrahlung beruht, wurde in einer neu entwickelten, an das Ionenfallen-Massenspektrometer gekoppelten Ionisationskammer untersucht. Dabei konnten die wichtigsten Primär- und Sekundärreaktionen charakterisiert, sowie Sprengstoffionen identifiziert und den Peaks in den IM-Spektren zugeordnet werden. Diese Zuordnung beruht auf dem Vergleich von experimentell bestimmten und berechneten IM. Da die aktuell verfügbaren Berechnungsmethoden insbesondere für Anionen zu große Abweichungen zu den experimentell bestimmten IM aufweisen, wurde auf Basis der Bewertung verfügbarer Methoden eine neue Hybridmethode entwickelt und charakterisiert.

## ABSTRACT

The aim of this thesis was the elucidation of different ionization methods (resonance-enhanced multiphoton ionization - REMPI, electrospray ionization - ESI, atmospheric pressure chemical ionization - APCI) in ion mobility (IM) spectrometry. In order to gain a better understanding of the ionization processes, several spectroscopic, mass spectrometric and theoretical methods were also used. Another focus was the development of experimental techniques, including a high resolution spectrograph and various combinations of IM and mass spectrometry.

The novel high resolution 2D spectrograph facilitates spectroscopic resolutions in the range of commercial echelle spectrographs. The lowest full width at half maximum of a peak achieved was 25 pm. The 2D spectrograph is based on the wavelength separation of light by the combination of a prism and a grating in one dimension, and an etalon in the second dimension. This instrument was successfully employed for the acquisition of Raman and laser-induced breakdown spectra.

Different spectroscopic methods (light scattering and fluorescence spectroscopy) permitting a spatial as well as spectral resolution, were used to investigate the release of ions in the electrospray. The investigation is based on the 50 nm shift of the fluorescence band of rhodamine 6G ions of during the transfer from the electrospray droplets to the gas phase.

A newly developed ionization chamber operating at reduced pressure (0.5 mbar) was coupled to a time-of-flight mass spectrometer. After REMPI of H<sub>2</sub>S, an ionization chemistry analogous to H<sub>2</sub>O was observed with this instrument. Besides H<sub>2</sub>S<sup>+</sup> and its fragments, H<sub>3</sub>S<sup>+</sup> and protonated analyte ions could be observed as a result of proton-transfer reactions.

For the elucidation of the peaks in IM spectra, a combination of IM spectrometer and linear quadrupole ion trap mass spectrometer was developed. The instrument can be equipped with various ionization sources (ESI, REMPI, APCI) and was used for the characterization of the peptide bradykinin and the neuroleptic promazine.

The ionization of explosive compounds in an APCI source based on soft x-radiation was investigated in a newly developed ionization chamber attached to the ion trap mass spectrometer. The major primary and secondary reactions could be characterized and explosive compound ions could be identified and assigned to the peaks in IM spectra. The assignment is based on the comparison of experimentally determined and calculated IM. The methods of calculation currently available exhibit large deviations, especially in the case of anions. Therefore, on the basis of an assessment of available methods, a novel hybrid method was developed and characterized.

# CONTENTS

1	Introduction .....	7
2	Theoretical and methodological principles .....	11
2.1	Spectroscopy .....	11
2.1.1	Laser-induced fluorescence of large organic molecules in the gas phase .....	11
2.1.2	Fabry-Pérot etalon.....	12
2.1.3	Raman Spectroscopy .....	13
2.1.4	Laser-induced breakdown spectroscopy.....	15
2.2	Ion mobility and mass spectrometry .....	16
2.2.1	Kinetic theory of ions in dense gases .....	16
2.2.2	Ion-neutral interaction potentials.....	20
2.2.3	Mobility simulations.....	22
2.2.4	Time-of-flight mass spectrometer.....	25
2.2.5	Linear quadrupole ion trap mass spectrometer .....	26
2.2.6	Ionization processes.....	28
3	Experimental.....	37
3.1	Laser-induced fluorescence study of rhodamine 6G in the electrospray process .....	37
3.2	Etalon spectrometer .....	38
3.3	REMPI-ToF mass spectrometer with reduced pressure ionization chamber .....	39
3.4	Ion mobility mass spectrometer.....	39
4	Results and discussion.....	43
4.1	Spectroscopy .....	43
4.1.1	Laser-induced fluorescence study of rhodamine 6G in the electrospray process .....	43
4.1.2	High resolution spectrometer utilizing two-dimensional wavelength separation.....	57
4.2	Ion mobility mass spectrometry.....	69
4.2.1	REMPI mass spectrometry of H <sub>2</sub> S at reduced pressure .....	69
4.2.2	Atmospheric pressure ionization chamber and dual-gate IM spectrometer connected to ion trap mass spectrometer .....	74
4.2.3	Formation of negative ions by soft X-rays and ionization chemistry of alkyl nitrates.....	81
4.2.4	Mass-mobility-correlations and computation of collision cross sections .....	103
5	Outlook.....	123
6	References.....	125
7	Appendix.....	133
8	Table of symbols and abbreviations .....	139

# 1 INTRODUCTION

The Latin word *spectrum*, meaning “appearance”, “image” or “apparition” and stemming from *specere*, “to look”, is applied, in the scientific field, to the separation of electromagnetic waves due to their wavelengths. Thus, a spectroscopy is an instrument that performs and visualizes this separation and a spectrometer is a device that additionally assigns wavelengths. In optical spectroscopy, compounds are investigated by means of their interaction with electromagnetic radiation. By analogy, in a mass spectrometer, a number of substances are ionized and separated by their mass-to-charge ratio  $m/z$ . The ionization is necessary for this process, because the separation is carried out with the help of electric fields. Although ion mobility (IM) spectrometry shares many similarities with mass spectrometry, there are some important differences. Most prominently, these instruments usually operate at atmospheric pressure and separate ions based on their collision cross sections, or – more broadly speaking – their shape, instead of their mass. All these instruments are used in the field of chemical analysis in order to gain information about substances.

In this thesis, spectrometers of all three types were employed in a range of experiments. The common denominator of all of them is the participation of photons. In a number of applications, the commonly encountered spectral resolution of commercially available optical spectrometers in the nanometer range is insufficient. One of these applications is laser-induced breakdown spectroscopy (LIBS), where atomic spectral lines are recorded after a plasma is generated, usually on a solid surface, by a laser. Since the specific lines of elements can be very close together it is necessary to have a high resolution as well as a good calibration. Raman spectroscopy can require high resolutions as well, especially when mixtures are analyzed or rotational resolved spectra are recorded. The established instruments of this type are either scanning spectrometers, such as those in the Czerny-Turner configuration, or echelle spectrometers. Here, a novel type of spectrograph was developed, based on the separation of light in two dimensions by two different principles. In the first dimension, the incoming light passed through a combination of a prism and a grating, resulting in a line spectrum of a resolution in the range of 1 nm. In the second dimension, this spectrum was separated further by a Fabry-Pérot etalon, resulting in a resolution down to 25 pm. In contrast to the linear detectors found in conventional spectrometers, this instrument takes advantage of the abundance of charge-coupled device (CCD) cameras available. The spectrometer has the advantage of obtaining the entire spectrum in one experiment and the potential of a compact footprint. The novel device was developed from the ground up using commercial optical components except for the etalon, which was specifically developed for the task. The transformation of the raw 2D image into a traditional line spectrum was accomplished by employing multi-parameter line fits in both dimensions using second order polynomials. These lines were found using a broadband light source and a Ne lamp. The latter was also used for wavelength calibration. Furthermore, the analytical capabilities of the instrument were demonstrated successfully in the detection of Raman and LIB spectra.

Laser-induced fluorescence (LIF) was used to investigate the fate of ions during electrospray ionization (ESI). New insights could be gained on the release of these ions from the droplets formed during the spraying process. For this purpose, the fluorescent dye rhodamine 6G (R6G) was used as a probe since it exhibits a shifted fluorescence in solution compared to the gas phase. Spatially resolved LIF spectra could be obtained with a special slit spectrograph. The influence of different ESI parameters such as the location relative to the spray axis, the distance from the spray capillary and solvent and sheath gas flow rates could be investigated.

Laser radiation was also used itself in the ionization of compounds. Conventionally, laser-based ionization sources are limited to substance particularly suited to this type of ionization, i.e. compounds possessing aromatic systems such as benzene, toluene, ethylbenzene and xylenes (BTEX), polycyclic aromatic hydrocarbons (PAH) and their derivatives. In order to expand the range of substances accessible by this ionization source, intermediates (dopants) have to be found that are ionized by the laser first before subsequently ionizing the target analyte in ion-molecule reactions (IMR). This kind of ionization scheme is only feasible in an intermediate ( $> 10$  mbar) or atmospheric pressure regime, where the probability of such IMR is greatly increased. The resonance-enhanced multiphoton ionization (REMPI) of  $\text{H}_2\text{S}$  could be demonstrated in an intermediate pressure ionization cell in front of a time-of-flight (ToF) mass spectrometer. In addition to  $\text{H}_2\text{S}^+$  and its fragments,  $\text{H}_3\text{S}^+$  was also observed, indicating its production in a proton-transfer reaction (PTR). The use of this reaction in subsequent IMR for the ionization of other compounds was also demonstrated.

The detection of explosive compounds is one of the main commercial applications of IM spectrometry relevant to the field of security. Especially in airports or at public events, there is a need for fast, reliable, sensitive and cost efficient explosive detectors. Since the resolution of IM spectrometers is low compared to mass spectrometry, it is essential to understand the ionization chemistry in order to reduce the likelihood of false positive or false negative detections. Therefore, the final part of the thesis is concerned with the production of ions in IM spectrometry. To that end, a combination of IM spectrometer and linear quadrupole ion trap mass spectrometer was constructed and successfully employed. A reduced design, incorporating only the ionization chamber of the IM spectrometer in front of the trap, was used to investigate the ionization chemistry of explosive compounds. The ionization was performed with a soft X-ray source. The primary ions produced in this source are the same encountered in conventional IM spectrometers operated with radioactive  $^{63}\text{Ni}$  sources. The subsequent atmospheric pressure chemical ionization (APCI) of the analytes can be applied to a broad range of substances. The complex product ion spectra comprised of fragment and adduct ions observed for the class of alkyl nitrates was analyzed in detail. The effects of drift gases, common dopants, such as methylene chloride, as well as those of less common additives, such as  $\text{N}_2\text{O}$ , were investigated.



The applicability of IM spectrometry, especially to the detection of unknown compounds, would greatly benefit from a reliable prediction of mobilities. So far, most work in this regard is limited to predictions within classes of similar compounds, such as those of homologous series, based on simple empirical correlations. In order to increase the scope of these investigations, some work was done on calculating collision cross sections and IM. In these calculations, simple models of the interaction of molecular ions and buffer gasses were compared and combined with more advanced trajectory simulations based on DFT calculations. In addition to explosive compounds, these methods were also applied to some amines well-known in the literature.



## 2 THEORETICAL AND METHODOLOGICAL PRINCIPLES

### 2.1 Spectroscopy

#### 2.1.1 Laser-induced fluorescence of large organic molecules in the gas phase

Fluorescence is one of the processes which allow an electronically excited molecule to return to the ground state (Fig. 1). During this process, a photon is spontaneously emitted by the molecule. The absorption process usually starts from the vibrational ground state, but can leave the molecule in a vibrationally and electronically excited state. The fluorescence process starts with a molecule in the vibrational ground state of the lowest electronically excited state (Kasha's rule), but can leave the molecule in a vibrationally excited state of the electronic ground state. Therefore, the wavelength spectrum of the fluorescence is shifted towards shorter wavelengths compared to the absorption spectrum. One difference between fluorescence and phosphorescence is that during the transition, the multiplicity does not change. In practice, the lifetimes are also different, with the lifetimes of common fluorescent dyes in the ns range.<sup>1</sup>

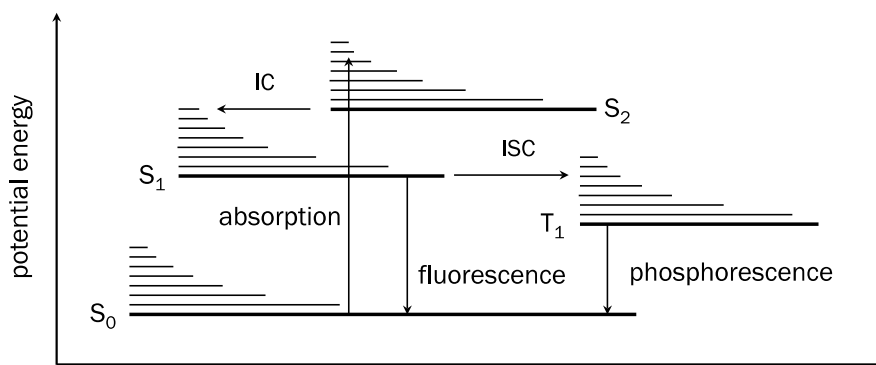


Figure 1: Simplified Jablonski diagram of the processes upon the absorption of a photon by a large organic molecule, S<sub>0</sub> - ground state, S<sub>1</sub> - first excited singlet state, S<sub>2</sub> - second excited singlet state, T<sub>1</sub> - triplet state, IC - internal conversion, ISC - intersystem crossing

Molecular beam studies present one possibility of recording LIF spectra in the gas phase. These can be quite different from the spectra recorded in solvents because of the solvation effects on the fluorescence. The difficulty in recording gas phase LIF spectra is due to the intensity of the luminescence. On the one hand, the efficiency of the fluorescence is determined by the absorption cross section of the molecule. For this reason, the excitation wavelength is usually chosen to coincide with the strongest absorption band. The absorption spectrum in the gas phase can be shifted compared to the gas phase, similarly to the effect of solvatochromism observed in different solvents.<sup>2</sup> The intensity is also determined by the fluorescence quantum yield. In addition to solvation effects, such as the stabilization of the excited state, that are not encountered in the gas phase, the drift gas constituents can quench the fluorescence. The effect of different gases on the fluorescence intensity of the R6G ions has been studied.<sup>3</sup> Due to the low signal intensities, that are mainly a result of the low particle densities in the gas phase, efficient detectors, such as photomultiplier tubes or electron-multiplying charge-coupled device (EMCCD) cameras are used.

Early experiments utilizing LIF in the gas phase include the investigation of ions<sup>4</sup> and radicals formed in gas phase reactions<sup>5</sup> in pressure chambers. More recent applications are the investigation of the matrix-assisted laser desorption and ionization (MALDI) process by observing the emission of common matrix molecules,<sup>6</sup> the investigation of combustion processes in a pressure chamber by exploiting the temperature and pressure dependence of the absorption and emission process as well as fluorescence quenching.<sup>7</sup> However, the most comprehensive work on LIF of gas phase ions was done in Paul or Penning ion traps.<sup>8</sup>

The basis for the experiments described in this work are gas phase fluorescence spectra of a number of dye molecules recorded by M. Kordel in a Paul trap.<sup>9</sup> One of the dyes investigated, the R6G ion, exhibits a substantial hypsochromic shift of 50 nm in the gas phase spectrum compared to that of an ethanolic solution (Fig. 2).

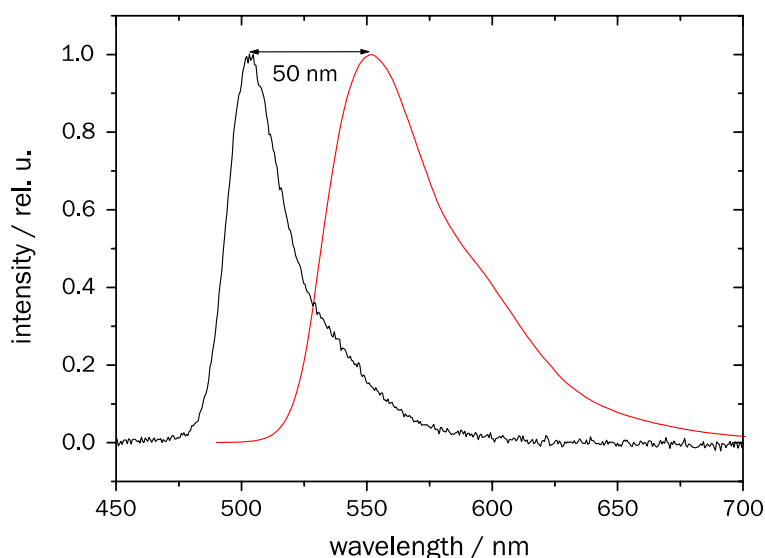


Figure 2: R6G emission spectra: gas phase spectrum recorded in ion trap (black,  $\lambda_{\text{ex}} = 457.9$  nm), solution spectrum in EtOH (red,  $\lambda_{\text{ex}} = 480$  nm); taken from the dissertation of M. Kordel (p. 103)<sup>9</sup>

### 2.1.2 Fabry-Pérot etalon

A Fabry-Pérot interferometer consists of two parallel reflecting planes separated by an air gap. A Fabry-Pérot etalon is a single optically flat substrate with reflecting coatings on both sides. Both exhibit the same transmission characteristics, provided the substrate (usually fused silica) is completely transparent. If a light wave enters the etalon under an angle  $\alpha$ , the wave is reflected multiple times. The incident and reflected waves undergo constructive or destructive interference, depending on their phase difference.<sup>10</sup> The phase difference in turn depends on  $\alpha$ , the thickness of the etalon  $d$  and the frequency of the wave  $\nu$ . If the first two are constant, only certain frequencies produce constructive interference. These frequencies are related by

$$\delta\nu = \frac{c}{2d\sqrt{n^2 - \sin^2\alpha}}, \quad (1)$$

where  $c$  is the speed of light,  $n$  is the refractive index of the etalon medium and  $\delta\nu$  is the free spectral range of the etalon. The maximum of constructive interference is achieved if  $\nu$  is an integer multiple of  $\delta\nu$ .

For a given  $\nu$ , there are a number of  $\alpha$  for which the  $\nu$  becomes an integer multiple of  $\delta\nu$ . Thus, a divergent but monochromatic point source produces concentric rings on a screen placed behind the etalon (an example can be seen in chapter 4.1.1.3, Fig. 25). The resolving power of an etalon is given by

$$\left| \frac{\nu}{\Delta\nu} \right| = \frac{2\nu nd}{c} \mathcal{F}, \quad (2)$$

where  $\Delta\nu$  is the peak width and  $\mathcal{F}$  is called the finesse of the etalon. The finesse is defined as  $\mathcal{F} = \delta\nu/\Delta\nu$  and depends on the reflectivity  $R_{\text{et}}$  of the etalon mirrors

$$\mathcal{F} = \frac{\pi\sqrt{R_{\text{et}}}}{1 - R_{\text{et}}}. \quad (3)$$

The transmission  $T$  of the etalon is given by the Airy function (simplified case,  $\alpha = 0$ )

$$T = \frac{1}{1 + \left(\frac{2\mathcal{F}}{\pi}\right)^2 \sin^2\left(\frac{2\pi\nu nd}{c}\right)}. \quad (4)$$

The resulting transmission spectrum of an ideal etalon is shown in figure 3. The finesse of a real etalon is affected by the quality and parallelism of the mirror surfaces as well as absorption and scattering by the substrate.

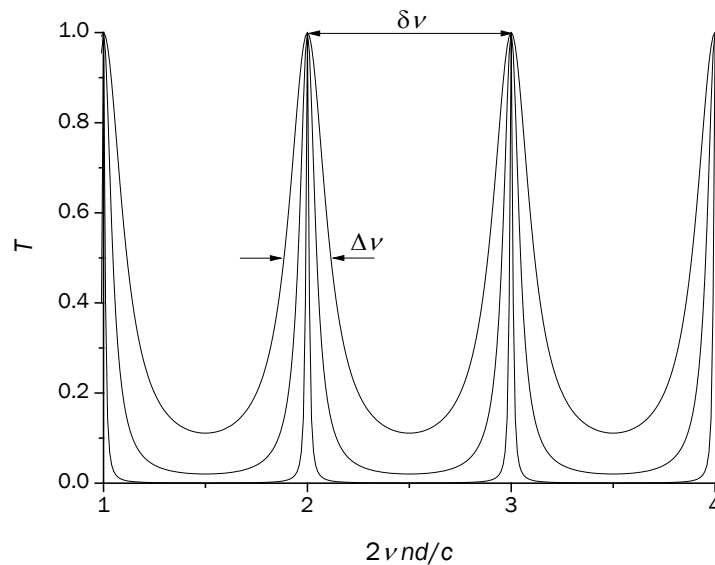


Figure 3: Transmission  $T$  of an ideal etalon as a function of frequency  $\nu$  for different values of finesse  $\mathcal{F}$  (top:  $R_{\text{et}} = 50\%$ , middle:  $R_{\text{et}} = 75\%$ , bottom:  $R_{\text{et}} = 95\%$ ), also shown are the free spectral range  $\delta\nu$  and the peak width  $\Delta\nu$

### 2.1.3 Raman Spectroscopy

Raman spectroscopy can be used to probe molecular vibrations, similar to IR spectroscopy. Unlike IR spectroscopy however, it is not absorption spectroscopy. A light wave and a molecule can interact even if the wavelength is not equal to any transition in a molecule. In that case the light wave can undergo scattering. Usually, this process is elastic and the wavelength does not change. This process is called Rayleigh scattering.

However, the scattering can also be inelastic when the molecule absorbs some energy by reaching a vibrationally excited state and the wavelength of the scattered photon is increased. The energetic state of the molecule and the photon during the scattering interaction is called a virtual state and the process is called Stokes scattering. The energy difference between incident and scattered photon is called the Stokes shift and it is equal to the energy difference between the initial (ground) state and the vibrationally excited state of the molecule (Fig. 4). If the molecule loses energy in the interaction and the wavelength of the photon is decreased, the process is called super-elastic, or anti-Stokes scattering.<sup>11</sup> A corresponding anti-Stokes shift is observed if the molecule was in a vibrationally excited state before interacting with the photon but returns to the ground state afterwards.

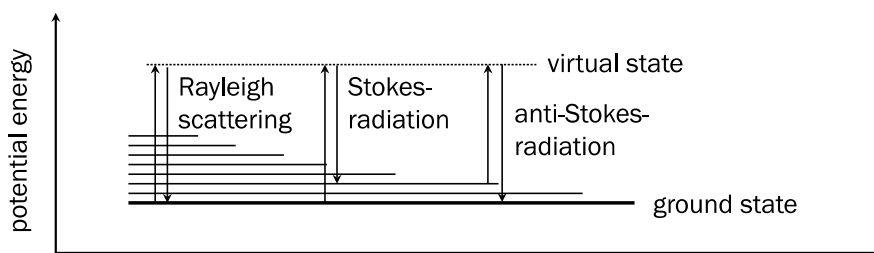


Figure 4: Simplified diagram of vibrational states and transitions during Rayleigh and Raman scattering

The selection rules for Raman spectroscopy are different from those of IR spectroscopy because the intensity of Raman bands depends on the change of the polarizability of the molecule while in an IR transition the dipole moment changes. Thus, a bond in a symmetrical molecule is IR inactive but Raman active, and a bond in an unsymmetrical molecule is IR active and may or may not be Raman active. Therefore, both techniques yield complementary information. However, the Raman effect is weak, Raman cross sections can be up to  $10^8$  times weaker than resonant IR cross sections.<sup>11</sup> As a consequence, highly intense lasers are preferably used for Raman spectroscopy. Filters are used to shield the detector from the intense Rayleigh scattered laser light. The Raman intensity depends on the polarization and the intensity of the laser and the orientation of the molecule as well as the population density of its initial state. Since the population of the vibronic states in a molecules in thermal equilibrium corresponds to the Boltzmann distribution, the Stokes radiation is stronger than the anti-Stokes radiation. Since the wavelengths of the detected Stokes and anti-Stokes radiation depend on the wavelength of the laser, Raman spectra are reported as a function of the Raman shift. This shift is conventionally given as a wavenumber

$$\Delta w = \frac{1}{\lambda_0} - \frac{1}{\lambda_1}, \quad (5)$$

where  $\Delta w$  is the Raman shift,  $\lambda_0$  is the excitation wavelength and  $\lambda_1$  is the spectrum wavelength.

It is possible to increase the Raman intensity in a number of ways. If a wavelength is chosen so that a real state is populated instead of virtual state, resonance Raman can be observed. Even higher intensities can be observed in coherent anti-Stokes Raman scattering (CARS). Two lasers are tuned so that their frequency difference is equal to a Raman active vibration in the molecule.

A non-linear effect stimulates the emission of the Stokes radiation and the vibration state of the molecule is populated. Thus, the anti-Stokes scattering from that state is enhanced by a factor of  $10^4$ - $10^5$  if the number density of the molecules is high enough.<sup>11</sup>

If overtones are encountered or rotationally resolved Raman spectra are to be recorded, high spectral resolution is required. In crystalline solids, lattice vibrations can be observed. These bands are in the range of  $2$ - $3\text{ cm}^{-1}$  and thus require a resolution of about  $50\text{ pm}$  with a typical Raman setup.

#### 2.1.4 Laser-induced breakdown spectroscopy

LIBS is a type of atomic emission spectroscopy. A solid or liquid sample is subjected to a focused, highly intense, short laser pulse.<sup>12</sup> The energy transferred into the sample is mostly transformed into heat in the condensed phase. The sample is transferred into the gas phase, where further interaction with the radiation leads to the ionization of the sample. The ionized molecules usually have a larger absorption cross section for the laser radiation than the initial neutrals. The two models used to describe the gas phase ionization process are multiphoton ionization and cascade ionization. As a result of this process, which is referred to as breakdown, the sample decomposes into atoms, ions and electrons and thus, a hot plasma plume is generated.

Upon cooling, the ions and electrons recombine. The newly formed atoms are left in an electronically excited state and emit their excess energy as photons of their well characterized atomic emission lines. It is therefore possible, upon spectral separation of the emission, to identify the atomic composition of the sample. However, during the first stages of recombination, continuous radiation is emitted due to free-free electron transmissions (unbound electrons transfer kinetic energy into photons, called bremsstrahlung), and free to bound electron recombinations.<sup>12</sup> Additionally, in this interval, the elemental lines are Stark broadened. However, the bremsstrahlung decays faster than the atomic emissions (since the excited states are repopulated as long as recombination occurs), so that after several hundred ns, the narrow atomic lines can be detected. Using a gated detector, it is therefore possible to separate the two kinds of radiation.

Gated detection can either be accomplished by means of a chopper wheel or, more elegantly, by using an intensified charge-coupled device (ICCD). Since atomic lines can be very closely spaced, a high resolution spectrometer is necessary in order to differentiate between lines and to unambiguously identify atoms based on their line spectra. Commonly used spectrometer types include echelle spectrometers and Czerny-Turner spectrometers. The advantages of LIBS include the possibility of spatial and depth profiling of samples, little to no sample preparation and the ability to perform stand-off detection.<sup>13</sup> In addition to information about the sample composition, the intensity distribution among different lines of one element allows conclusions about the population of its electronic states and therefore its temperature.

## 2.2 Ion mobility and mass spectrometry

### 2.2.1 Kinetic theory of ions in dense gases

In this chapter a general overview of the fundamental results of the kinetic theory of gases as they concern IM spectrometry shall be given. A comprehensive discussion can be found e.g. in the book “Transport Properties of Ions in Gases” by Mason and McDaniel that was also used as the basis for this chapter.<sup>14</sup>

The equations presented here provide a link between the observable in IM spectrometry, which is the ion mobility  $K$ , the state functions and the details of the molecular basis of this value, the scattering of ions and buffer gas molecules under the influence of a homogeneous electric field. For most practical applications of IM spectrometry, the ions of interest are large molecular ions while the drift gas atoms or molecules are usually small. The drift gases most frequently used are He, N<sub>2</sub> and air. Most IM spectrometers operate at atmospheric pressure and room temperature or elevated temperatures. In drift tube IM spectrometers, the energy transferred to the ions due to the electric field is of similar magnitude as the thermal energies of the molecules and ions. The theory only applies to these conditions. One prerequisite is that the mean free paths of the ions and molecules are small compared to the container. Additionally, equilibrium conditions are assumed. The following discussion is mainly based on a classical mechanics interpretation and solution of the Boltzmann equation. More comprehensive treatments are available e.g. in the form of the Chapman-Enskog theory.

The first important equation that applies to gases and liquids alike is Fick’s law of diffusion

$$\mathbf{J} = -D\nabla n_i, \quad (6)$$

where  $\mathbf{J}$  is the ionic flux,  $D$  is the diffusion coefficient and  $n_i$  is the number density of the ions. This law relates how ions diffuse in a gas according to the gradient of their concentration when no electric field is applied. This diffusion is due to the thermal motion of the ions and the drift gas as well as the scattering resulting from collisions that randomize the travel direction. At atmospheric pressure the number of these collisions is very high. The homogenous electric field employed in drift gas IM spectrometry acts on the ions in such a way that it attracts them along its field lines. The directed motion resulting from this attraction is superimposed on the thermal motion and, in the limit of low electric fields, the resulting average drift velocity  $v_d$  is proportional to the electric field strength  $E$ ,

$$v_d = KE. \quad (7)$$

The constant of proportionality is  $K$ , the ion mobility.  $K$  and  $D$  both depend on the ion and buffer gas combination. In an ideal gas and in the limit of vanishing fields, the Einstein relation (also called Nernst-Townsend relation)

$$K = \frac{qD}{k_B T}, \quad (8)$$

where  $q$  is the charge,  $k_B$  the Boltzmann constant and  $T$  is the temperature, applies. At the low field conditions considered, the average velocities of the ions are described by the Maxwell-Boltzmann distribution. This implies that the thermal motion of the ions is much faster than the motion due to the field, which is valid for drift tube IM spectrometry. The



macroscopic quantity  $v_d$  is averaged over the processes of ion acceleration due to the field and the collision with the drift gas molecules. In the literature, mobilities are reported at various temperatures. Reduced mobilities  $K_0 = (p/1013 \text{ mbar})(273.15 \text{ K}/T)K$  are often calculated from the experimental temperature and pressure  $p$  in an attempt to unify measurements to “standard” conditions. However, the generalization is only valid for small differences, especially in the temperature.

As was mentioned above, the aim of this chapter is to produce a link between the observable macroscopic quantities and the molecular collisions that are responsible for them. In order to provide a perception of the spatial dimensions these collisions take place in, the mean free path of the particles is considered. The mean free path  $\lambda_{\text{MFP}}$  at atmospheric pressure is

$$\lambda_{\text{MFP}} = \frac{1}{\sqrt{2}n_x\Omega}, \quad (9)$$

with the number density  $n_x$  and the collision cross section  $\Omega$ . if an ideal gas is assumed,  $n_x$  can be obtained from  $n_x = p/k_B T$  and the number density of the ions can be ignored as it is very small compared to that of the drift gas. In  $\text{N}_2$  at atmospheric pressure and 273.15 K,  $\lambda_{\text{MFP}} = 62 \text{ nm}$  [ $\Omega(\text{N}_2) = 43 \text{ \AA}^2$ ].<sup>1</sup> The mean free path of large molecular ions will be smaller due to the larger cross sections. Therefore, the collisions take place in very small volumes and at a high rate compared to the space of many cm inside a drift tube IM spectrometer and the drift times recorded on these distances in the range of ms. At this point, the concept of the cross section is encountered for the first time and should be explained. The collision cross section can be visualized as the radial area around a “target” particle that a point-like “projectile” particle has to penetrate in order to result in a collision. The concept is derived from classical considerations of the molecular scattering of hard spheres. In the calculation of the mean free path above, both particles are  $\text{N}_2$  molecules. In the context of IM spectrometry, the cross sections of the collisions of molecular ions and neutral gas molecules are much more interesting.

In order to obtain these results, momentum-transfer theory will be applied. Besides treating the particles involved classically, the approximation of a constant collision frequency is also made. Additionally, the number density of the drift gas is considered small enough, so that only binary collisions are important. Finally, the number density of the ions is so small, that ion-ion collisions are irrelevant and the collisions only result in small changes of the equilibrium conditions of the drift gas. The mathematical readability is improved by using a center-of-momentum frame. The discussion will be somewhat simplified in that only averaged scalar values (root mean squared values) of the vector quantities electric field and velocity are used. In the case of the latter, these values represent averages of many collisions.

The force exerted on an ion is  $F = qE$  and the acceleration is  $a_i = qE/m_i$ , where  $m_i$  is the mass of the ion. In the mean time between two collisions  $\tau_c$ , the ion gains a velocity of  $qE\tau_c/m_i$ .<sup>15</sup> This velocity is not equal to the drift velocity, because the ion loses some energy in the collision. In drift experiments, no macroscopic acceleration of the ion can be observed. Instead, a steady drift velocity  $v_d$  is found. Thus, the momentum has to be transferred to drift gas molecules. The average momentum transferred to the drift gas results in

$$m_g(v_g' - v_g) = qE\tau_c, \quad (10)$$

## 2 Theoretical and methodological principles

the change of the velocity  $v_g$  before the collision to the velocity  $v_g'$  after the collision, with  $m_g$ , the mass of a buffer gas molecule.

The drift gas velocity due to the flow is negligible and since the thermal motion is randomized, averaging over many collisions leads to  $v_{g,avg} = 0$  and  $m_g v_g' = qE\tau_c$ .<sup>15</sup> By the same argument, the ion can be scattered in any direction, and thus the ion velocity after the collision is  $v_i' = v_g'$ . This argument is only fully correct for a completely elastic collision. Since by the first law of motion, the momentum has to be conserved in the collision,

$$m_i v_i + m_g v_{g,avg} = m_i v_i' + m_g v_g' . \quad (11)$$

And because on average,  $v_i \equiv v_d$ <sup>15</sup> and  $v_{g,avg} = 0$  (see above), it follows that  $v_d = (1+m_g/m_i)v_g'$ . Introducing (10) into this formula yields

$$v_d = \frac{qE\tau_c}{m_i} + \frac{qE\tau_c}{m_g} = \frac{1}{\mu} qE\tau_c , \quad (12)$$

with the reduced mass  $\mu = (m_g m_i)/(m_g + m_i)$  (throughout this work,  $\mu$  is always an actual mass, related to the atomic mass unit through  $\mu = M\mu$ ). The only variable in this expression that cannot be determined experimentally is  $\tau_c$ . This can be obtained from a basic kinetic formula. Considering a frame of reference where the position of the drift gas neutral is fixed, the ion has a relative velocity  $v_r$  and in the time  $\tau_c$ , the distance the ion travels is  $v_r \tau_c$ . The target area around the neutral is the momentum transfer or diffusion cross section  $\Omega_D$ . By the definition of the cross section, the ion will encounter exactly one neutral in the volume  $v_r \tau_c \Omega_D$  because  $\tau_c$  is the time between two collisions. This volume can be easily calculated from the number density of the drift gas

$$n_x = \frac{1}{v_r \tau_c \Omega_D} . \quad (13)$$

Combining (12) and (13) yields

$$v_d = \frac{qE}{\mu v_r n_x \Omega_D} . \quad (14)$$

The relative velocity can be calculated from  $v_r^2 = v_i^2 + v_g^2$ . Since a single collision is considered here,  $v_d$  does not vanish.<sup>15</sup> However, the motion of the neutrals is entirely thermal, thus  $m_g v_g^2/2 = 3k_B T/2$ . At very low fields, thermal energy of the ions is much higher than the energy induced by the field and it can be approximated by  $m_i v_i^2/2 = 3k_B T/2$  as well. The combination of the two leads to

$$v_r^2 = \frac{3k_B T}{\mu} , \quad (15)$$

and (14) becomes

$$v_D = \frac{\sqrt{\mu}}{\sqrt{3k_B T}} \frac{qE}{\mu n_x \Omega_D} = \sqrt{\frac{1}{3\mu k_B T}} \frac{qE}{n_x \Omega_D} . \quad (16)$$

With (7) the, the equation for the mobility

$$K = \frac{v_D}{E} = \sqrt{\frac{1}{3\mu k_B T}} \frac{q}{n_x \Omega_D} , \quad (17)$$

is obtained. The assumption of the ion energy to be purely thermal is not correct, even for moderate field strengths. The field energy is not only converted into the drift movement of the ions, a part is also transferred to the buffer gas in collisions. The expression for the ion energy is therefore

$$\frac{1}{2}m_i v_i^2 = \frac{3}{2}k_B T + \frac{1}{2}m_i v_d^2 + \frac{1}{2}m_g v_d^2. \quad (18)$$

The first term is the thermal energy, the second is the field energy resulting in drift motion and the third part is the field energy transferred to the neutrals in collisions. An effective ion temperature  $T_{\text{eff}}$  can be defined as

$$T_{\text{eff}} = T + \frac{m_g v_d^2}{3k_B}. \quad (19)$$

If  $m_i \gg m_g$ , the energy of ions is mostly determined by  $v_i$  as the light buffer gas molecules do not alter the path of the ions and do not absorb much energy. Therefore, little field energy is converted into random thermal motion of the ions. This leads to the low field criterion  $m_g v_d^2/2 \ll 3k_B T/2$ . In practice, both of these conditions are often true and  $T$  is used instead of  $T_{\text{eff}}$  because the errors are small.

Equation (17) provides a connection between the macroscopically observable quantity  $K$  and the microscopic variable  $\Omega_D$ , which is an inherent property of a given combination of drift gas and ion. At this point, some observations about the mobility can be made. First, the mobility is better considered as a factor of the value of  $E/n_x$ , not  $E$  alone. The proportionality predicted by the expression can be experimentally reproduced very well. It is also noteworthy that the mobility only depends on the square root of the reduced mass while the cross section dependence is linear. Additionally, because only the reduced mass has an influence, the term essentially becomes a constant for very large ions. The temperature dependence represented in (17) is only true if atomic ions like  $\text{Li}^+$  drift in an atomic gas like He. In this case, both species behave like rigid spheres. For almost all molecular ions,  $\Omega_D$  is a function of the temperature that is mainly dependent on the nature of the ion neutral interaction potential.

The results above were obtained using average values for speed and temperature and classical mechanics to describe the collisions instead of ion distribution functions (describing the distribution of ions with different velocities/energies) and quantum mechanics. The first order results obtained by these methods are similar, although the expression for  $T_{\text{eff}}$  and the numerical factors are different. For example, the result of the Chapman-Enskog theory, which is most often used in the literature, is

$$K = \frac{3q}{16n_x} \sqrt{\frac{2\pi}{\mu k_B T_{\text{eff}}}} \frac{1}{\Omega^{(1,1)}(T_{\text{eff}})}. \quad (20)$$

In addition of the numerical factor of  $3(\pi)^{1/2}/16$  (instead of  $3^{-1/2}$ ), the cross section is also different. While  $\Omega_D$  is evaluated at an average (thermal) energy,  $\Omega^{(1,1)}$  is the thermally averaged collision cross section (when only first order distortions of the ion distribution function are considered).

## 2.2.2 Ion-neutral interaction potentials

The momentum transfer cross section can be calculated from quantities that are commonly encountered in crossed-beam scattering experiments

$$\Omega_D(\varepsilon) = 2\pi \int_0^\pi (1 - \cos \theta) \sigma(\theta, v_r) \sin \theta \, d\theta, \quad (21)$$

where  $\varepsilon$  is the incident particle energy  $\varepsilon = \mu v_r^2/2$ ,  $\theta$  is the angle of deflection and  $\sigma(\theta, v_r)$  is the differential cross section. That is,  $\theta$  is the angle between the incident particle beam and the detector axis (which is equivalent to the direction of the scattered particle) and  $\sigma$  is the ratio of observed events at the detector versus the incident number of particles. The thermally calculated cross section can then be calculated from

$$\Omega^{(1,1)}(T) = \frac{1}{2} (k_B T)^{-3} \int_0^\infty \Omega_D(\varepsilon) e^{\frac{-\varepsilon}{k_B T}} \varepsilon^2 \, d\varepsilon. \quad (22)$$

For the numerical determination of  $\Omega_D$  from interaction potential  $V(r)$  (see following chapter), two integrations are necessary. First,  $\theta$  has to be determined from  $\varepsilon$  and the impact parameter  $b$ . The latter is defined as the shortest distance between the (stationary) target and the incident projectile trajectory before deflection. In terms of the ion-neutral distance  $r$ , the integration is

$$\theta(b, \varepsilon) = \pi - 2b \int_{r_0}^\infty \left( 1 - \frac{b^2}{r^2} - \frac{V(r)}{\varepsilon} \right)^{-\frac{1}{2}} \frac{dr}{r^2}, \quad (23)$$

where  $r_0$  is the distance of closest approach and can be determined from  $b^2/r_0^2 + V(r_0)/\varepsilon = 1$ . Instead of calculating  $\sigma$ ,  $b$  and  $\theta$  are used according to  $\sigma(\theta, \varepsilon) \sin \theta = b |d\theta/db|^{-1}$ . The cross section  $\Omega_D(\varepsilon)$  can then be obtained using

$$\Omega_D(\varepsilon) = 2\pi \int_0^\infty (1 - \cos \theta) b \, db. \quad (24)$$

Using (23) and (24), the collision cross section, and therefore the mobility, can be calculated from model potentials. These potentials are strictly only correct for atom-atomic ion interactions. More generally, they can also be applied to spherical objects. Averaged over the drift time, due their rotations, the ions can also be approximated as spherical objects.

### 2.2.2.1 Polarization limit

The longest range attractive potential is the polarization potential  $V_{\text{pol}}$ . In SI units, it is

$$V_{\text{pol}}(r) = -\frac{q^2 \alpha_d}{32\pi \varepsilon_0 r^4}, \quad (25)$$

with the dipole polarizability of the drift gas  $\alpha_d$  (which in SI units has the dimension of  $\text{Fm}^2$  instead of the usually tabulated cgs polarizability volume in  $\text{\AA}^3$ ) and the vacuum permittivity  $\varepsilon_0$ .

For  $E/n_x$  and  $T$  very close to 0, this potential becomes dominant and the result is exact unless the neutral molecule possesses a permanent dipole or quadrupole moment. The limit of vanishing field  $E/n_x$  and  $T$  is therefore called the polarization limit. The integration according to (23) and (24) has been done numerically and the expression

$$K_{pol} = \lim_{\substack{E/n_x \rightarrow 0 \\ T \rightarrow 0}} \frac{f_{pol}}{\sqrt{\alpha_d \mu}}, \quad (26)$$

where the numerically determined factor  $f_{pol}$  (in SI units) is  $f_{pol} = 5.9545 \times 10^{-37} \text{ m}^3 \text{ kg V}^2 \text{ s}^2$ , was found for the polarization limit mobility  $K_{pol}$  at atmospheric pressure.<sup>14</sup>

### 2.2.2.2 Lennard-Jones potential

A realistic potential has attractive and repulsive terms. The Lennard-Jones potential, also called the (12-6) potential, approximates the short range repulsion by an  $r^{-12}$  dependence and the long range attraction by an  $r^{-6}$  dependence

$$V(r) = \varepsilon_{LJ} \left[ \left( \frac{r_m}{r} \right)^{12} - 2 \left( \frac{r_m}{r} \right)^6 \right], \quad (27)$$

where  $\varepsilon_{LJ}$  is the depth of the potential minimum and  $r_m$  is the position of the minimum. However, the potential is often used to describe the interaction of two neutral particles. It is not very suitable for ion-neutral interactions because the attractive  $r^{-4}$  dependence resulting from the polarization energy is missing. Therefore, a combination of the polarization and Lennard-Jones potential can be introduced in the form of the (12-6-4) potential

$$V(r) = \frac{\varepsilon_{LJ}}{2} \left[ (1 + \gamma) \left( \frac{r_m}{r} \right)^{12} - 4\gamma \left( \frac{r_m}{r} \right)^6 - 3(1 - \gamma) \left( \frac{r_m}{r} \right)^4 \right], \quad (28)$$

where  $\gamma$  is a dimensionless scaling parameter that determines the relative strength of the two components.

### 2.2.2.3 Hard core (12-4) potential

The models mentioned above treat the particles as point charges, which is a good enough approximation for atomic ions but does not apply to large molecular ions. Particularly the assumption that the center of mass and the center of charge coincide is problematic. Therefore, a different potential can be used to better reflect the spatial dimensions. The (12-4) core potential

$$V(r) = \frac{\varepsilon_c}{2} \left[ \left( \frac{r_m - a}{r - a} \right)^{12} - 3 \left( \frac{r_m - a}{r - a} \right)^4 \right], \quad (29)$$

adds a rigid spherical core of diameter  $a$  to a potential that describes the short range repulsion by the usual  $r^{-12}$  dependence and the long attraction by the polarization potential. The parameter  $a$  can be roughly equated with the distance from the center of mass to the center of charge. In the limit of vanishing  $E/n_x$  and  $T$ , the potential produces the polarization potential because the well depth  $\varepsilon_c$  is defined as

$$\varepsilon_c = \frac{q^2 \alpha_d}{48\pi^2 \varepsilon_0^2 r_m^4 (1 - a^*)^4}, \quad (30)$$

with the reduced core diameter  $a^* = a/r_m$ . A reduced temperature can also be calculated from  $T^* = k_B T / \varepsilon_c$ . In the literature, the integration for (23) and (24) was done numerically. Values were tabulated for the reduced cross section  $\Omega^{(1,1)*}$  as function of  $a^*$  and  $T^*$ ,<sup>16</sup> from which the experimental cross sections  $\Omega_D$  can be calculated through

$$\Omega_D = \pi r_m^2 \Omega^{(1,1)*}. \quad (31)$$

The reduced mass of large molecular ions, where  $m_i \gg m_g$ , is mainly determined by the drift gas, thus  $\mu \approx m_g$ . But, generally speaking, heavier ions are expected to be larger and thus have a larger cross section as well and therefore, the mobility should decrease with the mass. This is not universally true but for similar molecules, e.g. in homologous series, the trend can be verified. In order to correlate the mass and the mobility, a simple assumption can be made. The assumption is the first approximation of a constant "density" of the molecular ions and therefore

$$r_m = r_0 \left[ 1 + f_x \left( \frac{m_i}{m_g} \right)^{\frac{1}{3}} \right], \quad (32)$$

where  $f_x$  is a constant describing the relative density of ion and neutral.<sup>15</sup> A slightly modified version, setting  $f_x$  to unity and introducing a constant correction factor  $z$

$$r_m = (r_0 + z m_i) \left[ 1 + \left( \frac{m_i}{m_g} \right)^{\frac{1}{3}} \right], \quad (33)$$

was also reported.<sup>17</sup>

Evaluation of experimental data recorded for several amines with the potentials mentioned above showed that a good fit could be achieved with the (12-4) core potential.<sup>18</sup>

### 2.2.3 Mobility simulations

The methods mentioned so far require that the parameters that describe the potentials are extracted from fits to experimental data. These parameters can then be used to predict the mobilities of other ions only when the ions are similar, e.g. from the same homologous series. Since computers have been widely available, several groups have worked on calculating ion mobilities based on trajectory simulations. To this end, the geometry of a molecular ion is obtained either from ab initio or semiempirical calculations. Each atom in the molecules is thus associated with a set of coordinates and the interaction with the buffer gas is calculated for each atom in the molecular ion. The molecular ion is then rotated in space and the process is repeated until a sufficient number of orientations have been considered. The interaction can be treated as an elastic scattering process between hard spheres. Alternatively, a potential for the interaction of the buffer gas particle with the atoms in the ion (e.g. the Lennard-Jones potential) can be used to calculate the trajectory.

### 2.2.3.1 Projection approximation

The hard sphere projection approximation (PA') method was the first method to be developed and widely used.

As the name implies, the method involves projecting the three dimensional structure of the molecular ion onto a two dimensional area after choosing the orientation randomly.<sup>19</sup> Each atom in the molecular ion is treated as an individual hard sphere with which the collision can occur. Each type of atom (H, C, N, O, ...) is assigned a different hard sphere radius. The radius is the sum of the radii of the atom in the molecular ion and the buffer gas atom, i.e. the largest distance for which the hard spheres would collide. The buffer gas atom can thus be treated as a point mass.

For the computation, a box of area  $A_{\text{box}}$  is put around the projected molecule. The collision cross section is then performed by Monte Carlo integration. A point on the 2D plane is chosen at random, and assigned the sample  $x_i$ . The total number of samples is  $N_x$ . The point represents the trajectory of a particle (e.g He) in relation to the molecule on the plane. The advantage of the PA' method is that no actual trajectory has to be calculated and it is therefore less computationally intensive than the other methods described below. A "hit" is counted if the sample  $x_i$  is closer to any of the atoms in the molecular ion than its corresponding hard sphere radius. The program is therefore looped over all atoms in the molecular ion and if a hit is encountered for any atom,  $x_i = 1$ . In the case of "no hit",  $x_i = 0$ . The ratio of "hits" versus all samples multiplied by the area of the box is the cross section  $\Omega'_{\text{PA}'}$  for this specific orientation

$$\Omega'_{\text{PA}'} = \frac{1}{N_x} \sum_{i=1}^{N_x} x_i A_{\text{box}}. \quad (34)$$

The number of samples can be chosen before, but it can also be optimized dynamically by comparing the standard deviations of subsequent  $\Omega'_{\text{PA}'}(N_x)$ ,  $\Omega'_{\text{PA}'}(N_x+1)$ ,  $\Omega'_{\text{PA}'}(N_x+2)$ , ...,  $\Omega'_{\text{PA}'}(N_x+n)$ , and looping until the standard deviation is below a certain value, e.g. 1 %. The molecular is then again rotated and the procedure is repeated. The rotation can be implemented by a random algorithm as well. The sequence of rotation and Monte-Carlo integration is repeated until a representative set of geometries has been evaluated. The final, orientationally averaged, cross section  $\Omega_{\text{PA}'}$  is calculated by averaging the cross sections obtained for all geometries. Mathematically succinct, the calculation can be expressed as

$$\Omega_{\text{PA}'} = \frac{1}{4\pi} \int_0^{2\pi} d\chi \int_0^{\pi} \sin \varphi d\varphi \int_0^{2\pi} d\gamma \int_0^{\infty} b M(\chi, \varphi, \gamma, b) db, \quad (35)$$

where  $\chi$ ,  $\varphi$  and  $\gamma$  are angles describing the molecules rotation in space,  $b$  is the impact parameter and  $M(\chi, \varphi, \gamma, b)$  is a function that returns unity if a hit is encountered and 0 if not.<sup>20</sup>

The quality of the calculation is based on how the hard sphere radii are obtained for each type of atom. The simplest approach is using the van-der-Waals radii of atoms. As these are calculated for neutral atoms, however, the ionic interactions are ignored. Therefore, the hard sphere radii can also be fitted to experimental data.

The values for He and C for example, were determined for  $C_{60}^+$  fullerene ions as their geometry is well known and they are very rigid. Another possibility is the calculation of the radii based on tabulated values of potential (28).<sup>21</sup>

### 2.2.3.2 Exact hard sphere scattering

In the PA' model, only the binary choice of the buffer gas particles being either scattered or not is made. The scattering angle is not considered and long range attractive interactions are completely ignored. While these simplifications produce reasonable results for the ions of small molecular, the values calculated for larger structures can be wrong. Larger molecular ions likely possess concave surfaces and so reflections and multiple collisions have to be taken into account. To account for these effects, the exact hard sphere scattering (EHS) model was developed.<sup>22</sup> The cross section  $\Omega_{\text{EHS}}$  is calculated according to (24) by determining the scattering angle  $\theta$  for multiple randomly chosen starting values of  $b$  for a single geometry and repeating the procedure for different, also randomly chosen orientations. The trajectory of an incoming buffer gas particle, including multiple deflections, is followed until the particle leaves the ionic system. The interactions are approximated by hard sphere collisions. In compressed form, the integration is done for

$$\Omega_{\text{EHS}} = \frac{1}{4\pi^2} \int_0^{2\pi} d\chi \int_0^{\pi} \sin \varphi d\varphi \int_0^{2\pi} d\gamma \int_0^{\infty} 2b(1 - \cos \theta(\chi, \varphi, \gamma, b)) db. \quad (36)$$

It should be mentioned that the EHS method still ignores all long range attractive interactions. Being reasonably efficient, computation-wise, it is still the method of choice for large polyatomic ions possessing concave surfaces.

More recently, the EHS model has been improved upon and expanded to a model incorporating scattering on electron density isosurfaces (SEDI).<sup>23,24</sup> In this model, the atoms are not approximated by rigid spheres. Instead, an appropriate cut-off value for the electron density calculated from DFT is chosen and converted into a surface around the molecule. The scattering is then calculated between the buffer gas neutral and this surface. This approach is expedient, as the electrons, and not the cores, are primarily responsible for the scattering process. The aforementioned cut-off value is scaled to reproduce the mobilities of one ion species and then used for all calculations. The cut-off value is the only adjustable parameter, eliminating the need for atom specific values like the hard-sphere radii.

In the simulation, the surface is represented by a three-dimensional mesh. The distance between the points on this mesh is systematically reduced until the values obtained for the mobility converge. That way it was found that a distance of about 0.1 Å was needed, implying that the SEDI calculation is computationally more expensive than the other methods. The cross sections were then determined using (36) and instead of evaluating the collisions of hard spheres, the buffer gas atoms were scattered on the electron density isosurface.

The results achieved by the SEDI method are in good agreement with experimental data for anions and cations alike, since the differences in the expansion of the electron cloud are accounted for, unlike in the other methods which are only parametrized for cations.



Another advantage is that SEDI is taking effects of chemical bonding, e.g. hybridization, into account. Additionally, the surfaces obtained from the electron density are much smoother than the surface resulting from approximating molecules by hard spheres. The latter may result in multiple scattering due to the unrealistic surface roughness and yield overestimated cross section values.

In the standard SEDI model, attractive interactions are still not considered. However, a hybrid method combining SEDI and trajectory calculation (see next chapter) has been demonstrated, yielding better agreement with experimental observations where attractive interactions are important.<sup>25</sup>

### 2.2.3.3 Trajectory method

The most computationally expensive calculation, but the only method that realistically incorporates the ion-neutral interaction potential, is called the trajectory method (TM).<sup>26</sup> In this approach a randomly chosen geometry of the molecular ion is chosen and the trajectory of an approaching buffer gas particle with random  $b$  is calculated. The actual movement of the particle is calculated from a Lennard-Jones potential (see 2.2.2.2) with an added ion induced dipole interaction term. A time-step is chosen and the position of the particle after this time is determined from its thermal velocity and its acceleration and deflection due to the potential. The time-step is variable and dynamically optimized based on the change of trajectory. Each trajectory is followed until the buffer gas particle is at a predetermined distance from the molecule. A sufficient number of particle trajectories with different  $b$  are recorded for each orientation and a sufficient number of orientations of the molecular ion are randomly chosen. The cross section  $\Omega_{\text{TM}}$  is thus obtained by solving (23), (24) and (22). In order to accurately determine the potential, it is necessary to obtain values for  $\epsilon_{\text{LJ}}$  and  $r_{\text{m}}$  by fitting to experimental data. For that end,  $\text{C}_{60}^+$  fullerene ions were also chosen. In order to unambiguously identify  $\epsilon_{\text{LJ}}$  and  $r_{\text{m}}$ , the mobilities recorded at different temperatures had to be evaluated.

Another approach to determine these coefficients based on the universal force field has been reported.<sup>27,28</sup> In this version, which was modified for  $\text{N}_2$ , in addition to the ion-induced dipole interaction, an ion-induced quadrupole interaction is approximated and the possible orientations of the diatomic  $\text{N}_2$  molecule are considered.

## 2.2.4 Time-of-flight mass spectrometer

ToF mass spectrometers are well known in the literature and only a brief description follows.<sup>29</sup> In a ToF mass spectrometer, an initial ion bunch is accelerated by an electric field in the extraction region and then allowed to fly unobstructedly for a defined length before hitting the detector, typically a micro-channel plate (MCP). In order to accomplish this, the mean free path of the ions has to be larger than the flight path length. If the length of the flight path is 1 m, the pressure has to be at least  $6 \times 10^{-5}$  mbar (using the cross section of  $\text{N}_2$ , see chapter 2.2.1).

Since the force on an ion is  $F = qE$  but the acceleration is  $a_i = qE/m_i$ , the constant flight velocity an ion has on its flight path depends on its  $m/z$ . Therefore, the time of flight in the field free region is also related to the  $m/z$ .

$$t_f = \frac{s\sqrt{m_i}}{\sqrt{2qU}}, \quad (37)$$

where  $t_f$  is the time of flight,  $s$  is the length of the flight path and  $U$  is the electric potential. For ions,  $q = ze$ , where  $e$  is the elementary charge. Therefore, (37) can be rearranged to

$$\frac{m_i}{z} = \frac{2t_f^2 eU}{s^2}. \quad (38)$$

Since  $s$  and  $U$  are constant during a measurement, the spectrometer can be calibrated by measuring the slope of  $t_f^2$  versus the  $m/z$  of ions of known mass.

The instrument employed in this work uses a reflectron. This is an electrostatic mirror consisting of an electrode stack placed in the flight path, which forces the ions on a U-turn to the detector. The advantage of the device, besides allowing a longer flight path on an instrument with a smaller footprint, is that it exhibits negative flight time dispersion. This is in contrast to the flight path, which possesses positive flight time dispersion. Ions with different kinetic energies before the extraction pulse will have slightly different flight times, limiting the resolution. An ion with a higher kinetic energy will penetrate deeper into the reflectron than an ion of equal  $m/z$  but lower kinetic energy. In a properly tuned instrument, both ions arrive at the detector at the same time (within a certain range of kinetic energies).

Additionally, the instrument is equipped with a Wiley-McLaren type two-stage ion extraction. This allows a spatial focusing of ions starting at different positions in the source. In the first stage the electric field is stronger than in the second stage. Ions further away from the second stage are thus accelerated for a longer time and reach the field free flight path at the same time as ions starting closer to the second stage.

The combination of reflectron and two-stage ion extraction allows a compensation of the spatial and energetic distribution of the ion bunch. The reflectron is capable of compensating the additional energetic spread of the ions due to the ion extraction. Due to the Liouville's theorem (which states that the phase-space distribution is constant in a closed system),<sup>30</sup> a complete focusing of the ions in energetic and spatial direction is not possible. However, the combination of the two systems can compensate many different effects and is therefore quite versatile.

### 2.2.5 Linear quadrupole ion trap mass spectrometer

The underlying principles of linear quadrupole ion trap mass spectrometers are well known in the literature.<sup>29,31</sup> A commercial instrument [linear trap quadrupole (LTQ) XL, Thermo Fisher Scientific, USA] was used in the studies and the vacuum side of the instrument was not subjected to any changes. As in the previous chapter, only a brief description of the operation follows.

Electrodynamic quadrupoles and multipoles focus ions on their central axis due to a radio frequency (RF) field applied to the rods. They can be used to guide ions at transitional pressures between atmospheric pressure and the vacuum of mass analyzers, e.g. in atmospheric pressure ionization (API) mass spectrometry. At pressures, where the mean free path of the ions is much lower than the axial length of the multipole, the ions are thermalized and can even be focused in the axial direction by collisions with the buffer gas. Depending on their mass, ions can be trapped up to several seconds in a multipole if they are confined axially by trapping-electrodes before and after the multipole.

The LTQ is set of three main parts (Fig. 5). The first part is the ionization source which was exchanged for a newly developed design described in chapter 4.2.2. The second part is the transfer stage and the third is the mass analyzer.

The atmospheric pressure side and the first pressure stage are connected by a transfer capillary [length = 102 mm, inner diameter (ID) = 550  $\mu\text{m}$ ] off-axis in front of skimmer. The ions are focused into the skimmer by a voltage. At this stage, the ions can acquire a high kinetic energy and undergo fragmentation if the voltage is not carefully chosen. Subsequently, the ions pass a series of multipoles in differentially pumped pressure stages before being guided into the analyzer section of the instrument.

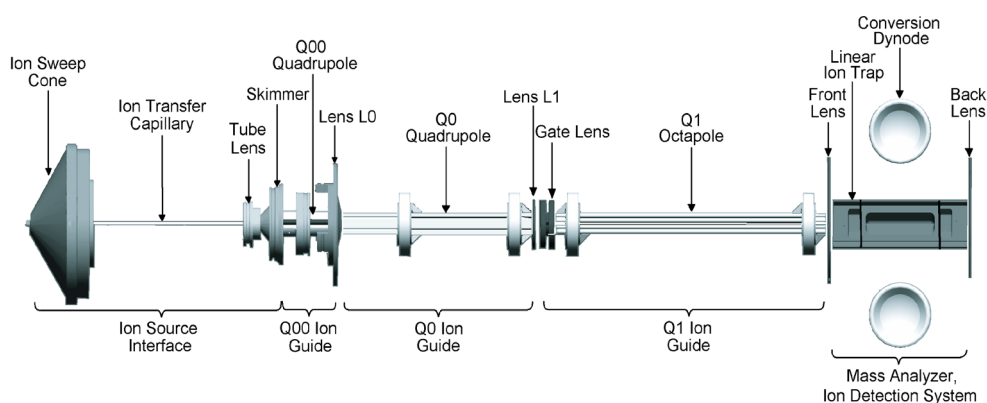


Figure 5: Scheme of LTQ mass spectrometer. The atmospheric pressure side is to the left of the transfer capillary. The first pressure stage ( $p = 1$  mbar) is between the capillary and the skimmer. The second stage is between the skimmer and lens L0 ( $p = 0.07$  mbar). The third stage is between lenses L0 and L1 (intermediate pressure between second and fourth stage). The fourth stage (mass analyzer) follows ( $p = 10^{-3}$  mbar)<sup>32</sup>

There, the ions are trapped in the linear ion trap quadrupole, which consists of three sets of hyperbolically shaped rods. The outer sets act as the trapping electrodes. In the linear trap, a pressure of  $10^{-3}$  mbar is maintained through a steady influx of He gas. The purpose of the gas is the vibrational cooling and focusing of the ions. Ions are trapped by an RF field of 1.2 MHz. After the ions are thermalized, a mass-dependent instability in the trapping field is generated by slowly systematically increasing the amplitude of the trapping voltage.

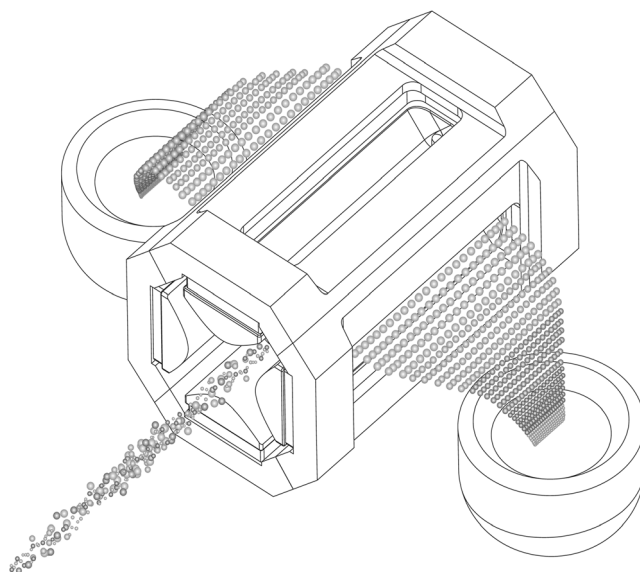


Figure 6: Visualization of mass analyzer (main segment). Ions enter the detector and exit via holes in the quadrupole rods based on their  $m/z$ , whereupon they collide with the conversion dynode<sup>32</sup>

Thus, at smaller amplitudes, ions of low  $m/z$  are ejected through slits in the rods, while heavier ions only exit at higher amplitudes. They are then sequentially analyzed by two pairs of conversion dynodes and channel electron multipliers (Fig. 6).

In addition to mass analyses, it is possible to further characterize ions in  $MS^n$  experiments by ejecting all ions except for the target ions and subsequently fragmenting them. The ions are excited by an additional alternating current, collide with the He buffer gas and undergo collision induced dissociation.

### 2.2.6 Ionization processes

A critical property of all analytical processes relying on the formation of ions and their subsequent detection is the ionization process. Depending on the choice of ionization source and parameters, the sensitivity as well as the selectivity of the detection of a specific analyte can be decisively improved. The following chapter aims to give an overview of the molecular properties that determine the ionization process and to introduce the ionization sources used.

#### 2.2.6.1 Ionization energies, electron and proton affinities

Different ionization sources produce different kinds of ions. The most obvious difference is between sources in the positive and the negative mode, which produce cations and anions, respectively. Another distinction is whether ions are formed by the addition or subtraction of electrons or by the formation of adducts with another ion. Ionization sources can also be classified according to the degree of fragmentation taking place into “hard” and “soft” ionization sources. The former term mainly refers to electron ionization (EI), where fragmentation is usually observed. The latter term is generally applied to ionization sources that produce mainly molecular ions or protonated molecules, e.g. chemical ionization.<sup>29</sup>

The formation of molecular cations is governed by the ionization energy (IE), the energy difference between the ground state of the molecule and the ground state of the ion.<sup>29</sup> The removal of an electron from a neutral is always endothermic and the value of the IE is therefore always positive. In contrast to atoms, in molecules the adiabatic IE as the difference of the ground state molecule and ion is distinct from the vertical IE resulting from the formation of vibrationally excited ions. In accordance with the Franck-Condon principle, the removal of an electron leaves the molecular ion in the geometry of the neutral. For most molecular ions, the lowest energy geometry is different from the corresponding neutral geometry and therefore, the vertical IE is larger than the adiabatic IE. While the adiabatic IE is the value that is usually tabulated, the vertical IE is the quantity actually encountered in most experiments. IE are usually determined by photoelectron spectroscopy.

Molecular anions are formed by the addition of an electron to the molecule. Stable anions can only be formed if the attachment process is exothermic. The electron affinity (EA) is the energy a molecule in the ground state gains upon addition of an electron.<sup>33</sup> The adiabatic EA is the difference between the ground state molecule and ion, while the vertical EA is the value encountered in an experiment when the ion is formed in the neutral geometry. A third quantity observed experimentally is the vertical detachment energy.

This is the energy difference between the ion in the ground state and the neutral formed in the ion geometry, which is generally energetically above the neutral's ground state. EA are also measured in photoelectron spectroscopy. As EA are usually much lower than IE, the wavelength range is different and some variations of the technique are called photodetachment spectroscopy.

In many chemical and electrochemical ionization sources, the ions are not formed as molecular ions but as protonated species instead. In these cases, the proton affinity (PA) of the molecule determines the ionization. The PA of a molecule M is the negative of the enthalpy change  $\Delta_r H$  of the reaction



In general, only polar molecules possess positive PA. To decide whether a molecule will actually form stable protonated molecules, not only the PA but the gas-phase basicity, which is the negative of the free enthalpy change  $\Delta_r G$  of reaction (39), has to be considered.<sup>34</sup>

The efficiency of the ionization process is usually described by an ionization cross section (see discussion of cross section in 2.2.1). The property depends upon the molecule and the nature of the ionizing particle that can be a photon, an electron or an ion or neutral itself.

IE, EA and PA are important quantities in API because of the charge competition taking place when multiple collisions between ions and neutral species can occur. In these collisions, the molecules with the highest IE, EA or PA (depending on the type of ion) will be preferably ionized. Therefore, the number of ions formed by molecules with lower values of these quantities will be reduced if molecules exhibiting a larger value of the respective quantity are present. This is a challenge often encountered in IM spectrometry as it can lead to the complete suppression of analytes of lower concentrations in mixtures. Charge competition is one example of IMR that can take place at atmospheric pressure. Other examples include the formation of adducts, fragmentation reactions and the formation of covalent bonds.

### 2.2.6.2 Electrospray ionization

The fundamentals of electrosprays have been studied for over a century and electrosprays have been applied e.g. in spray painting. As an ionization source in mass spectrometry, ESI was first reported by Malcolm Dole and developed into a versatile analytical technique by John Fenn.<sup>35</sup> The latter received a Nobel Prize in Chemistry in 2002 for his contributions.

ESI is a soft ionization technique for the direct formation of ions from a polar liquid at atmospheric pressure. The liquid is transported through a capillary by a pump (except in nanoelectrospray). A high voltage electric potential is applied to the metal capillary, also called the ESI emitter (Fig. 7). The electric field  $E_c$  at the tip of the emitter is

$$E_c = \frac{2V_c}{r_c \ln\left(\frac{4d}{r_c}\right)}, \quad (40)$$

where  $V_c$  is the potential applied to the emitter,  $r_c$  is the outer radius of the tip and  $d$  is the distance from the counter electrode. The diameter of the capillary has a much stronger influence on the electric field strength than the distance from the counter electrode.

The emitter can be viewed as a special kind of electrolytic cell. In the positive mode, electrons are constantly withdrawn from the solvent by oxidation reactions of its molecules, resulting in an excess of positive charges in the solution at the tip of the capillary. Charge repulsion leads to the formation of the so-called Taylor cone. Charged droplets are released from the tip of the cone. The diameter of these droplets is proportional to the waist of the cone jet but also depends on the flow rate and the solvent.

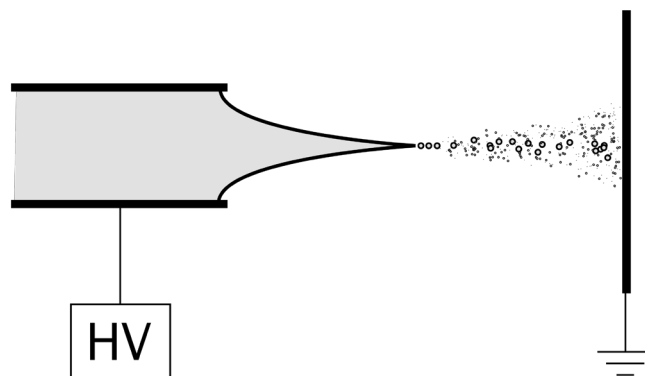


Figure 7: Scheme of ESI process. Under the influence of the high voltage (HV), the liquid forms the Taylor cone and a jet of charged droplets is ejected. Evaporation of the solvents leads to the shrinking of the droplets and in turn to fission of droplets at the Rayleigh limit and the formation of progeny droplets. This process is repeated until free ions are formed. In this example, the ions are discharged on the counter electrode that is connected to the ground.

The readily measurable total current  $I$  carried by the spray is

$$I \approx f\left(\frac{\epsilon_{\text{sol}}}{\epsilon_0}\right) \sqrt{\gamma \kappa Q \frac{\epsilon_{\text{sol}}}{\epsilon_0}}, \quad (41)$$

where  $\gamma$  is the surface tension,  $\kappa$  is the conductivity of the solution,  $Q$  is the volumetric flow rate and  $\epsilon_{\text{sol}}$  is the permittivity of the solvent and  $f(\epsilon_{\text{sol}}/\epsilon_0)$  is a tabulated function that is 18 for common solvents such as water, methanol and acetonitrile.<sup>36,37</sup>

The radius  $r_{d,0}$  of the initial droplets is

$$r_{d,0} \approx \sqrt[3]{\frac{Q\varepsilon_{\text{sol}}}{\kappa}}, \quad (42)$$

and the charge carried by one droplet  $q_d$  is

$$q_d \approx 5.6\pi \sqrt{\varepsilon_0 \gamma r_{d,0}^3} \approx 5.6\pi \sqrt{\varepsilon_0 \gamma \frac{Q\varepsilon_{\text{sol}}}{\kappa}}. \quad (43)$$

Equations (41) through (43) were determined in the cone-jet mode. The equations show that the solvent influences the ionization process. The analyte can also have an influence, as can other substances present, if they affect the values of  $\gamma$ ,  $\kappa$  or  $\varepsilon_{\text{sol}}$ . This is especially true in the case of electrolytes or surfactants. From (42), the volume of the initial droplets  $V_{d,0}$  is

$$V_{d,0} \approx \frac{4}{3}\pi \frac{Q\varepsilon_{\text{sol}}}{\kappa}. \quad (44)$$

Combining this with (43) shows that the charge density of the initial droplets is decreasing with the flow rate while it is increasing with the conductivity as

$$\frac{q_d}{V_{d,0}} \approx 4.2 \sqrt{\frac{\varepsilon_0 \gamma \kappa}{Q\varepsilon_{\text{sol}}}}. \quad (45)$$

The frequency of droplet formation can be calculated from  $I/q_d$ . According to (41) and (43), the frequency should not change with the flow rate since both quantities vary with the square root of  $Q$ . However, it should increase with the conductivity.

When the droplets are traveling away from the emitter, the solvent evaporates and the size of the droplet decreases. The rate of shrinking increases as the droplet becomes smaller, since the reduced radius  $r_d$  results in an increased vapor pressure  $p_i$  of the solvent according to the Kelvin equation<sup>1</sup>

$$p_i = p'_i \exp\left(\frac{2\gamma V_m}{r_d RT}\right), \quad (46)$$

where  $p'_i$  is the vapor pressure of the liquid at a planar surface,  $V_m$  is the molar volume of the liquid and  $R$  is the gas constant. Applying this equation to methanol reveals that while  $p_i$  of the droplet of  $r_d = 20 \mu\text{m}$  is 17.5 kPa, virtually identical to the value of a planar surface (16.9 kPa)<sup>38</sup>, the value for a droplet of  $r_d = 1 \mu\text{m}$  is already 35.3 kPa.

While the droplet is shrinking, the charge remains constant. Thus, the charge density increases until the Rayleigh limit is reached when the charge  $q_{\text{Ry}}$  on the droplet is

$$q_{\text{Ry}} = 8\pi \sqrt{\varepsilon_0 \gamma r_d^3}. \quad (47)$$

At this point, in a process called Coulomb fission, the droplet releases a jet of small, monodisperse progeny droplets which comprise only about 1-2 % of the droplets mass but carry 15-20 % of its charge.<sup>35</sup> The process is repeated until free, gaseous ions are formed. It was found experimentally that about 40 % of the solvent evaporates between successive fissions.

The formation of free ions can proceed via different ways. The two models most often used to describe the ion release are the ion evaporation model (IEM) and the charged residue model (CRM). The CRM is useful in the case of very large analytes, where the complete evaporation of solvent will ultimately lead to the gas-phase macromolecule that retains the charges the droplet was carrying. The IEM is relevant when the analyte molecules are small (comparable to the solvent). When the droplet reaches a radius of less than 10 nm, the analyte ions are ejected instead of Coulomb fission taking place.<sup>39</sup> This process is called ion evaporation.

### 2.2.6.3 *Resonance-enhanced multiphoton ionization*

There are multiple laser-based ionization techniques. The most widely used today is undoubtedly MALDI. But there are several other methods that preceded it. One technique that was initially developed for the ionization of samples in the vacuum of mass spectrometers is REMPI.<sup>40,41</sup> The IE of most organic molecules are in the range of 6-13 eV.<sup>42</sup> Using VUV radiation, this energy can be transferred by a single photon. This method is called single photon ionization (SPI).

However, the energy of a photon of a wavelength of  $\lambda = 266$  nm emitted by a frequency-quadrupled Nd:YAG laser, a laser commonly encountered, is 4.66 eV. Therefore, most organic molecules can only be ionized by the absorption of multiple photons. Thus, short and ultrashort laser pulses are used. The ionization process is especially efficient if a first photon absorbed by the molecule excites it to an electronically excited state (Fig. 8). If the energy difference between this excited state and the IE is smaller than the photon energy, the absorption of another photon leads to an electron in a state above the IE. Thus, the molecule dissociates into the molecular cation and a free electron. This process is called (1+1) REMPI. This can either be achieved by a one-color or a two-color experiment. In the latter case, a first laser is tuned to the wavelength of the absorption maximum (e.g. for the  $S_0 \rightarrow S_1$  transition in Fig. 8) and a second laser is used to ionize the molecule. If only one laser is used, only molecules that possess an intermediate state close enough to the ground state but also to the IE can be ionized. Therefore, REMPI is a selective ionization source. By varying the wavelength of a laser, different molecules are efficiently ionized.

In addition to this simple two photon ionization, processes involving multiple photons, such as (2+1) REMPI (where the intermediate state is only reached by the absorption of two photons involving a virtual state) and (1+1+1) REMPI (via two intermediate states) also exist. However, these are less efficient and require higher laser energies.

As is indicated in the figure, the excitation can also lead to a vibrationally excited state. Similarly, the ionizing photon can impart an excess energy that can result in the fragmentation of the molecule. Additional fragmentation can arise if the laser energy is very high. In a process described by the ladder-switching mechanism, the ion that is formed can absorb additional photons and be in turn fragmented.<sup>43</sup> This can be used experimentally as a way of intentional fragmentation for the identification of substances.



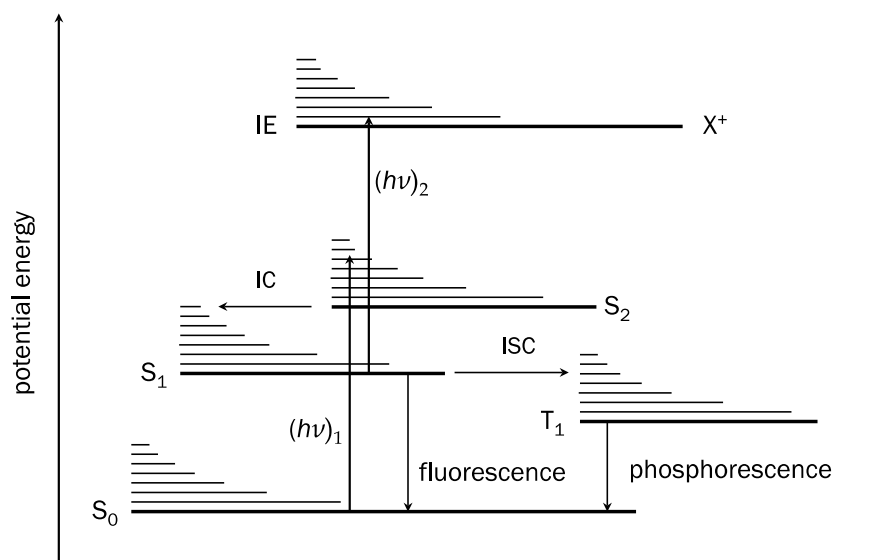


Figure 8: Simplified Jablonski diagram of the processes upon the absorption of photons by a molecule,  $S_0$  - ground state,  $S_1$  - first excited singlet state,  $S_2$  - second excited singlet state,  $(h\nu)_1$  - first photon,  $(h\nu)_2$  - second photon  $T_1$  - triplet state,  $IC$  - internal conversion,  $ISC$  - intersystem crossing,  $IE$  - ionization energy,  $X^+$  - ionized molecule

In addition to being used as a simple ionization source, REMPI can also be used for spectroscopy. Using tunable lasers, the ionization efficiency as a function of the REMPI wavelength can be recorded. As this efficiency is directly linked to the transition probability for the first absorption a spectrum is obtained. In the vacuum, rotationally resolved spectra can thus be obtained.

REMPI can also be employed at atmospheric pressure, where the term atmospheric pressure laser ionization (APLI) is sometimes used. It was first introduced into IM spectrometry by Lubman and Kronick.<sup>44</sup> Using readily available Nd:YAG lasers, the method has most successfully been used for the study of aromatic compounds such as PAH and BTEX.<sup>45</sup> Using a molecule such as toluene as a dopant that is ionized by the laser and can ionize the analyte by IMR, the method can also be used for other substance classes, such as explosive compounds or neuroleptics.<sup>46,47</sup> While usually limited to gas phase samples, the introduction of a vaporizer similar to APCI, the scope of the technique could be expanded to the investigation of liquid samples.<sup>48</sup>

#### 2.2.6.4 Electron attachment spectroscopy

In addition to photoelectron spectroscopy, another technique to gain information about molecular anions is electron attachment spectroscopy. While the technique was not used in this work, literature data is used in the interpretation of the IMR and therefore a short overview shall be given here. The basis of this method is a crossed beam experiment between a beam of neutral analyte molecules and a beam of energy selected electrons. The anions formed as a result are mass-spectrometrically recorded as a function of the electron energy. The vacuum device used to generate electrons of a well-defined energy is called electron monochromator.

There are different types, including the trochoidal electron monochromator, in which the electrons emitted by a heated filament are aligned by the homogeneous electric field of a pair of Helmholtz coils and focused by a stack of electrodes.<sup>49</sup> In this configuration, the electrons are deflected on a trochoidal path and are dispersed depending on their velocities. They then reach an aperture that only permits electrons of a well-defined velocity into the reaction chamber of the instrument. The velocity, and therefore the kinetic energy, can then be selected by changing the strength of the magnetic field. It is also possible to generate electrons with energies very near 0 eV. After the attachment takes place, the resulting ions are detected. The attachment can either be associative, forming molecular anions, or dissociative (dissociative electron attachment, DEA), in which case fragments are observed. The resulting ion yield curves of a specific ion versus the electron energy allow conclusions about the attachment process.

The results obtained at very low electron energies, corresponding to thermal energies encountered in IM spectrometry at atmospheric pressure, are of special interest in this thesis. The mass spectra obtained at these energies correspond to the primary ions produced in the IM spectrometer. In the literature, some examples of explosives have been described.<sup>50</sup>

### ***2.2.6.5 Atmospheric pressure chemical ionization by soft X-radiation***

The first work on the use of X-radiation as an ionization source was performed by Thomson and Rutherford, shortly after the discovery of X-rays.<sup>51</sup> A century later, Bruker introduced a miniaturized X-ray ionization source into IM spectrometry.<sup>52</sup> Only some work has been published on X-ray ionization in mass spectrometry<sup>53</sup> and IM spectrometry.<sup>54</sup> In this work, the X-ray source developed by Bruker was utilized in the generation of ions. In IM spectrometry, the detection scheme with this source involves the production of primary ions by X-ray photoionization followed by APCI of the analyte molecules. The source employed in this work uses 4 kV of acceleration voltage for the electron gun and a Rh target mounted directly on a Be window. The resulting output spectrum is composed of continuous bremsstrahlung with a maximum photon energy of 4 keV superimposed with Rh emission lines at 2.7 and 2.8 keV, which are the Rh L $\alpha$  and L $\beta$ -lines as the electron energy is below that of the Rh K-lines. This energy range

The interaction of an X-ray with the N<sub>2</sub> and O<sub>2</sub> molecules of the air can result in Rayleigh or Compton scattering and cause ionization by the photoelectric effect. In the range of very soft X-rays, only the latter is observed. Inelastic scattering of an X-ray photon by N<sub>2</sub> or O<sub>2</sub> with an energy greater 400 eV (the binding energy of a K-shell electron in N<sub>2</sub>) leads to the emission of a photoelectron with a kinetic energy equal to the difference to the incident photon. In the case of the characteristic Rh line, the photoelectron energy is 2.4 keV. Subsequently, the K-shell is repopulated by an electron from higher shell, e.g. the L-shell. The energy difference can be released as a photon. However, the probability for the 2p $\rightarrow$ 1s fluorescence in N<sub>2</sub> is below 5 %.<sup>55</sup> Instead, the excess energy leads to the emission of an Auger electron, which is the dominant process for all light elements. In N<sub>2</sub>, K-LL Auger electrons of 310-390 eV were observed and the main spectral feature was found at 362.5 eV.<sup>56</sup> In O<sub>2</sub>, Auger electrons of 450-520 eV were observed with the most intense feature at 500.3 eV.

The photoelectrons, as well as the Auger electrons possess an energy still high enough to ionize further air molecules. Therefore, the majority of the air molecules are not ionized directly by X-ray photons but in a cascade of inelastic collisions with electrons. The result of this process is the formation of a number of ions, namely  $N_2^+$ ,  $N_2^{2+}$ ,  $N^+$  and  $N^{3+}$  and the oxygen analogues.

Partial cross sections  $\sigma_{PI}$  for dissociative photoionization of  $N_2$  and  $O_2$  into the different fragments were determined between in the X-ray energy  $E_{hv}$  range of 100-800 eV.<sup>57</sup> The cross sections vary over two orders of magnitude. At  $E_{hv} = 799.4$  eV, a total cross section  $\sigma_{PI}(N_2) = 2.81 \times 10^{-19}$  cm<sup>2</sup> and partial cross sections of  $\sigma_{PI}(N^+) = 2.06 \times 10^{-19}$  cm<sup>2</sup>,  $\sigma_{PI}(N_2^{2+}) = 6.90 \times 10^{-20}$  cm<sup>2</sup>,  $\sigma_{PI}(N_2^+) = 4.1 \times 10^{-21}$  cm<sup>2</sup> and  $\sigma_{PI}(N^{3+}) = 2.25 \times 10^{-21}$  cm<sup>2</sup> were obtained. Thus, in nitrogen, the singly charged molecular ions are formed in addition to atomic ions. In  $O_2$ , the partial cross sections of the fragmentation channels are far larger than of the molecular ion formation.

At atmospheric pressure, the multiply charged ions can transfer the additional charges to  $N_2$  forming additional  $N_2^+$ .  $N^+$  does not react with neutral  $N_2$  because the  $IE(N) = 14.53$  eV is below that of  $IE(N_2) = 15.58$  eV.<sup>58</sup> Instead, it forms  $N_3^+$  adducts. If present,  $H_2O$  is ionized by electron transfer yielding  $H_3O(H_2O)_n^+$ . These are the same primary ions commonly observed in radioactive IM spectrometry in the positive mode.

The high kinetic energy electrons are thermalized in inelastic collision with the drift gas molecules before undergoing associative electron attachment to  $O_2$  ( $EA(O_2) = 0.44$  eV).<sup>59</sup> The  $O_2(H_2O)_n^-$  ions are the primary ions in the negative mode.



### 3 EXPERIMENTAL

This chapter is divided into individual sections dedicated to the different experimental setups used throughout this work. General remarks that pertain to all experiments follow.

IM spectrometers were assembled in the faculty workshop. Specifics are given in the corresponding sections. Several mass flow controllers (MFC; Model 5850E, Brooks Instruments, Hatfield, PA, USA) set to different flow ranges were used to supply gases. All gas fittings were obtained from Swagelok, Solon, OH, USA. A TDS 5052 oscilloscope (Tektronix, Beaverton, OR, USA) was used to record spectra. The amplifier used was a DLCPA-200 (Femto Messtechnik, Berlin, Germany). Multiple variable high voltage supplies (Applied Kilovolts, Goring-by-Sea, UK) were used. Heating cables, PT100 sensors and temperature controllers were obtained from Horst, Lorsch, Germany. A digital delay generator DG645 (Stanford Research Systems, Sunnyvale, CA, USA) was used for controlling the temporal sequence of some experiments. Pyroelectric Energy Detectors (Sirah Lasertechnik, Grevenbroich, Germany) were used to measure laser energies. All optical components used were acquired from Thorlabs, Newton, NJ, USA, except where stated. Ion trajectory simulations were carried out with the electrostatic field solving software Simion 8.0 (Scientific Instrument Services, Ringoes, NJ, USA) and buffer gas interaction was incorporated using the statistical diffusion simulation (SDS) model.<sup>60</sup> The planning and design of the custom ionization chambers and additional parts was done using the computer-aided design software SOLIDWORKS (Dassault Systèmes SOLIDWORKS, Waltham, MA, USA). Quantum chemical computations were carried out using the Gaussian 09 package.<sup>61</sup> Most data analyses were done using the software OriginPro (OriginLab, Northampton, MA, USA). The incorporated scripting language LabTalk was used for automated evaluation, including data fitting.

Unless otherwise stated, all substances were acquired from Sigma-Aldrich Germany. All gases (including synthetic air, in the following simply referred to as air) were obtained from Air Liquide, Düsseldorf, Germany.

#### 3.1 Laser-induced fluorescence study of rhodamine 6G in the electrospray process

The experimental setup of the experiment is shown in figure 9. The laser used was a Nd:YAG laser NL640/SH/TH ( $\lambda = 355$  nm, pulse duration ca. 5 ns, pulse energy 100  $\mu$ J, repetition rate 10 kHz; EKSPILA, Vilnius, Lithuania) which was guided by two dielectric mirrors as a means of diverting the residual first and second harmonics radiation. An iris diaphragm was used to restrict the beam diameter to 2 mm. The commercial ESI probe of an Ion Max source (Thermo Fisher Scientific, Waltham, MA, USA) was fitted with a gauge 34 stainless steel capillary [ID = 83  $\mu$ m, outer diameter (OD) = 184  $\mu$ m]. The source was fixed to a translation stage so that the distance to the counter electrode, an Al disk (diameter = 80 mm) connected to ground, could be varied. Samples were supplied using a syringe pump (ALADDIN-1000, World Precision Instruments, Sarasota, FL, USA). The detection system, perpendicular to both laser beam and spray direction (see Fig. 9), consisted of a commercial objective lens lens (AF NIKKOR 50 mm, 1:1.8, Nikon, Tokyo, Japan) attached to a slit spectrograph (Dados Spectrograph, 200 lines/mm grating; Baader Planetarium, Mammendorf, Germany).

This instrument possesses three slits of different thicknesses cut into a mirror. A camera (Tucsen 1.3C; Tucsen Imaging Technology, Fujian, China) mounted to a viewport allows the observation of which portion of the spray is analyzed by the spectrograph. After passing the spectrograph, the light is directed onto an EMCCD camera (iXON<sup>EM+</sup> A-DU888-DC-UVB; Andor Technology, Belfast, GB). The obtained image was wavelength calibrated using residual second ( $\lambda_{em,2nd} = 532$  nm) and third harmonic scattered light ( $\lambda_{em,3rd} = 355$  nm). Areas of similar intensity on each slits were averaged (refer to Fig. 13, right in chapter 4.1.1.3 for an example of the raw data collected, the averaging was done in y-direction). R6G was obtained from Exciton, Dayton, Ohio, USA.

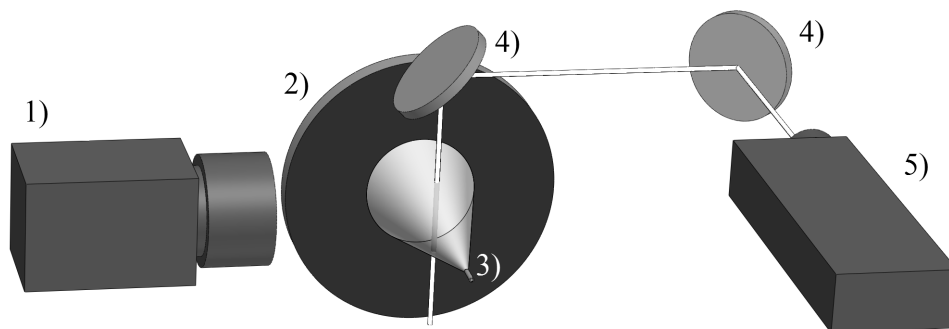


Figure 9: Experimental setup of ESI-LIF experiment: 1) spectrograph/EMCCD camera, 2) counter electrode, 3) ESI capillary, 4) dichroic mirrors, 5) Nd:YAG laser

### 3.2 Etalon spectrometer

As the aim of this work was the establishment of a novel type of spectrometer, the working principal of the instrument is discussed in the results section (chapter 4.1.2). Here, only a description of the parts used will be given. The optical path consisted of a variable slit set to 50  $\mu\text{m}$ , a collimating lens (focal length = 100 mm), the etalon (custom made to specifications by Laseroptik Garbsen, Germany; reflectivity 97%, thickness 200  $\mu\text{m}$ , diameter 1", wavelength range 350–650 nm), a prism (Thorlabs F2, 50 mm base length), a grating (Thorlabs, 600 grooves/mm, 28.78° blaze angle), a commercial objective lens (DX AF-S Nikkor, 55–200 mm, Nikon, Tokyo, Japan) mounted to a CCD camera (Model ST-8300M/C, 3326  $\times$  2504 pixels; Diffraction Limited/Santa Barbara Instrument Group (SBIG), Ottawa, Canada). The source light was projected onto the slit by a collimator assembly consisting of a spherical and a cylindrical lens. A Pen-Ray Ne discharge lamp (Ultra-Violet Products (UVP), LLC, Upland, CA, USA) and a conventional incandescent light bulb were used for the spectral calibration (wavelength and intensity, respectively).

Raman measurements were carried out using a Nd:YAG laser (NL640/SH/TH,  $\lambda = 532$  nm, pulse energy 200  $\mu\text{J}$ , repetition rate 10 kHz; EKSPILA, Vilnius, Lithuania) and a notch filter (Thorlabs NF533-17,  $\lambda_{center} = 533$  nm,  $\Delta\lambda_{FWHM} = 17$  nm) was used to suppress Rayleigh scattered light. The LIBS measurements were performed using another Nd:YAG laser (Minilite I,  $\lambda = 1064$  nm, pulse duration ca. 6 ns, repetition rate 10 Hz, pulse energy 5 mJ; Continuum, San Jose, CA, USA). LIBS reference measurements were recorded with a commercial echelle spectrometer (ARYELLE-Butterfly prototype, LTB Lasertechnik Berlin, Berlin, Germany).

### 3.3 REMPI-ToF mass spectrometer with reduced pressure ionization chamber

The reflectron ToF mass spectrometer used for this part of the thesis was an RFT10 (Stefan Kaesdorf, Munich, Germany). Stefan Kaesdorf also designed and built the reduced pressure ionization chamber. The experimental setup is shown in figure 10. Gaseous analytes enter via a 1/16" stainless steel capillary (ID = 254  $\mu\text{m}$ ). The ions were created in the chamber operated at  $p_1 = p_2 = 0.5$  mbar by the interaction with either of two lasers. The first one was a Nd:YAG-pumped OPO (NT342A-20-SHWW, EKSPILA, Vilnius, Lithuania), the second one was a dye laser (PrecisionScan, Sirah Lasertechnik, Grevenbroich, Germany) using rhodamine B as the laser dye ( $\lambda_{\text{pump}} = 532$  nm,  $\lambda_{\text{max,dye}} = 302.6$  nm, laser energy 5 mJ). The ions are propelled by the electric fields between  $E_1$ ,  $E_2$  and  $E_3$  towards the 500  $\mu\text{m}$  pinhole in  $E_3$ . They are then focused by  $E_4$  to the spot between the repeller  $E_5$  and the extraction electrode  $E_6$  in the ion extraction chamber at  $p_3 = 10^{-5}$  mbar. They pass several ion optic elements (not shown) and enter the reflectron in the reflectron chamber at  $p_4 = 10^{-7}$  mbar before hitting the detector, an MCP (Standard Chevron MCP Set, type BUI-S40-10-D-SET, pore size 10  $\mu\text{m}$ , active area diameter 40 mm; BURLE Electro-Optics, Sturbridge, MA, USA). The field free flight path of the ToF mass spectrometer is 876 mm.

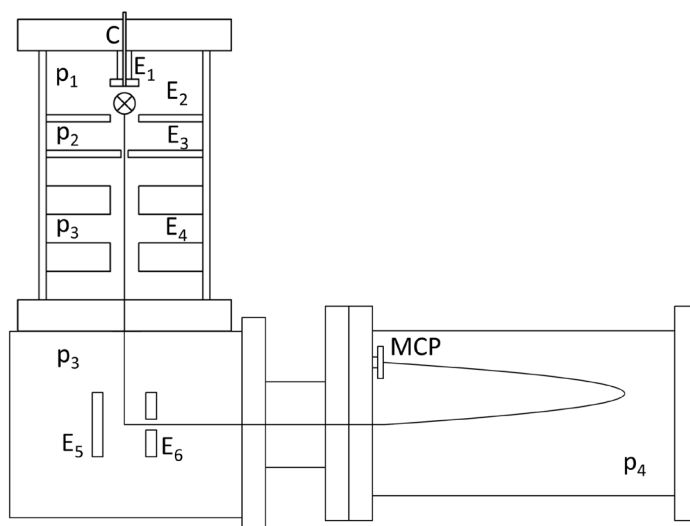


Figure 10: Scheme of ToF mass spectrometer with reduced pressure ionization chamber, C: capillary for sample introduction, laser beam perpendicular to image plane marked by cross,  $E_{1-3}$ : electrodes on reduced pressure side,  $E_4$ : ion optics,  $E_5$  and  $E_6$ : ion extraction,  $p_{1-2}$ : pressure ranges in reduced pressure chamber (for the experiments reported  $p_1 = p_2$ ),  $p_3$ : ion extraction chamber pressure,  $p_4$ : reflectron chamber pressure, MCP

### 3.4 Ion mobility mass spectrometer

In chapters 4.2.2 and 4.2.3 two experimental setups are introduced, that combine IM and mass spectrometer. While the atmospheric pressure chambers were built in-house, the mass spectrometer used was a commercial linear quadrupole ion trap mass spectrometer (LTQ XL, Thermo Fisher Scientific, Waltham, MA, USA). The LTQ is equipped with ion transfer optics and pressure stages for the transfer of ions from atmospheric pressure to the vacuum of the mass analyzer (refer to chapter 2.2.5 for a functional description of the instrument).

Two modes of operation were used. The first mode, called the “normal mass range”, allows the detection of ions between  $50 < m/z < 2000$ . This is the mode used for most experiments. In order to see smaller ions it is necessary to use the “low mass range”. In this mode, it is possible to detect ions between  $15 < m/z < 200$ . The difference between the modes is the configuration of the transmitting ion optics and the trapping potentials in the instrument. The LTQ features a third mode, the “high mass range” for the detection of ions between  $100 < m/z < 4000$ . However, this mode was not used in the experiments reported here.

The construction of a dual gate IM spectrometer that can be coupled to the LTQ was an aim of this thesis. Therefore, the spectrometer is discussed in the results section. The ESI source used for the experiments was the ESI probe of the Ion Max (Thermo) source equipped with a gauge 32 steel capillary (ID = 108  $\mu\text{m}$ , OD = 235  $\mu\text{m}$ ).

Alternatively, the instrument could be equipped with an APLI source. In this source, the substances were introduced into the ionization chamber via a vaporization tube which belonged to the standard APCI source of the LTQ. A laser beam was permitted into the ionization chamber via laser windows. Two different lasers were used for the experiments, one was a Nd:YAG laser operating at  $\lambda = 266 \text{ nm}$  (NL204/FH, pulse energy 300  $\mu\text{J}$ , repetition rate 50 Hz; EKSPILA, Vilnius, Lithuania) and the second was the Nd:YAG-pumped OPO mentioned above.

The design was shortened to only the ionization chamber, omitting the ion gates, for the X-ray ionization source. The construction of this chamber is also discussed in the result section. The X-Ray tube used in the experiments was provided by Bruker Daltonic, Leipzig, Germany. The source is a miniaturized design featuring an electrostatic, thermionic electron gun (hole anode) housed in a ceramic tube which has electrical feedthroughs on one side and a 125  $\mu\text{m}$  Be window with the Rh target directly on the inside of this window on the other. The tube has a diameter of ca. 8 mm and a length of 40 mm. The electron gun is operated with 4 kV. The power consumption is 720 mW.

The thermodesorption unit used for these experiments consists of a 1/16" T-connector (Swagelok, Solon, OH, USA) that is heated to 250  $^{\circ}\text{C}$  by a heating cable (Fig. 11). On one side of the T-connector, the sample gas is introduced. On another side, a 1/16" stainless steel capillary (ID = 1,016 mm) is placed that leads into the ionization chamber. On the third side, a syringe can be inserted through a sleeve, sealing the assembly. The syringe has a gauge 26s (ID = 127  $\mu\text{m}$ , OD = 474  $\mu\text{m}$ ) needle that reaches into the 1/16" capillary entering the chamber. That way, the sample gas is flowing laminarly around the needle.

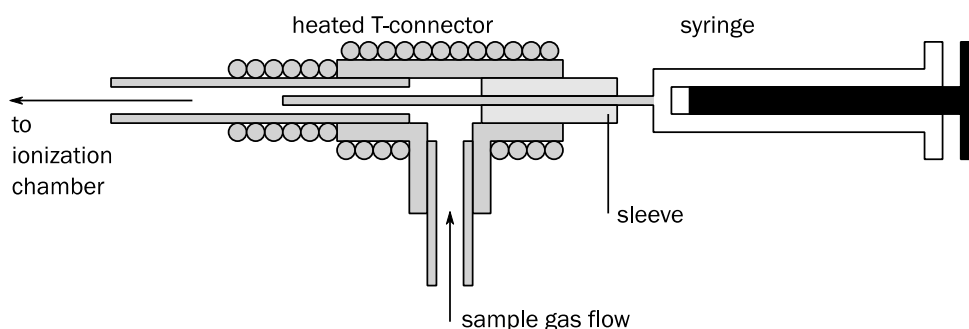
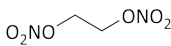
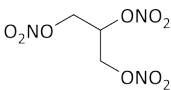
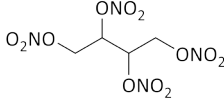
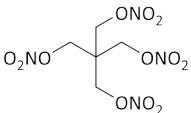


Figure 11: Scheme of thermodesorption unit



Table 1: Structures of investigated alkyl nitrates and their vapor pressures

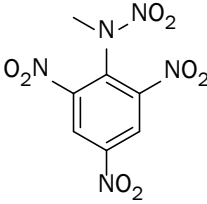
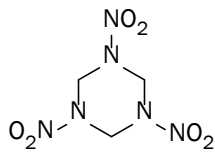
Name	Ethylene glycol dinitrate	Nitroglycerin	Erythritol tetranitrate	Pentaerythritol tetranitrate
Abbreviation	EGDN	NG	ETN	PETN
Structure				
Molar mass in g/mol	152.1	227.09	302.11	316.14
Vapor pressure in Pa, 25 °C	10.2 <sup>a</sup>	0.0641 <sup>a</sup>	3.19 × 10 <sup>-3</sup> <sup>b</sup>	1.55 × 10 <sup>-6</sup> <sup>a</sup>

<sup>a</sup>Reference<sup>62</sup>, <sup>b</sup>Reference<sup>63</sup>

This heating cable reaches up to this part of the capillary ensuring a homogeneous temperature in the entire unit. The analyte, solved in 5 µl of hexane is injected via the syringe and vaporized in the gas stream. The sample gas flow rate was controlled by an MFC. Gas mixing was achieved by using an individual MFC for each gas. The flows were chosen to represent the desired ratios while the sum flow was kept constant. Both gas flows were joined in another T-connector.

Two classes of explosive compounds were investigated. The first class are alkyl nitrates (table 1). Their characteristic group is R-O-NO<sub>2</sub>. A second class of explosives are nitroaromatic compounds such as TNT. The nitro group R-NO<sub>2</sub> is directly attached to the aromatic ring. A third class are nitramine compounds, where the nitro group is bonded to an amine, yielding R<sup>1</sup>-NR<sup>2</sup>-NO<sub>2</sub>. The focus of the work was on the alkyl nitrate compounds. Therefore, only two examples of these compounds were investigated (table 2). All explosives were provided by Bruker.

Table 2: Structures of investigated nitramine compounds and their vapor pressures<sup>62</sup>

Name	2,4,6-Trinitrophenyl-methylnitramine	1,3,5-Trinitroperhydro-1,3,5-triazine
Short name	Tetryl	RDX
Structure		
Molar mass in g/mol	287.15	222.12
Vapor pressure in Pa, 25 °C	8.68 × 10 <sup>-7</sup>	4.40 × 10 <sup>-7</sup>

### 3 Experimental

IM spectrometric measurements of the explosive compounds were carried out by A. Beil at Bruker Daltonic in Leipzig. The instrument used was a prototype of the commercial RoadRunner IM spectrometer equipped with the same ionization source and a modified Raid (both Bruker).

## 4 RESULTS AND DISCUSSION

The following results section is divided into two parts. The first part presents experimental investigations that utilize spectroscopic techniques. The second part will deal with IM and mass spectrometry. The two parts are, however, not entirely separate. The main intention of the first part, particularly the chapter immediately following, is to demonstrate how spectroscopic techniques can be utilized to gain a deeper understanding of the different processes taking place during the ionization of compounds and the effects of different parameters of the ionization sources. In turn, this can lead to improvements of the ionization techniques employed in IM and mass spectrometry. These can either take the form of increasing the sensitivity of the method as a whole or by offering assistance in choosing the right conditions for a specific analysis.

### 4.1 Spectroscopy

Spectroscopic investigations can yield insights into processes that are relevant to IM and mass spectrometry. The ESI process is an example of an ionization process that, although widely used for analytical applications, is not yet completely understood. Thus, in the first chapter, LIF spectroscopy was used to elucidate the underlying processes further, particularly as they pertain to IM spectrometry.

The second chapter of the spectroscopy part details a novel type of high resolution spectrometer, based on the separation of light in two dimensions, utilizing two different separation principles. In one dimension, a coarse spectrum is produced by the combination of a prism and a grating. In the second dimension, a Fabry-Pérot etalon is used to achieve a resolution of up to 25 pm. The analytical application of this spectrometer is demonstrated with examples of Raman and LIBS.

#### 4.1.1 Laser-induced fluorescence study of rhodamine 6G in the electrospray process

As mentioned above, this chapter deals with the application of LIF spectroscopy to the investigation of the ESI process. Parts of these results have been published in the *Zeitschrift für Physikalische Chemie*.<sup>64</sup>

##### 4.1.1.1 Experimental means and goals

ESI is one of the ionization techniques widely used in mass spectrometry due to its simplicity, applicability to liquid samples and the ability to softly ionize polar compounds. It has also been introduced into IM spectrometry and was used in our group.<sup>65</sup> The underlying processes of ESI are not yet completely understood and the influence of parameters such as electrical fields applied, solvent composition and flow rates, supportive gas flow rates and the effects of electrolytes may alter the observed processes. The aims of the investigations reported here is to improve the understanding of these processes and use these insights for optimizing the design of the ionization regions of ESI-IM spectrometers. An understanding of the temporal and spatial evolution of the spray cone and the ion release is crucial in achieving this goal. A twofold detection scheme is employed. An imaging strategy is used to evaluate the spatial distribution of the spray and a spectroscopic technique aids the differentiation between solvated and free ions.

As shown in chapter 2.1.1 (Fig. 2), the R6G ion exhibits a significant hypsochromic shift between the spectrum of the gas phase and that of an ethanolic solution. The shift was also found comparing the spectra of R6G ions still solvated in the droplets of the electrospray and that of the free R6G ions in the gas phase.<sup>66</sup> This observation provided the means to investigate the evolution of the electrospray droplets during the ESI process in a spatially resolved way as well as the influence of important parameter on this process. The fluorescence of R6G in MeOH solution exhibits a maximum at  $\lambda_{\text{max,sol}} = 555 \text{ nm}$ . The maximum of the emission in the gas phase is shifted to  $\lambda_{\text{max,free}} = 505 \text{ nm}$ .

#### 4.1.1.2 Prior results

The results described below were preceded by experiments carried out by M. Zühlke and K. Zenichowski. A setup consisting of an ESI source and a flat counter electrode was illuminated by the beam of a frequency tripled Nd:YAG laser ( $\lambda_{\text{ex}} = 355 \text{ nm}$ ). The light emitted perpendicularly to the laser beam was observed with an EMCCD camera. In order to avoid the scattering and differentiate between the emission of solvated and free R6G ions, a liquid crystal tunable transmission filter was placed in front of the spray. In this way, different regions of the spray could be observed by changing the position of the laser relative to the capillary. In these experiments, it could be shown that along the center axis of the spray and closer to the capillary, solvated droplets prevail, while towards the outside of the spray cone and farther away from the tip, gaseous dye can be found at higher abundance. An advantage of this setup is that spatial information is garnered in two dimensions at the cost of a limited spectral resolution due to the filter. Further details about the results of the studies with this setup can be found in the paper.<sup>64</sup>

#### 4.1.1.3 Image acquisition and identification of observed features

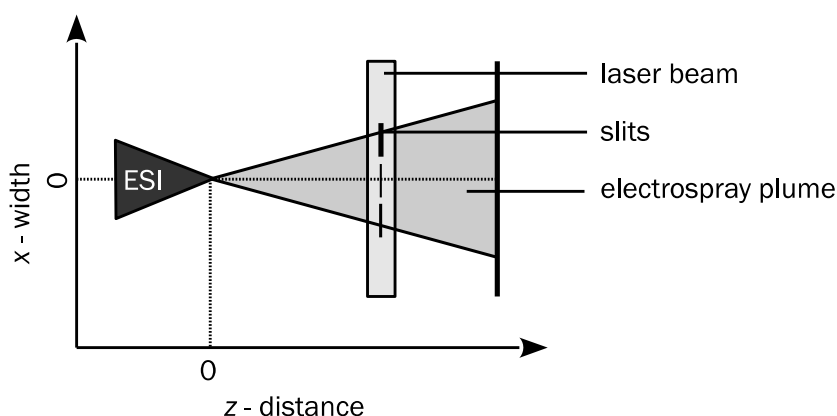


Figure 12: Scheme of the experiment, viewed from the side, the spray propagates vertically in the image plane to the right, the laser intersects the spray horizontally in the image plane, the slits of the spectrograph are aligned with the laser beam

An improvement of the setup could be made by replacing the simple filter with a slit spectrograph. This spectrograph is a type of instrument also used in astronomy that has the advantage that the incoming light is guided onto three slits by a mirror. This mirror can be observed through a viewing port without interfering with the spectral measurement. Therefore, the exact point of observation is always certain. With the spectrograph in front of the EMCCD camera, spectral information can be obtained for different positions along the laser beam. In order to achieve this, the laser beam has to be aligned with the slits (Fig. 12). The slits can be placed on different positions along the spray and different spectra are obtained along the length of the slits. Moving the laser beam and the spectrometer allows the acquisition of spectral images at variable distances from the capillary. The resulting raw image of the emission of R6G excited with  $\lambda_{\text{ex}} = 355$  nm can be seen in figure 13.

The different slits result in dark lines parallel to the x-axis in the raw image. The setup allows to record spectra near the central axis of the electrospray and on the outside of the spray cone at the same time. In the 2D spectrum, the fluorescence emission is visible above 500 nm. The brightest feature is the emission of solvated R6G at  $\lambda_{\text{max,sol}} = 555$  nm (the intensity of which is hereafter referred to as  $I_{555}$ ) and the highest intensity can again be seen close to the spectrometer axis. The peak at  $\lambda_{\text{max,free}} = 505$  nm due to free R6G (the intensity of which is hereafter referred to as  $I_{505}$ ) is also visible and this is the brightest near the outside. In addition to the fluorescence peaks, a peak arising due to scattered laser light at  $\lambda_{\text{max,scat}} = 355$  nm (the intensity of which is hereafter referred to as  $I_{355}$ ) is also visible. A 400–700 nm bandpass filter was used to reduce the intensity of the scattered incident light. It is still visible in the spectrum, however, and information can be gained from the scattered light as well. An increased scattering intensity is expected for larger droplets and, of course, a high number density of droplets. If inner-filter effects at high R6G concentrations are neglected, the emission intensity  $I_{555}$  of solvated R6G should be independent of the droplet size as long as the amount of R6G molecules is constant. Therefore, information about the droplet size can be gained by comparing the scattering intensity  $I_{355}$  and fluorescence intensity  $I_{555}$ . However, the number density of the droplets has to be taken into account, since many small droplets will result in high values of  $I_{555}$  at low values of  $I_{355}$  as well.

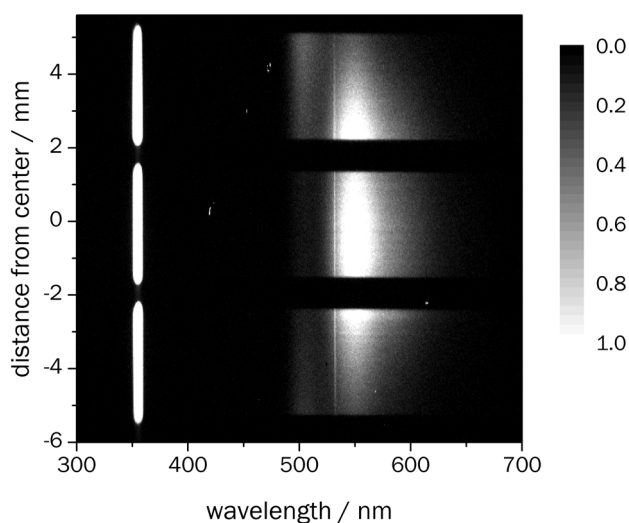


Figure 13: Raw 2D image of R6G emission obtained from EMCCD camera with wavelength scale on the x-axis and distance from the central axis of the spray on the y-axis

#### 4.1.1.4 Evolution of the spray with the distance from the capillary

Emission spectra were recorded at different positions between the ESI capillary and counter electrode at two different flow rates (Fig. 14). The intensity  $I_{555}$  decreases with distance from the capillary. This is mainly due to the spreading ESI cone and the resulting reduced number density of droplets. It is interesting to note that a slight increase of the flow rate to 5  $\mu\text{l}/\text{min}$  leads to an additional peak in the emission spectrum at  $\lambda_{\text{max,sol}} = 566 \text{ nm}$ . This peak is likely arising due to dimers of R6G formed at higher concentrations as a result of solvent evaporation.<sup>67</sup> This additional peak is seen as a shoulder of the peak at  $\lambda_{\text{max,sol}} = 555 \text{ nm}$  instead of a shift of the entire peak as would be expected in solution. The explanation could be that small droplets containing high concentrations of R6G exist concurrently with larger droplets exhibiting smaller R6G concentrations. These different droplets emit varying spectra and thus a superposition and not a mixture of the two is found.

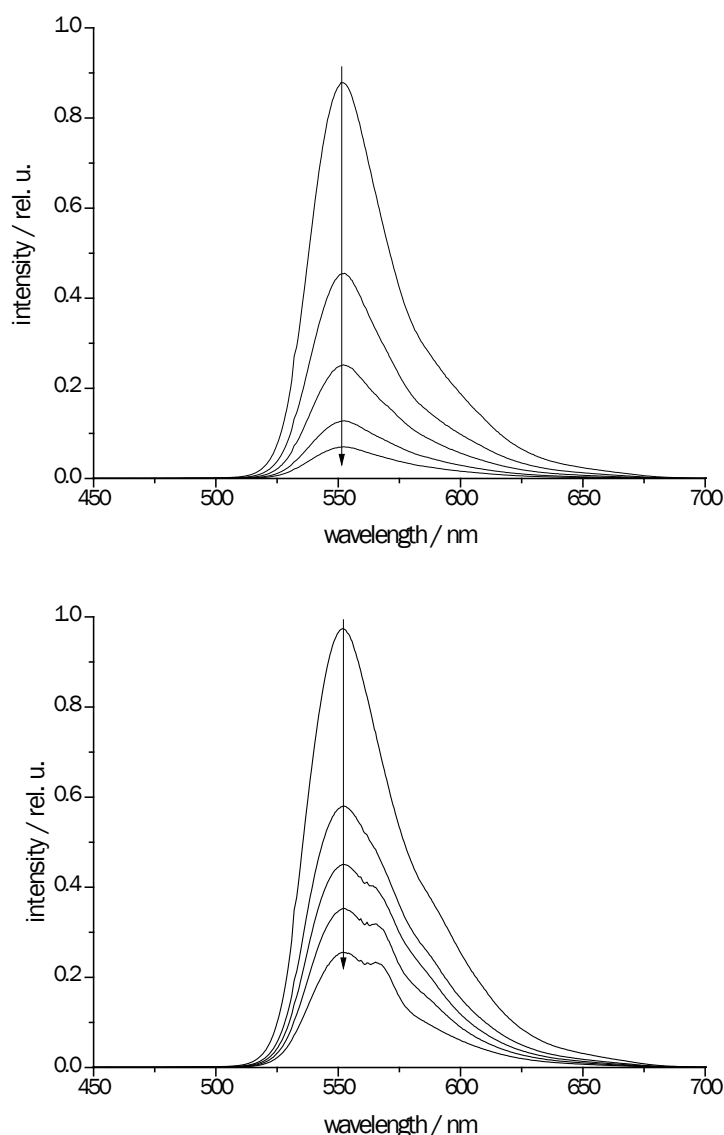


Figure 14: Emission spectra of R6G (50  $\mu\text{M}$  in methanol,  $\lambda_{\text{ex}} = 355 \text{ nm}$ ) recorded close to spray axis for distances: 3 mm, 5 mm, 7 mm, 10 mm, 12 mm (arrows indicate increasing distance), solvent flow rate top: 4  $\mu\text{l}/\text{min}$ , bottom: 5  $\mu\text{l}/\text{min}$

It is also interesting that this dimer peak is only found at high flow rates. It is well known that the ionization efficiency in ESI is reduced with increasing flow rates.

A possible explanation of the dimer peak could be that the charge per droplet is lower at higher flow rates as more  $\text{Cl}^-$  counter ions per  $\text{R6G}^+$  ions are found in the droplets. Thus, the concentration of R6G in the droplets before the Rayleigh limit is reached can be higher.

Next, the scattering intensity  $I_{355}$  and sum fluorescence ( $I_{\text{LIF}} = I_{505} + I_{555}$ ) are shown as functions of the distance from the capillary at different flow rates (Fig. 15). As expected,  $I_{355}$  decreases with the distance due to the expansion of the electrospray cone and the decrease of the droplet size. The scattering intensities are generally slightly higher at higher flow rates. At low flow rates and large distances, the signal drops more steeply. This can be attributed to the higher ESI efficiency at low flow rates and the resulting reduction of large droplets due to fission upon reaching the Rayleigh limit.

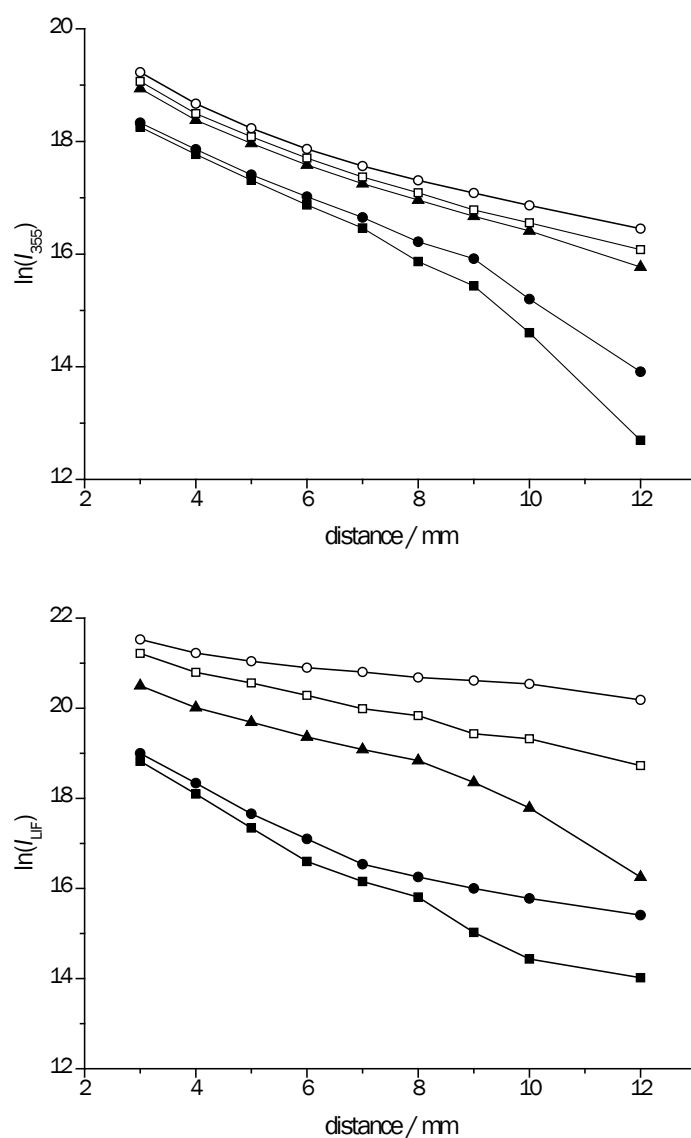


Figure 15: Dependence of top: intensity of scattered light and bottom: sum fluorescence of R6G (50  $\mu\text{M}$  in methanol) on distance at different solvent flow rates: 1.5  $\mu\text{l}/\text{min}$  (■), 2  $\mu\text{l}/\text{min}$  (●), 3  $\mu\text{l}/\text{min}$  (▲), 4  $\mu\text{l}/\text{min}$  (□), 5  $\mu\text{l}/\text{min}$  (○)

Although the number density of the resulting progeny droplets is high, their contribution to the scattering is small because they are only one tenth of the size of the parent droplets.<sup>35</sup> Due to the increased vapor pressure of the smaller droplets (see (46) in chapter 2.2.6.2), they also evaporate much faster.

Compared to the decrease of the scattering intensity, the decrease in the fluorescence intensity  $I_{\text{LIF}}$  with the distance is less pronounced. For the lower flow rates the slope of this decline is even smaller at higher distances. These findings can be attributed to the fact that R6G in the smallest droplets and free R6G are still fluorescing, while the influence of these droplets on the scattering intensity is negligible. It should be noted, however, that inner-filter effects can become important for the small droplets and the fluorescence quantum yield in the gas phase can be different from the solution.

As noted above, three bands are found in the typical electrospray spectra of R6G recorded at low flow rates (Fig. 16, top). These are a peak of the scattered laser light with intensity  $I_{355}$ , a broad band due to the fluorescence of solvated R6G with intensity  $I_{555}$  and a peak due to the fluorescence of free gaseous R6G with intensity  $I_{505}$  that was not observed in the spectra recorded at high flow rates (Fig. 14). Another quantity, the relative fraction of gaseous ions  $\chi_{505} = I_{505}/I_{\text{LIF}}$ , where  $I_{\text{LIF}}$  is the sum fluorescence will also be used later in the discussion. In the spectrum recorded closest to the capillary, peak due to solvated ions is the most intense. The intensity of the scattering peak is also very high. At higher distances, the peak due to solvated ions becomes a shoulder of the peak of the free R6G ions, which are by far the most intense. The scattering intensity is significantly reduced. At even higher distances, all peaks lose intensity.

The clear separation of the two fluorescence peaks at  $\lambda_{\text{max,free}} = 505 \text{ nm}$  and  $\lambda_{\text{max,sol}} = 555 \text{ nm}$  as well as the absence of any bands in between suggest the IEM to best explain the ion release for the small R6G ions.<sup>35</sup> As the Rayleigh limit is reached for sufficiently small droplets, the free R6G<sup>+</sup> ions are emitted from these parent droplets instead of solvent progeny droplets, bringing the remaining parent droplet below the Rayleigh limit once again. Calculations show that R6G<sup>+</sup> complex ions with one solvent molecule should exhibit fluorescence with a bathochromic shift of about 2 nm.<sup>66</sup> It is reasonable to assume that the addition of further solvent molecules would result in even larger shifts. The absence of any shift in the wavelength of the maximum of the peak associated with the solvated R6G emission thus indicates that such partly solvated complex ions do not occur. If the R6G<sup>+</sup> ions would remain inside the solvent droplets until all of the solvent evaporates as would be the case if the CRM would apply, these intermediate wavelength peaks should be observed.

Integrating the fluorescence peaks associated with free and solvated R6G yields a look at the evolution of the spray with distance from the capillary (Fig. 16, bottom). The fluorescence of solvated R6G ions  $I_{555}$  strongly decreases from 5 mm to 7.5 mm. At higher distances,  $I_{555}$  decreases further, although not as steeply. This decrease can be explained by a decreasing number of droplets, both due to the expansion of the droplet cloud perpendicularly to the spray axis and the evaporation of droplets. The intensity of free gaseous R6G ions increases from 5 mm to 7.5 mm and then slowly decreases as well. This first increase is due to the release of ions only taking place at a certain distance from the capillary, after there was some time for the evaporation of the solvent to take place. The decrease at higher distances is due to the reduced number of droplets releasing ions there.



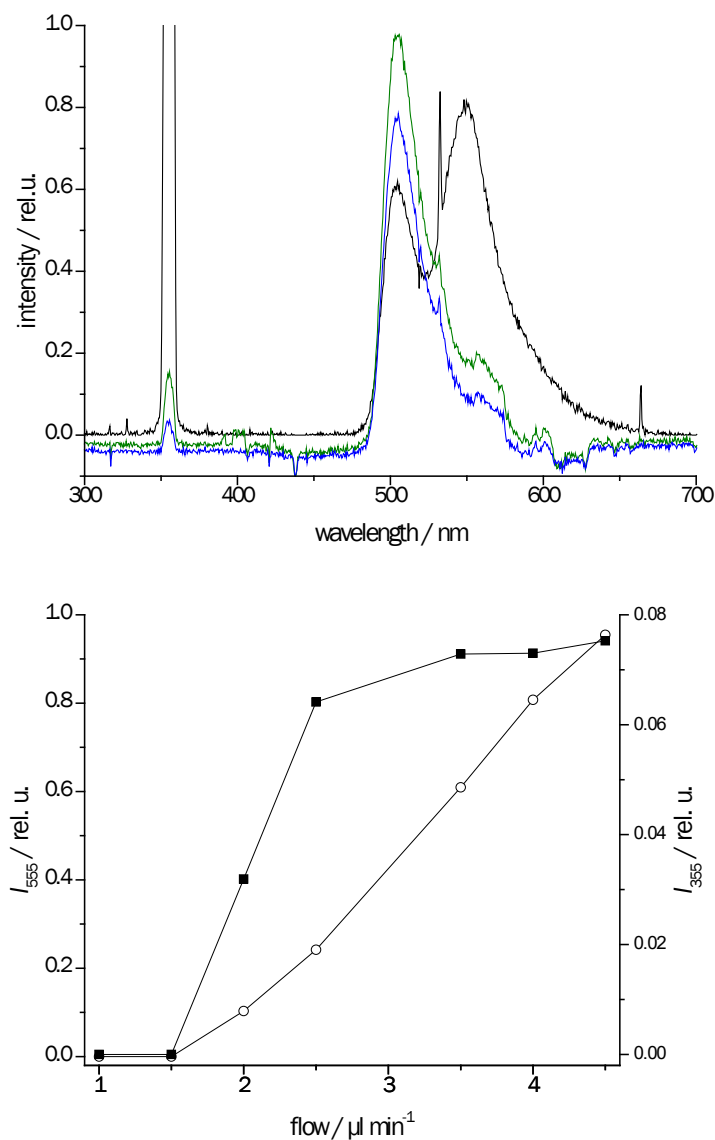


Figure 16: Top: emission spectra during laser irradiation of R6G (50 μM in methanol) recorded at different distances: 5 mm (black trace), 10 mm (green trace), 12.5 mm (blue trace), flow rate 1 μl/min; bottom:  $I_{505}$  (■) and  $I_{555}$  (○) as functions of the distance

#### 4.1.1.5 Influence of the flow rate on the release of ions

The influence of the flow rate between 1-5 μl/min at a distance of 10 mm on the emission spectra of R6G is shown in figure 17. At higher flow rates, more ions could theoretically be produced in the same time interval at a constant R6G concentration, since higher amounts of R6G are transferred during the same time. In the spectra, a decrease of the intensity of the free R6G peak  $I_{505}$  can be seen while the intensity of scattered light  $I_{355}$  and the intensity of the solvated R6G fluorescence peak  $I_{555}$  increase. The intensity of scattered light  $I_{355}$  increases steeply between the spectra recorded at 1.5 μl/min and 2.5 μl/min, while the increase at higher flow rates is much less pronounced. The intensity of the solvated R6G fluorescence peak  $I_{555}$  increases continuously but less steeply from 1.5 μl/min to 5 μl/min.

From (42) (chapter 2.2.6.2) can be seen that the size of the initial droplets increases with the flow rate while according to (45) the charge density decreases. This means, the Rayleigh limit is reached later and further away from the capillary. The frequency of droplet formation should be independent from the flow rate.

The observations support this picture. The steeper increase of the scattering signal  $I_{355}$  compared to the intensity of the solvated R6G peak  $I_{555}$  can be attributed to the larger droplets. The additional solvent in the same time increases the size of the droplets, but not the number of droplets formed in this time. The combination of larger droplets and decreased charge densities results in less release of R6G into the gas phase and consequently a decrease of  $I_{505}$ .

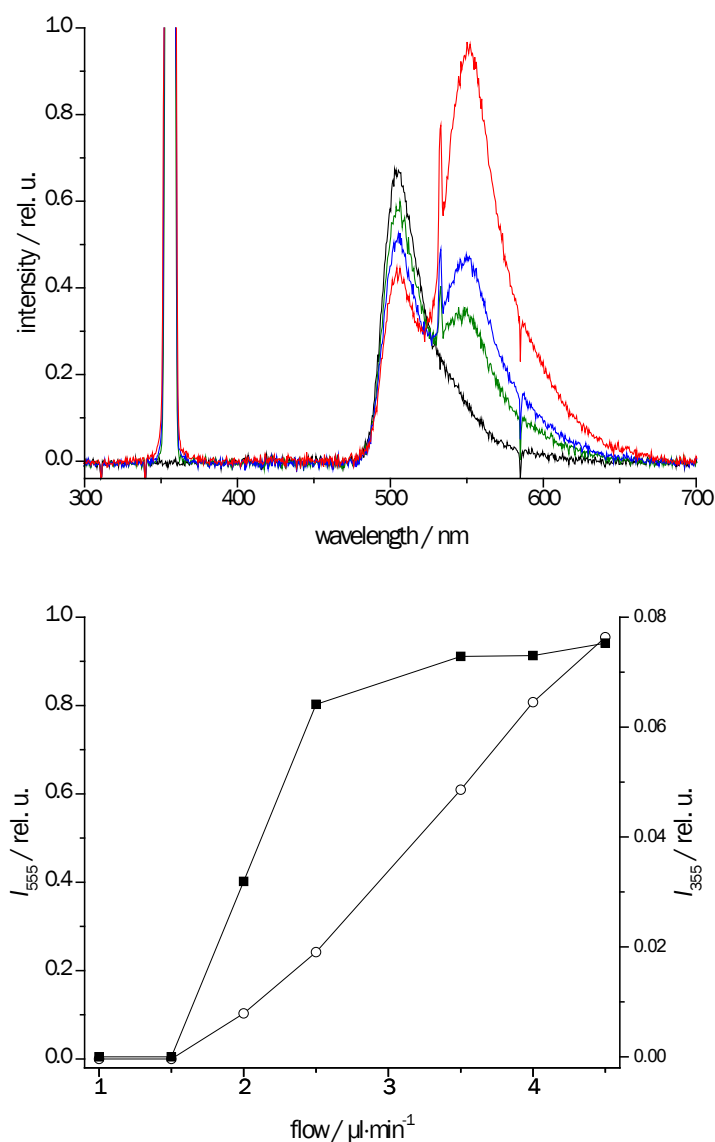


Figure 17: Top: emission spectra during laser irradiation of R6G (50  $\mu\text{M}$  in methanol) recorded at different flow rates: 1.5  $\mu\text{l}/\text{min}$  (black trace), 2  $\mu\text{l}/\text{min}$  (green trace), 3  $\mu\text{l}/\text{min}$  (blue trace), 3.5  $\mu\text{l}/\text{min}$  (red trace) at a distance of 10 mm; bottom:  $I_{555}$  (○) and  $I_{355}$  (■) (same relative scale) as functions of the flow rate at a distance of 10 mm

#### 4.1.1.6 Impact of the concentration of electrolytes in the solution

Another factor that can influence the efficiency of ESI is the concentration of electrolytes that are present in the solution beside the analyte. Such electrolytes are often present in ESI-IM spectrometry and ESI mass spectrometry applications and they are sometimes added for better limits of detection or linear ranges. They are especially important in the investigation of biological samples, where buffers are often used. As R6G is ionic itself, the influence of the concentration of R6G was investigated from 10  $\mu\text{M}$  to 50  $\mu\text{M}$  at two distances (Fig. 18). At a distance of 5 mm, the peak due to solvated R6G at  $\lambda_{\text{max,sol}} = 555 \text{ nm}$  is observed almost exclusively. The intensity of this band increases with the R6G concentration, while  $I_{355}$  remains almost constant. At a distance of 10 mm, the fluorescence peak of free R6G at  $\lambda_{\text{max,free}} = 505 \text{ nm}$  appears, signifying the appearance of gaseous R6G ions. Upon increasing the R6G concentration in the solution,  $I_{505}$  increases while  $I_{555}$  and the sum fluorescence decrease. The scattering intensity  $I_{355}$  also decreases.

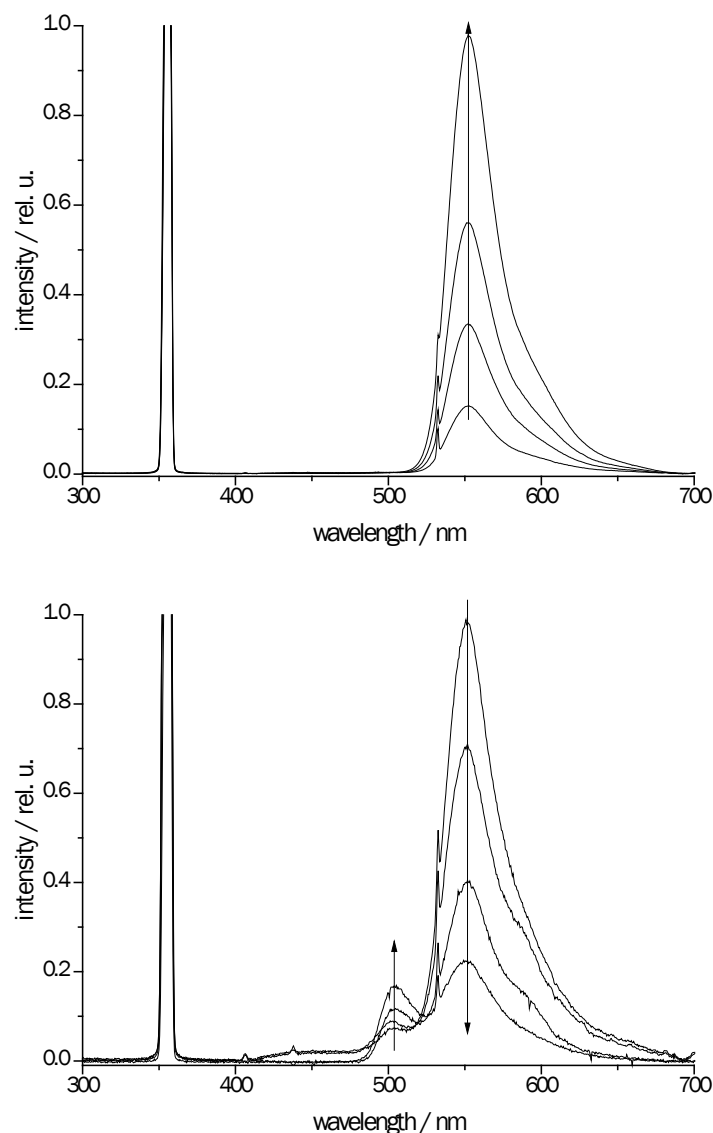


Figure 18: Emission spectra during laser irradiation of R6G recorded at different R6G concentrations in methanol (10  $\mu\text{mol/l}$ , 20  $\mu\text{mol/l}$ , 30  $\mu\text{mol/l}$ , 50  $\mu\text{mol/l}$ ; arrows indicate effect of concentration increase) at a flow rate of 3  $\mu\text{l/min}$  and a distance of top: 5 mm; bottom: 10 mm

According to (42) (chapter 2.2.6.2), an increase of the conductivity leads to smaller initial droplets. The charge density in the droplets increases as can be seen from (44). From (41) and (43) can be concluded that more droplets are formed in the same time. The findings at 10 mm support the equations. The smaller droplets possessing a higher charge density reach the Rayleigh limit sooner and closer to the emitter. As a consequence, R6G is released closer to the capillary as well, leading to the increase of  $I_{505}$ .

The decrease of the sum fluorescence intensity  $I_{LIF}$  could be due to a lower quantum yield of the gaseous ions. The higher concentration of R6G in the droplets could also cause inner-filter effects. Additionally, the increased number of droplets and higher charge densities could lead to charge repulsion and a spreading of the electro spray cone.

At still higher distances (15 mm), the observations are similar. Here,  $I_{505}$  is even more intense compared to  $I_{555}$ .

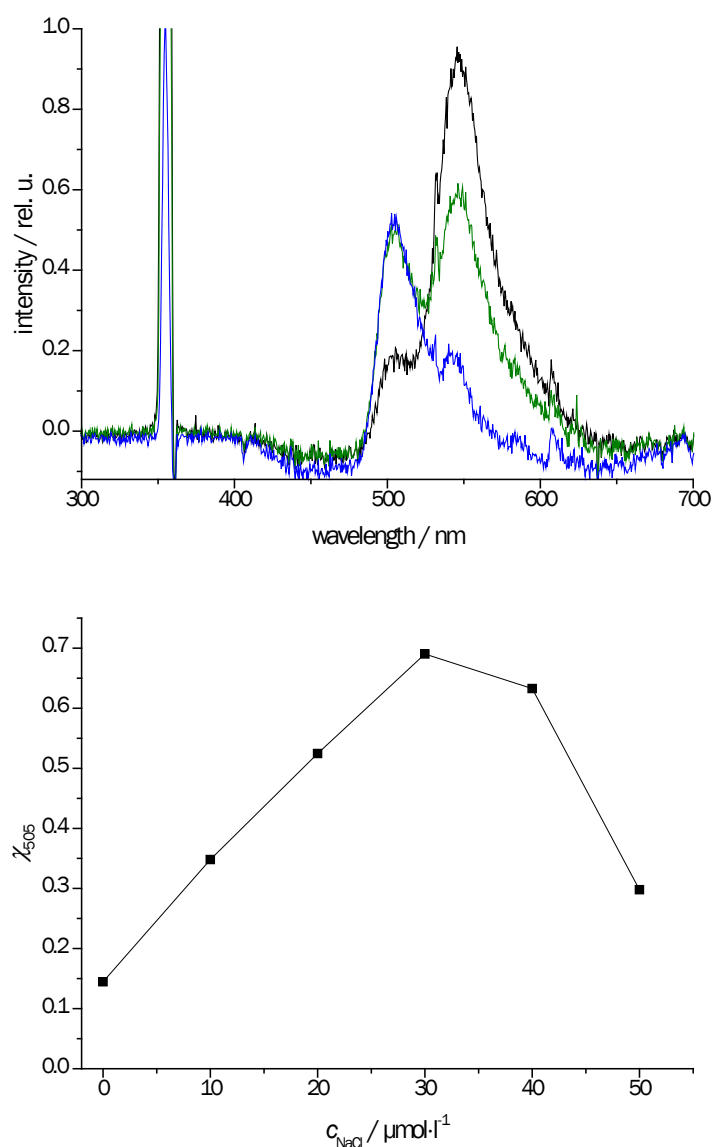


Figure 19: Top: emission spectra during laser irradiation of R6G (20 μM) after adding NaCl: 0 (black trace), 10 μmol/l (green trace), 40 μmol/l (blue trace) at a flow rate of 1 μl/min and a distance of 10 mm from the capillary; bottom:  $\chi_{505}$  as a function of NaCl concentration ( $c_{R6G} = 20 \mu\text{M}$ , flow rate 1 μl/min, distance 10 mm)

In order to investigate the influence of an additional electrolyte, NaCl (0-50  $\mu\text{M}$ ) was added to a 20  $\mu\text{M}$  R6G solution (Fig. 19). Adding up to 30  $\mu\text{M}$  of NaCl results in an increase of  $I_{505}$  at a constant decrease of  $I_{555}$ . The fraction  $\chi_{505}$  increases accordingly with the NaCl concentration up to 30  $\mu\text{M}$ . The fraction remains almost constant up to 40  $\mu\text{M}$  of NaCl before decreasing again for 50  $\mu\text{M}$  of NaCl.

These results support the view that the more efficient ion release observed for increasing R6G concentrations is mainly an effect of the increased conductivity of the solution. The addition of NaCl increases the conductivity as well and also leads to smaller droplets with a higher charge density. Consequently, the Rayleigh limit for sufficiently small droplets is reached sooner and R6G is ejected into the gas phase.

The electrolyte ions compete with the R6G for release, resulting in the decrease of the R6G fluorescence intensity at high NaCl concentration.

#### 4.1.1.7 Influence of supporting gas flows

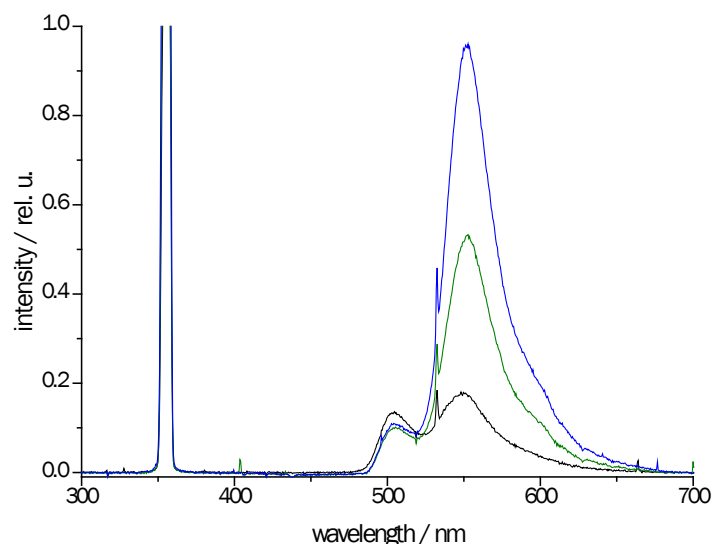


Figure 20: Emission spectra during laser irradiation of R6G (50  $\mu\text{mol/l}$ ) at different sheath gas flow rates: 0 (black trace), 100 ml/min (green trace), 200 ml/min (blue trace), solvent flow rate 1  $\mu\text{l/min}$ , distance 5 mm

In many applications, gas flows are used in ESI to support the evaporation of the solvent. One type of gas flows often encountered is the sheath gas, which is typically issued radially around the ESI capillary. Sometimes and especially when working with high solvent flow rates or less volatile solvents, a second, heated gas flow is employed (the process is then referred to as heated ESI). The heated gas is kept further away from the tip, so as not to interfere with the initial steps of the ESI process, namely the formation of the Taylor cone. This type of ESI can be especially useful in IM spectrometry, where there are no pumps that could reduce the solvent load on the spectrometer.

The influence of the sheath gas flow was investigated up to 200 ml/min N<sub>2</sub> (Fig. 20). Upon applying sheath gas, the sum fluorescence is increasing due to the focusing of spray, i.e. a reduction of the spray cone angle. Scattering intensity  $I_{355}$  and solvated R6G fluorescence intensity  $I_{555}$  are increased, while the intensity of free R6G  $I_{505}$  is slightly decreased. This observation can be explained by the higher concentration of solvent in the gas phase. The higher scattering intensity indicates an increased size and number of droplets are present. The focusing of the spray is specifically important for mass spectrometry, because inlet the capillary samples only a small part of the cone. This part can be increased by focusing the spray cone. However, using increased pressure or a reduced diameter of the sheath gas outlet and therefore increasing the velocity of the sheath gas (sonic spray) can support the evaporation. This was shown later in ESI-IM spectrometry, but not investigated with this experiment because the source was not available at the time.<sup>65</sup>

Heated ESI was performed using a heated gas stream perpendicular to the spray axis at the point of illumination by the laser (Fig. 21). The flow rate was kept constant, so that any perturbations of the spray remained constant. The effect of different gas temperatures was investigated, the temperature was measured at the same point where the spectra were obtained. An increase of the temperature results in an increase of  $I_{505}$  and a decrease of  $I_{555}$  and  $I_{355}$ . The heated gas directly improves the desolvation process by decreasing the droplet size as is implied by the decrease intensity of the scattering peak. Solvent evaporation is also supported as can be seen in the reduction of the peak associated with solvated R6G. This leads to an improved ion release and potentially better sensitivity.

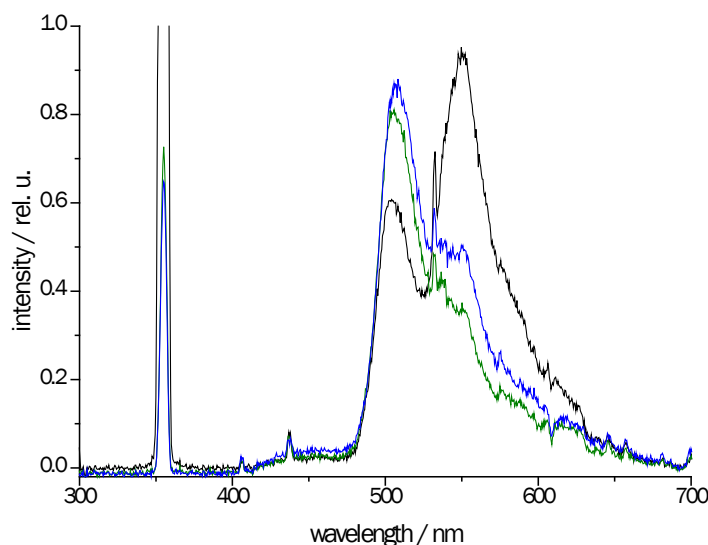


Figure 21: Emission spectra during laser irradiation of R6G (50  $\mu\text{mol/l}$ ) at different heated gas temperatures: 150 °C (black trace), 200 °C (green trace), 250 °C (blue trace), heated gas flow rate 1.3 l/min, solvent flow rate 3  $\mu\text{l/min}$ , distance 10 mm

## 4.1.1.8 Investigation of the release of lucigenin into the gas phase

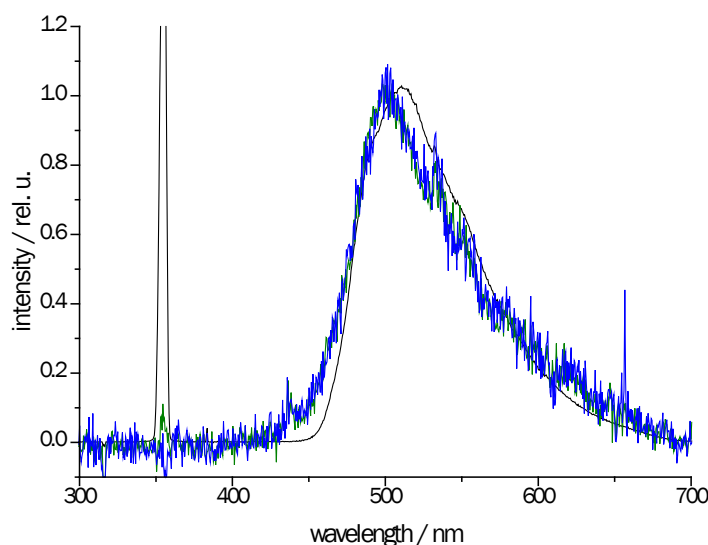


Figure 22: Normalized emission spectra during laser irradiation of lucigenin ( $50 \mu\text{mol}/\text{l}$  in MeOH), recorded at different distances from the tip of the capillary: 5 mm (black trace), 10 mm (green trace), 15 mm (blue trace) at a flow rate of  $1 \mu\text{l}/\text{min}$

In conclusion of these experiments, the chemiluminescent dye lucigenin was also investigated. The gas phase fluorescence spectrum has not yet been reported. In figure 22, the spectra of the electrospray of lucigenin in MeOH are shown at a distance of 5, 10 and 15 mm from the capillary. At a distance of 5 mm, a strong scattering peak is observed as the analyte is predominantly found in large droplets. The fluorescence maximum found at  $\lambda_{\text{max, lucigenin, sol}} = 515 \text{ nm}$  is assigned to solvated lucigenin. Scattering is almost completely suppressed at the larger distances, it can be concluded that small droplets prevail. The fluorescence maximum is shifted to  $\lambda_{\text{max, lucigenin, free}} = 505 \text{ nm}$  for distances of 10 and 15 mm. This maximum is assigned to gaseous lucigenin. The difference between solvated and free lucigenin is much smaller than the one found for R6G. This can be explained by the electronic structures of the two compounds. R6G possesses a push-pull-system while lucigenin is symmetrical. The change in dipole moment upon excitation can thus be expected to be much smaller for lucigenin. Therefore, the effects of solvent relaxation, which are encountered in solution but not in the gas phase and account for the peak shift occurring in the transition from one to the other, are reduced for lucigenin as well.

### 4.1.1.9 Conclusions

LIF spectroscopy was used to probe R6G in the droplets produced by ESI. In the large parent droplets that are first produced, the acquired spectrum is equivalent to the spectrum of R6G in bulk solution. In the progeny droplets that are a result of Coulomb fission of the droplets, an increase of the concentration of R6G was manifest in a second emission band corresponding to the dimer emission found in highly concentrated R6G solution spectra.

Additionally, the emission of free R6G in the gas phase could be observed. An investigation of the changes in the LIF spectrum with the distance from the ESI capillary revealed that the intensity of the scattering that is mainly caused by large droplets decreases with the distance more strongly than the intensity of the LIF signals which are mostly independent of the droplet size. This is an indication of the droplet shrinkage and progeny and nanodroplet formation.

The emission band of free R6G could only be observed from a certain distance onward. At higher distances, the ratio of free and solvated R6G is quickly inverted before both signals lose intensity. The additional amount R6G being ejected by the ESI capillary in the same time interval at higher flow rates primarily results in an increase of the intensity of the peak associated with solvated R6G. An Addition of electrolytes to the solution up to a certain concentration facilitates the release of ions. Although the use of a sheath gas resulted in an increased signal in the space observed, the additional ions are still solvated. A heated gas flow, however, favors the release of ions into the gas phase.

In addition to the spectra of R6G, a shift of the fluorescence maximum between the solution and the gas phase was found for lucigenin for the first time. More generally speaking, this technique presents the possibility of recording gas phase fluorescence spectra of large molecules.



## 4.1.2 High resolution spectrometer utilizing two-dimensional wavelength separation

This chapter presents a 2D high resolution spectrometer and its applications. Work on these experiments was carried out within the context of a government funded project (ZIM program by the German Federal Ministry for Economic Affairs and Energy, BMWi, Grant No. KF2167702FK9). The project was carried out in cooperation with Optikexperten Raab-Photonik GmbH, who contributed the initial design and ENPASOS GmbH, who developed the software. The work carried out in the context of this thesis included establishing the spectrometer at our institute and the adaption of the system to the various light sources and analytical techniques. Parts of the results were reported in *Applied Spectroscopy*.<sup>68</sup>

### 4.1.2.1 Spectrometer concept

For many applications, resolutions in the three-digit picometer range that are attainable by standard spectrometers equipped with normal gratings or prisms are sufficient. If resolutions in the low two-digit picometer range are required, different optical elements have to be used. These are either only available for a very narrow wavelength range, require moving parts as in scanning Fabry-Pérot interferometers or need relatively large optical pathways as is the case for echelle spectrometers. The goal of this chapter was to achieve a high spectral resolution in a compact spectrometer setup that is capable of recording a wide wavelength range spectrum simultaneously.

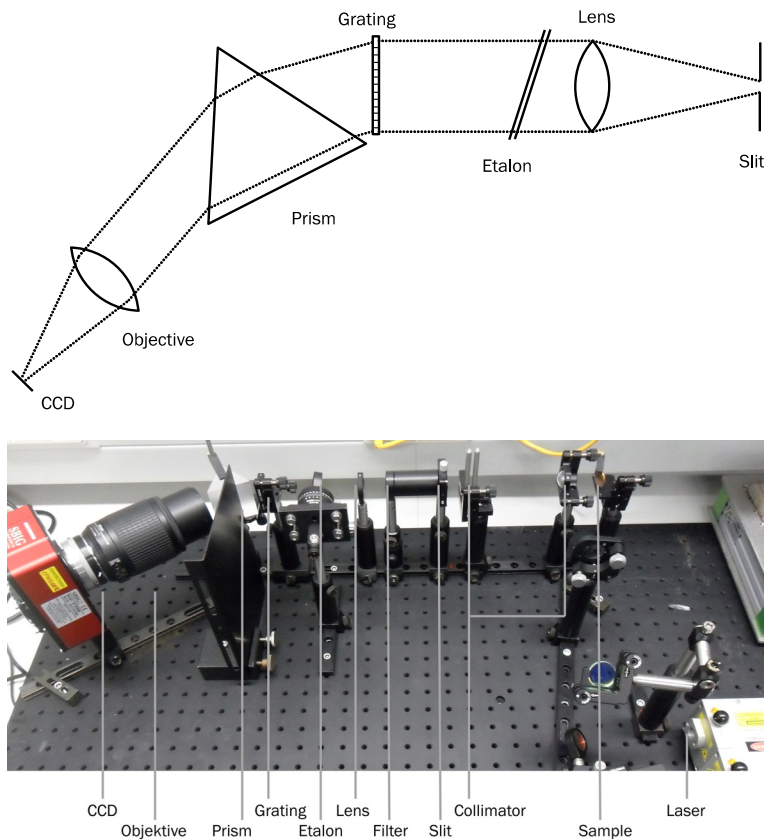


Figure 23: Top: scheme of the spectrometer concept; bottom: photograph of the experimental setup; labels indicate optical parts used

The concept of the spectrometer is based on the combination of standard dispersive elements with an interferometric element to achieve a coarse resolution in one direction and high resolution in the second direction on a two dimensional detector. Simulations in the ZEMAX software (ZEMAX LLC, Kirkland, WA, USA) showed that a combination of a prism and a grating as the dispersive elements with a Fabry-Pérot interferometer or etalon as the interferometric element would be promising. The light is collected on a two-dimensional CCD chip. A scheme of the spectrometer concept and a photograph of the experimental setup are shown in figure 23. The incoming light is directed onto a slit and undergoes wavelength separation by the prism and the grating. The result is a conventional line spectrum with a coarse resolution in x-direction on the CCD chip. A Ne spectrum is shown as an example of this line spectrum on the left of figure 24. The etalon is placed into the beam path in such a way that photons of a specific wavelength can only pass the etalon by constructive interference at certain y-values. In the resulting spectrum, the x-values yield the coarse resolution and the y-values contain the fine resolution of the spectrum (Fig. 24, right). In practice, more than one order, typically three orders, from the etalon were used to create redundancy for the analysis of the data in the software. Software for the evaluation of the 2D spectra had to be specifically written for the task.

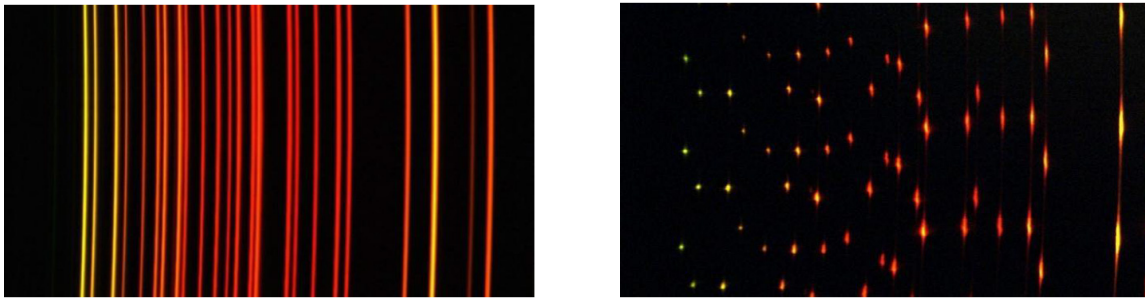


Figure 24: Ne spectrum recorded without (left) and with the etalon (right) in the beam path

The advantage of this kind of setup is that due to coarse pre-separation of wavelengths in one dimension, signals on the etalon resulting from photons of similar wavelengths are divided in another dimension, thus allowing evaluation of signals lying closer together and over a wider wavelength range. Additionally, this two-dimensional separation enables the use of two-dimensional detectors, which are widely available in the form of CCD chips. These have easily in excess of 100000 detection channels (pixels), which is far above the number generally available in line detectors.

#### 4.1.2.2 *Development overview*

While most optical components such as lenses, grating and prism were established by Raab-Photonik, crucial components such as the slit, the CCD camera and the objective used and especially the etalon had to be tested and optimized in the prototype. The work done in the context of this thesis was to operate the prototype in the university, including the calibration of the optical setup, as all components were mounted on a breadboard. Additionally, the setup was adapted and optimized for specific spectroscopic techniques, namely Raman spectroscopy and LIBS. To this end, samples of standards had to be established for each technique and proper light sources had to be found.

In the case of LIBS, it was possible to perform comparative measurements on a commercial instrument as a commercial echelle spectrometer was available. Furthermore, the 2D spectra needed for developing the evaluation software were recorded and the software was tested in close cooperation with ENPASOS. For this purpose, spectral images of broadband sources were produced. When continuous light passes through spectrometer, constructive interference of both elements occurs on continuous, slightly slanted lines. These lines are used by the software in the conversion of 2D image to standard intensity over wavelength spectra. Finally, the spectra were wavelength calibrated using suitable noble gas discharge lamps (Ne, Ar).

##### 4.1.2.3 Testing of components and characterization of the spectrometer

As detailed in the theory chapter, the finesse of an etalon is a function of the reflectivity of the mirrors used. The achievable resolution is determined by the finesse, so a high finesse is necessary to achieve a high resolution. Sensitivity, however, is decreased as the etalon line is narrowed and therefore the number of photons allowed to pass through is reduced.

A number of commercially available mirrors from various providers tested were tested in a Fabry-Pérot interferometer style setup (Fig. 25, left). The tuning of the interferometer was achieved by means of a diode laser passing through a diffuser before entering the interferometer. Adjustment was established by visually optimizing the interference pattern emerging (Fig. 25, right). It is necessary to use dielectric mirrors due to absorption losses that occur in metallic mirrors.

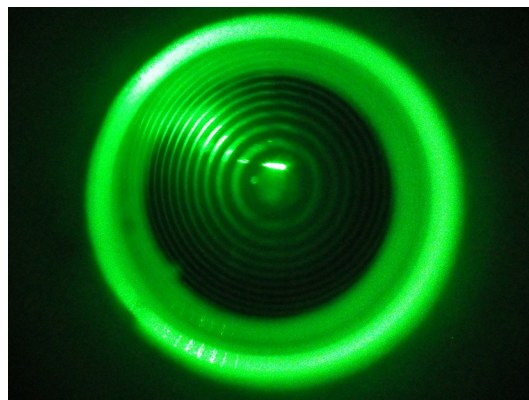
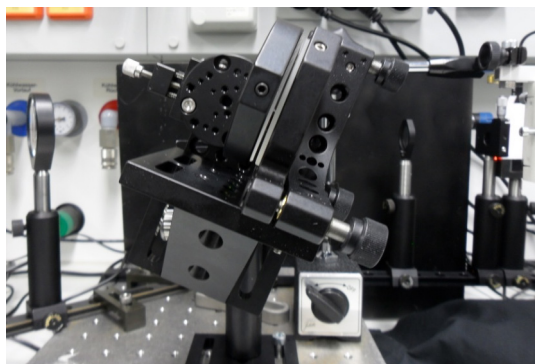


Figure 25: Left: photograph of Fabry-Pérot interferometer setup used for testing mirrors featuring a three adjuster mirror mount and a translation stage; right: interference pattern seen when correctly tuned Fabry-Pérot interferometer is illuminated by green diode laser passed through a diffuser

Broadband dielectric mirrors are commercially available. However, all of these possess very high reflectivities. Tests with commercial mirrors established that the transmission was too low to achieve a reasonable sensitivity with the spectrometer. Therefore, mirrors with lower reflectivity over a sufficiently broad wavelength range had to be manufactured. A comparison between the transmission spectra of commercially available mirrors and the mirrors specifically designed for the spectrometer is shown in figure 26. In addition to exhibiting very low transmissions below 0.01 %, there are some regions of higher transmission at certain wavelengths that would result in an inhomogeneous resolution of the spectrometer.

#### 4 Results and discussion

The mirrors produced for the spectrometer exhibit transmissions around 3–4 % between 350 and 640 nm. A variable slit was used to determine the optimum slit width. A value of 50  $\mu\text{m}$  was established as a good compromise between a sufficiently good coarse resolution and available light intensity. The excitation of both Raman and LIB spectra was accomplished by lasers. An improvement of the sensitivity of the spectrometer could be achieved by focusing of the incident light onto the slit by the combination of a cylindrical and a spherical lens. Two different cameras used with the spectrometer.

The first one was a simple CCD camera that is well suited during spectrometer adjustments because of its fast response. However, the sensitivity of this camera was too low to be used in the spectroscopic applications. Therefore, another CCD camera optimized for long integration times and thus improved sensitivity as well as 16 bit intensity depth per pixel resulting in an increased dynamic range was used for the applications.

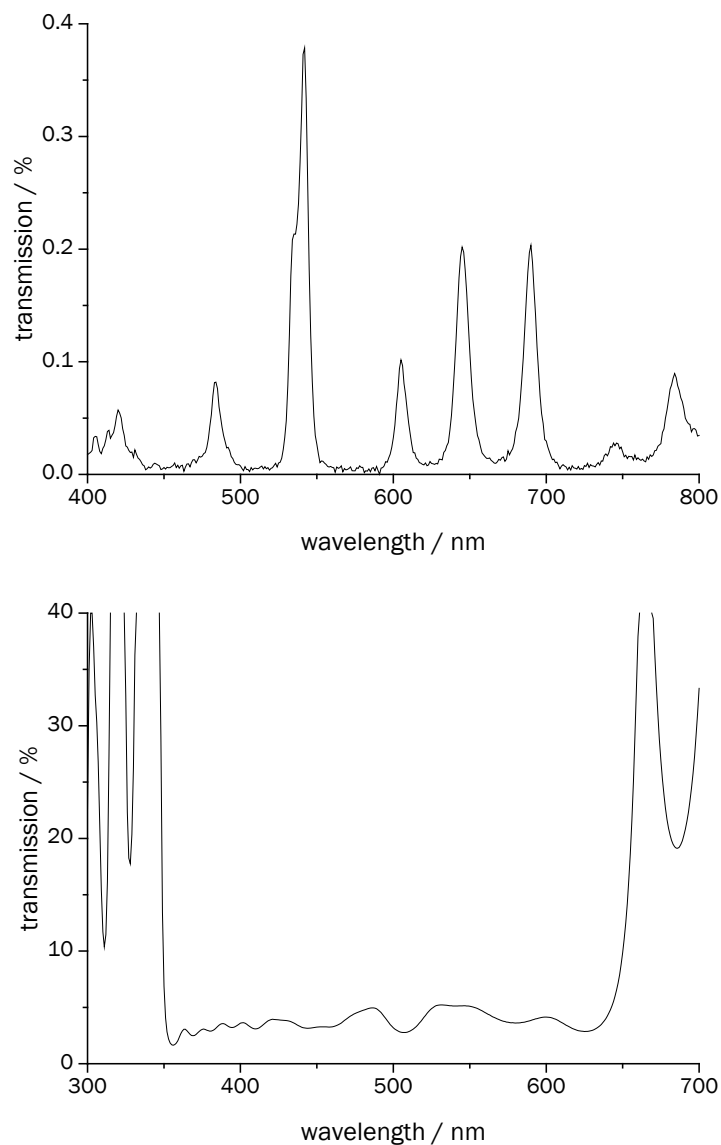


Figure 26: Top: transmission spectrum of high reflectivity broadband mirror (Thorlabs); bottom: transmission spectra of mirror specifically designed for application

#### 4.1.2.4 Data evaluation and processing

In this section, only a brief description of the data evaluation and processing will be given as the software implementation was done by Enpasos and is explained in detail in the paper.<sup>68</sup> As noted above, the dispersion of the incident light on the slit by the prism and the grating results in a line spectrum along the x-axis. Starting from an arbitrary wavelength, the software has to establish defined and equally spaced lines from this spectrum. The spacing of these lines roughly corresponds to the coarse resolution and the lines are called  $\lambda$ -lines hereafter. Moving the etalon into the optical path results in etalon spectra superpositioned over the coarse resolution spectrum along the y-axis of the image in a way that peaks appear along lines slightly slanted compared to the  $\lambda$ -lines. These lines will be referred to as m-lines, as each of these lines corresponds to one etalon mode. The smaller the angle between  $\lambda$ -lines and m-lines, the higher the resolution of the resulting spectrum will be as there are more pixels per m-line. This angle can be set by changing the angle of the etalon in the beam path. Within one free spectral range, one m-line ends at the wavelength at which the next m-line starts, corresponding to the same resonance in the different etalon modes. The  $\lambda$ -lines are chosen in such a way that each m-line starts at the top intersecting with the  $\lambda$ -line and ends intersecting the next  $\lambda$ -line below (and so on). The next m-line again starts at the top intersecting the same  $\lambda$ -line, by definition of the  $\lambda$ -line at the same wavelength. In order to aid reading out the spectrum, a third set of lines called s-lines are introduced that connect these intersections. The advantage of the s-lines is that they are almost parallel to the x-axis.

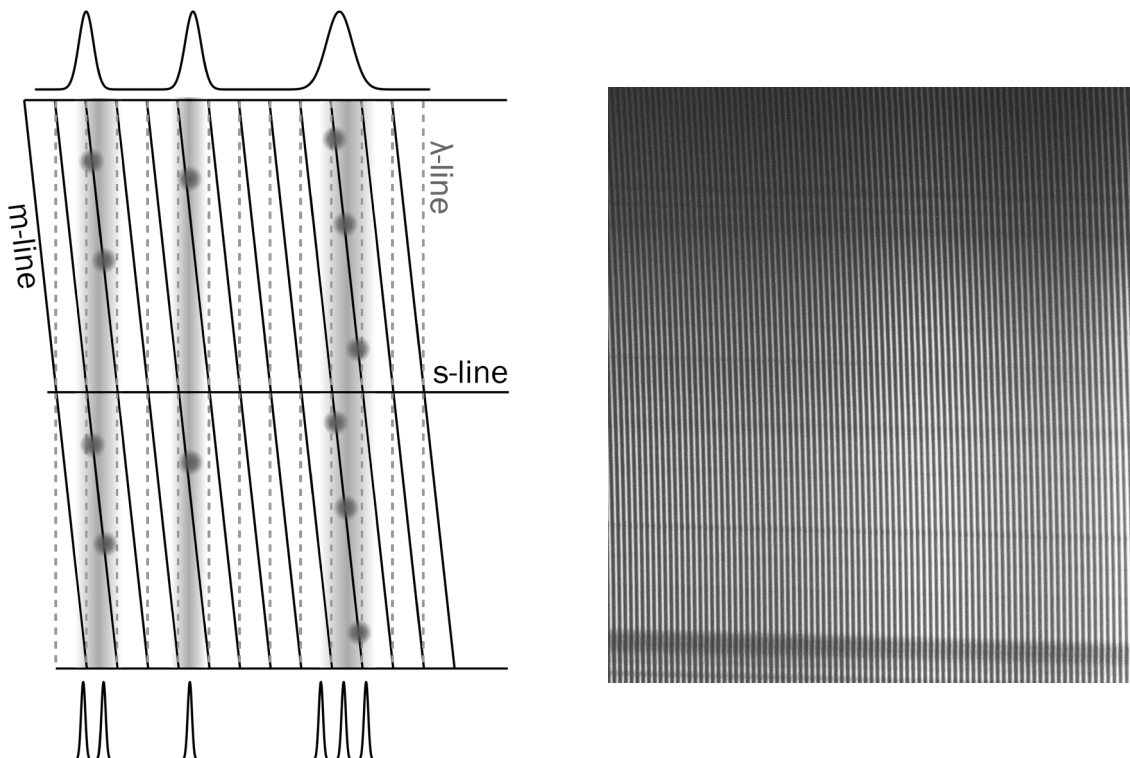


Figure 27: Left: Scheme of data evaluation process showing spectrum produced by dispersive elements (line features), superposition of two free spectral ranges of etalon (circular features),  $\lambda$ -lines, m-lines and s-lines as well as the resulting spectrum in coarse (above) and fine resolution (below); right: image of broadband source showing m-lines, resulting from constructive interference

On the left of figure 27, a scheme of the reconstruction process of the 2D-spectrum is shown. The first step in the process is the recording of a Ne spectrum. This is indicated by the line spectrum in the figure. The  $\lambda$ -lines (dashed lines in figure 27) with an arbitrary starting point but equal spacing are extrapolated from this spectrum. The lines in the real spectra exhibit a certain degree of curvature due to optical aberrations (see e.g. figure 24). The software uses second order polynomials to compensate for the curvature. The m-lines (slanted lines in figure 27) are calibrated using the spectrum of a broadband light source (Fig. 27, right). The exact positions of the m-lines are visible in the spectrum due to constructive interference along the m-lines and destructive interference in between. The m-lines are also fitted by second order polynomials. As mentioned above, the s-lines (horizontal lines in figure 27) pass through the intersections of  $\lambda$ -lines and m-lines. They are also approximated by second order polynomials. The spectrum is then created by reading the intensity along each m-line from the top to the bottom and joining them at the s-lines.

In practice, the spectra were recorded in such a way that between any two  $\lambda$ -lines not one but three m-lines can be found. In other words, three free spectral ranges of the etalon are recorded. This redundancy enables the software to average over the three free spectral ranges and correct deviations. The wavelength calibration of the resulting spectrum is done based on the known lines in the Ne-spectrum. Further discussion of the procedure can be found in the paper.

#### 4.1.2.5 Characterization and applications of spectrometer

The characterization of the spectrometer was done on the basis of the spectrum of a low pressure Ne discharge lamp. This spectrum exhibits narrow, discrete lines that are well known in the literature. The line width of most of the emission lines is less than 1 pm.<sup>69</sup> This is sufficiently small to treat the full width at half maximum (FWHM) of the Ne peaks found in the spectra solely as the resolution of the spectrometer. Therefore, the line widths encountered in the Ne spectrum were used in the optimization process of the spectrometer. This process included optimizing the angle between the incoming light and the camera axis and the angle of the prism and grating (refer to figure 23). The alignment and angle of the etalon also had to be optimized.

Table 3: Center wavelength of selected Ne peaks and their FWHM in coarse and high resolution mode with the etalon spectrometer (full slit height of 10 mm) and with the Aryelle spectrometer

Wavelength / nm	FWHM / pm		
	Coarse resolution	High resolution	Aryelle spectrum
585.2	455	63	31
588.2	418	51	33
594.5	447	64	39
597.6	411	41	46
603.0	414	50	36
607.4	423	59	34
616.4	451	51	36
621.7	423	56	34
630.5	430	51	36
Mean	$430 \pm 17$	$54 \pm 7$	$36 \pm 4$

#### 4.1.2 High resolution spectrometer utilizing two-dimensional wavelength separation

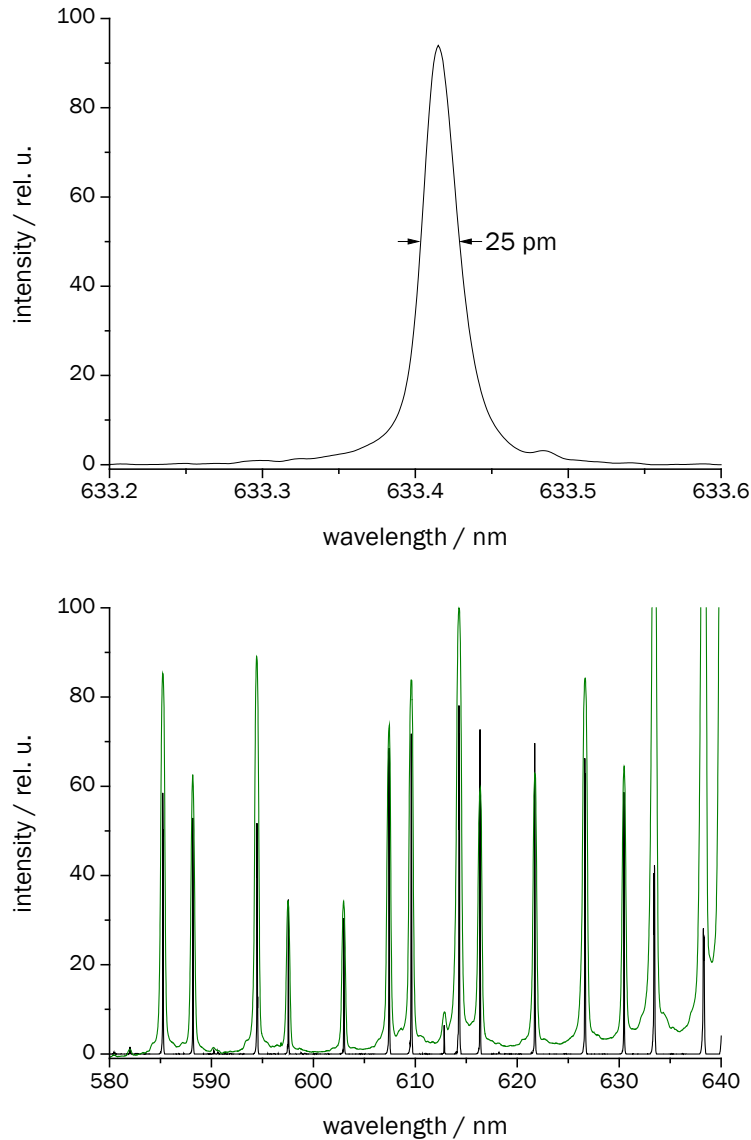


Figure 28: Top: Ne peak at  $\lambda = 633.4$  nm with a FWHM of 25 pm, recorded in high resolution mode with reduced entrance slit height (7 mm); bottom: Ne spectrum (full slit height of 10 mm) recorded in coarse (green, no intensity correction) and high (black, intensity correction) resolution modes

It was found that reducing the height of the entrance slit from 10 to 7 mm improved the resolution by avoiding spherical aberrations in the lenses. A linewidth of 25 pm could be achieved with this setup (Fig. 28, top). However, for the applications, the full slit height was used as the sensitivity was thus increased. On the bottom of figure 28, the Ne spectrum is shown in the coarse resolution mode without the etalon in the beam path and in the high resolution mode with the etalon in place. In table 3, selected lines of the spectrum are shown along with the FWHM recorded in the coarse and high resolution modes. For comparison, the table also shows the FWHM of the spectral lines of the same Ne lamp recorded with a commercial high resolution spectrometer. The latter is an echelle spectrometer (Aryelle) that was also used to record comparative LIB spectra. The values given in the table were recorded with the standard setup used to achieve reasonable sensitivity for the Raman and LIBS applications. The average FWHM of the Ne peaks is 54 pm.

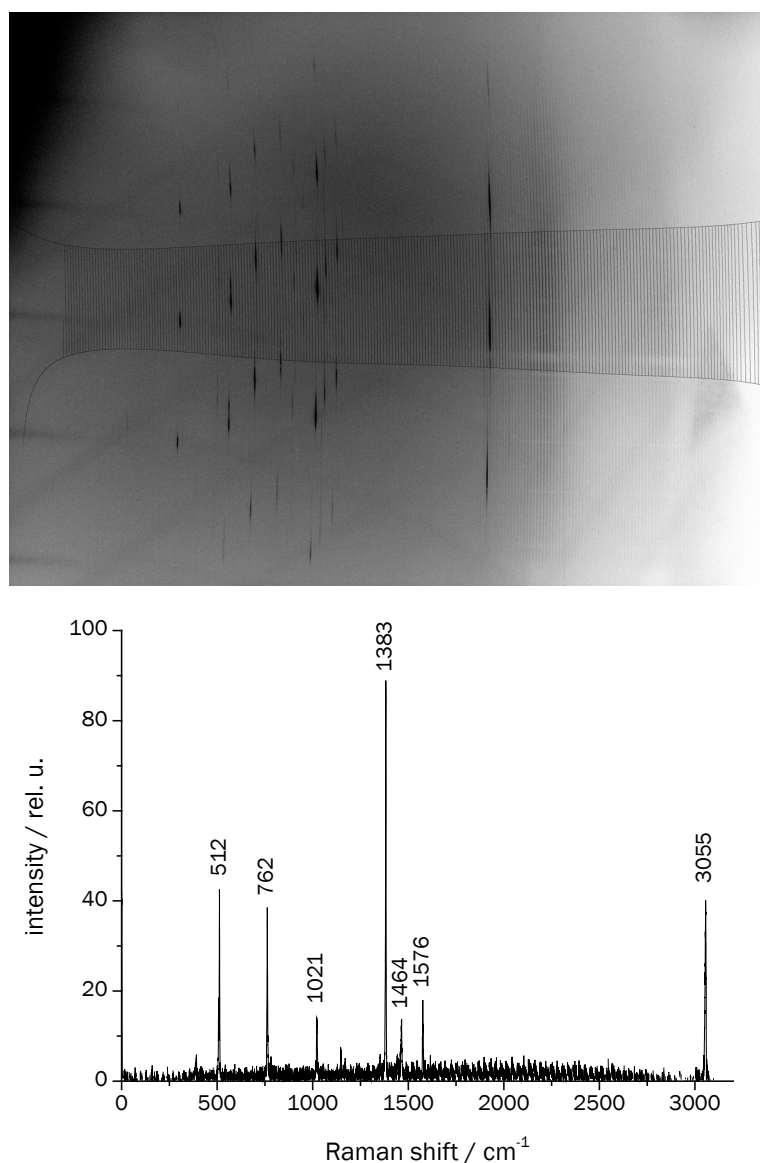


Figure 29: Raman spectrum of naphthalene excited with  $\lambda_{\text{ex}} = 532 \text{ nm}$ , top: raw data with m- and s-lines; bottom: evaluated spectrum with main features labeled

Raman spectra were recorded as a first application of the spectrometer. In figure 29, the raw image containing the conversion line matrix as well as the converted Raman spectrum of naphthalene are shown. A solid naphthalene sample was excited with a frequency-doubled Nd:YAG laser ( $\lambda_{\text{ex}} = 532 \text{ nm}$ ). The FWHM of the line at  $1383 \text{ cm}^{-1}$  is  $2.6 \text{ cm}^{-1}$  ( $\cong 87 \text{ pm}$ ). The spectrum is in good agreement with spectra from the literature.<sup>70</sup>

A selection of peaks and the Raman shifts reported by Srivastava & Sing and in this work are collected in table 4 along with assignments to specific molecular vibrations.

Another example of a Raman spectrum is shown in figure 30. A solid sample of benzoic acid was investigated in the same way as naphthalene. This spectrum is also in good agreement with literature spectra.<sup>71</sup> Selected peaks along with their Raman shifts and vibrational assignments reported by Krishnakumar & Mathammal and in this work are shown in table 5.



Table 4: Peaks observed in Raman spectrum of naphthalene and comparison to work published by Srivastava & Sing, vibration assignments<sup>70</sup>

Raman shift / $\text{cm}^{-1}$ [Srivastava & Sing] <sup>70</sup>	Raman shift / $\text{cm}^{-1}$ [this work]	Symmetry	Assignment
508	512	A'	CCC bending
759	762	A'	Breathing
1017	1021	A'	CC stretching
1375	1383	A'	C stretching; ring deformation
1459	1464	A'	CC stretching; CH-bending
1572	1576	A'	C=C stretching, in phase
3054	3055	A'	CH-stretching, out-of-phase

The Raman shifts for both substances are in good agreement, implying good wavelength calibration of the spectrometer. The calibration for the recording of the spectrum required to first place the Ne discharge lamp in front of the spectrometer before switching to the Raman setup. Integrating the calibration source into the spectrometer more elegantly could potentially increase the wavelength accuracy even further. The collection of light from the sample could also be improved in the future. The spectra are still an example of the sensitivity of the spectrometer, given the generally low intensities of Raman peaks.

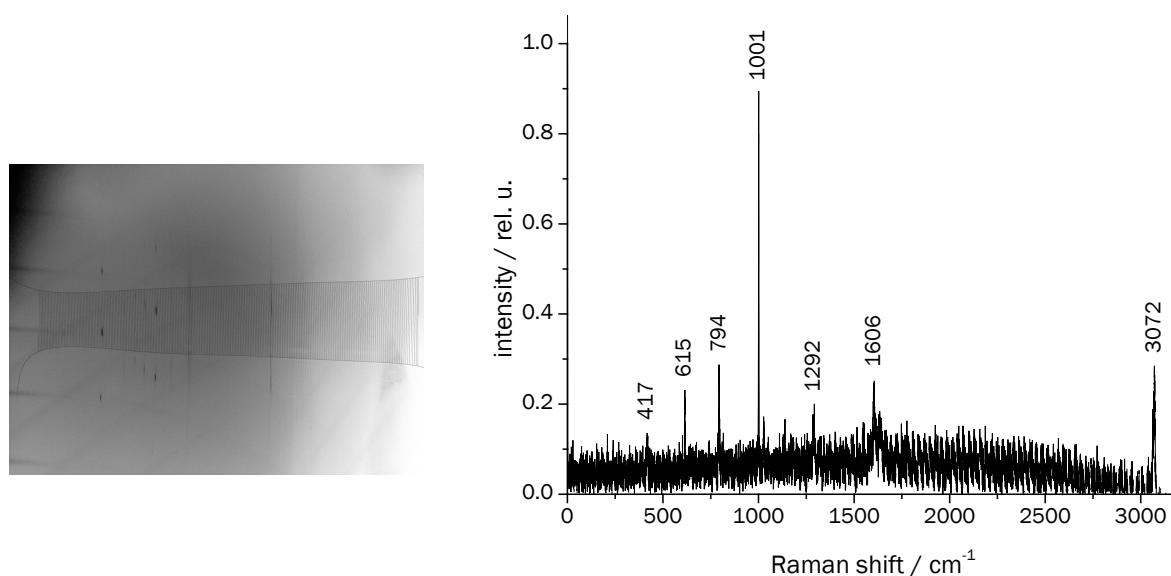
Figure 30: Raman spectrum of benzoic acid excited with  $\lambda_{\text{ex}} = 532 \text{ nm}$ , left: raw data with m- and s-lines; right: evaluated spectrum with main features labeled

Table 5: Peaks observed in Raman spectrum of benzoic acid and comparison to work published by Krishnakumar & Mathammal, vibration assignments<sup>71</sup>

Raman shift / $\text{cm}^{-1}$ Krishnakumar & Mathammal <sup>71</sup>	Raman shift / $\text{cm}^{-1}$ [this work]	Symmetry	Assignment
415	417	A''	Symmetric torsion; CC wagging; CH wagging
618	615	A'	CCO bending; Ring symmetric distortion
810	794	A''	CCO torsion; CC wagging; trigonal distortion; CH wagging
958	1001	A'	Ring trigonal distortion; CC stretching
1295	1292	A'	CH bending; CC stretching
1630	1606	A'	CC stretching; CH bending
3073	3072	A'	CH stretching

The line width is also in good agreement with expected convoluted Raman linewidth resulting from the resolution of the spectrometer and the excitation laser linewidth (both roughly 50 pm).

The second application chosen for the spectrometer is LIBS. The line widths encountered in LIB spectra are inherently narrow due to its nature of a gas phase atomic spectroscopy. High resolution combined with good wavelength accuracy is required in order to identify elements, especially in mixtures. The first measurements were carried out on a brass sample.

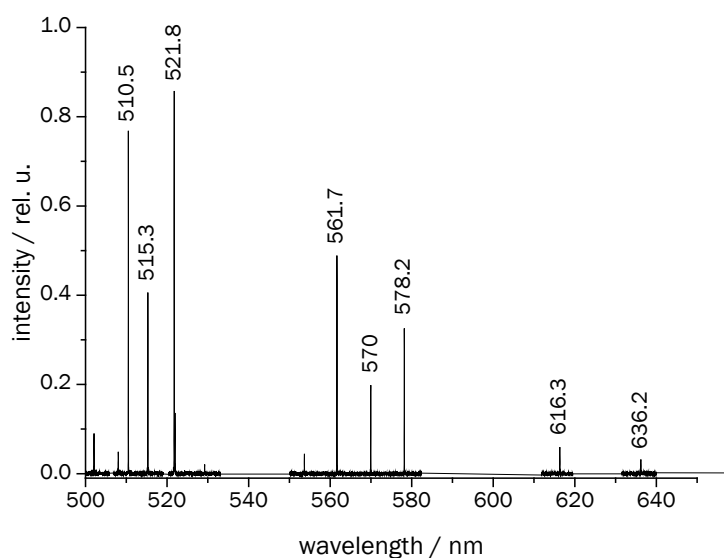


Figure 31: LIB spectrum of a brass standard recorded with Aryelle spectrometer

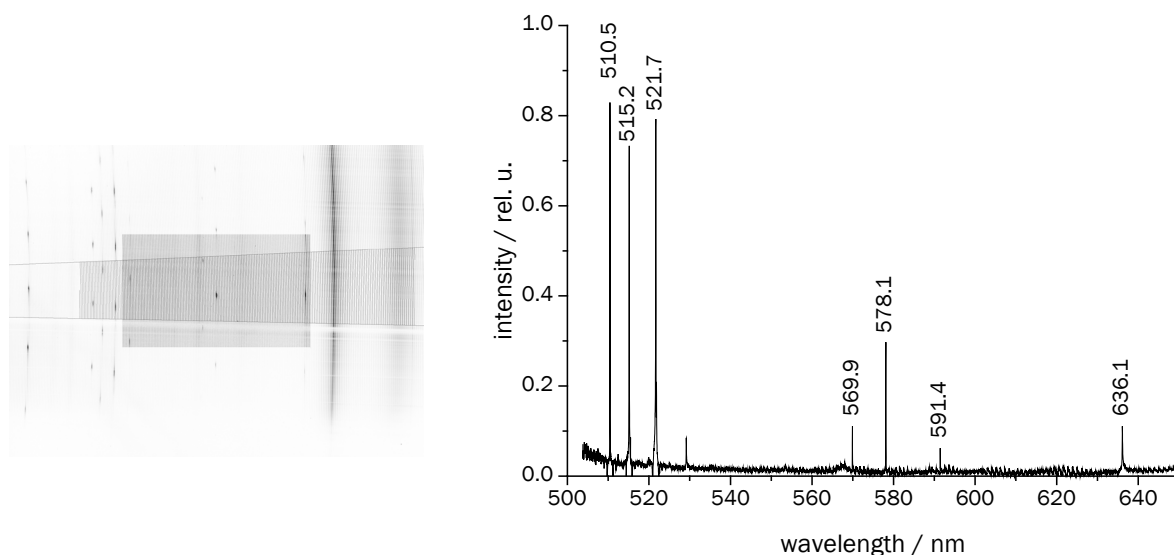


Figure 32: LIB spectrum of a brass standard, left: raw data with m- and s-lines; right: evaluated spectrum with main features labeled

The sample was first characterized on a commercial echelle spectrometer (LTB Aryelle, Fig. 31). The spectrometer uses a chopper to achieve time gating in order to avoid the background of thermal radiation present immediately after the ignition of the plasma. The FWHM of the line at  $\lambda = 578.2$  nm is 38 pm. For the etalon spectrometer, the plasma was generated by the focused beam of a Nd:YAG laser with  $\lambda = 1064$  nm. The CCD camera used for the measurements cannot be gated. Therefore, broadband thermal background is detected as an underground of the spectrum and the peaks exhibit a certain thermal broadening as well. By adjusting the intensity of the laser, these effects can be lessened somewhat and a good spectrum could still be recorded (Fig. 32). The FWHM of the peak at  $\lambda = 578.1$  nm is 52 pm, consistent with the values observed for Ne.

The spectra recorded with the echelle and etalon spectrometers show good agreement, an indication of the stable wavelength calibration of the etalon spectrometer. Not all peaks are recovered. This observation is due to the thermal effects discussed above. The peaks can be assigned to various Cu transitions and one Zn transition (table 6).

Table 6: Peaks observed in LIB spectrum of brass and assignments to transitions<sup>72</sup>

Species	Wavelength / nm	Lower Level Conf., Term, J	Upper Level Conf., Term, J
Cu I	510.6	$3d^9 4s^2 \ ^2D \ ^5I_2$	$3d^{10} 4p \ ^2P^o \ ^3I_2$
Cu I	515.3	$3d^{10} 4p \ ^2P^o \ ^1I_2$	$3d^{10} 4d \ ^2D \ ^3I_2$
Cu I	521.8	$3d^{10} 4p \ ^2P^o \ ^3I_2$	$3d^{10} 4d \ ^2D \ ^5I_2$
Cu I	529.2	$3d^9 (2D) 4s 4p (3P^o) \ ^4D^o \ ^7I_2$	$3d^9 4s (3D) 5s \ ^4D \ ^7I_2$
Cu I	570.0	$3d^9 4s^2 \ ^2D \ ^3I_2$	$3d^{10} 4p \ ^2P^o \ ^3I_2$
Cu I	578.2	$3d^9 4s^2 \ ^2D \ ^3I_2$	$3d^{10} 4p \ ^2P^o \ ^1I_2$
Zn I	636.2		

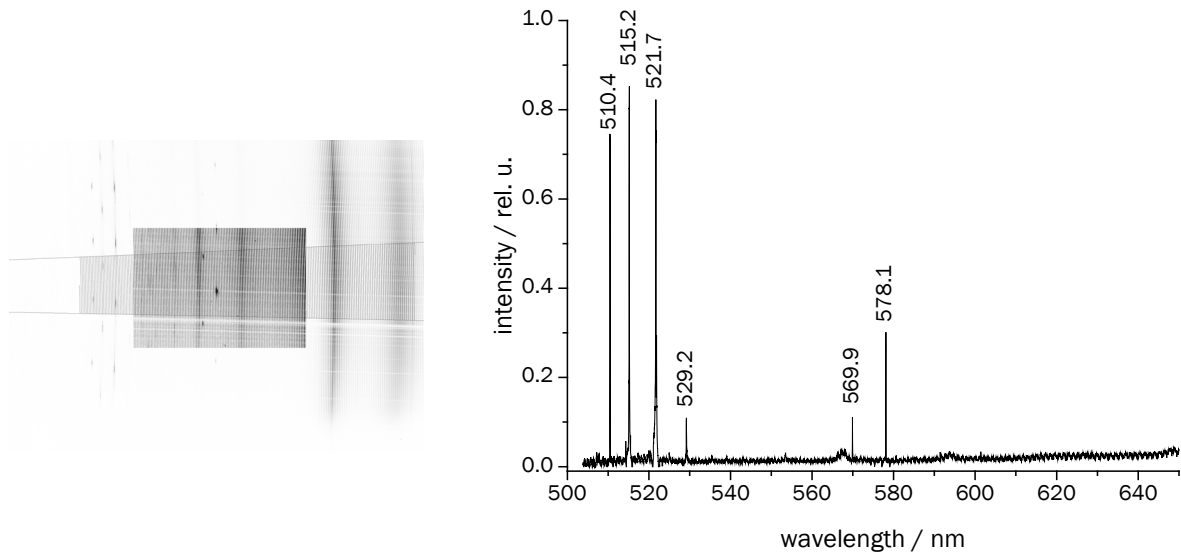


Figure 33: LIB spectrum of a 5 cent euro coin, left: raw data with m- and s-lines; right: evaluated spectrum with main features labeled

As a second, real world example, the LIB spectrum of a 5 cent euro coin was recorded (Fig. 33). The coin is made of Cu-covered steel, but only the top layer was ablated. Although it was a used coin showing surface deposits, the Cu transitions can be clearly observed in the spectrum. The ratios of the lines are different from the brass sample, an effect that can be attributed to the surface deposits on the coin and Zn content of the brass.

#### 4.1.2.6 Conclusions

The work done in this chapter is intended as a proof of concept that an etalon can be used as an interferometric device to achieve high resolutions in a compact 2D-spectrometer for broad wavelength ranges. Suggestions for future enhancements of the design are already discussed in the paper. Improvements could be made by using different optics, especially etalons with specifically tailored finesses. As could be shown in the Ne spectrum, spherical aberrations reduce the resolution of the spectrometer when using the full slit height. This could be countered either by using different lenses or by focusing the incoming light onto the slit more efficiently, thus eliminating the need for the full slit height. At any rate, optimizing the way the light is coupled into the spectrometer for each application would be beneficial. When the spectrometer is adopted for a specific application, the optics should be tailored for that purpose, e.g. using UV optics in a LIBS application. Using a different camera, such as an ICCD camera for LIBS, could also be advisable, as it would allow time gated detection.

In our work group, there is already a LIBS project underway that is also using the spectrometer. In this project, the spectrometer will be used in the characterization of soil samples. Various upgrades to the design are also in development. Among other things, the single lenses in the setup will be replaced by photographic lens assemblies, reducing chromatic aberrations and other artifacts. Light will be collected by a fiber assembly, in which on one side the single fibers are aligned in a row, replacing the slit on the spectrometer side. Additionally, the spectrometer will be housed in a rugged casing, reducing maintenance requirements, such as calibration.

## 4.2 Ion mobility mass spectrometry

IM spectrometry is an analytical technique whose advantages include its high sensitivity, applicability for many different compound classes and its potential for miniaturization. Stand-alone IM spectrometers are especially used in fields where a mobile analytical solution is needed or costs have to be decreased. The broad range of ionization techniques that can be coupled to IM spectrometry provide a wide range of fields of application. Traditionally, the spectrometers only operated with gas phase ionization techniques but the introduction of ESI and other API sources expanded the scope of IM spectrometry to the investigation of liquid samples. Recently, there has been a growing interest in the combination of IM and mass spectrometry. The principal quantity measured by IM spectrometers, the collision cross section, provides an additional level of information on samples. Mass spectrometry can also be a tool used to gain additional information about the signals encountered in stand-alone IM spectrometers when uncertainties arise. The knowledge of mass-mobility relations for specific substance classes supports the identification of specific compounds.

In this chapter, two mass spectrometers were used. A ToF mass spectrometer and an LTQ mass spectrometer. The ToF mass spectrometer is fitted with an ionization chamber working at reduced pressure. In this device, investigations of the products of REMPI were carried out that yielded insights into IMR previously encountered in an APLI IM spectrometer.

The LTQ mass spectrometer is a commercial API mass spectrometer. Thus, the transfer of ions from atmospheric pressure into the vacuum of the ion trap is handled by a commercial solution. In order to recreate the conditions in an IM spectrometer, a custom ionization chamber based on an X-ray source was built. The products of the ionization of several explosive compounds were investigated.

A custom drift tube, featuring a dual gate design, was also developed and coupled to the LTQ mass spectrometer. This device allows the concurrent acquisition of IM and mass spectra in combination with an ESI source. The same spectrometer was also fitted with an APLI source and interfaced to a gas chromatograph (GC) and a vaporization source.

### 4.2.1 REMPI mass spectrometry of H<sub>2</sub>S at reduced pressure

In this section, the generation of ions at reduced pressure is investigated using a custom ionization chamber coupled to a ToF mass spectrometer. The reactions following the APLI of H<sub>2</sub>S were previously investigated using IM spectrometry by R. Laudien and T. Beitz. The results presented here compliment that study. Parts of the findings were published in *Analytical and Bioanalytical Chemistry*.<sup>73</sup> The IM spectrometry results and further applications of the reduced pressure ionization chamber can be found in the paper as well.

In chapter 4.2, the investigation of ionization processes at atmospheric pressure is presented. Supplementary measurements were carried out in the vacuum with the ToF mass spectrometer equipped with an effusive inlet. In the vacuum, it is possible to investigate the primary products of ionization. This information is important for understanding the ionization processes at atmospheric pressure, because ions can undergo many collisions with neutral molecules under these conditions. These collisions can lead to IMR and consequently, the ions observed in vacuum and at atmospheric pressure can be quite different.

Investigations at reduced pressures present an important transition stage between these two extremes. Therefore, they can further enhance the understanding of the processes and intermediate ions involved.

The results presented here concern the process of REMPI. This laser-based ionization scheme can be used in the vacuum as well as at atmospheric pressure, where it is usually called APLI. The ionization chamber in front of ToF mass spectrometer was designed to operate at a pressure around 0.5 mbar. At this intermediate pressure, very few collisions between reactant ions and molecules take place. Therefore, reactions such as PTR from the primary ions can take place but secondary reactions of the products of these PTR are unlikely. The secondary reactions can take place at atmospheric pressure, however, and they sometimes result in the suppression of analyte ions. At atmospheric pressure, only the most stable ions, e.g. only the ions formed by molecules with the highest proton affinities, are observed. Ions that are only transitional at atmospheric pressure can be observed at intermediate pressures. H<sub>2</sub>S has been used as a reactant gas for REMPI in IM spectrometry as it has certain advantages.<sup>73</sup>

First, H<sub>2</sub>S is a permanent gas which makes it easier to handle and control the amount introduced in a gas phase IM spectrometer. In IM spectrometers equipped with <sup>63</sup>Ni sources, H<sub>2</sub>O is usually used as a reactant for APCI by PTR. However, ionizing H<sub>2</sub>O with commercial lasers in REMPI is not feasible because its IE is too high (IE(H<sub>2</sub>O) = 12.6 eV) and the ionization efficiency is low. As will be shown below, H<sub>2</sub>S can be ionized by commercial lasers (IE(H<sub>2</sub>S) = 10.5 eV).<sup>58</sup> APCI by PTR is a versatile ionization technique so long as the PA of the reactant is lower than that of the analyte. The PA of H<sub>2</sub>O is PA(H<sub>2</sub>O) = 691 kJ/mol, the PA of H<sub>2</sub>S is only slightly higher [PA(H<sub>2</sub>S) = 705 kJ/mol].<sup>58</sup> However, due to a lower tendency towards and better control of clustering with H<sub>2</sub>S, the effective PA is likely to be lower than in conventional water-based ionization chemistry, since the effective PA of clusters of the type H<sup>+</sup>(H<sub>2</sub>O)<sub>n</sub>, which prevail at atmospheric pressure, decrease with increasing values of n.<sup>74,75</sup>

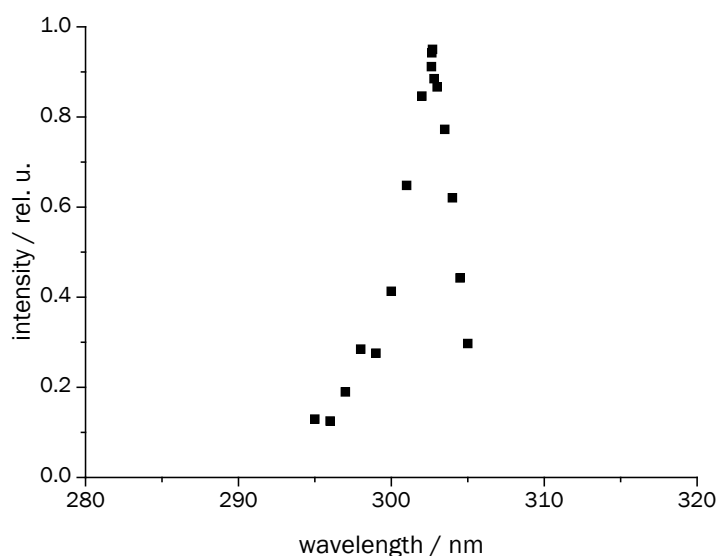


Figure 34: REMPI spectrum of H<sub>2</sub>S recorded at  $p(\text{H}_2\text{S}) = 0.05$  Pa in 0.5 mbar of N<sub>2</sub> in the reduced pressure chamber attached to the ToF mass spectrometer

The REMPI spectrum of H<sub>2</sub>S at atmospheric pressure was recorded in the IM spectrometer with a tunable dye laser. The maximum intensity was found at  $\lambda = 302.2$  nm. The spectrum can be found in the publication.<sup>73</sup> It was also recorded in the vacuum over a broad wavelength range. The peak at the relevant wavelength was determined to be the result of a 2+1 REMPI process and assigned to a transition from the  $^2b_1$  molecular orbital to the excited  $4p_{a_1} \ ^1B_1$  (000) state.<sup>76</sup> The REMPI spectrum could be reproduced in the reduced pressure chamber (Fig. 34). The spectrum was also recorded with a tunable dye laser, by recording the signal intensity of all ions as function of the laser wavelength. The laser energy was also recorded and the signal intensity corrected accordingly.

In the REMPI IM spectrum of H<sub>2</sub>S (not shown), only one peak is observed. More ionic species are observed in the EI spectrum (reproduced from the NIST database)<sup>58</sup> and the REMPI mass spectrum of H<sub>2</sub>S recorded at reduced pressure (Fig. 35). In the EI spectrum, peaks corresponding to S<sup>+</sup>, HS<sup>+</sup> and H<sub>2</sub>S<sup>+</sup> are observed.

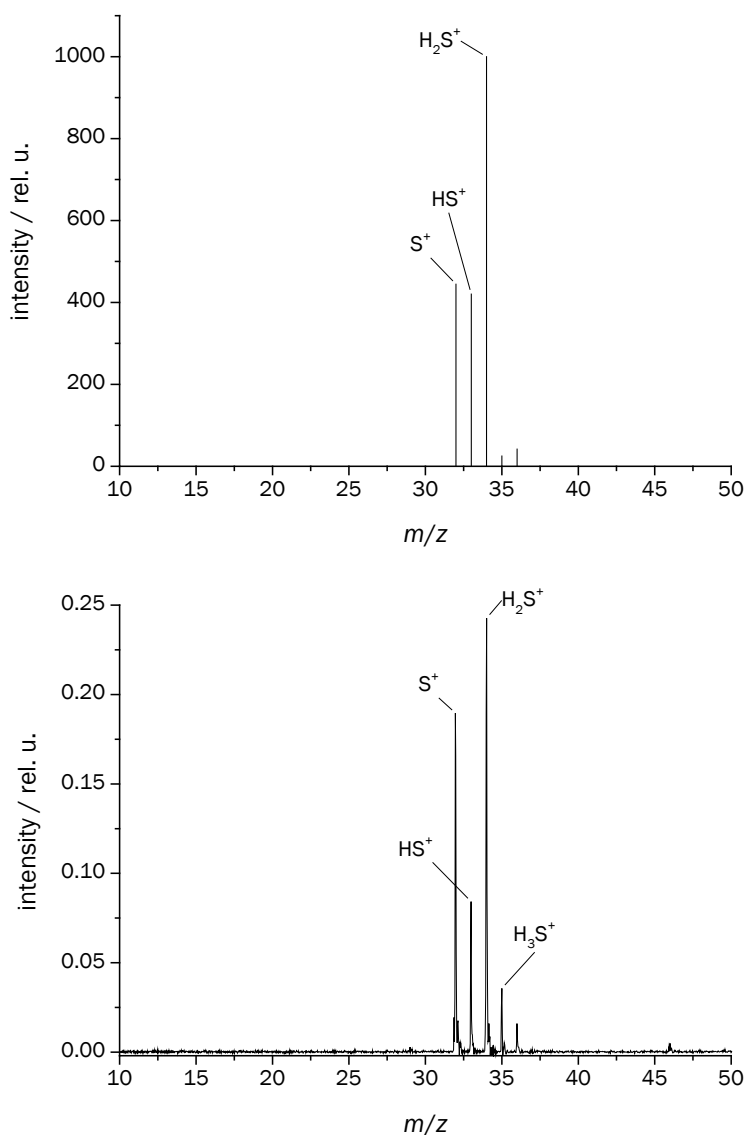


Figure 35: Mass spectra after ionization of H<sub>2</sub>S, top: EI spectrum (centroids) taken from NIST Mass Spectral Library;<sup>58</sup> bottom: REMPI spectrum ( $\lambda = 302.6$  nm,  $E_{\text{pulse}} = 4.6$  mJ) recorded at  $p(\text{H}_2\text{S}) = 0.05$  Pa in 0.5 mbar of N<sub>2</sub>

A simulation of the spectrum shows that the ratios of the peaks at  $m/z = 35$  and  $m/z = 36$  indicate they are the isomer peaks of  $^{34}\text{S}$ . The intensity of the  $\text{S}^+$  peak is higher in the REMPI mass spectrum. The appearance potential of  $\text{H}_2\text{S}^+$  is  $(10.4 \pm 0.1)$  eV, that of  $\text{HS}^+$  is  $(14.4 \pm 0.2)$  eV and that of  $\text{S}^+$  is  $(13.3 \pm 0.3)$  eV.<sup>77</sup>

These appearance potentials are not very relevant in EI due to large excess energies of the electrons above 70 eV. However, the 2+1 REMPI energy is in this range (302.2 nm  $\cong$  4.1 eV for one photon, 12.3 eV for three photons). Consequently, the formation of  $\text{S}^+$  and  $\text{HS}^+$  is caused by the absorption of another photon by  $\text{H}_2\text{S}^+$  and the formation of  $\text{S}^+$  is favored due to its lower appearance potential. In a study of 1+1 REMPI of  $\text{H}_2\text{S}$ , the fragmentation of  $\text{H}_2\text{S}^+$  yielding an excess of  $\text{S}^+$  over  $\text{HS}^+$  was found.<sup>78</sup> In addition to the ions found in EI,  $\text{H}_3\text{S}^+$  is also observed with about 10 % of the intensity of the  $\text{H}_2\text{S}^+$ -peak (confirmed by spectrum simulation) at a partial pressure  $p(\text{H}_2\text{S}) = 0.05$  Pa in the REMPI spectrum. Similar ratios were obtained in high pressure mass spectrometry experiments at  $p(\text{H}_2\text{S}) = 0.7$  Pa.<sup>79,80</sup>  $\text{H}_3\text{S}^+$  is the main peak observed in high pressure mass spectrometry experiments at  $p(\text{H}_2\text{S}) = 5\text{--}10$  Pa.

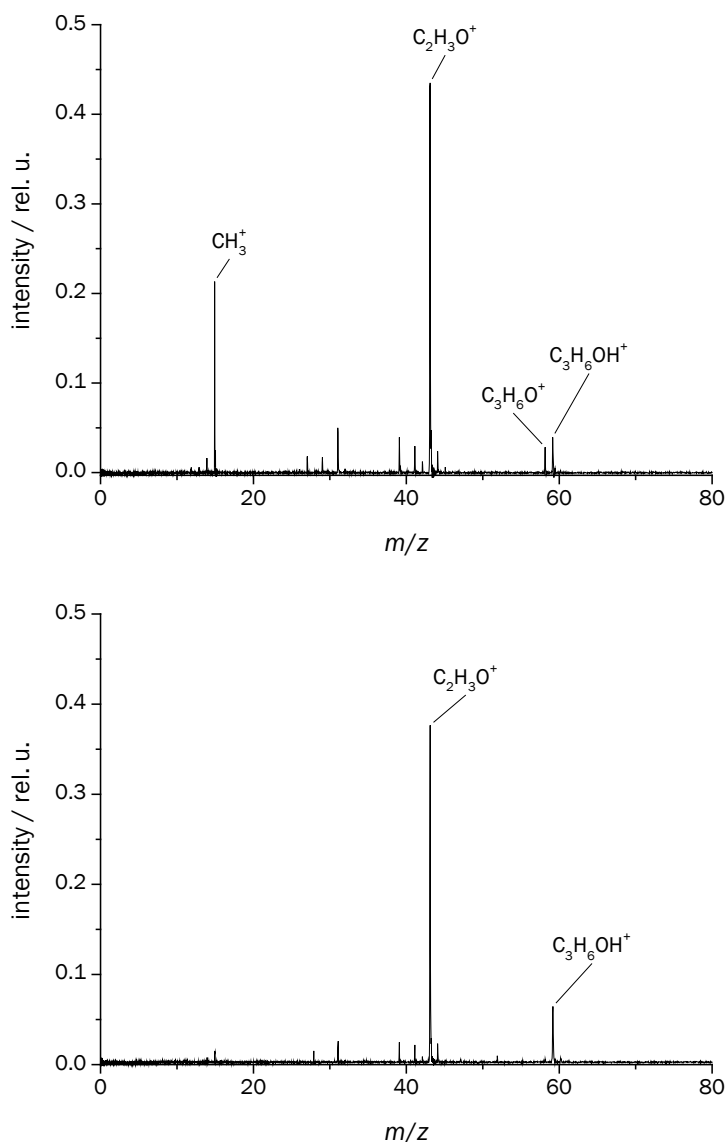


Figure 36: Mass spectra of top: 1+1+1 REMPI of acetone; bottom: REMPI of a mixture of  $\text{H}_2\text{S}$  and acetone;  $\lambda = 302.6$  nm,  $E_{\text{pulse}} = 4.6$  mJ,  $p(\text{H}_2\text{S}) = 0.04$  Pa,  $p(\text{acetone}) \approx 10$  Pa in 0.4 mbar of  $\text{N}_2$



In IM spectrometry at atmospheric pressure and a relatively high partial pressure of H<sub>2</sub>S, the primary ions will be almost completely converted to H<sub>3</sub>S<sup>+</sup>. At lower partial pressures, the primary ions will also prevail.

Several IMR of H<sub>3</sub>S<sup>+</sup> were investigated in the IM spectrometer. They have been studied in more detail in the drift cell. One example is the IMR of H<sub>3</sub>S<sup>+</sup> and acetone. In these experiments, a mixture containing 1000 ppm of H<sub>2</sub>S in N<sub>2</sub> was used and the pressure of the drift cell was held at 0.4 mbar, resulting in  $p(\text{H}_2\text{S}) = 0.04$  Pa. The pressure is slightly higher near the capillary, at the point where ionization occurs. Acetone was introduced in a small evaporation tube on the atmospheric pressure side of the gas feed. Considering the vapor pressure of acetone of roughly 300 mbar at 25 °C,  $p(\text{acetone}) = 10$  Pa in the ionization chamber at 0.4 mbar of N<sub>2</sub>.

At the relatively high laser energies used, the ionization of acetone due to a 1+1+1 REMPI process is also possible. Therefore, a spectrum in the presence of acetone but in the absence of H<sub>2</sub>S was recorded (Fig. 36, top). The mass spectrum of REMPI of a mixture of H<sub>2</sub>S and acetone is shown on the bottom of figure 36. In direct REMPI of acetone, CH<sub>2</sub>COH<sup>+</sup>, the protonated ketene is the main product ion. It is also the main species observed in EI.<sup>58</sup> In addition, CH<sub>3</sub><sup>+</sup> is also observed, as are radical cations and protonated acetone. In the presence of H<sub>2</sub>S, only the protonated ketene (fragment) and protonated acetone are found. Neither the radical cation, nor the radical fragment ion or primary ions of H<sub>2</sub>S ionization are found. The results indicate that 1+1+1 REMPI of acetone is taking place in parallel to PTR from the primary H<sub>2</sub>S ions. The PTR results in a much higher intensity of the protonated acetone peak.

#### 4.2.2 Atmospheric pressure ionization chamber and dual-gate IM spectrometer connected to ion trap mass spectrometer

In this and the following chapter, different API sources, namely ESI, APLI and APCI, are used with an LTQ mass spectrometer. These sources can be installed in an IM spectrometer placed in front of the mass spectrometer or in an ionization chamber replicating the conditions in the IM spectrometer in front of the mass spectrometer. The former approach has the advantage of a concurrent recording of IM and mass spectra. The second approach has a sensitivity advantage and can lead to the same insights in combination with the results of stand-alone IM spectrometry. In the following chapter, the results of the first approach are detailed. The results of the second approach are discussed in chapter 4.2.3.

The commercial LTQ mass spectrometer is already equipped with intermediate pressure stages and ion guides for the transfer of ions from atmospheric pressure to the high vacuum of the mass analyzer chamber. The first stage of the vacuum system is a capillary with an inner diameter of 550  $\mu\text{m}$  and a length of 102 mm. The drift axis of the IM spectrometer is lined up with this capillary. Depending on the ionization source, the ion cloud in an IM spectrometer has macroscopic dimensions of several millimeters, which is additionally increased by Coulomb repulsion of the ions. Without focusing, only the ions in the center of the spectrometer would reach the vacuum but not those on the outside. It is therefore necessary to focus the ion cloud into the small orifice of the capillary in order to achieve a high transmission of ions into the first vacuum stage. The nature of the ion trap mass spectrometer makes the mass analysis times (three digit millisecond range for high sensitivity) incompatible with direct acquisition of temporally resolved IM spectra (overall time of 20–50 ms, requiring a resolution below 1 ms). Therefore, a different approach for resolving the IM spectra has to be chosen. One possible solution is the use of a Bradbury-Nielsen ion gate at the end of the drift region. The spectrum can thus be scanned by allowing only ions packets of a well-defined drift time into the mass analyzer. This approach has the added advantage that it is irrelevant whether the time information is distorted or lost upon focusing the ions into the capillary. Therefore, a design can be chosen, where the ions further away from the capillary take longer to reach it than those on the center axis of the IM spectrometer. Any solution preventing this, for example an ion funnel, would be difficult to implement at atmospheric pressure. Ion trajectory simulations utilizing the charged particle optics simulation software SIMION were carried out based on the statistical diffusion simulation model by Appelhans and Dahl to account for the ion neutral collisions taking place at atmospheric pressure.<sup>60</sup> A stack of electrodes with inner diameters decreasing linearly in flight direction was found to be promising design. The electric field gradient in the first part of the electrode stack is steeper than the gradient used in the drift region. The ions are thus focused. A more moderate gradient in the middle part of the electrode stack prevents the ions from impacting on the electrodes. This lower field gradient essentially “draws” the ions through the funnel. Immediately around the capillary, the gradient is steep again. Simulated ion trajectories using optimized gradients are shown on the left of figure 37. It is apparent that the ions are heavily focused in the first segment of the electrode stack and near the capillary itself. Time markers are placed on the trajectories in regular intervals of 500  $\mu\text{s}$ . These show that the ions are essentially moving at the same velocity within the IM spectrometer but the temporal information is lost behind the ion gate.

#### 4.2.2 Atmospheric pressure ionization chamber and dual-gate IM spectrometer connected to ion trap mass spectrometer

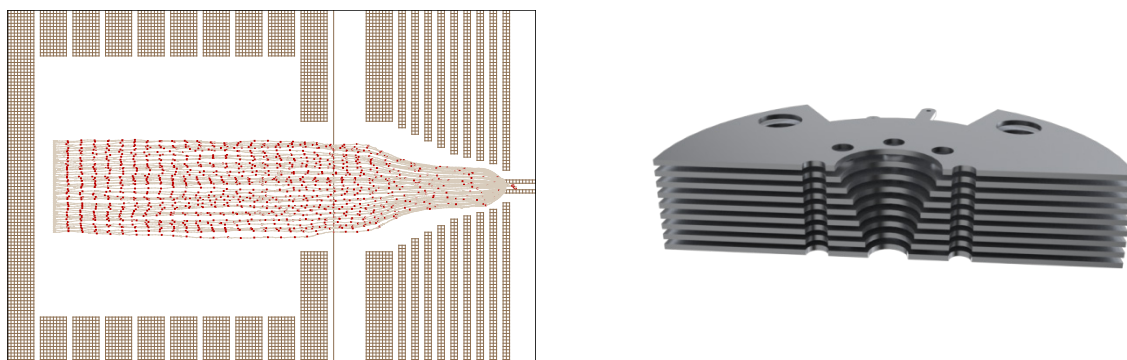


Figure 37: Electrode stack for focusing ions into the ion trap; left: SIMION simulation (including a part of the IM spectrometer, brown checkered regions – electrodes; brown line – position of ion gate; grey lines – ion paths, red dots signify 500  $\mu$ s time-steps); right: cut-away view of CAD model

Once the ions are near the orifice of the capillary, the transport is mostly a result of gas dynamics in conjunction with the pressure gradient. These effects are not accounted for in the simulation.

With this basic configuration of the transfer stage, the IM spectrometer could be designed. The construction was planned using the computer-aided design (CAD) software SolidWorks. On the right of figure 37, a model of the electrode stack is shown. The drift tube itself consists of 20 stainless steel drift rings separated by PEEK spacers. The drift rings have an inner diameter of 40 mm and are spaced 5 mm from each other. The total drift path is consequently 100 mm. The tube consists of two subsections. This design has the advantage that the screws holding the electrodes in place can be on a voltage of one the rings, thus reducing the voltage difference and reducing the risk of discharges. The length of the drift tube can also be modified easily. The Bradbury-Nielsen ion gates are constructed of two electrically independent frames containing each a set of wires. These wires have a diameter of 75  $\mu$ m and a spacing of 650  $\mu$ m. They are wound around the frames in such a way that they are connecting to one frame or the other alternately. The frames are equipped with a spring to ensure the tension of the wires (Fig. 38, left). This ion gate is placed in between the drift tube and the focusing stack. In the case of the ESI IM mass spectrometer, a second 50 mm long electrode stack is placed in front of the drift tube. This stack is referred to as the desolvation region because the ions produced by ESI can still be solvated when they enter this region. After passing through the desolvation region, they have shed their solvation shell. Between the desolvation region and the drift tube is a second ion gate.

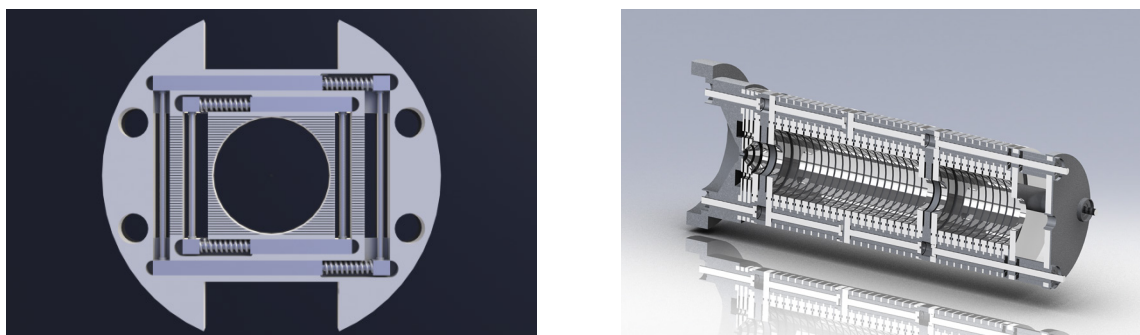


Figure 38: CAD models of left: ion gate frame; right: cut-away view of dual gate ion mobility spectrometer with connector for ion trap mass spectrometer

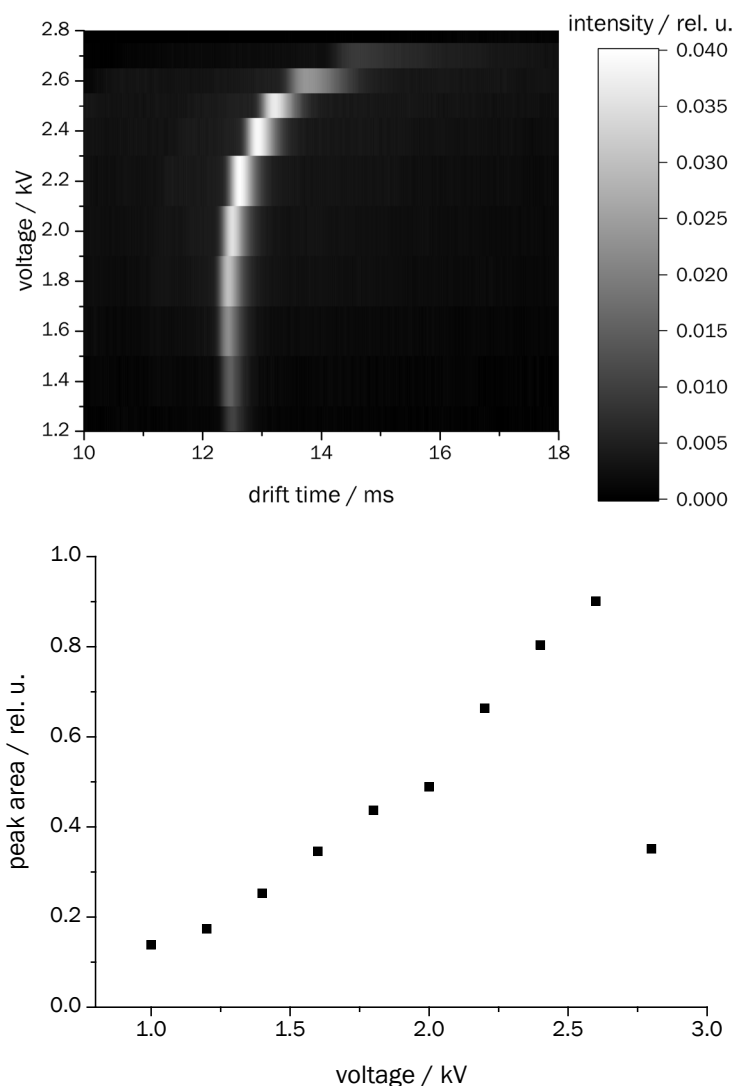


Figure 39: IM spectra of 2,6-di-*tert*-butylpyridine recorded with electrode stack and Faraday detector; top: influence of electrode voltage on peak shape; bottom: influence of electrode voltage on peak area

This second gate is necessary because ions are produced continuously by ESI and thus ion packets have to be generated at this gate. The ion gate in front of the focusing stack is then synchronized to this gate with a variable delay. The IM mass spectrum can then be constructed as this delay is equivalent to the drift time of the ions in the mass spectrum obtained at that specific delay. A cut-away rendering of the dual gate ion mobility spectrometer used for ESI is shown on the right of figure 38.

The dual gate IM spectrometer fitted with the focusing stack was equipped with a Faraday detector for the purpose of characterizing the ion transfer. In this setup, the voltage of each electrode in the stack could be adjusted individually while keeping the electric field gradient within the drift tube constant. IM spectra were recorded by creating packets of ions at the first ion gate in flight direction but keeping the second ion gate open. This mode of operation corresponds to a normal (single gate) ESI IM spectrometer. First, the individual voltages of the electrodes were optimized for maximum transmission. Then, the overall voltage on the stack relative to the drift voltage was varied. With increasing electrode stack voltage, the arrival time of the ions is increased and a broadening of the peaks is observed (Fig. 39, top). But the intensity of the peak is increasing as well up until a certain voltage (Fig. 39, bottom).

#### 4.2.2 Atmospheric pressure ionization chamber and dual-gate IM spectrometer connected to ion trap mass spectrometer

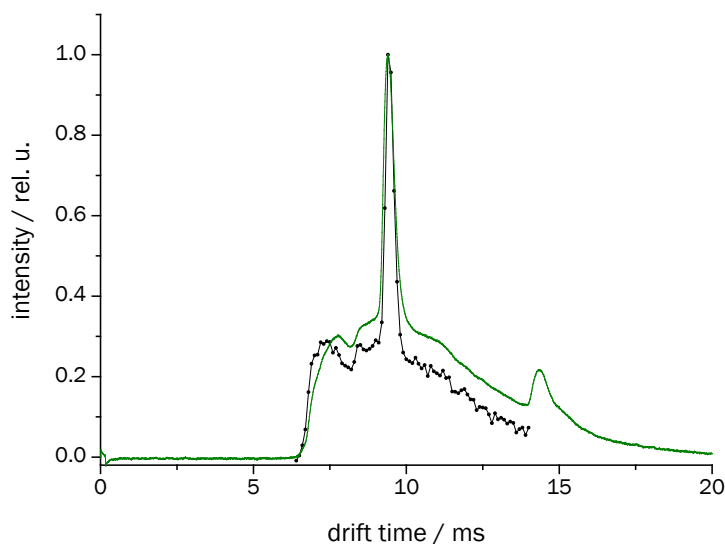


Figure 40: IM spectrum of 2,6-di-*tert*-butylpyridine recorded with the second ion gate before the detector left open (green trace) and reconstructed from scanning the second ion gate (black trace)

If the field gradient is too high, the ions cannot pass the last electrode and are discharged there.

The dual gate scanning technique can also be implemented in front of the Faraday detector. The IM spectra obtained in this way can then be compared to the spectra recorded in real-time (Fig. 40). A spectrum with a rather broad underground was chosen in order to highlight how features are reproduced. The spectra are in good agreement.

Two biomolecules were chosen to demonstrate the capabilities of the IM mass spectrometer. The first example is the oligopeptide bradykinin (Fig. 41). The mass spectrum shows that singly and doubly charged bradykinin ions ( $[M+H]^+$  at  $m/z = 1061$  and  $[M+2H]^{2+}$  at  $m/z = 531$ ) are produced in the ESI process. These can be separated in the IM spectrum as well. The IM spectrum that would be generated by a stand-alone spectrometer can be obtained when the total ion count (TIC, the overall signal intensity due to all ions) is plotted over the drift time. The first peak around 15 ms can be identified as the doubly charged ion when only the signal intensity of the corresponding mass is plotted over the drift time.

## 4 Results and discussion

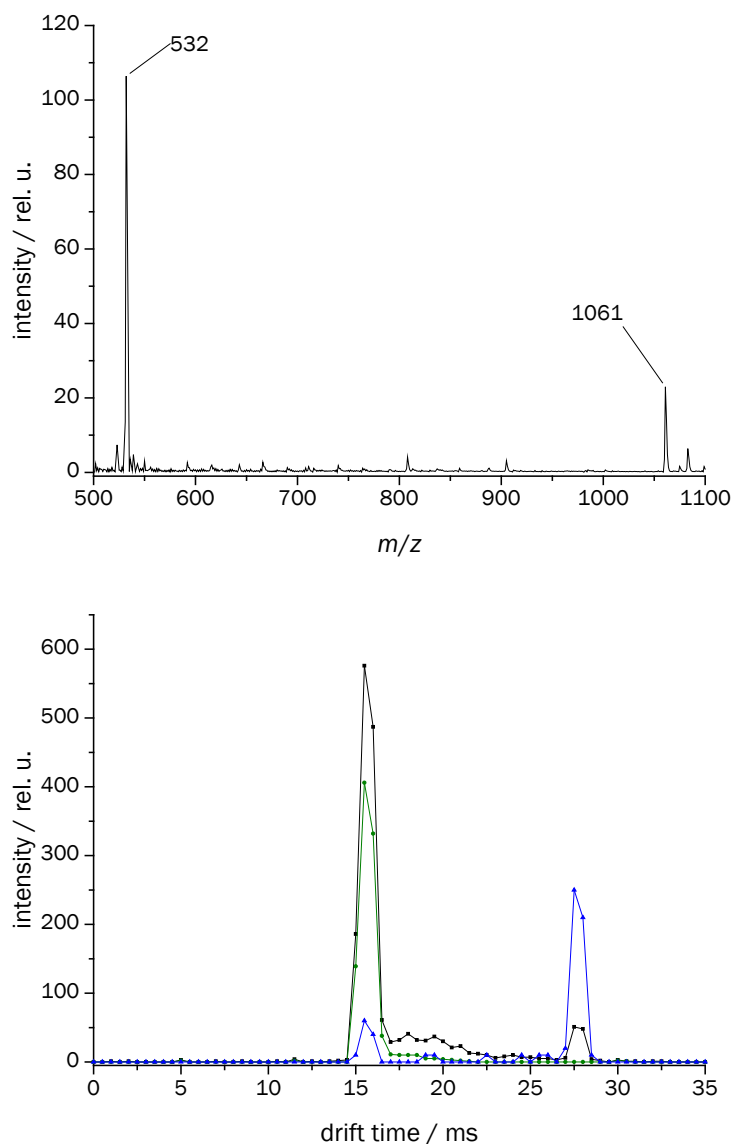


Figure 41: ESI-IM mass spectra of bradykinin; left: mass spectrum without mobility filter; right: IM spectra reconstructed from scanned spectra, TIC (black trace),  $m/z = 531$  (green trace),  $m/z = 1061$  (blue trace, intensity magnified by a factor of 10)

Accordingly, the peak at 28 ms can be associated with the singly charged ion by plotting only the intensity of the equivalent mass. The spectrum of the enzyme lysozyme was investigated as well (Fig. 42). The mass spectrum shows multiply protonated ions ( $[M+nH]^{n+}$ ;  $n = 7-9$ ) that are very common in ESI spectra of large biomolecules. In the stand-alone spectrum of lysozyme, a broad peak at a high drift time is found. The observation in the scanned IM mass spectrum of the TIC is similar, but the mass selected IM spectra show that the drift times of each mass is slightly different. The fact that the drift times of the differently charged ions are this similar could indicate that the shape of the protein is affected by the higher charges. The repulsion due to the charges could result in an unfolding of parts of the ions that would in turn cause an increase of the collision cross sections.

#### 4.2.2 Atmospheric pressure ionization chamber and dual-gate IM spectrometer connected to ion trap mass spectrometer

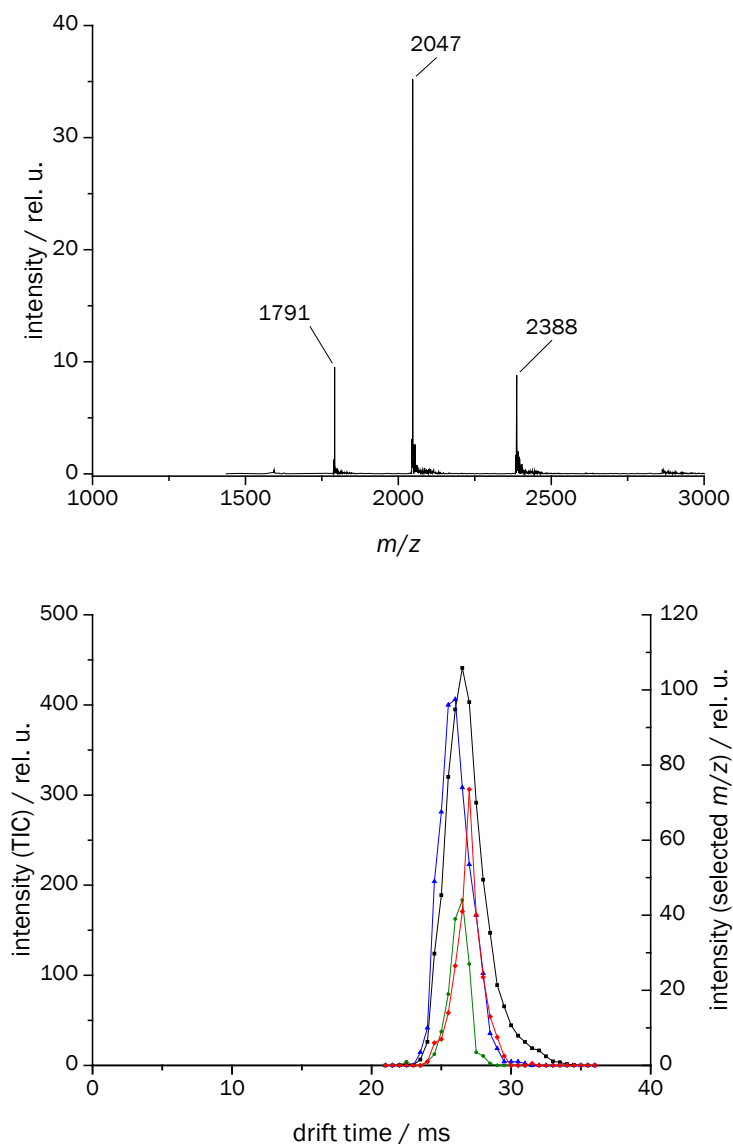


Figure 42: ESI-IM mass spectra of lysozyme; top: mass spectrum without mobility filter; bottom: IM spectra reconstructed from scanned spectra, TIC (black trace, left  $y$ -axis),  $[M+8H]^{8+}$  ( $m/z = 1791$ , green trace, right  $y$ -axis),  $[M+7H]^{7+}$  ( $m/z = 2047$ , blue trace, right  $y$ -axis),  $[M+6H]^{6+}$  ( $m/z = 2388$ , red trace, right  $y$ -axis)

The design of the instrument was subsequently modified in order to accommodate APLI. The desolvation tube and first ion gate were replaced by an ionization region fitted with laser windows and feedthroughs for a GC capillary and a ceramic vaporizer tube. The second ion gate is kept in place. However, the first gate is not needed in APLI, since an ion packet is generated by the laser pulse. With this setup, gaseous samples can be introduced through a GC coupled to the instrument and liquid samples could be transferred into the gas phase through the vaporizer tube. The construction of this instrument was also a part of my thesis. The results were reported in *Analytical and Bioanalytical Chemistry* and the *International Journal for Ion Mobility Spectrometry*.<sup>47,48</sup> These papers also include results by C. Brendler, who used the instruments to elucidate some of the results he had obtained in standalone IM spectrometers operated with APLI of gaseous and liquid samples. The results were also published in his thesis.<sup>81</sup> These publications can be considered examples of the feasibility of the instrument.

#### 4 Results and discussion

Therefore, only one result of this particular configuration (APLI) will be shown here. In figure 43, two APLI mass spectra of the neuroleptic promazine are shown. The spectra were obtained in the mobility filter mode. In this mode, instead of scanning the second drift gate with narrow opening times, the second gate is left open for longer times, letting ions of a range of drift times into the mass spectrometer. While the main ion observed in the range 9-12 ms is the molecular cation at  $m/z = 284$ , this ion is not observed in the range 6-9 ms. Instead, a number of fragment ions are observed, albeit in much lower intensity. The most intense fragment ion is found at  $m/z = 239$  and can be identified as  $[M-C_2H_7N]^+$ . Another fragment ion,  $[M-C_5H_{12}N]^+$  ( $m/z = 198$ ), corresponds to deprotonated phenothiazine structure.

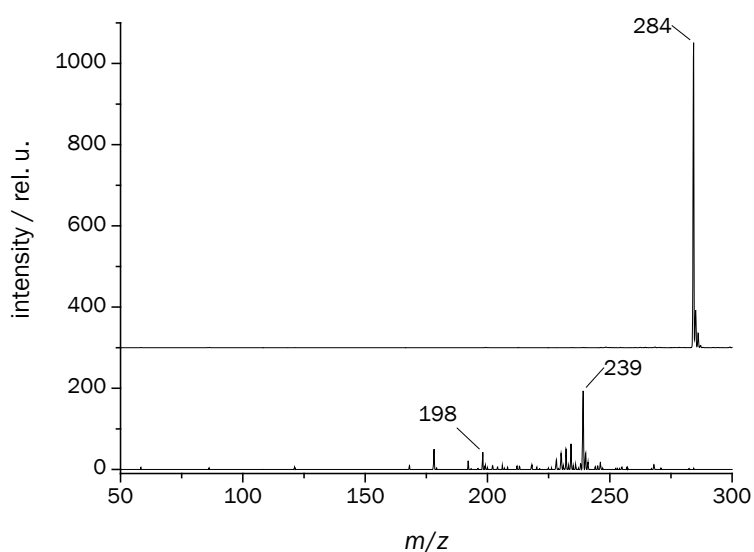


Figure 43: Mobility selected APLI mass spectra of promazine; upper trace: gate opening 9-12 ms; lower trace: gate opening 6-9 ms, intensity magnified by a factor of 100; observation of the following ions:  $[M-C_5H_{12}N]^+$  ( $m/z = 198$ ),  $[M-C_2H_7N]^+$  ( $m/z = 239$ ),  $M^+$  [ $m/z = 284$ ]



### 4.2.3 Formation of negative ions by soft X-rays and ionization chemistry of alkyl nitrates

The detection of negative ions is advantageous for compounds exhibiting high EA. The number of possible substances that interfere with the detection is reduced because many such substances do not possess a positive EA. Additionally, even if an interfering compound has a positive EA, as long as it is lower than that of the analyte, charge competition favors the latter. In practice, dopants such as methylene chloride are added. Thus, no compound with an EA below that of Cl will be detected. The NO<sub>2</sub> and NO<sub>3</sub> functional groups are electron withdrawing groups that are capable of stabilizing the excess electron. Therefore, most nitrate esters and nitroaromatic compounds possess high EA. Both classes of substances are important analytes because they are often found in explosive compounds.

#### 4.2.3.1 Construction of an atmospheric pressure X-ray ionization chamber

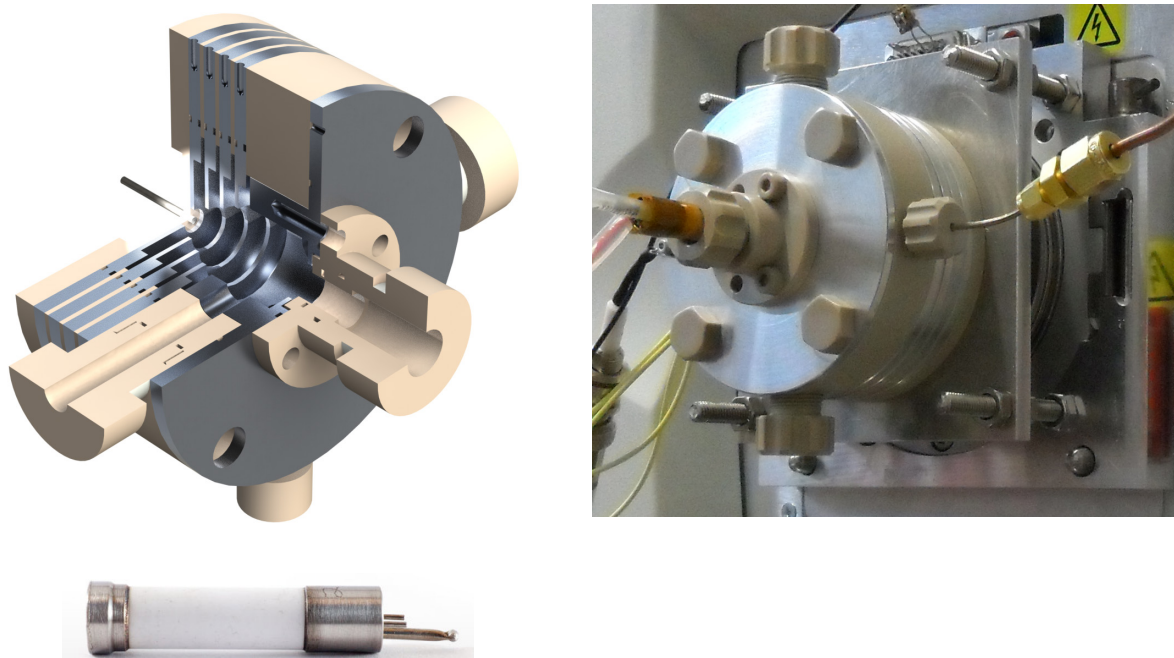


Figure 44: Ionization chamber for APCI and laser ionization; top left: rendering of CAD model; top right: photograph; bottom right: photograph of X-ray source

The aim of this part of the work was to construct a chamber for the ionization of samples at atmospheric pressure and the subsequent efficient transfer of the ions formed into the LTQ mass spectrometer. The design of the transfer electrodes discussed in chapter 4.2.2 was simplified for this chamber. The stack consisted of four ring electrodes (1 mm thick, 3 mm apart) with linearly decreasing inner diameters (from 17 mm to 5 mm). The electric fields conditions were similar to those described in the previous chapter. The ionization chamber itself is 18 mm long and has a constant inner diameter of 20 mm. Between all electrodes are spacers consisting of PEEK with grooves for O-rings made of FKM. A 100  $\mu$ m polyimide foil is placed between the X-ray tube and the chamber with a sealing O-ring. The samples are introduced via the 1/16" stainless steel capillary of the thermodesorption unit (see chapter 3.4) with a gas-tight fitting. As the chamber is sealed off against the atmosphere, the pumping system of the LTQ can be used to evacuate it.

The pressure in the chamber can then be regulated by adjusting the sample gas flow. The flow rate was kept at 1.7 l/min for all experiments, resulting in atmospheric pressure in the chamber. The chamber was heated to 100 °C by a heating cable. A rendering of the CAD model, as well as photographs of the chamber (without heating cable) and the X-ray source are shown in figure 44. The chamber is also equipped with two fused silica laser windows that were not used for the experiments reported here but included for future experiments utilizing laser-based ionization techniques.

#### 4.2.3.2 Formation of primary ions

In this chapter, the formation of primary ions in the negative mode will be described. The interaction of soft X-rays with the air molecules  $N_2$  and  $O_2$  leads to the release of electrons with a broad distribution of kinetic energies (see chapter 2.2.6.5). The highly energetic electrons are thermalized in a cascade of collisions and the resulting thermal electrons are attached to molecules with a positive EA. Since  $N_2$  does not have a positive EA, the most abundant molecule capable of forming anions in air is  $O_2$ . Consequently,  $O_2^-$  is observed in the negative mass spectrum resulting from X-ray ionization of air (Fig. 45).  $O_2^-$  forms stable adducts with traces of water<sup>82</sup> that are also observed in conventional IM spectrometry.<sup>83</sup> In the spectrum,  $[O_2+H_2O]^-$  ( $m/z = 50$ ) is observed. Additionally, the  $CO_2$  adducts  $[O_2+CO_2]^-$  ( $m/z = 76$ ) and  $[O_2+CO_2+H_2O]^-$  ( $m/z = 94$ ) are also detected. The binding enthalpies are  $\Delta_B H([O_2+H_2O]^-) = -93.3$  kJ/mol for the first compound and  $\Delta_B H([O_2+CO_2]^-) = -79.5$  kJ/mol for the second.<sup>58</sup> They are therefore very stable and even traces of  $H_2O$  and  $CO_2$  result in reduced sensitivity in IM spectrometry. The binding enthalpies  $\Delta_B H$  of  $[O_2+CO_2+H_2O]^-$  is not available in the literature. However, the high abundance of the adduct in the spectrum suggests that its stability is even higher. The adducts  $[O_2+O_2+N_2]^-$  and  $[O_2+CO_2+H_2O+N_2]^-$  could account for the peaks at  $m/z = 92$  and  $m/z = 122$ . Even larger complexes might exist at atmospheric pressure. However, their  $\Delta_B H$  will be smaller and they will therefore not survive the transfer into the vacuum.

In contrast to the spectra of corona discharge (CD) sources, nitrogen oxoanions, such as  $NO_2^-$  and  $NO_3^-$  are not observed in the X-ray spectrum.  $HCO_2^-$ ,  $CO_3^-$  and  $O_3^-$  are not detected, either, although they occur in the spectrum of radioactive sources.<sup>84</sup> It can be concluded, that dissociative electron attachment (DEA) to  $O_2$  resulting in the formation of  $O^-$ , which is the prerequisite for the formation of  $CO_3^-$  and  $O_3^-$ , does not happen at a significant amount in the X-ray source. The spectrum of APCI by soft X-radiation is thus different from that of CD and  $^{63}Ni$  sources in that the number of observed species is the smallest. The limited number of possible reaction channels results in more predictable analyte spectra. The explanation of this absence of reaction products of  $O^-$  could be linked to the different reaction volumes of the three sources. In CD, the majority of the charges are created at the tip of the needle in a confined volume of very few mm from the tip. The penetration depth of beta-electrons from  $^{63}Ni$  ( $E_{kin} = 67$  keV) in air is in the order of 10-15 mm.<sup>75</sup> However, soft X-rays have a penetration depth of 40/45 mm (for 2.7/2.8 keV). Therefore, the ionization volume is much larger. Consequently, the charge density in that volume is much smaller. Hence, the likelihood of second order effects is greatly reduced.

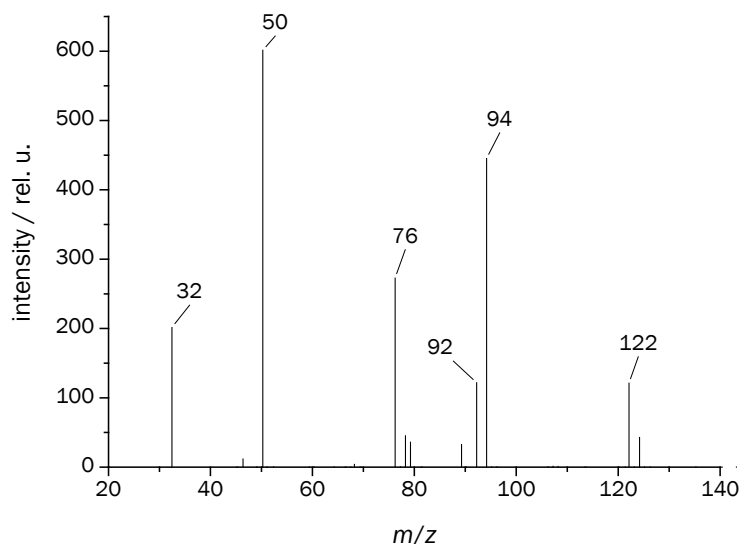


Figure 45: Mass spectrum of primary ionization products in air containing traces of H<sub>2</sub>O; observation of the following ions: O<sub>2</sub><sup>-</sup> ( $m/z = 32$ ), [O<sub>2</sub>+H<sub>2</sub>O]<sup>-</sup> ( $m/z = 50$ ), [O<sub>2</sub>+CO<sub>2</sub>]<sup>-</sup> ( $m/z = 76$ ), [O<sub>2</sub>+CO<sub>2</sub>+H<sub>2</sub>O]<sup>-</sup> ( $m/z = 94$ ), [O<sub>2</sub>+O<sub>2</sub>+N<sub>2</sub>]<sup>-</sup> ( $m/z = 92$ ), [O<sub>2</sub>+CO<sub>2</sub>+H<sub>2</sub>O+N<sub>2</sub>]<sup>-</sup> ( $m/z = 122$ )

O<sup>-</sup> is not formed directly but in a two stage process. One collision with an electron results in the cleavage of the O<sub>2</sub> bond, whereupon a second, thermal electron is attached to the O radical. The formation of CO<sub>3</sub><sup>-</sup> and O<sub>3</sub><sup>-</sup> is then a result of the reaction of O<sup>-</sup> with CO<sub>2</sub> or O<sub>2</sub>. These processes are unlikely at the lower charge density.

The next experiments were performed to further investigate the CO<sub>2</sub> clusters observed. CO<sub>2</sub><sup>-</sup> could be observed in crossed beam experiments. However, it is metastable due to its negative EA (EA(CO<sub>2</sub>) = -0.6 eV). The formation of CO<sub>2</sub><sup>-</sup> results in autodetachment after a lifetime of only 90 μs.<sup>85</sup> The fact that CO<sub>2</sub><sup>-</sup> can be observed at all is because the energy required for vertical electron detachment is 0.3 eV of vibrational energy.<sup>86</sup> Adducts of the type (CO<sub>2</sub>)<sub>x</sub><sup>-</sup> ( $x \geq 4$ ) are formed by thermal electrons.<sup>87</sup> Upon direct attachment, O<sup>-</sup> can be formed only by electrons above 4 eV (DEA resonance at 4.4 eV). At the temperature in the source, the energy of thermal electrons is about 45 meV.

Ions resulting from the formation of O<sup>-</sup> are found during CD in CO<sub>2</sub>.<sup>88</sup> In an IM mass spectrometer equipped with a <sup>63</sup>Ni, only ions of the type [O<sub>2</sub>+(CO<sub>2</sub>)<sub>x</sub>]<sup>-</sup> ( $x > 1$ ) and [O<sub>2</sub>+H<sub>2</sub>O+(CO<sub>2</sub>)<sub>x</sub>]<sup>-</sup> ( $x > 0$ ) were found.<sup>89,90</sup> However, no (CO<sub>2</sub>)<sub>x</sub><sup>-</sup> or ions due to O<sup>-</sup> production, such as O<sub>3</sub><sup>-</sup> or CO<sub>3</sub><sup>-</sup>, are observed in the X-ray spectrum (Fig. 46). The absence of the former, which are also absent in the <sup>63</sup>Ni source, can be explained by the weakly bound electron in (CO<sub>2</sub>)<sub>x</sub><sup>-</sup> and the corresponding high probability of charge transfer resulting in O<sub>2</sub><sup>-</sup> formation. The lack of O<sup>-</sup> based ions can have two reasons. In addition to the charge density argument above, the high DEA energy associated with the formation of O<sup>-</sup> from CO<sub>2</sub> limits the number of electrons in that energy range. In the X-ray source, primarily near thermal ions are contributing to the formation of ions. Therefore, the electrons possessing the required energy to induce DEA are few. Therefore, the only ions containing CO<sub>2</sub> observed in the X-ray source are a result of adduct formation with O<sub>2</sub><sup>-</sup>. The signals of CO<sub>4</sub><sup>-</sup> ( $m/z = 76$ ) and of [CO<sub>4</sub>+H<sub>2</sub>O]<sup>-</sup> ( $m/z = 94$ ) observed in a mixture of CO<sub>2</sub> and N<sub>2</sub> (Fig. 46, top) are due to traces of O<sub>2</sub> and H<sub>2</sub>O (note the different intensity scales of the N<sub>2</sub> and air spectra).

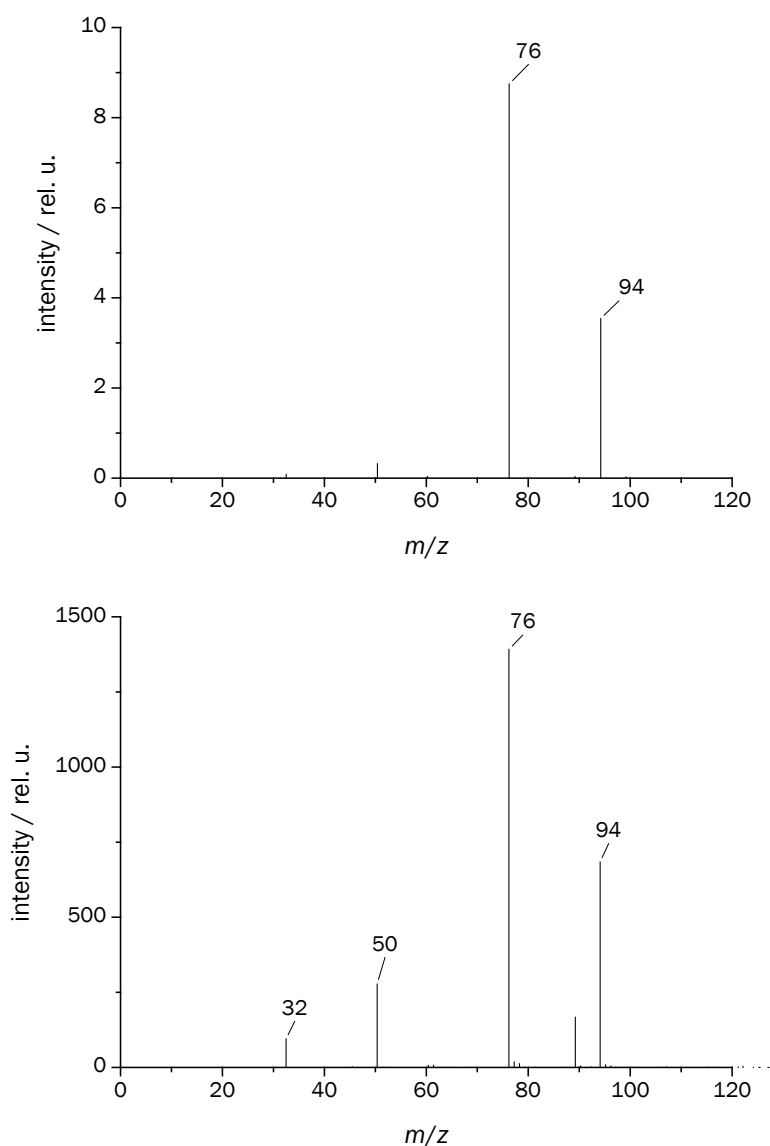


Figure 46: Mass spectra of primary ionization products in mixtures of  $N_2$ , air and  $CO_2$ ; top:  $N_2:CO_2$  (1:7) containing traces of  $H_2O$  and  $O_2$ ; bottom:  $O_2:CO_2:N_2$  (1:2:13); observation of the following ions:  $O_2^-$  ( $m/z = 32$ ),  $[O_2+H_2O]^-$  ( $m/z = 50$ ),  $CO_4^-$  ( $m/z = 76$ ),  $[CO_4+H_2O]^-$  ( $m/z = 94$ )

DFT calculations at the B3LYP/6-311+G(d,p) level were performed by T. Ritschel on the  $[O_2+CO_2]^-$  adduct and its constituent ions and molecules. They revealed the formation of a covalent bond and consequently the observed species can be referred to as  $CO_4^-$  (Fig. 47, left). The energy of the reaction



was obtained as  $\Delta_r H = 1.58$  eV. The newly formed bond is long (1.71 Å) compared to the neutral C-O bonds (1.16 Å)<sup>38</sup> in  $CO_2$ . The two original C-O bonds are elongated by 0.05 Å as well. The O-O bond is also elongated by 0.1 Å. A consequence of the high stability is that very few analytes possess EA high enough to acquire the charge in an electron transfer reaction from  $CO_4^-$ . The production of  $CO_4^-$  is therefore undesirable because it limits detection sensitivity.

In accordance with the above, the adduct  $[\text{O}_2+\text{CO}_2+\text{H}_2\text{O}]^-$  can be described as  $[\text{CO}_4+\text{H}_2\text{O}]^-$  and the binding enthalpy  $\Delta_B H$  with respect to dissociation into the constituents is in the range of 0.5 eV (depending on geometry, see Fig. 47, right).

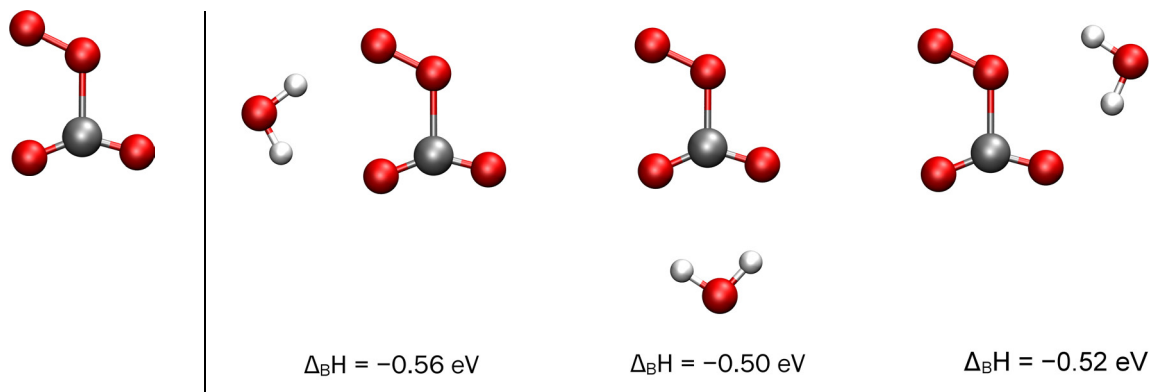


Figure 47: Structures calculated by DFT of left:  $\text{CO}_4^-$ ; right:  $[\text{CO}_4+\text{H}_2\text{O}]^-$  as well as  $\Delta_B H$  of  $[\text{CO}_4+\text{H}_2\text{O}]^-$  with respect to dissociation into  $\text{CO}_4^-$  and  $\text{H}_2\text{O}$

The experiments revealed that  $\text{CO}_4^-$  is already formed at low amounts of  $\text{CO}_2$  in the air in the chamber. Atmospheric  $\text{CO}_2$  can be an issue in IM spectrometers because the filters customary used are subject to aging and break-in. The dependence of the intensities of the primary, desired ionization product  $\text{O}_2^-$  and the interfering  $\text{CO}_4^-$  (and their corresponding water adducts) on the volume fraction of  $\text{CO}_2$  in the drift gas is shown in figure 48. The mole fraction of  $\text{CO}_2$  in the earth's atmosphere is about 400 ppm.<sup>91</sup> At that amount, a high intensity of the  $\text{CO}_2$  based ions is observed.

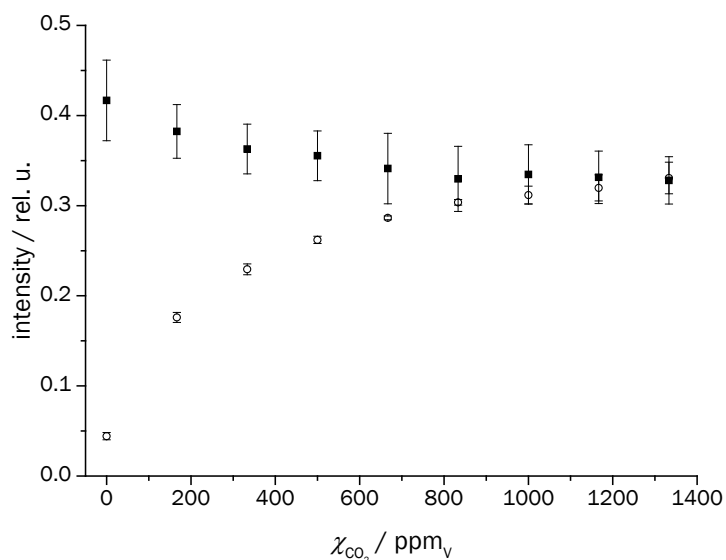


Figure 48: Intensities of the sum of  $\text{O}_2^-$  ions and  $[\text{O}_2+\text{H}_2\text{O}]^-$  ions (■) and the sum of  $\text{CO}_4^-$  ions and  $[\text{CO}_4+\text{H}_2\text{O}]^-$  ions (○) as a function of the gas phase volume fraction  $\chi$  of  $\text{CO}_2$  in air

#### 4.2.3.3 Formation of dopant ions

Dopants are substances commonly added to the ionization region of the IM spectrometer that influence the ionization chemistry positively with regard to the analytical task. This positive influence can either be the suppression of the ionization of interfering compounds, or the formation of adducts and an associated increase in the sensitivity of the detection.

The first dopant investigated was the gas  $\text{N}_2\text{O}$ . Although it is generally not found in IM spectrometers, it could provide benefits as a deliberately added dopant. This application will be investigated further in chapter 4.2.3.5. Like  $\text{CO}_2$ ,  $\text{N}_2\text{O}$  has a slightly negative  $\text{EA}(\text{N}_2\text{O}) = -0.15$  eV and its anions are metastable.<sup>92</sup> They are consequently not detected in the chamber. However, unlike  $\text{CO}_2$ ,  $\text{N}_2\text{O}$  has a relatively large DEA cross section  $\sigma_{\text{DEA}}$  at 0 eV of about  $10^{-18}$  cm<sup>2</sup>.<sup>93</sup> One product of DEA to  $\text{N}_2\text{O}$  reported in the literature is  $\text{NO}^-$ . This can be produced directly or in a decay of  $(\text{N}_2\text{O})_x^-$  via  $[\text{O}+(\text{N}_2\text{O})_{x-1}]^-$  adducts.<sup>86</sup>  $\text{NO}^-$  is not observed directly in the spectrum obtained following ionization by soft X-rays. However, the adducts  $[\text{O}+\text{N}_2\text{O}]^-$  and  $[\text{NO}+\text{N}_2\text{O}]^-$  can be found (Fig. 49 top). The adduct  $[\text{O}+\text{N}_2\text{O}]^-$  can also be written as  $\text{N}_2\text{O}_2^-$  and the ion is known in the literature [ $\text{EA}(\text{N}_2\text{O}_2) = 3.35$  eV].<sup>58</sup>  $[\text{NO}+\text{N}_2\text{O}]^-$  is also covalently bound, the ion can therefore be written  $\text{N}_3\text{O}_2^-$  [ $\text{EA}(\text{N}_3\text{O}_2) = 0.25$  eV]. Because of the very low EA,  $\text{N}_3\text{O}_2^-$  transfers an electron to  $\text{O}_2$  in air (Fig. 49 bottom). Additional peaks are observed in air at  $m/z = 76$  and  $m/z = 94$ . They could be attributed to  $[\text{O}_2+\text{N}_2\text{O}]^-$  and  $[\text{O}_2+\text{N}_2\text{O}+\text{H}_2\text{O}]^-$ , although the  $m/z$  is isobaric with  $\text{CO}_4^-$  and  $[\text{CO}_4+\text{H}_2\text{O}]^-$ .

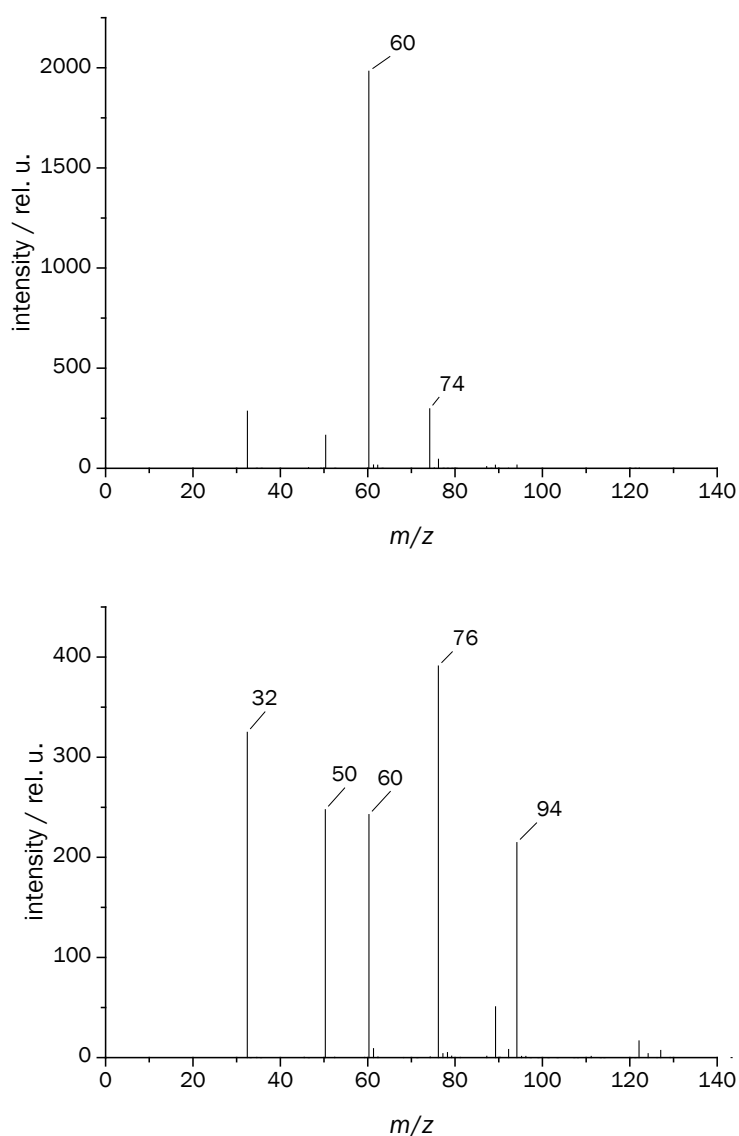


Figure 49: Mass spectra of primary ionization products in mixtures of  $\text{N}_2\text{O}$  in top:  $\text{N}_2$  (1:7) and bottom: air ( $\text{O}_2:\text{N}_2\text{O}:\text{N}_2 = 1:3:20$ ); observation of the following ions:  $\text{O}_2^-$  ( $m/z = 32$ ),  $[\text{O}_2+\text{H}_2\text{O}]^-$  ( $m/z = 50$ ),  $\text{N}_2\text{O}_2^-$  ( $m/z = 60$ ),  $\text{N}_3\text{O}_2^-$  ( $m/z = 74$ ),  $[\text{O}_2+\text{N}_2\text{O}]^-$  ( $m/z = 76$ ),  $[\text{O}_2+\text{N}_2\text{O}+\text{H}_2\text{O}]^-$  ( $m/z = 94$ )

The dopant most commonly used in IM spectrometric detection of anions, particularly of explosives, is  $\text{CH}_2\text{Cl}_2$ . DEA to  $\text{CH}_2\text{Cl}_2$  results in the formation of  $\text{Cl}^-$ . The bond dissociation enthalpy in  $\text{CH}_2\text{Cl}_2$  is  $D_0(\text{CH}_2\text{Cl}-\text{Cl}) = 3.2 \text{ eV}$  and below  $\text{EA}(\text{Cl})$ .<sup>94</sup> DEA is therefore exothermic by 0.4 eV. By contrast, the electron transfer reaction with  $\text{O}_2^-$  is slightly endothermic due to  $\text{EA}(\text{O}_2) = 0.44 \text{ eV}$ .<sup>59</sup> The beneficial effect of the dopant  $\text{Cl}^-$  on the detection of analytes can either be its role in the formation of ions or the suppression of the ionization of interfering substances which could be detrimental to the evaluation of IM spectra. Direct influence of the ionization can either proceed via proton abstraction from or adduct formation with the analyte. In the former case,  $[\text{M}-\text{H}]^-$  ions are formed, in the latter  $[\text{M}+\text{Cl}]^-$  adducts are observed. Both channels can be more efficient than direct electron transfer from  $\text{O}_2^-$ . The formation of adducts can have the added advantage of shifting peaks to higher drift times, at which fewer other substances appear and the detection becomes more unambiguous. The effect of the suppression of the ionization of substances is due to the relatively high  $\text{EA}(\text{Cl}) = 3.6 \text{ eV}$ .<sup>58</sup> Interfering substances with lower EA are not ionized except if adducts are formed. Water adducts of the type  $[\text{Cl}+\text{H}_2\text{O}]^-$  are stable. These peaks are consequently observed if traces of water are present in the ionization chamber. The presence of  $\text{CO}_2$  reduces the amount of  $\text{Cl}^-$  formed (Fig. 50), limiting potential reaction partners for analytes. This effect is already observed at volume fractions  $\chi(\text{CO}_2) < 200 \text{ ppm}$ . The formation of  $\text{CO}_4^-$  yields additional energy (see above), and  $\Delta_B H$  of the water adduct of  $\text{CO}_4^-$  is even higher. Electron transfer from  $\text{CO}_4^-$  can therefore not take place. The presence of  $\text{CO}_2$  in an IM spectrometer consequentially has a negative effect on the detection of target analytes. Filters are therefore used, but they have a limited capacity. Therefore, monitoring  $\text{CO}_2$  concentrations in IM spectrometers is advisable.

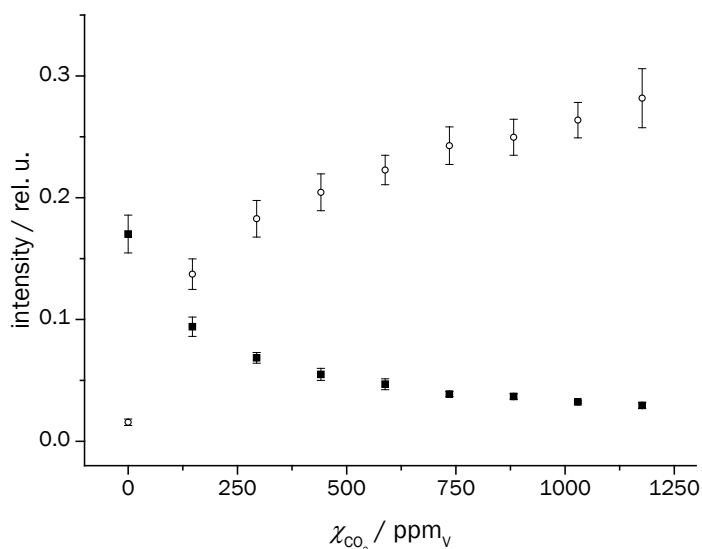


Figure 50: Intensities of the sum of  $\text{Cl}^-$  ions and  $[\text{Cl}+\text{H}_2\text{O}]^-$  ions (■) and the sum of  $\text{CO}_4^-$  ions and  $[\text{CO}_4+\text{H}_2\text{O}]^-$  ions (○) as a function of the gas phase volume fraction  $\chi$  of  $\text{CO}_2$  in  $\text{N}_2$

#### 4.2.3.4 Ion formation of alkyl nitrates

DEA to PETN near an electron energy of 0 has been studied in vacuum using an electron monochromator.<sup>50</sup> Under these conditions, mainly fragments were detected. The highest yield was observed for  $\text{NO}_3^-$  (80.5 %) and most of the other ions also contained only nitrogen oxoanions and oxygen ions:  $\text{NO}_2^-$  (11.1 %),  $\text{O}^-/\text{OH}^-$  (3.5 %),  $\text{N}_2\text{O}_4^-$  (1.4 %). The most abundant fragment containing carbon was  $\text{C}_3\text{H}_3\text{O}^-$  (1.6 %). The molecular ion  $\text{M}^-$  was only found in traces ( $8 \times 10^{-6}$  %). Calculations by authors on the enthalpies of formation of  $\text{NO}_2^-$  ( $\Delta_f H = -0.81$  eV),  $\text{NO}_3^-$  ( $\Delta_f H = -1.33$  eV) and  $\text{N}_2\text{O}_4^-$  ( $\Delta_R H = -3.14$  eV) concluded these reactions to be exothermic. Due to their close chemical relationship, similar primary products can be expected for the other alkyl nitrates investigated.

The spectrum resulting from the X-ray ionization of air at atmospheric pressure in the presence of nitroglycerin (NG) is shown in figure 51. In air, as shown above, the primary ion is  $\text{O}_2^-$ . All other ions are a consequence of IMR of  $\text{O}_2^-$  with NG. The nitrate ion was the main product observed, as was the case in the vacuum study. However, in addition to the nitrogen oxoanions, the adduct ion  $[\text{M}+\text{NO}_3]^-$ , molecular ion  $\text{M}^-$  and large fragment ion  $[\text{M}-\text{NO}_2]^-$  are also observed at high intensities.

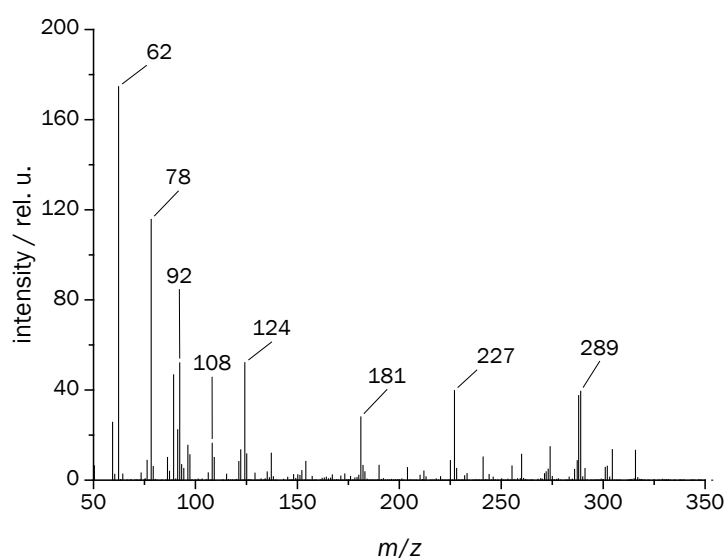


Figure 51: Mass spectrum of ionization products of 200 pmol of NG in air; observation of the following ions:  $\text{NO}_3^-$  ( $m/z = 62$ ),  $[\text{O}_2+\text{NO}_2]^-$  ( $m/z = 78$ ),  $[\text{N}_2\text{O}_4]^-$  ( $m/z = 92$ ),  $[\text{N}_2\text{O}_5]^-$  ( $m/z = 108$ ),  $[\text{N}_2\text{O}_6]^-$  ( $m/z = 124$ ),  $[\text{M}-\text{NO}_2]^-$  ( $m/z = 181$ ),  $\text{M}^-$  ( $m/z = 227$ ),  $[\text{M}+\text{NO}_3]^-$  ( $m/z = 289$ )

The nitrate adducts are the main ions used for the detection NG. The structure of these adducts was obtained by DFT calculations (Fig. 52 left). The stability of the adducts arises from an interaction of the nitrate O atoms and the H atom of the outer methylene groups of NG. The binding enthalpy of the adduct with respect to dissociation into the nitrate ion and neutral NG was calculated as  $\Delta_B H([\text{NG}+\text{NO}_3]^-) = -1.02$  eV. The structure of NG changes upon adduct formation in order to minimize steric repulsion and maximize electrostatic and polarization interaction.



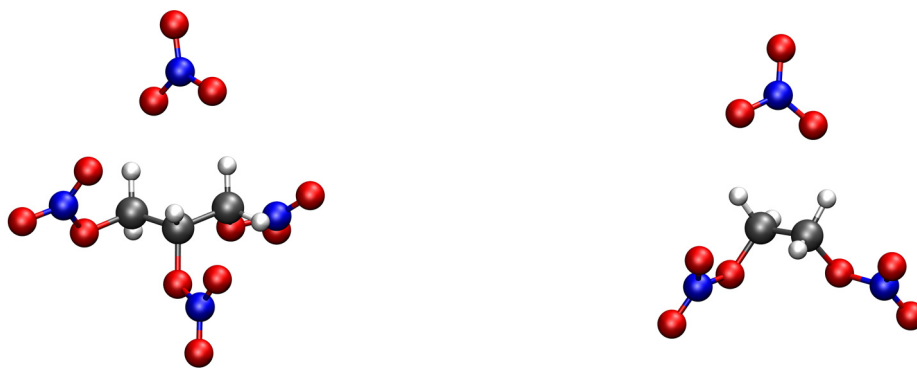


Figure 52: Structures calculated by DFT of left:  $[\text{NG}+\text{NO}_3]^-$  and right:  $[\text{EGDN}+\text{NO}_3]^-$

Nitrate adducts are also formed by EGDN, ETN and PETN. The detection efficiencies depend on two factors. First, the DEA cross sections of the alkyl nitrate determine the  $\text{NO}_3^-$  intensity. Secondly, the rate of adduct formation as well as the stability of the adduct control the intensity of the adduct ion. An example of different detection efficiencies is the concurrent measurement of NG and EGDN, when EGDN is present in excess (Fig. 53). Even though the ratio of amounts is 1000:1 for EGDN, the intensity ratio is 3:1 for the NG adduct. DFT calculations were performed on  $[\text{EGDN}+\text{NO}_3]^-$  as well (Fig. 52, right). The calculated  $\Delta_B H([\text{EGDN}+\text{NO}_3]^-) = -0.86 \text{ eV}$  is smaller than that of the NG cluster. The difference arises due to a steric hindrance in the interaction of  $\text{NO}_3^-$  with the H atoms in EGDN. The interaction has to happen between H atoms attached to neighboring C atoms. As a consequence, the EDGN molecule is distorted in the adduct.

As mentioned in the beginning of the chapter, in the vacuum DEA experiments almost no M<sup>-</sup> ions were found. They are however observed at atmospheric pressure. Their intensity is low for EGDN and ETN but high for NG and PETN. The authors of the DEA paper performed Hartree-Fock calculations adding a negative charge to an optimized PETN neutral.<sup>50</sup> They concluded that the charge density is localized at one nitrate group and possesses nodes along the N-O and C-O bonds.

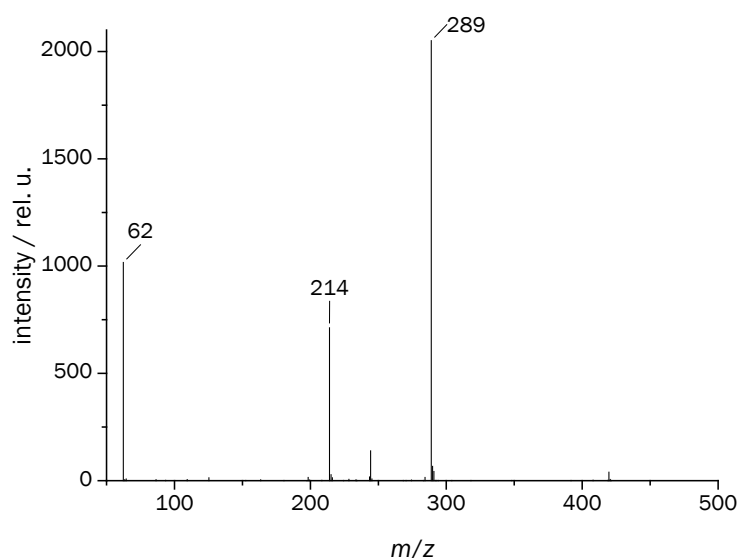


Figure 53: Mass spectrum of ionization products of 50 pmol of NG and 50 nmol of EGDN in air; observation of the following ions:  $\text{NO}_3^-$  ( $m/z = 62$ ),  $[\text{EGDN}+\text{NO}_3]^-$  ( $m/z = 214$ ),  $[\text{NG}+\text{NO}_3]^-$  ( $m/z = 289$ )

Our DFT calculations on NG revealed a substantially elongated N-OC bond (Fig. 54 left). The energy required for the dissociation of  $\text{NG}^-$  into  $[\text{NG}-\text{NO}_2]$  and  $\text{NO}_2^-$  was calculated as  $-1.58$  eV. The observation of the molecular ion at appreciable amounts compared to the low abundance in vacuum could be explained by collision stabilization at atmospheric pressure. An alternative explanation of the appearance could be bond cleavage yielding  $\text{NO}_2^-$  or  $\text{NO}_3^-$  and the subsequent intramolecular formation of either a  $[(\text{NG}-\text{NO}_2)+\text{NO}_2]^-$  or  $[(\text{NG}-\text{NO}_3)+\text{NO}_3]^-$  adduct ion. In the  $[(\text{NG}-\text{NO}_2)+\text{NO}_2]^-$  ion (Fig. 54 right), the  $\text{NO}_2^-$  is coordinated via the H atoms of the outer C atoms, similar to the coordination observed in the  $[\text{NG}+\text{NO}_3]^-$  adduct ion.



Figure 54: Structures calculated by DFT of left:  $\text{NG}^-$  and right:  $[(\text{NG}-\text{NO}_2)+\text{NO}_2]^-$

The binding enthalpy obtained was  $\Delta_B H([(NG-NO_2)+NO_2]^-) = -1.62$  eV. As this value is close to the bond dissociation energy, the adduct is of similar stability as the  $\text{M}^-$  ion. Both explanations could therefore pertain.

Nitrogen oxoanions are the most abundant ions observed in vacuum as well as at atmospheric pressure. The spectrum of the nitrogen oxoanions formed by DEA to NG was obtained in the low mass range (see chapter 3.4) of the LTQ (Fig. 55). The spectra obtained for the other alkyl nitrates were similar.

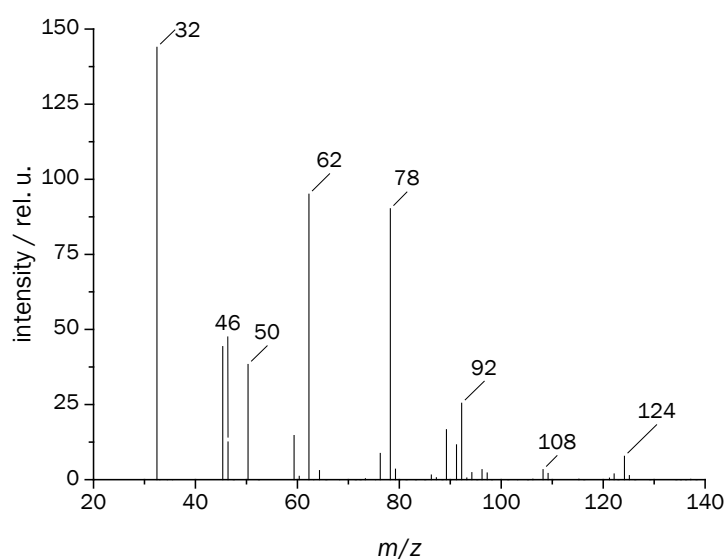


Figure 55: Mass spectrum of ionization products of 200 pmol of NG in air obtained in the low mass range; observation of the following ions:  $\text{O}_2^-$  ( $m/z = 32$ ),  $\text{NO}_2^-$  ( $m/z = 46$ ),  $[\text{O}_2+\text{H}_2\text{O}]^-$  ( $m/z = 50$ ),  $\text{NO}_3^-$  ( $m/z = 62$ ),  $[\text{O}_2+\text{NO}_2]^-$  ( $m/z = 78$ ),  $[\text{N}_2\text{O}_4]^-$  ( $m/z = 92$ ),  $[\text{N}_2\text{O}_5]^-$  ( $m/z = 108$ ),  $[\text{N}_2\text{O}_6]^-$  ( $m/z = 124$ )

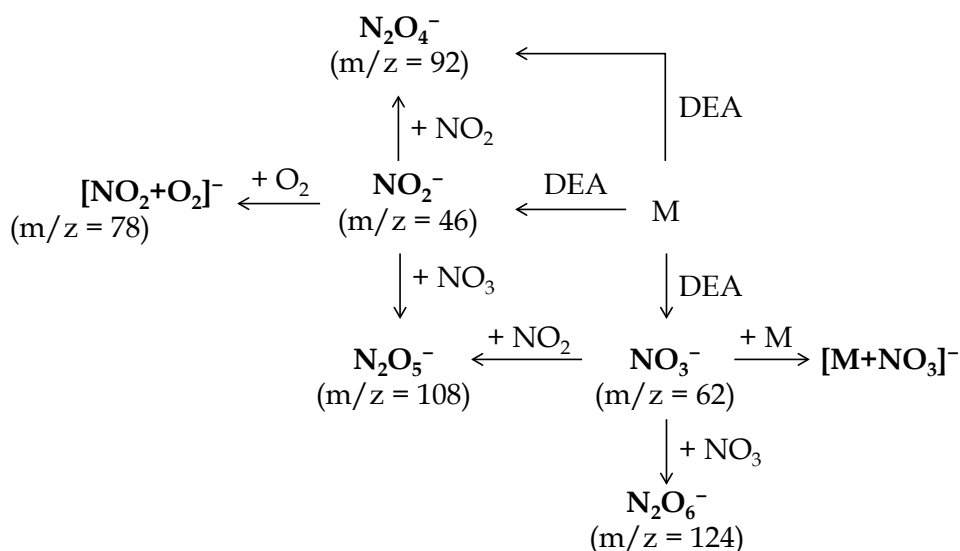


Figure 56: Scheme showing possible reaction channels leading to the formation of different nitrogen oxoanions after DEA to alkyl nitrates

At atmospheric pressure, the adduct species  $[\text{O}_2 + \text{NO}_2]^-$ ,  $[\text{N}_2\text{O}_5]^-$  and  $[\text{N}_2\text{O}_6]^-$  were observed in addition to  $\text{NO}_2^-$ ,  $\text{NO}_3^-$  and  $\text{N}_2\text{O}_4^-$  already found in vacuum. Protonated species, such as  $\text{HN}_2\text{O}_5^-$  and  $\text{HN}_2\text{O}_6^-$  were also observed. Possible reaction channels leading to the formation of these adduct ions are outlined in figure 56.

The efficiency of the nitrogen oxoanion formation strongly depends upon the drift gas. In  $\text{N}_2$ , almost no nitrogen oxoanions are observed while in the presence of  $\text{O}_2$  they are the most abundant ions. Their formation can therefore be attributed to the presence of  $\text{O}_2^-$  ions. This can be explained by the lower charge density in an  $\text{N}_2$  atmosphere in the chamber as electrons are not captured.<sup>75</sup> The thermalized electrons possess a high mobility and are discharged at the electrodes at a higher rate. In air, the charge density is higher due to the lower IM of  $\text{O}_2^-$ . DEA to the alkyl nitrates yields also neutral fragments  $\text{NO}_2$  and  $\text{NO}_3$ . These are not efficiently as efficiently ionized in  $\text{N}_2$  as they are in the presence of  $\text{O}_2^-$  ions.

In order to illustrate the effect of the alkyl nitrate concentration on the ratio of nitrogen oxoanions to alkyl nitrate ions and adducts two spectra obtained at different PETN concentrations were recorded (Fig. 57). At high concentrations, more neutral PETN can interact with  $\text{NO}_3^-$  and  $\text{NO}_2^-$  formed by DEA. Consequently, the  $[\text{PETN} + \text{NO}_3]^-$  adducts are found in much higher abundance. This finding indicates that the number density of neutral PETN in the chamber was higher than that of neutral nitrogen oxides formed by DEA of PETN.

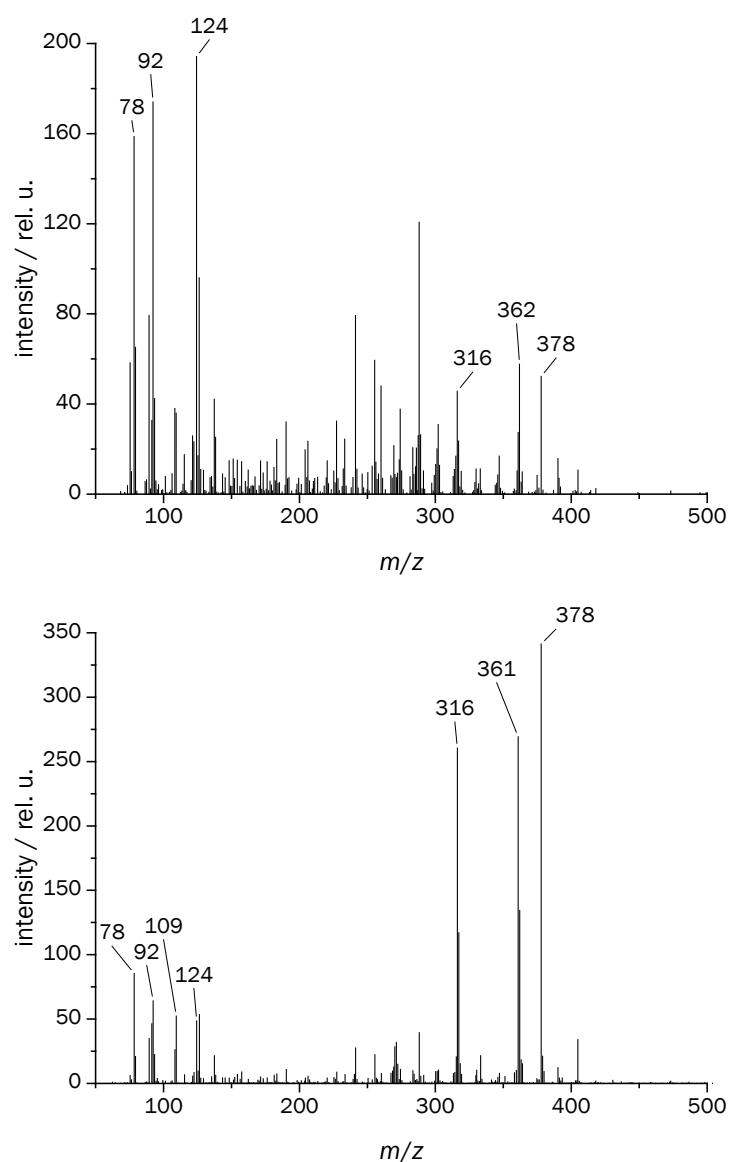


Figure 57: Mass spectra of ionization products of top: 50 pmol and bottom: 500 pmol of PETN in air; observation of the following ions:  $[\text{O}_2+\text{NO}_2]^-$  ( $m/z = 78$ ),  $\text{N}_2\text{O}_4^-$  ( $m/z = 92$ ),  $\text{HN}_2\text{O}_5^-$  ( $m/z = 109$ ),  $\text{N}_2\text{O}_6^-$  ( $m/z = 124$ ),  $\text{M}^-$  ( $m/z = 316$ ),  $[\text{M}-\text{H}+\text{NO}_2]^-$  ( $m/z = 361$ ),  $[\text{M}+\text{NO}_2]^-$  ( $m/z = 362$ ),  $[\text{M}+\text{NO}_3]^-$  ( $m/z = 378$ )

#### 4.2.3.5 Ionization of alkyl nitrates in the presence of dopants

The addition of methylene chloride to the drift gas results in the formation of  $\text{Cl}^-$  (see chapter 4.2.3.3). The dopant is often used in IM spectrometry. In this case, the adduct ion  $[\text{M}+\text{Cl}]^-$  is used for the detection. The influence of the dopant was investigated by recording the spectra of the ionization of NG and in the presence of  $\text{Cl}^-$  (Fig. 58). The  $[\text{M}+\text{Cl}]^-$  adduct ions were observed in both cases. DFT calculation reported in the literature suggest the  $[\text{NG}+\text{Cl}]^-$  adduct ion ( $\Delta_{\text{B}}H([\text{NG}+\text{Cl}]^-) = 1.21 \text{ eV}$ ) is more stable than the  $[\text{NG}+\text{NO}_3]^-$  adduct ion ( $\Delta_{\text{B}}H([\text{NG}+\text{NO}_3]^-) = 0.99 \text{ eV}$ ).<sup>95,96</sup> The second value is in good agreement with our own result (see above). In addition to  $\text{Cl}^-$  and  $[\text{Cl}+\text{H}_2\text{O}]^-$  mentioned above, the adduct ion  $[\text{NO}_2+\text{Cl}]^-$  is also observed in high abundance.

#### 4.2.3 Formation of negative ions by soft X-rays and ionization chemistry of alkyl nitrates

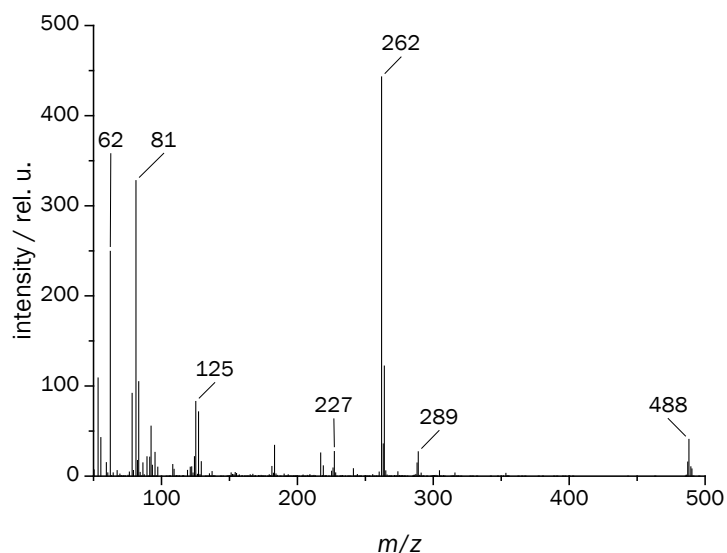


Figure 58: Mass spectrum of ionization products of 50 pmol of NG in the presence of 80  $\mu\text{mol}$  of  $\text{CH}_2\text{Cl}_2$  in air; observation of the following ions:  $[\text{NO}_3]^-$  ( $m/z = 62$ ),  $[\text{NO}_2+\text{Cl}]^-$  ( $m/z = 81$ ),  $\text{N}_2\text{O}_6^-$  ( $m/z = 125$ ),  $\text{M}^-$  ( $m/z = 227$ ),  $[\text{M}+\text{Cl}]^-$  ( $m/z = 262$ ),  $[\text{M}+\text{NO}_3]^-$  ( $m/z = 289$ ),  $[\text{2M}-\text{H}+\text{Cl}]^-$  ( $m/z = 488$ )

The  $[\text{NG}+\text{NO}_3]^-$  adduct is still detected in the spectrum, which is in agreement with the relatively high intensity of  $\text{NO}_3^-$  detected. The formation of  $\text{NO}_3^-$  can have two explanations. In the literature, it was found that the  $[\text{NG}+\text{Cl}]^-$  adduct was not stable at temperatures of 111-122  $^\circ\text{C}$  and fragmented into  $\text{NO}_3^-$  and  $[(\text{NG}-\text{NO}_3)+\text{Cl}]^-$ .<sup>95</sup> These experiments were carried out at a temperature of 100  $^\circ\text{C}$  in the chamber. The possibility of a fraction of the adducts fragmenting at this temperature as well cannot be excluded. The authors also calculated the  $\text{EA}(\text{NG}) = 2.58 \text{ eV}$ .<sup>95</sup> It is considerably higher than that of  $\text{O}_2$ . Therefore, the dissociation after electron attachment or electron transfer reaction to NG is the second possibility of  $\text{NO}_3^-$  formation. Once formed,  $\text{NO}_3^-$  does not transfer its electron to Cl because of its  $\text{EA}(\text{NO}_3) = 3.9 \text{ eV}$  being higher than  $\text{EA}(\text{Cl}) = 3.6 \text{ eV}$ .<sup>58</sup>

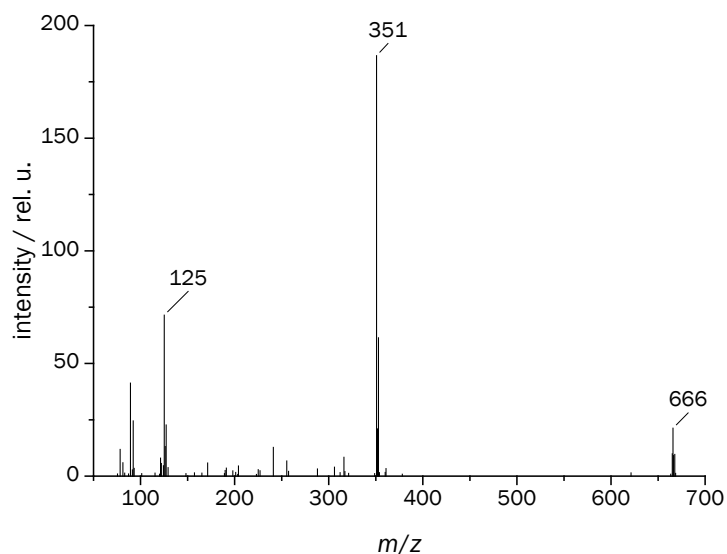


Figure 59: Mass spectrum of ionization products of 50 pmol of PETN in the presence of 80  $\mu\text{mol}$  of  $\text{CH}_2\text{Cl}_2$  in air; observation of the following ions:  $\text{HN}_2\text{O}_6^-$  ( $m/z = 125$ ),  $[\text{M}+\text{Cl}]^-$  ( $m/z = 351$ ),  $[\text{2M}-\text{H}+\text{Cl}]^-$  ( $m/z = 666$ )

Ultimately, the ratio of formation of either  $\text{Cl}^-$  to  $\text{NO}_3^-$  ions depends on the ratio of the number densities of methylene chloride and the alkyl nitrate.

The spectrum that resulted from the ionization of PETN in the presence of methylene chloride in the same amounts is shown in figure 59. At these conditions,  $[\text{PETN}+\text{Cl}]^-$  and  $[2\text{PETN}-\text{H}+\text{Cl}]^-$  are the only PETN containing species observed in the spectrum shown. At higher PETN concentration,  $[\text{PETN}+\text{NO}_3]^-$ ,  $[\text{PETN}+\text{NO}_2]^-$  and  $\text{PETN}^-$  are also detected.

As mentioned,  $\text{Cl}^-$  is by far the dopant ion most commonly encountered in IM spectrometers used in the detection of explosives. However, not many alternative dopants have been reported in the literature, it therefore seemed worthwhile investigating a number of such alternatives. Therefore, the next investigations concerned the dopants ethyl bromide and methyl iodide. Their ionization results in the formation of  $\text{Br}^-$  and  $\text{I}^-$ , respectively, by DEA.

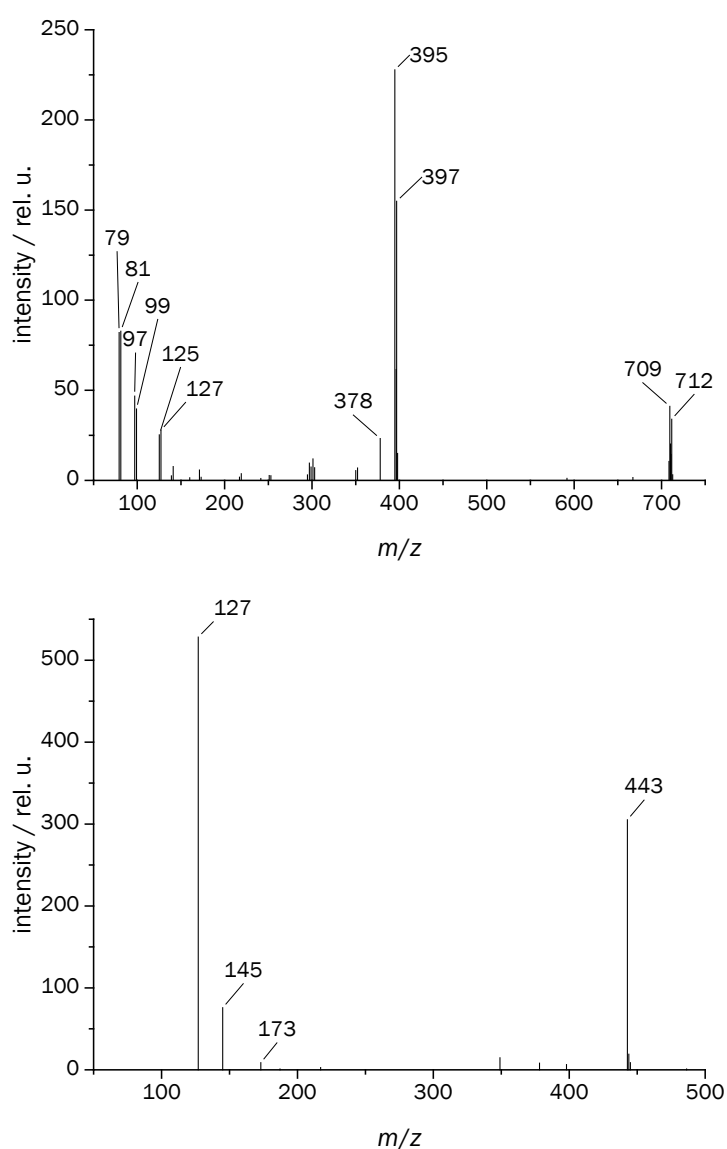


Figure 60: Mass spectra of ionization products of 500 pmol of PETN in the presence of top: 3.3  $\mu\text{mol}$  of  $\text{C}_2\text{H}_5\text{Br}$  and bottom: 800 nmol of  $\text{CH}_3\text{I}$  in  $\text{N}_2$ ; observation of the following ions: top:  $\text{Br}^-$  ( $m/z = 79, 81$ ),  $[\text{Br}+\text{H}_2\text{O}]^-$  ( $m/z = 97, 99$ ),  $[\text{Br}+\text{NO}_2]^-$  ( $m/z = 125, 127$ ),  $[\text{M}+\text{NO}_3]^-$  ( $m/z = 378$ ),  $[\text{M}+\text{Br}]^-$  ( $m/z = 395, 397$ ),  $[2\text{M}-\text{H}+\text{Br}]^-$  ( $m/z = 710, 712$ ); bottom:  $\text{I}^-$  ( $m/z = 127$ ),  $[\text{I}+\text{H}_2\text{O}]^-$  ( $m/z = 145$ ),  $[\text{I}+\text{NO}_2]^-$  ( $m/z = 173$ ),  $[\text{M}+\text{I}]^-$  ( $m/z = 443$ )

At low amounts of substance of the analyte (50 pmol), only the  $[M+Br]^-$  and  $[M+I]^-$  adduct ions are observed in  $N_2$ . In case of PETN in the presence of  $Br^-$ , at higher amounts the dimer adduct  $[2M-H+Br]^-$  and the DEA product  $[M+NO_3]^-$  are also detected (Fig. 60 top). However, their abundance is significantly lower than in the case of the  $Cl^-$  spectrum. The addition of methyl iodide leads to very simple spectra regardless of the concentration (Fig. 60 bottom).

Only ions resulting from the dopant and the  $[M+I]^-$  adduct are observed. No iodide bridged dimers were observed. The yield of these dimers decreases from  $Cl^-$  via  $Br^-$  to  $I^-$ .  $[NO_2+Br]^-$  and  $[NO_2+I]^-$  are also observed. The intensity trend is the same as for the dimers.

In air, the intensities of the ions resulting from DEA to the alkyl nitrates increases compared to the  $Br^-$  adducts (Fig. 61), similar to the results obtained for  $Cl^-$ . Consequently, especially at high alkyl nitrate concentration,  $[M+NO_3]^-$  adducts also appear.

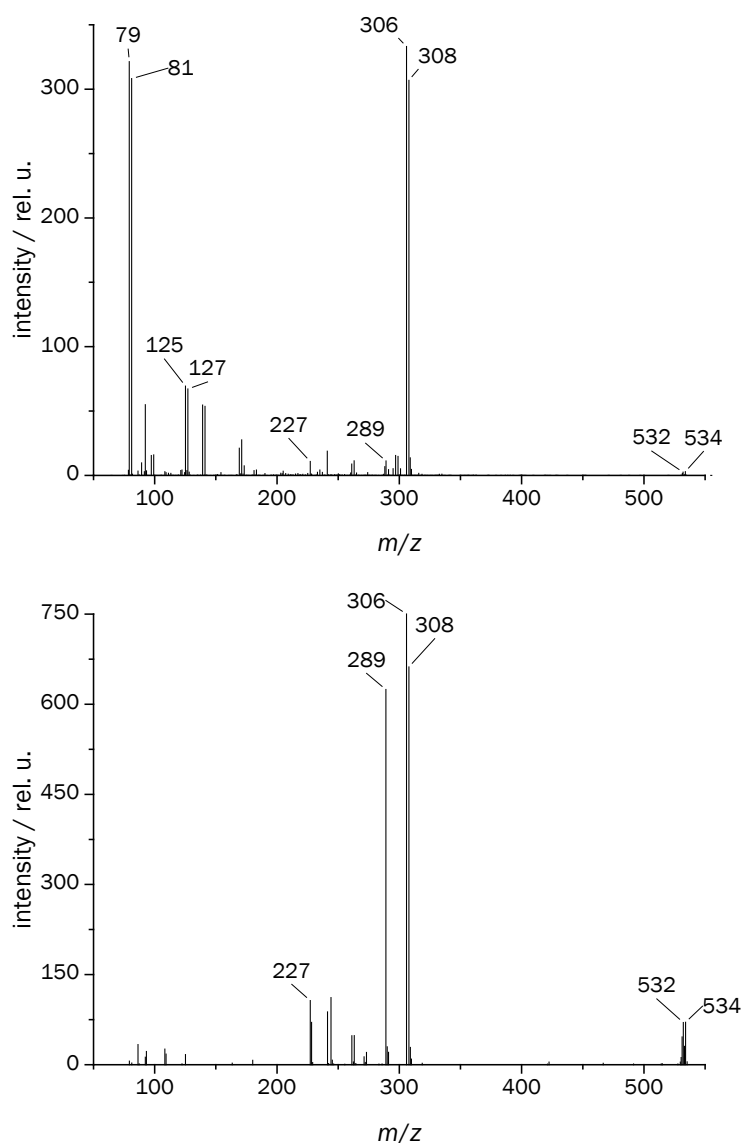


Figure 61: Mass spectra of ionization products of top: 50 pmol and bottom: 500 pmol of NG in the presence of  $3.3 \mu\text{mol}$  of  $C_2H_5Br$  in air; observation of the following ions:  $Br^-$  ( $m/z = 79, 81$ ),  $[Br+NO_2]^-$  ( $m/z = 125, 127$ ),  $M^-$  ( $m/z = 227$ ),  $[M+NO_3]^-$  ( $m/z = 289$ ),  $[M+Br]^-$  ( $m/z = 306, 308$ ),  $[2M-H+Br]^-$  ( $m/z = 532, 534$ )

However, the relative intensities are lower in the presence of  $\text{Br}^-$  than in the case of  $\text{Cl}^-$ . The ratio of DEA products to  $\text{Br}^-$  adducts again increases with the concentration of the alkyl nitrates. In the presence of methyl iodide, almost no DEA products are observed even in air. The reason could be the high  $\sigma_{\text{DEA}}$  of methyl iodide. No comparable DEA cross sections for the three substances are available in the literature. However, DEA rate constants are available. The rate constant decreases dramatically from  $\text{CH}_3\text{I}$  ( $1.8 \times 10^{-7} \text{ cm}^3/\text{s}$ )<sup>97</sup> to  $\text{C}_2\text{H}_5\text{Br}$  ( $9 \times 10^{-11} \text{ cm}^3/\text{s}$ )<sup>98</sup> and again but much less steeply to  $\text{CH}_2\text{Cl}_2$  ( $4.6 \times 10^{-12} \text{ cm}^3/\text{s}$ ).<sup>99</sup> Since cross sections and rate constants are related, it is reasonable to assume a much higher  $\sigma_{\text{DEA}}$  of methyl iodide as well. Due to the high cross sections, electrons are almost exclusively captured by methyl iodide either directly or by transfer from  $\text{O}_2^-$ . Thus, very little DEA to alkyl nitrates occurs. The different rate constants explain the differences in the yields of DEA products between methylene chloride and ethyl bromide as well.

DFT calculation on the  $[\text{NG}+\text{X}]^-$  ( $\text{X} = \text{Cl}, \text{Br}, \text{I}$ ) adduct ions were also performed. The results suggested the adduct ions are energetically stable. Two different stable structures were obtained, in agreement with results previously described in the literature (Fig. 62).<sup>95</sup> One structure arises do to the association of the  $\text{Cl}^-$  ion to the NG molecule. The other possibility is a rearrangement under formation of a covalent bond between Cl and a  $[\text{NG}-\text{NO}_3]$  fragment associated to the  $\text{NO}_3^-$  ion. The C-N bond cleavage and subsequent C-Cl bond formation can either take place at the center or at one of the outer C-atoms in the NG molecule. Similar structures were obtained for all halide ions  $\text{X}^-$ . The binding enthalpy  $\Delta_B H$  with respect to dissociation into NG and  $\text{X}^-$  decrease from  $\text{Cl}^-$  via  $\text{Br}^-$  to  $\text{I}^-$  (table 7). The relative stability of the  $[\text{NG}+\text{X}]^-$  adduct ions compared to the rearranged adduct  $[(\text{NG}-\text{NO}_3)+\text{X}]+\text{NO}_3^-$  decreases from  $\text{Cl}^-$  via  $\text{Br}^-$  to  $\text{I}^-$  as well.

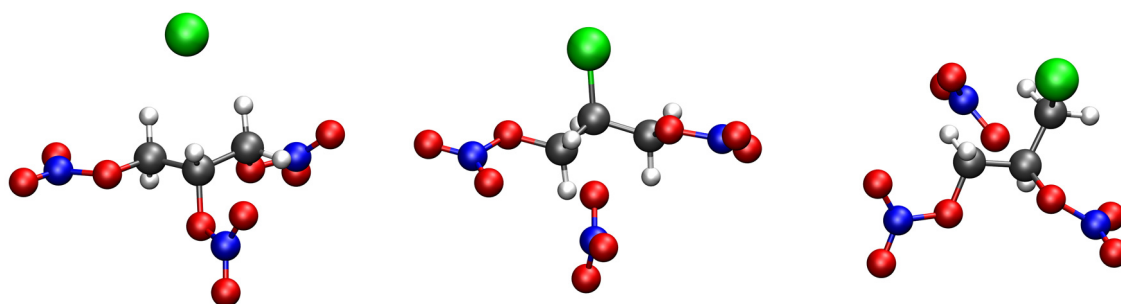


Figure 62: Structures calculated by DFT of  $[\text{NG}+\text{Cl}]^-$  (left) and  $[(\text{NG}-\text{NO}_3)+\text{Cl}]+\text{NO}_3^-$  (substitution at middle: center C; right: outer C) (analogous structures were obtained for  $[\text{NG}+\text{Br}]^-$  and  $[\text{NG}+\text{I}]^-$ )

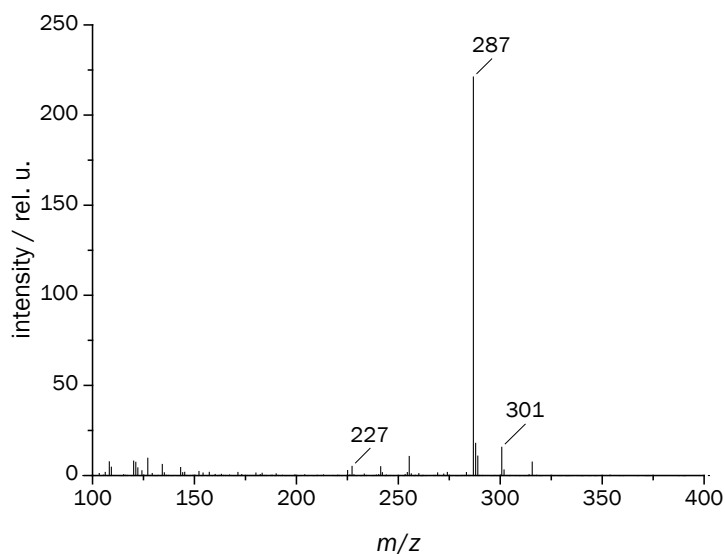
As a result, the  $[\text{NG}+\text{I}]^-$  adduct ion is more stable than its rearranged equivalent. There is almost no energetic difference for  $\text{Br}^-$  and rearrangement is favored in case of  $\text{Cl}^-$ . The opposite would be expected comparing the EA ( $\text{EA}(\text{Cl}) = 3.6 \text{ eV}$ ,  $\text{EA}(\text{Br}) = 3.4 \text{ eV}$ ,  $\text{EA}(\text{I}) = 3.1 \text{ eV}$ ,  $\text{EA}(\text{NO}_3) = 3.9 \text{ eV}$ ).<sup>58</sup> Overall, rearrangement and charge redistribution appears to be more important than the EA for the stability of the adduct ion formed. For  $\text{I}^-$ , the substitution at the outer C-atom is more favorable than substitution at the center C-atom, likely due to steric effects. The dissociation into  $[(\text{NG}-\text{NO}_3)+\text{X}]$  and  $\text{NO}_3^-$  requires about  $-1 \text{ eV}$  in all cases.



Table 7:  $\Delta_B H$  calculated by DFT for  $NG+X$  and  $[((NG-NO_3)+X)+NO_3]^-$  with respect to dissociation into  $NG$  and  $X^-$ ; values in parentheses are with respect to dissociation into  $[(NG-NO_3)+X]$  and  $NO_3^-$ 

Structure	$\Delta_B H / \text{eV}$		
	(X = Cl)	(X = Br)	(X = I)
$[NG+X]^-$	-1.25	-1.11	-0.95
$[((NG-NO_3)+X)+NO_3]^-$ (center)	-1.48 (-1.01)	-1.12 (-1.01)	-0.77 (-1.00)
$[((NG-NO_3)+X)+NO_3]^-$ (outer)	-1.47 (-1.00)	-0.98 (-0.83)	-0.81 (-0.99)

The last new dopant investigated was nitrous oxide. One of its advantages is that as a gaseous substance, it can be readily added in precise amounts to the sample gas. The primary ions observed after the ionization of  $N_2O$  are detailed in chapter 4.2.3.3 (Fig. 49). In the spectrum obtained for NG in the presence of  $N_2O$  (Fig. 63), the main peak is due to adduct ion  $[M+N_2O_2]^-$ . Additionally, an  $[M+N_3O_2]^-$  adduct ion is also observed at an intensity corresponding to the ratio of reactant ions (Fig. 49, top). Although the  $\sigma_{DEA}$  of  $N_2O$  is relatively small, the electrons are captured efficiently. As a consequence, products of DEA to NG are not observed at an amount of substance of 50 pmol. At higher amounts, these DEA products are observed.

Figure 63: Mass spectrum of ionization products of 50 pmol of NG in a mixture of  $N_2O$  and  $N_2$  (1:7); observation of the following ions:  $M^-$  ( $m/z = 227$ ),  $[M+N_2O_2]^-$  ( $m/z = 287$ ),  $[M+N_3O_2]^-$  ( $m/z = 301$ )

#### 4.2.3.6 Presence of interfering substances: lactic acid

Lactic acid found is found ubiquitously in perspiration. It is present on the fingertips and therefore found on many surfaces that are sampled for explosive detection. The sampling is done mechanically by swabs being wiped over these surfaces. In addition to the traces of explosives that might be present, large amounts (by comparison) of lactic acid are also transported onto the swabs. The presence of lactic acid was found to be a major issue in the detection of explosives in real world applications by Bruker Daltonic.

One result of the presence of lactic acid can be suppression of the signals of the target explosive ions, resulting in the instrument not detecting the explosive even though it is present (called a false negative detection). On the other hand, if the lactic acid produces ions or adduct ions with a mobility very close to the mobility of a target explosive ion, the presence of lactic acid might result in an alarm, even though no explosive compound is present. Although the consequences of this second scenario, called a false positive detection, are less severe than those of a false negative detection, the implications in a time sensitive environment, such as an airport, can also be adverse.

The spectrum obtained at equal amounts of EGDN and lactic acid is shown in figure 64. Many adduct ion species arise due to the interfering compound. The most intense peak is due to the lactate ion ( $m/z = 89$ ). Other ions observed are adducts of lactate with oxygen [ $C_3H_6O_3+O_2$ ] $^-$  ( $m/z = 122$ ) and nitrate [ $C_3H_6O_3+NO_3$ ] $^-$  ( $m/z = 152$ ). A dimer of lactic acid with lactate is also observed ( $m/z = 152$ ). The identity of the ion of this mass with EGDN $^-$  can be excluded because of the intensity of the peak while almost no EGDN $^-$  is observed in the spectrum of pure EGDN in air. The peak at  $m/z = 241$  could either be due to an adduct of lactic acid, lactate and nitrate or an adduct of EGDN with lactate. The peak of the adduct ion [EGDN+NO $_3$ ] $^-$  ( $m/z = 214$ ) is decreased due to the competing adduct formation of NO $_3^-$  with lactic acid. This observation shows the twofold interference caused by the presence of lactic acid. On the one hand, additional peaks arise in the spectrum, complicating the identification of the explosive. On the other hand, the competing adduct formation compromises sensitivity. The addition of common dopants cannot mitigate these problems, due to the high EA of the lactate radical (EA(C $_3$ H $_5$ O) = 3.9 eV), which is in the same range as the value of Cl.<sup>58</sup> As mentioned in the beginning of this paragraph, a sample could potentially contain much higher amounts of lactic acid than the amount of the explosive compound, which could suppress all analyte peaks.

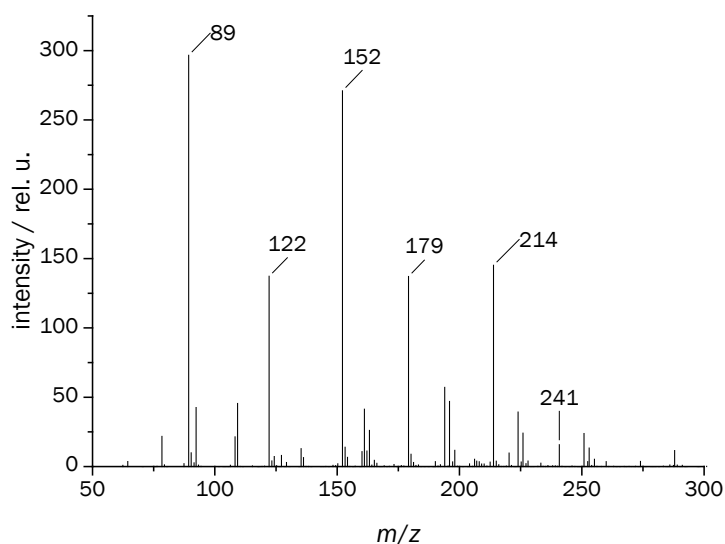


Figure 64: Mass spectrum of ionization products of 5 nmol of EGDN in the presence of 5 nmol of lactic acid in air; observation of the following ions:  $C_3H_5O_3^-$  ( $m/z = 89$ ), [ $C_3H_6O_3+O_2$ ] $^-$  ( $m/z = 122$ ), [ $C_3H_6O_3+NO_3$ ] $^-$  ( $m/z = 152$ ), [ $C_3H_6O_3+C_3H_5O_3$ ] $^-$  ( $m/z = 152$ ), [EGDN+NO $_3$ ] $^-$  ( $m/z = 214$ ), [EGDN+C $_3$ H $_5$ O $_3$ ] $^-$  / [ $C_3H_6O_3+C_3H_5O_3+NO_3$ ] $^-$  ( $m/z = 241$ )

#### 4.2.3.7 Further explosives: the nitramines tetryl and RDX

Another class of explosives that were investigated are nitroaromatic compounds. There are two major differences compared to the alkyl nitrates. First, the nitroaromatic compounds exhibit an aromatic structure compared to the aliphatic alkyl nitrates. Secondly, the functional groups in the former are characterized by C-NO<sub>2</sub> bonds in contrast to the C-O-NO<sub>2</sub> bonds present in the latter. The most well-known nitroaromatic compound, TNT, forms stable molecular anions. In N<sub>2</sub>, TNT<sup>-</sup> is observed exclusively. In air and in the presence of Cl<sup>-</sup>, the main ion detected is the [TNT-H]<sup>-</sup> ion. At atmospheric pressure, no fragmentation is observed, although fragmentation occurs in vacuum.<sup>100</sup>

Another example of a nitroaromatic explosive is tetryl. In addition to the nitro groups, the compound also bears a nitramine group. This functional group bears a C-N-NO<sub>2</sub> bond. The main peak in the spectrum of tetryl (Fig. 65, top) is due to the [M-NO<sub>2</sub>]<sup>-</sup> ion. The fragmentation most probably occurs at the N-N bond in the nitramine group.

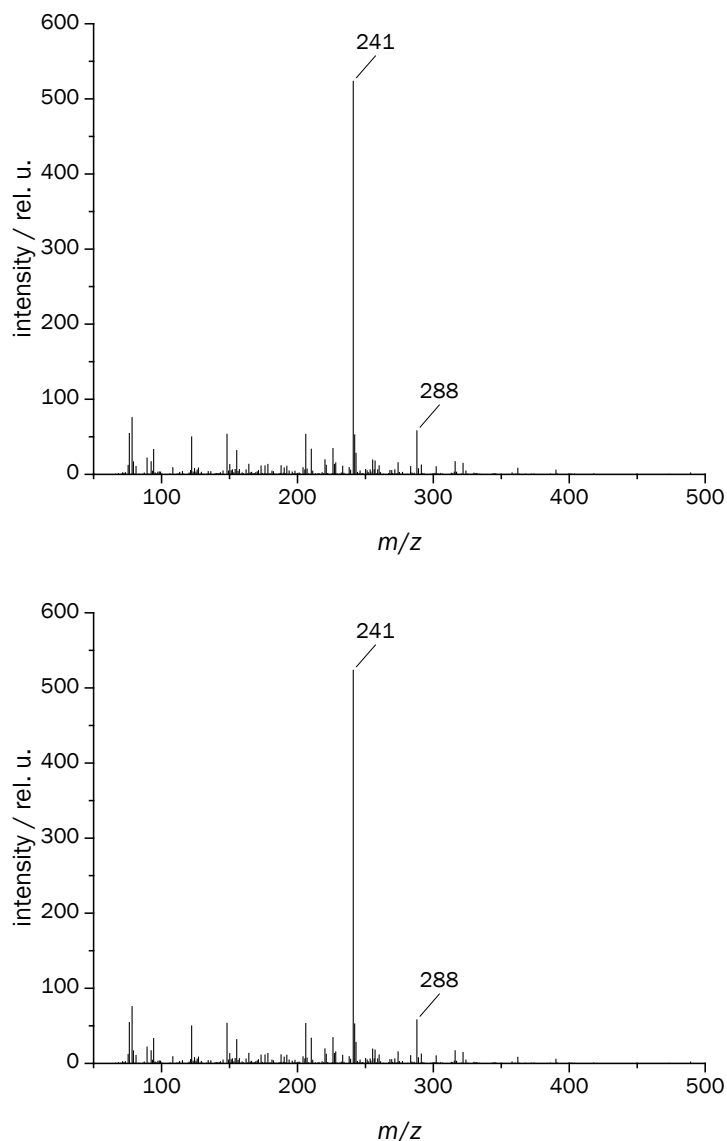


Figure 65: Mass spectra of ionization products of 500 pmol of tetryl in air with a desorber temperature of top: 250 °C (the standard used in all other experiments) and bottom: 150 °C; observation of the following ions: [M-NO<sub>2</sub>]<sup>-</sup> ( $m/z = 241$ ), [M+H]<sup>-</sup> ( $m/z = 288$ )

In addition to fragmentation upon DEA, the fragmentation could also occur thermally at the elevated temperature in the thermodesorption unit. An indication of this is the observation of an  $[M+H]^-$  ion after a reduction of the temperature in the thermodesorption (Fig. 65, bottom). However, this temperature reduction also results in a strong overall decrease in sensitivity of the detection.

As in the case of the alkyl nitrates, the addition of methylene chloride and the detection of tetryl as an  $[M+Cl]^-$  adduct ion (Fig. 66, top) is commonly used in IM spectrometry for the identification.<sup>101</sup> The effect of the dopant methyl iodide was also investigated for tetryl. Similar to the results obtained in the case of the alkyl nitrates, the spectrum obtained in the presence of  $I^-$  shows a shift in the ratio between the monomer and dimer ions towards the monomer (Fig. 66, bottom).

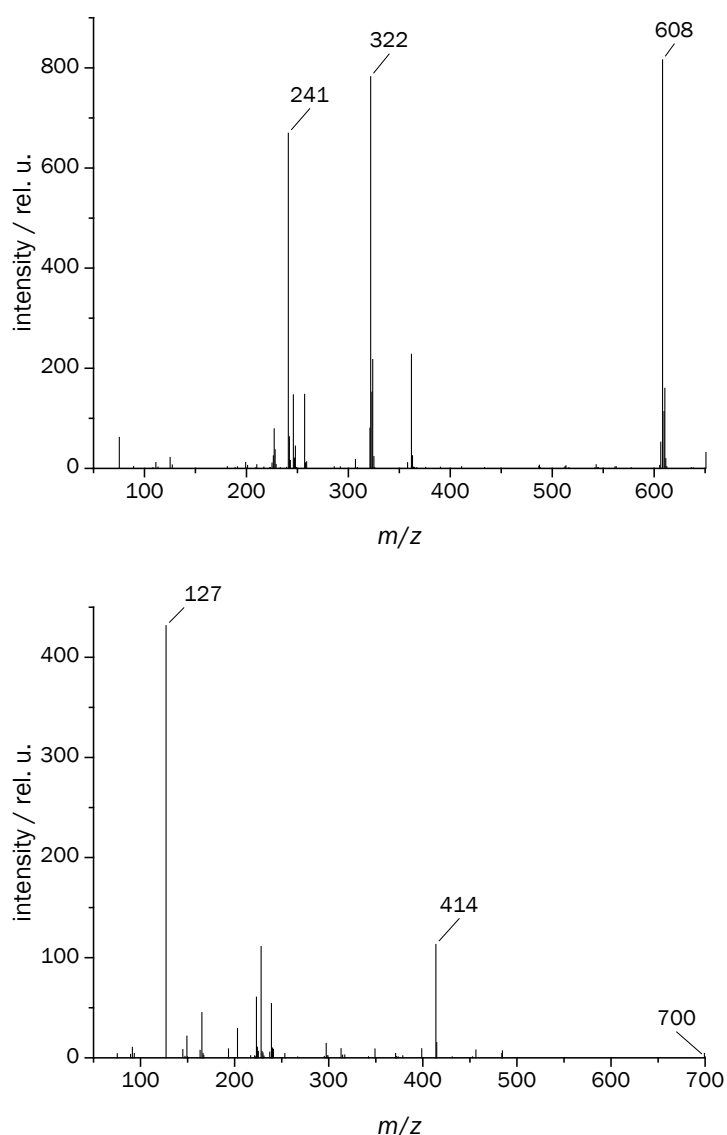


Figure 66: Mass spectra of ionization products of 500 pmol of tetryl in the presence of top: 80  $\mu\text{mol}$  of  $\text{CH}_2\text{Cl}_2$  in air and bottom: 800 nmol of  $\text{CH}_3\text{I}$  in  $\text{N}_2$ ; observation of the following ions: top:  $[M-\text{NO}_2]^-$  ( $m/z = 241$ ),  $[M+\text{Cl}]^-$  ( $m/z = 322$ ),  $[2M-\text{H}+\text{Cl}]^-$  ( $m/z = 608$ ); bottom:  $I^-$  ( $m/z = 127$ ),  $[M+I]^-$  ( $m/z = 414$ ),  $[2M-\text{H}+I]^-$  ( $m/z = 700$ )

A second nitroamine, RDX, was also investigated. The ion species resulting from DEA to RDX were also obtained in the vacuum.<sup>102</sup> The main reaction channel was due to the observation of  $\text{NO}_2^-$ . Additionally,  $[\text{M}-\text{NO}_2]^-$  ( $m/z = 176$ ),  $[\text{M}-\text{NO}_2\text{HNO}_2]^-$  ( $m/z = 129$ ),  $\text{CH}_2\text{NCH}_2\text{NNO}_2^-$  ( $m/z = 102$ ),  $\text{NO}_2\text{HNO}_2^-$  ( $m/z = 93$ ),  $\text{C}_2\text{HN}_2\text{O}_2^-$  ( $m/z = 85$ ),  $[\text{M}-\text{NO}_2\text{HNO}_2\text{HNO}_2]^-$  ( $m/z = 82$ ) and  $\text{CN}^-$  ( $m/z = 26$ ) were detected with DEA peaks observed at an electron energy near 0 eV. Additional DEA peaks were observed at higher energies. However, they were generally less intense. No unfragmented parent ions could be obtained in these experiments. Hartree-Fock calculations by the authors indicated that the energy of thermal electron attachment cannot explain the rich fragmentation. They therefore concluded that the fragmentation is rather a result of the formation of stable neutral fragments. The calculations also showed that the excess electron in the molecular anion is localized in one of the  $\text{NO}_2$  group. The formation of  $\text{NO}_2^-$  was calculated to be exothermic by 0.34 eV, derived as the difference between the nitramine bond dissociation enthalpy of  $D_0(\text{N}-\text{NO}_2) = 1.93$  eV (calculated by authors) and  $\text{EA}(\text{NO}_2) = 2.27$  eV.<sup>58</sup> The calculated EA of the resulting fragment was obtained as  $\text{EA}([\text{RDX}-\text{NO}_2]) = 2.88$  eV. Thus, the energy released in this channel should be even higher with about 0.95 eV. The authors propose that at high electron energy, the  $[\text{RDX}-\text{NO}_2]^-$  fragment is formed in an excited state and decomposes yielding  $\text{NO}_2^-$ .

The spectrum obtained after the ionization of RDX at atmospheric pressure shows rich fragmentation as well (Fig. 67, left). The most intense peak observed was due to the  $[(\text{M}-\text{H})+\text{NO}_2]^-$  adduct ion. A number of nitrogen oxoanions were also detected. In contrast to the results obtained in the vacuum, peaks due to  $[\text{M}-\text{O}]^-$  ( $m/z = 206$ ),  $[\text{M}-\text{H}]^-$  ( $m/z = 221$ ), and  $[\text{M}+\text{O}_2]^-$  ( $m/z = 254$ ) also obtained. Interestingly, another adduct ion,  $[(\text{M}-\text{H})+\text{N}_2\text{O}_2]^-$  ( $m/z = 281$ ) was also observed. The possible fragmentation of RDX leading to the release of  $\text{N}_2\text{O}_2^-$  is indicated on the right of figure 67. Two different adducts of RDX dimers were also observed in the spectrum.

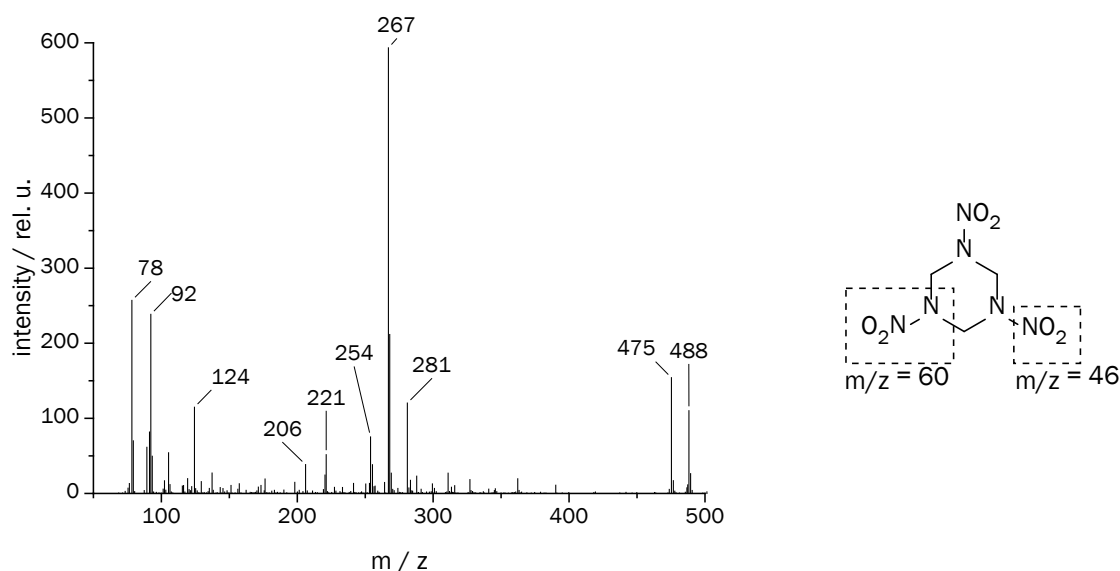


Figure 67: Left: mass spectrum of ionization products of 500 pmol of RDX in air with a desorber temperature of 150 °C; observation of the following ions:  $[\text{O}_2+\text{NO}_2]^-$  ( $m/z = 78$ ),  $[\text{N}_2\text{O}_4]^-$  ( $m/z = 92$ ),  $[\text{N}_2\text{O}_5]^-$ ,  $[\text{N}_2\text{O}_6]^-$  ( $m/z = 124$ ),  $[\text{M}-\text{O}]^-$  ( $m/z = 206$ ),  $[\text{M}-\text{H}]^-$  ( $m/z = 221$ ),  $[\text{M}+\text{O}_2]^-$  ( $m/z = 254$ ),  $[(\text{M}-\text{H})+\text{NO}_2]^-$  ( $m/z = 267$ ),  $[(\text{M}-\text{H})+\text{N}_2\text{O}_2]^-$  ( $m/z = 281$ ),  $[(2\text{M}-\text{H})+\text{O}_2]^-$  ( $m/z = 475$ ),  $[2(\text{M}-\text{H})+\text{NO}_2]^-$  ( $m/z = 488$ ); right: dashed boxes indicate possible fragmentation sites in the RDX molecule

#### 4 Results and discussion

As in the case of tetryl, thermal fragmentation of RDX cannot be excluded. The spectrum shown was already recorded at a reduced desorption temperature. At higher temperatures, an increase of the fragmentation was obtained. At temperature below 150 °C, a strong decrease of the signal intensity was observed.

The RDX spectrum obtained upon the addition of the dopant methylene chloride is very much simplified (Fig. 68, top). The highest ion yield was obtained for the  $[M+Cl]^-$  adduct ion. Dimer adducts with  $Cl^-$  were also observed. Similarly, upon the addition of methyl iodide, the  $[M+I]^-$  adduct ion is detected (Fig. 68, bottom). In presence of  $I^-$ , no dimers are observed.

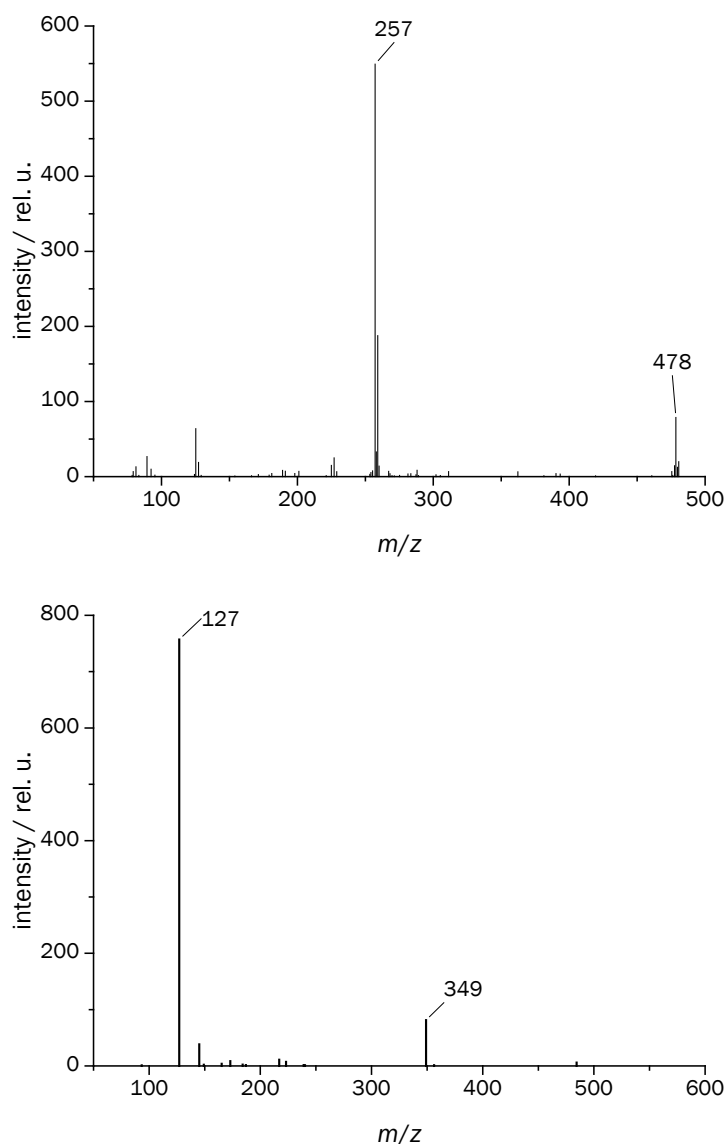


Figure 68: Mass spectra of ionization products of 50 pmol of RDX in the presence of top: 80 μmol of  $CH_2Cl_2$  and bottom: 800 nmol of  $CH_3I$  in air; observation of the following ions: top:  $[M+Cl]^-$  ( $m/z = 257$ ),  $[(2M-H)+Cl]^-$  ( $m/z = 478$ ); bottom:  $I^-$  ( $m/z = 127$ ),  $[M+I]^-$  ( $m/z = 349$ )

#### 4.2.4 Mass-mobility-correlations and computation of collision cross sections

The interpretation of IM spectra is not always straight forward. While the collision cross section is an ion specific quantity, the identity of the ions observed in the spectrum is not always known. The combinations of IM and mass spectrometry can help elucidate the IM spectra, an example of which was shown in the previous chapter. In the absence of such instruments, mathematical models permitting the prediction of collisions cross sections based on the structure of the ions can be a helpful resource to the IM spectrometrists. Additionally, such investigations can yield deeper insights into the interactions of ions and drift gas neutrals.

The most simple of these models empirically correlate the IM with the ions  $m/z$ . More advanced correlations strive to incorporate models of the interaction of ion and drift gas neutrals. A computationally more elaborate approach is the optimization of ion geometries by quantum chemical methods and the subsequent calculation of collision cross sections based on trajectory simulations between the ions and drift gas neutrals. The former approach has the disadvantage of being empirical and the consequential necessity of IM data from compounds similar to those investigated. Additionally, since the calculations are always based on an ion's  $m/z$ , the correlations fail to discriminate isobaric ions. The second approach has the disadvantage of potentially high systematic errors in the calculated IM.

In this chapter, several different methods were applied in the calculation of the IM of explosive compounds. An attempt was made to combine the advantages of the correlation and the simulation approach.

##### 4.2.4.1 Correlation of ion mobility and mass

In the case of similarly shaped ions and the absence of other effects, such as different attractive interactions of the ions with drift gas neutrals, the IM correlates with the ion's  $m/z$ . Deviations from this correlation can contain information about the sizes and shapes of the analytes or the aforementioned interactions. Good correlations for similar substances can be used to identify unknown IM peaks via the calculated masses. Using the ions identified in the previous chapter, it is possible to assign the peaks in the IM spectra of NG and PETN (Fig. 69). The IM spectra of all alkyl nitrates were measured by Andreas Beil at Bruker Daltonics Leipzig.

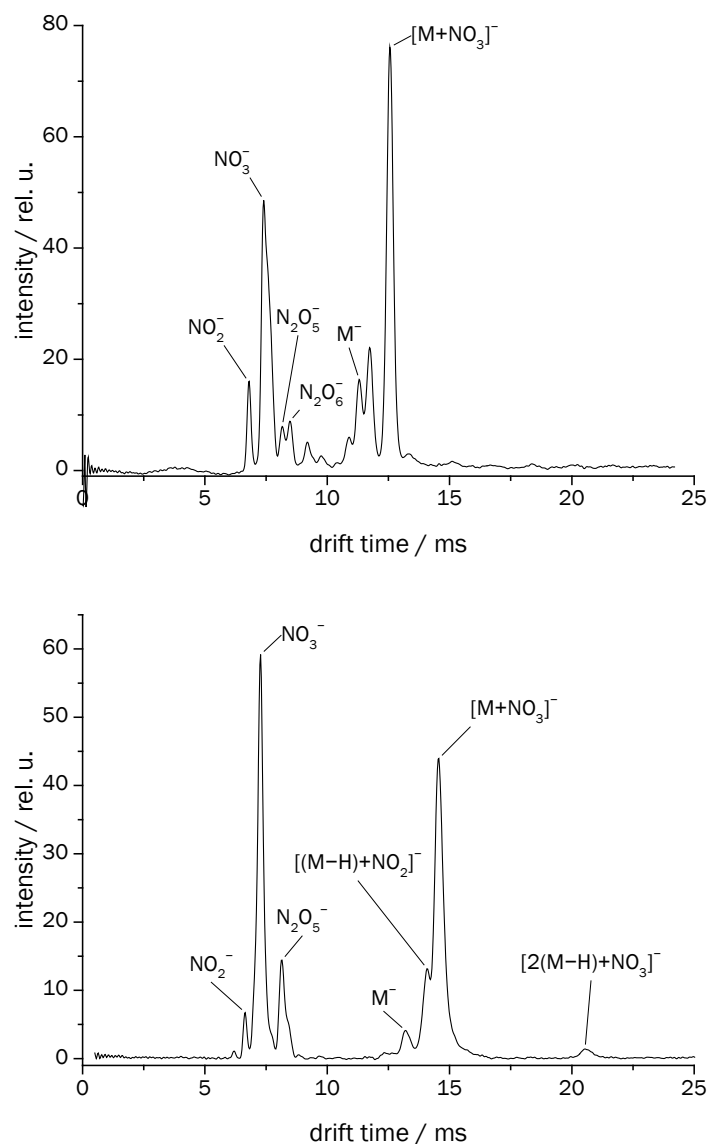


Figure 69: IM spectra of top: NG and bottom: PETN, provided by A. Beil (IM spectrometer, air 55 °C, thermodesorber 200 °C, 100 ng substance)

In table 8, the experimental reduced mobilities  $K_{0,\text{exp}}$  obtained from these measurements are reported. Where available, literature values are also given. These values show relatively large deviations although according to the theoretic framework outlined in chapter 2.2.1 the  $K_0$  values are fundamental physical quantities that should be independent of the instrument. Not all reported numbers are actually values of mass identified ions. Several different ionization sources were used and the identity of the products between different sources is only assumed. Further discrepancies may arise due to differences in the instruments, such as resolution and temperature.  $K_0$  values obtained with low resolution instruments have a higher uncertainty. The temperature dependence of  $K_0$  values (although the convention should eliminate it) has been shown in different cases. As this problem is known,  $K_0$  determinations are often done by using internal standards. However, if different standards are used, differing values might also occur.



Table 8: Ionic species identified in mass spectra and mobility of IM spectrometric peaks assigned to the same species obtained in the present experiments and taken from the literature (the publications cited sometimes include multiple values for the same species)

Species	$m/z$	$K_{0,\text{exp}} / \text{cm}^2\text{V}^{-1}\text{s}^{-1}$	$K_{0,\text{lit}} / \text{cm}^2\text{V}^{-1}\text{s}^{-1}$
$\text{NO}_2^-$	46	2.42	
$\text{NO}_3^-$	62	2.22	2.48 <sup>a</sup> /2.46 <sup>a</sup> /2.53 <sup>a</sup>
$\text{N}_2\text{O}_5^-$	108	1.99	
$\text{N}_2\text{O}_6^-$	124	1.92	
$[\text{EDGN}+\text{NO}_3]^-$	214	1.45	1.43 <sup>a</sup> /1.576 <sup>a</sup>
$[\text{RDX}-\text{H}]^-$	221	1.45	1.47 <sup>*,b</sup>
$[\text{TNT}-\text{H}]^-$	226	1.45	1.48 <sup>c</sup> /1.54 <sup>c</sup>
$\text{NG}^-$	227	1.43	1.45 <sup>t,c,d</sup>
$[\text{Tetryl}-\text{NO}_2]^-$	241	1.37	
$[\text{ETN}-\text{NO}_2]^-$	256	1.42	
$[\text{NG}+\text{Cl}]^-$	262	1.35	1.47 <sup>a,c</sup> /1.4 <sup>d</sup>
$[(\text{RDX}-\text{H})+\text{NO}_2]^-$	267	1.36	1.43-1.45 <sup>*,a</sup> 1.4 <sup>*,d</sup>
$[\text{NG}+\text{NO}_3]^-$	289	1.28	1.32 <sup>a</sup> /1.40 <sup>a</sup> /1.31 <sup>d</sup>
$[\text{ETN}+\text{H}]^-$	303	1.27	
$\text{PETN}^-$	316	1.23	1.22 <sup>t,a</sup> /1.25 <sup>t,a</sup>
$[\text{ETN}+\text{OH}]^-$	319	1.23	
$[\text{PETN}+\text{Cl}]^-$	351	1.16	1.2 <sup>d</sup>
$[(\text{PETN}-\text{H})+\text{NO}_2]^-$	361	1.15	
$[\text{ETN}+\text{NO}_3]^-$	364	1.16	
$[\text{PETN}+\text{NO}_3]^-$	378	1.11	1.38 <sup>a</sup> /1.14 <sup>d</sup>
$[2(\text{RDX}-\text{H})+\text{NO}_2]^-$	488	0.955	
$[2(\text{ETN}-\text{H})+\text{NO}_3]^-$	664	0.833	
$[(2\text{PETN}-\text{H})+\text{Cl}]^-$	666	0.787	
$[2(\text{PETN}-\text{H})+\text{NO}_3]^-$	692	0.790	

<sup>a</sup>Reference<sup>101</sup>, <sup>b</sup>Reference<sup>103</sup>, <sup>c</sup>Reference<sup>104</sup>, <sup>d</sup>Reference<sup>105</sup> \*value reported for  $\text{RDX}^-$  and  $[\text{RDX}+\text{NO}_2]^-$ , respectively; †value reported for  $[\text{NG}-\text{H}]^-$  and  $[\text{PETN}-\text{H}]^-$ , respectively

The most straightforward approach to obtaining a mass-mobility correlation is the plot of the inverse mobility over  $m/z$ .<sup>106</sup> This procedure is purely empirical. The underlying assumption is that the collision cross sections vary linearly with the ion mass. Depending on the data, other empirical fitting procedures may be chosen.<sup>107</sup> In the case of the explosive compounds investigated, the linear regression results in a reasonably good fit (Fig. 70). The coefficient of determination obtained for the linear regression is  $R_{\text{COD}}^2 = 0.996$ . The function thus obtained can be used to calculate approximate  $m/z$  values for given  $K_0$  values or vice versa.

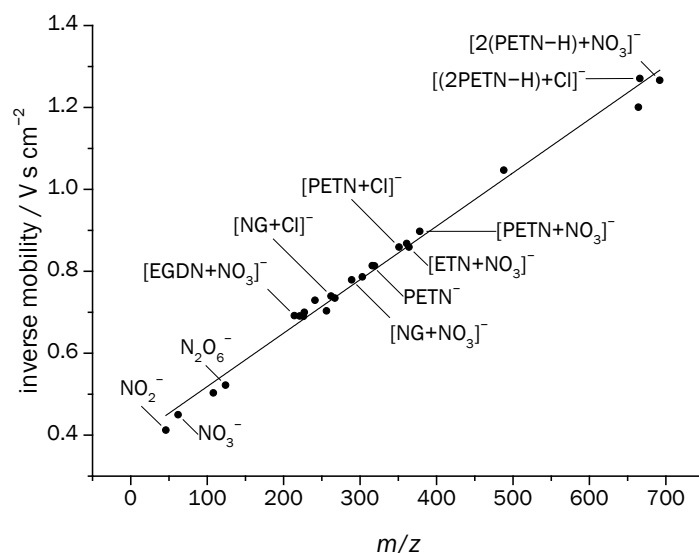


Figure 70: Inverse reduced mobilities  $K_0^{-1}$  obtained by IM spectrometry as a function of  $m/z$  obtained by mass spectrometry, assignment of some species for orientation, solid line is linear regression

#### 4.2.4.2 Prediction of mass-mobility correlation by (12-4) potential core model

In order to ascribe a physical meaning to the correlation of the mobility with the mass, it is useful to use a model that incorporates interaction potentials. The (12-4) potential presented in chapter 2.2.2.3 has been successfully used in reproducing such correlations in the literature.<sup>17,18</sup> The potential and the corresponding procedure of calculating cross sections were first reported by Mason, O'Hara and Smith.<sup>16</sup> The details and equations are given in the chapter mentioned. Only briefly, a correction for the discrepancy between the center of mass and the center of charge is introduced as a core of the molecule represented as a hard sphere. The collision integral is evaluated from the temperature  $T$  and the core diameter  $a$ . The values are tabulated in relation to the potential minimum position  $r_m$ . This in turn can be calculated as a function of the cubed root of the mass and a parameter  $r_0$ .<sup>17</sup>

Since the tabulate values of  $\Omega^{(1,1)*}$  are only given for a limited number of  $a^*$  and  $T^*$  values the following procedure was used to obtain values for specific  $a^*$ ,  $T^*$  pairs. A two-dimensional interpolation between the tabulated values<sup>16</sup> was carried out based on the Renka-Cline triangulation<sup>108</sup> implemented in the software Origin. For this calculation, the decadic logarithms of  $T^*$  and  $\Omega^{(1,1)*}$  were used because they produced a smooth interpolation (Fig. 71). The values obtained by the Renka-Cline procedure were not smooth if the numbers were used as given, whereas the values obtained for the logarithmic values were still smooth upon exponentiation.

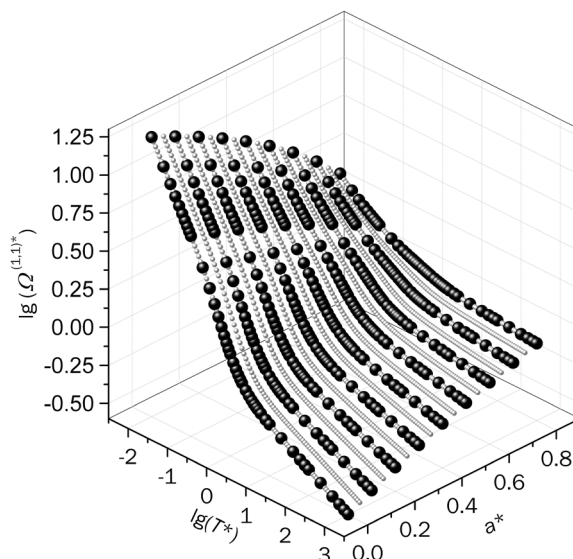


Figure 71: Decadic logarithm of the reduced cross section  $\Omega^{(1,1)*}$  as a function of the reduced core diameter  $a^*$  and the decadic logarithm of the effective temperature  $T^*$ ; tabulated<sup>16</sup> (black spheres) and interpolated values (grey spheres)

The fitting procedure itself was performed as follows. Variable ranges were defined for  $a^*$  and  $r_0$ . Good results could be obtained for values of  $a^*$  between 0 and 0.8 and  $r_0$  values between 1.5 Å and 3 Å. For each variable, a set of 50 equally spaced points was determined to be sufficient after it was verified that 100 points resulted in the same values. All calculations were performed based on the experimental temperature. For each value of  $r_0$ , the resulting  $r_m$  were calculated for each ion according to (32). Then,  $T^*$  was computed (also for each ion) with the well depth  $\varepsilon_c$  defined in (30). Subsequently, the  $a^*$  and  $T^*$  produced the  $\Omega^{(1,1)*}$  values,  $\Omega_D$  values and, using (20), the mobilities  $K$  for each ion based on the interpolation mentioned above. Thus, for each pair of  $a^*$  and  $r_0$ , a set of mobilities was obtained. The sum of the squared deviations of these calculated mobilities from the experimental values was evaluated. Finally the pair of  $a^*$  and  $r_0$  that produced the best fit (i.e. the lowest sum of squared deviations) was chosen.

The resulting values of  $r_m$ ,  $a$ ,  $\varepsilon_c$ ,  $\Omega_D$  and the experimental and calculated  $K$  obtained in case of the explosive compounds investigated are listed in table 9. Although the third digit (fourth digit in the case of values below 1) to the right of the decimal point in the values of the experimental mobilities is generally below the precision of the measurements, it is still given as a point of comparison to the calculated values. All 15 digits of the experimental  $K_0$  values obtained as a result of averaging were used in the fitting procedure as double precision data variables were used.

The mobility values are shown in figure 72 as a function of the  $m/z$  of the ions as well as a correlation between experimental and calculated values. While most calculated mobilities are close to the experimental values, a systematic deviation can be seen at very low mobilities, especially in the case of the dimer ion adducts. Additionally, it is evident that discrepancies exist for some ions, e.g.  $N_2O_5^-$  and  $N_2O_6^-$ . This is an indication that the shape of these two ions is more compact than those of the rest and their mobilities are therefore higher than would be expected from the  $m/z$  correlation. Put another way, the actual  $r_m$  values should be smaller than the calculated ones.

#### 4 Results and discussion

Table 9: Results of fitting the (12-4) core potential model to the data of the explosives compounds,  $a^* = 0.1633$  and  $r_0 = 2.633 \text{ \AA}$

Species	$m/z$	$K_{\text{exp}} / \text{cm}^2\text{V}^{-1}\text{s}^{-1}$	$K_{\text{calc}} / \text{cm}^2\text{V}^{-1}\text{s}^{-1}$	$r_m / \text{Å}$	$a / \text{Å}$	$\epsilon_c / \text{meV}$	$\Omega_{\text{D,calc}} / \text{Å}^2$
$\text{NO}_2^-$	46	2.424	2.470	5.739	0.9369	15.44	82.59
$\text{NO}_3^-$	62	2.223	2.228	6.063	0.9900	12.39	86.97
$\text{N}_2\text{O}_5^-$	108	1.987	1.834	6.761	1.104	8.015	98.38
$\text{N}_2\text{O}_6^-$	124	1.915	1.746	6.955	1.136	7.155	101.9
$[\text{EGDN}+\text{NO}_3]^-$	214	1.446	1.435	7.818	1.276	4.483	119.2
$[\text{RDX}-\text{H}]^-$	221	1.447	1.418	7.873	1.285	4.357	120.4
$[\text{TNT}-\text{H}]^-$	226	1.449	1.406	7.913	1.292	4.271	121.2
$\text{NG}^-$	227	1.429	1.404	7.920	1.293	4.255	121.4
$[\text{Tetryl}-\text{NO}_2]^-$	241	1.371	1.374	8.027	1.311	4.033	123.7
$[\text{ETN}-\text{NO}_2]^-$	256	1.422	1.343	8.137	1.328	3.820	126.1
$[\text{NG}+\text{Cl}]^-$	262	1.352	1.332	8.179	1.335	3.741	127.0
$[(\text{RDX}-\text{H})+\text{NO}_2]^-$	267	1.361	1.323	8.214	1.341	3.678	127.8
$[\text{NG}+\text{NO}_3]^-$	289	1.283	1.285	8.364	1.366	3.422	131.1
$[\text{ETN}+\text{H}]^-$	303	1.271	1.262	8.455	1.380	3.277	133.1
$[\text{PETN}]^-$	316	1.229	1.243	8.537	1.394	3.153	135.0
$[\text{ETN}+\text{OH}]^-$	319	1.230	1.239	8.556	1.397	3.125	135.4
$[\text{PETN}+\text{Cl}]^-$	351	1.164	1.195	8.747	1.428	2.860	139.8
$[(\text{PETN}-\text{H})+\text{NO}_2]^-$	361	1.152	1.183	8.805	1.438	2.786	141.1
$[\text{ETN}+\text{NO}_3]^-$	364	1.164	1.179	8.822	1.440	2.765	141.5
$[\text{PETN}+\text{NO}_3]^-$	378	1.114	1.163	8.900	1.453	2.669	143.3
$[2(\text{RDX}-\text{H})+\text{NO}_2]^-$	488	0.9553	1.056	9.457	1.544	2.093	156.6
$[2(\text{ETN}-\text{H})+\text{NO}_3]^-$	664	0.8330	0.9385	10.20	1.664	1.550	174.9
$[(2\text{PETN}-\text{H})+\text{Cl}]^-$	666	0.7870	0.9374	10.20	1.666	1.545	175.1
$[2(\text{PETN}-\text{H})+\text{NO}_3]^-$	692	0.7896	0.9236	10.30	1.682	1.488	177.6

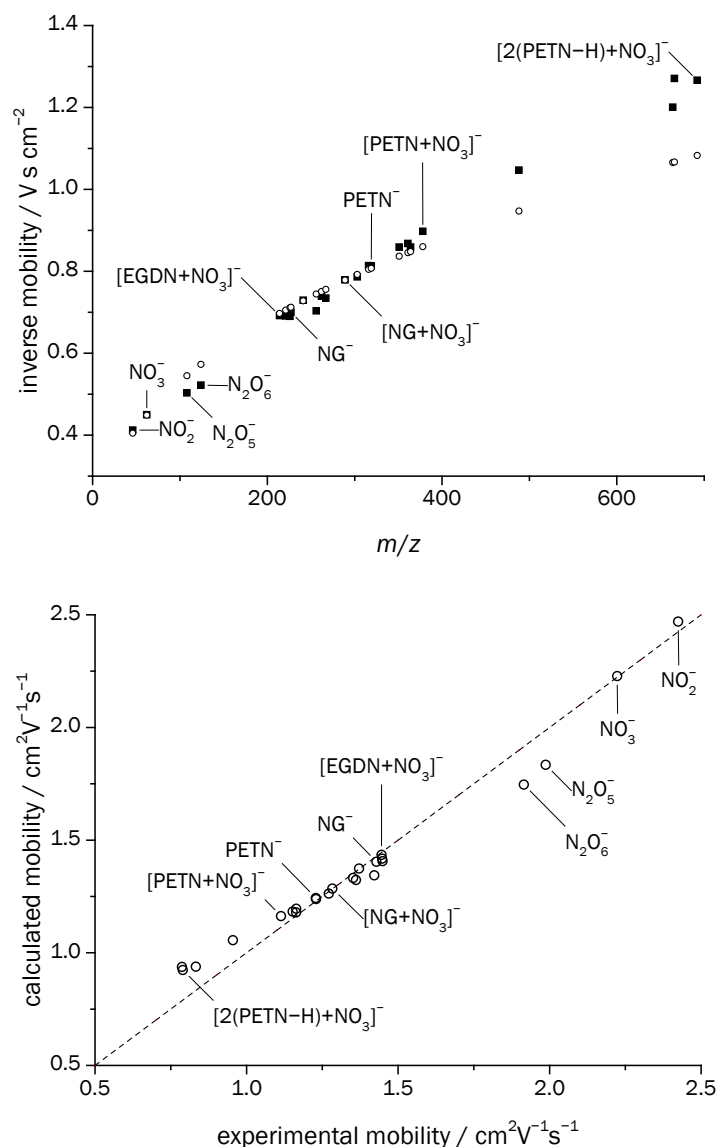


Figure 72: Fit to (12-4) potential optimizing  $a^*$  and  $r_m$ , top: inverse mobility as a function of  $m/z$ , experimental values (■), calculated values (○); bottom: correlation of calculated with experimental mobilities

Berant and Karpas introduced a model for the dependence of  $r_m$  from  $r_0$  that uses a third parameter, a constant correction factor  $z$  [Eq. (33)].<sup>17</sup> The fitting procedure detailed above was expanded by sampling each set of  $a^*$  and  $r_0$  for 20 points of  $z$  between 0 and  $0.005 \text{ \AA}/u$ . A higher number of points did not improve the results. The results of the fit are shown in figure 73 (data is given in chapter 7, table 12). The optimized values are  $a^* = 0.2122$ ,  $r_0 = 2.265 \text{ \AA}$  and  $z = 7.895 \times 10^{-4} \text{ \AA}/u$ . Comparing the results of this calculation with the previous one shows the correction factor to be effective. The deviations observed for the larger dimer ion adducts are compensated by this refinement. However, the deviations of the values for  $N_2O_5^-$  and  $N_2O_6^-$  are still observed, as these cannot be compensated by a fit in which the mobility is calculated purely as a function of  $m/z$ .

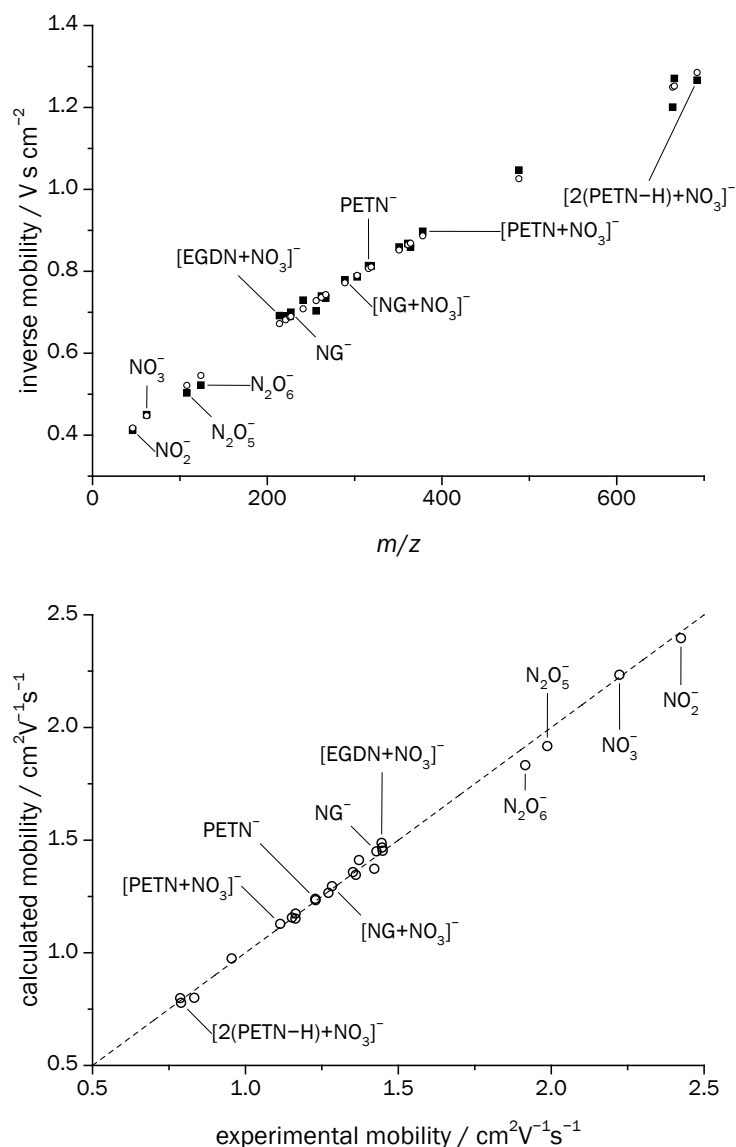


Figure 73: Fit to (12-4) potential optimizing  $a^*$ ,  $r_m$  and  $z$ , top: inverse mobility as a function of  $m/z$ , experimental values (■), calculated values (○); bottom: correlation of calculated with experimental mobilities

#### 4.2.4.3 Prediction of mobilities based on DFT calculations and trajectory simulations

In the absence of mobility values of reference compounds from which the mobilities of unknown compounds can be deduced, ab initio calculations are the only way of predicting mobilities. The structures of many of the ions observed in the spectra of the explosive compounds were obtained by DFT calculations carried out by T. Ritschel. In order to calculate mobilities from these structures, it was necessary to perform trajectory simulations using one of the methods outlined in chapter 2.2.3. These simulations were performed using the software Mobcal. The original Mobcal program by the Jarrold group was written in Fortran 77 and the source code is available from Prof. M. F. Jarrold's homepage (<http://www.indiana.edu/~nano/software.html>).<sup>22,26</sup> The original version of Mobcal can only be used for mobility simulations in He and incorporates all methods described in chapter 2.2.3.

The results obtained with this software are labeled TM(He), PA'(He) and EHS(He) below. A modified code of the program written by Capuzano et al. was kindly supplied by Prof. M. F. Bush.<sup>28</sup> This code is based on the version written by Kim et. al.<sup>27</sup> In the modified version of Mobcal, the TM (see chapter 2.2.3.3) was expanded to account for collisions of ions with the diatomic N<sub>2</sub> molecule. Results obtained with this modification are labeled TM(N<sub>2</sub>) below. A third version of Mobcal, written in our group, was also used. In this version, the PA' method (see chapter 2.2.3.1) was modified. The hard sphere radii were increased to match those of the different atoms in the ion to a projection of the N<sub>2</sub> molecule in all possible rotations (see chapter 4.2.4.4). The values calculated with this version of the software are labeled PA'(N<sub>2</sub>) below. Collision cross sections were obtained for the explosive compound ions using the different versions of Mobcal on the structures calculated by DFT (Fig. 74, top; data is given in chapter 7, table 13).

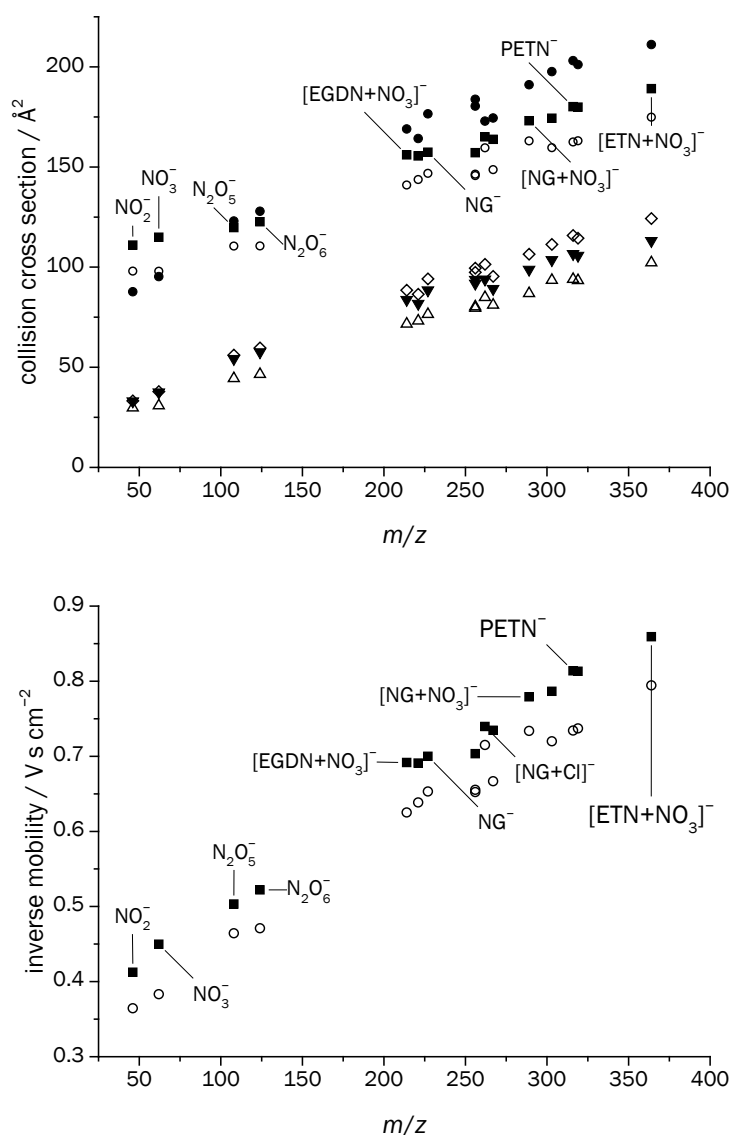


Figure 74: Top: collision cross sections obtained experimentally (■) and using geometries from DFT calculations and Mobcal: TM (Δ), PA' (▼) and EHS (◊) in He; TM adapted to N<sub>2</sub> (○); PA' method in N<sub>2</sub> (●); bottom: comparison of experimental mobilities (■) and mobilities calculated from TM adapted to N<sub>2</sub> (○)

From a quick evaluation of the figure it is obvious that the values obtained with the original version of Mobcal are systematically too small. This finding was expected as these simulations were included for reference and for comparison, only. The values obtained with the Mobcal versions optimized for the drift gas  $N_2$  generally deviate less than 10 % from the experimental values. Yet both models fail to accurately predict the mobilities as the deviation is systematic. However, compared to the purely  $m/z$  based correlations, the advantage of this kind of simulation also becomes apparent. The deviations from a smooth  $m/z$  dependence of the cross sections are qualitatively reproduced, particularly by the TM( $N_2$ ) calculation. All values obtained by the TM( $N_2$ ) are too small. The software was developed purely for the calculation of mobilities of cations. Apparently, the collision cross sections of anions are, due to the additional electron, larger than those of the corresponding cations.

#### 4.2.4.4 Combination of (12-4) potential with trajectory simulations

The results of the previous chapters illustrate the advantages and drawbacks of correlation and simulation approaches to mobility predictions. Therefore, a combination of both methods was attempted. In the (12-4) potential approach, the entire molecular ion is represented by one rigid sphere. In the trajectory simulations, the electrostatic interactions of the localized charge on the ion and the induced dipole moment in  $N_2$  are not well represented. The mobilities obtained by the latter are also not readily scaled to match empirical data. The combination of both methods proposed in this chapter treats the collisions of individual atoms within molecular ions by hard spheres collisions simulated in Mobcal and then scales the “geometric” cross sections thus obtained to experimental data by means of the (12-4) potential. The formalism introduced in chapter 2.2.2.3 lends itself to this approach. Since the cross section calculated from the (12-4) potential is given by (31) (chapter 2.2.2.3) as a function of the dimensionless reduced cross section  $\Omega^{(1,1)*}$ , the hard sphere scattering interaction is already treated independently from the effect of the (12-4) potential. Accordingly, the following approach was chosen.

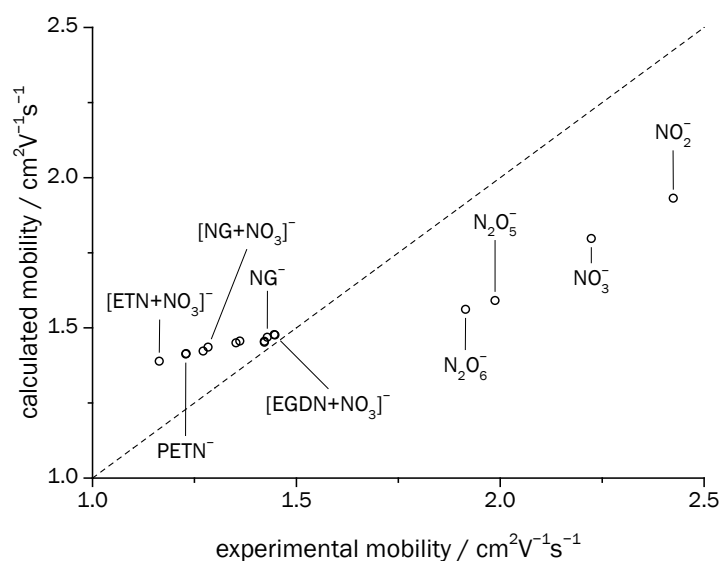


Figure 75: Correlation of experimental mobilities with mobilities obtained using  $r_m$  obtained from PA' in He



The  $r_m$  of the explosive compound ions were obtained from PA' collision cross sections according to  $r_m = (\Omega_{PA'}/\pi)^{1/2}$ . The values of  $a^*$ ,  $\varepsilon_c$  and consequently  $T^*$  were calculated using these  $r_m$ . Thus, the fitting procedure according to the (12,4) potential was performed using  $a^*$  as the only variable. The first approach relied on using the PA'(He) value of  $\Omega_{PA'}$  obtained in the original Mobcal version. The lowest sum of squared residuals was obtained for a value of  $a^* = 0.3313$ . However, the agreement of this fit with the experimental data was poor (Fig. 75, chapter 7, table 14). The reason for this mismatch between the calculated and experimental values is that the He atoms are much smaller than the N<sub>2</sub> molecules. Therefore, the  $r_m$  obtained from the PA'(He) model are inadequate for the fitting procedure.

To improve the results, a new model taking into account the larger  $r_m$  in N<sub>2</sub> had to be introduced. For this reason, the hard sphere radii used in Mobcal were increased to accommodate N<sub>2</sub> by scaling the parameters according to the difference in van der Waals radii of He and N and also considering the bond length of N<sub>2</sub>. The resulting hard sphere parameters can be considered those of an N<sub>2</sub> molecule and the corresponding atom (in the ion) averaged over all possible rotations of N<sub>2</sub>. This approach seemed feasible as an approximation considering the large number of collisions taking place in an IM spectrometer in the typical drift times of ions. In addition to the hard sphere radii, the experimental parameters such as the molecular mass and the polarizability were also updated. For a comparison to the other values, the PA' collision cross sections obtained with this modified version of Mobcal were already presented in chapter 4.2.4.3. The agreement to the experimental cross sections is already better than those obtained with the original Mobcal. However, the PA' values are larger than experimental cross sections. A possible explanation could be that the scaling based on the van der Waals radii is inadequate. However, since there is no calibration data of, e.g. C<sub>60</sub><sup>+</sup> fullerene ions in N<sub>2</sub>, this approach seemed the least arbitrary. But, as a consequence, the values thus obtained should be considered a first approximation that serves to illustrate the possibility of combining simple trajectory simulations with  $m/z$  correlation procedures.

In figure 76, the mobility values obtained by the PA'(N<sub>2</sub>) method are shown in addition to the values obtained by the fitting procedure according to the (12-4) potential with the values of  $r_m$  calculated by  $r_m = (\Omega_{PA'}/\pi)^{1/2}$ , where  $\Omega_{PA'}$  is the collision cross section obtained in the PA'(N<sub>2</sub>) method, and the optimized  $a^* = 0.2020$ . The values of  $r_m$  as well as the mobilities can be found in chapter 7, table 15. The agreement between the experimental and calculated values is excellent.

The method has two advantages compared to the fit to the (12-4) potential based purely on  $m/z$  reported in chapter 4.2.4.2. First, there is only one parameter,  $a^*$ , that has to be optimized, reducing the computational effort as well as the likelihood of overfitting, yielding a higher confidence in the physical meaning of values of  $r_m$  and  $a$ . The second advantage is the ability to predict differences in the IM of isobaric ions, as well as IM trends that are not reproduced by simple functions of  $m/z$ .

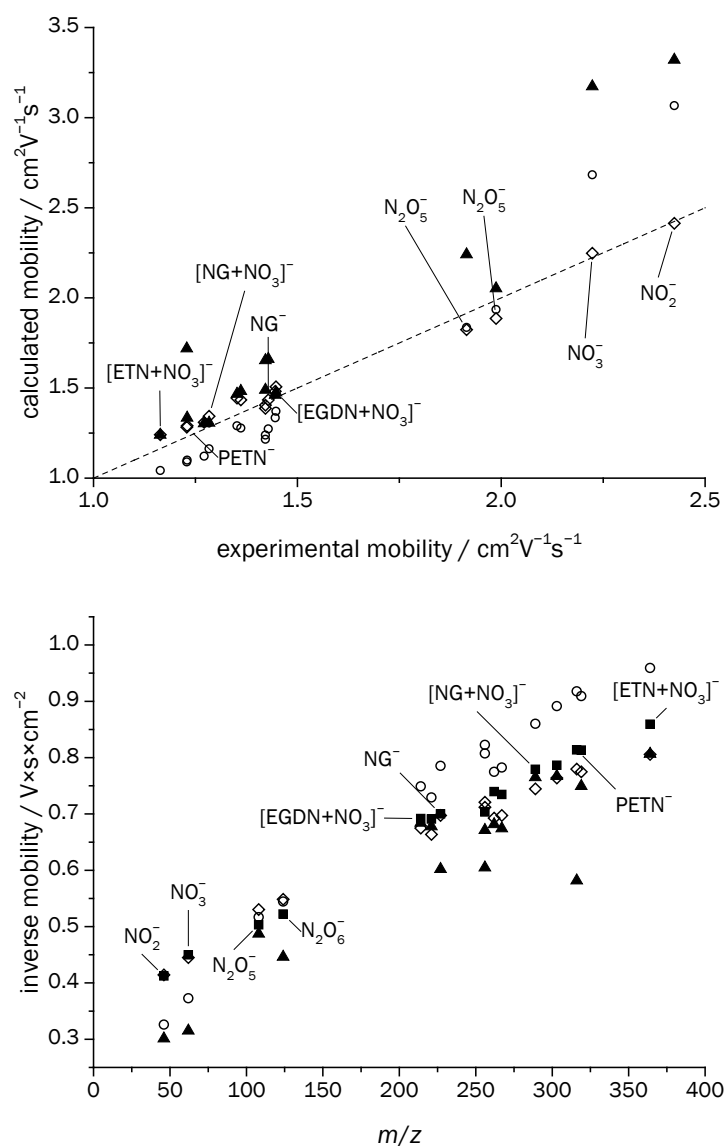


Figure 76: Top: Correlation of experimental and calculated mobilities; bottom: inverse mobilities as a function of ion  $m/z$ ; experimental values (■),  $PA'$  in  $N_2$  (○),  $r_m$  from  $PA$  and  $a$  from DFT structures (▲);  $r_m$  from  $PA'$  in  $N_2$  and  $a^*$  fitted ( $a^* = 0.2020$ ) (◇)

A further improvement of the method would be if in addition to calculation of  $r_m$  values from the trajectory simulations, the values of  $a$  could also be calculated. The justification for such an approach is that while the simulations account for the collision between the buffer gas neutrals and the single atoms making up the ions, they do not consider the electrostatic interaction between the neutral and the ion as a whole. As the (12-4) potential models these interactions reasonably well, it could therefore be beneficial to include it in the calculation. The parameter  $a$  is introduced to account for the possible inequality of the positions of the center of mass and the center of charge in a molecular ion (see chapter 2.2.2.3).

Therefore, the approach used was to calculate the center of mass  $c_m$  from the optimized DFT geometry according to

$$c_{m,x} = \frac{\sum_{i=1}^{N_x} x_i m_i}{\sum_{i=1}^{N_x} m_i}, c_{m,y} = \frac{\sum_{i=1}^{N_x} y_i m_i}{\sum_{i=1}^{N_x} m_i}, c_{m,z} = \frac{\sum_{i=1}^{N_x} z_i m_i}{\sum_{i=1}^{N_x} m_i}, \quad (49)$$

where  $N_x$  is the number of atoms in the molecular ion;  $x_i, y_i, z_i$  describe the position of each atom in space and  $m_i$  is the mass of each ion. Similarly, the center of charge  $c_c$  was calculated by

$$c_{c,x} = \frac{\sum_{i=1}^{N_x} x_i q_{M,i}}{\sum_{i=1}^{N_x} q_{M,i}}, c_{c,y} = \frac{\sum_{i=1}^{N_x} y_i q_{M,i}}{\sum_{i=1}^{N_x} q_{M,i}}, c_{c,z} = \frac{\sum_{i=1}^{N_x} z_i q_{M,i}}{\sum_{i=1}^{N_x} q_{M,i}}, \quad (50)$$

where  $q_M$  is the Mulliken charge of each atom in the ion. In the case of the singly charged anions investigated, the denominator becomes negative unity. The magnitude of the distance between point is then the parameter  $a = |c_g - c_c|$ . The mobilities are then calculated based on the tabulated values of  $\Omega^{(1,1)*}$  obtained for each ion by inserting  $a$ , obtained from the above calculation directly from the DFT optimized structures, and  $r_m$  from the PA'(N<sub>2</sub>) results.

The results of the calculation, including the values of  $a$ , are shown in table 16 (chapter 7). Additionally, the mobility values are plotted in figure 76. The mobility values obtained by this procedure fail to reproduce the experimental data adequately. The particular method of obtaining the values of  $a$  from the DFT structures is therefore apparently not well suited to the (12-4) potential. This is especially apparent in cases where the value of  $a$  is very low. The resulting mobility values show the strongest deviations. Examples are the values of NO<sub>2</sub><sup>-</sup>, NO<sub>3</sub><sup>-</sup> and PETN<sup>-</sup>. The Mulliken charges apparently do not represent the location of the additional charge well in all cases. Conversely, it could be argued that the calculation of mobilities from the (12-4) potential fails if  $c_g$  and  $c_c$  coincide in a molecule. However, the localization of  $c_c$  close  $c_g$  in the PETN<sup>-</sup> ion is inconsistent with the observation of the additional electron density at one nitrate group in the anion (see chapter 4.2.3.4) and seems unlikely from a chemical point of view. Therefore, the first explanation is more likely.

The method is still noteworthy in the context of this chapter, since the calculation relies solely on theoretically obtained parameters, whereas the previously described procedures involved fitting the parameters to experimental data. Although, the approach described does not seem to offer an advantage over the results obtained with e.g. the TM(N<sub>2</sub>) version of Mobcal, the incorporation of the (12-4) potential into the mobility simulation appears promising. In the future, this could be implemented by either finding a more appropriate way of calculating the values of  $a$  from the theoretically obtained ion structures, or by directly incorporating the (12-4) potential into the simulation. The latter approach would be especially promising in the case of the TM. Commonly, in the TM, the effect of the potential between each atom in the ion and the drift gas neutral is evaluated in turn. It seems reasonable to additionally incorporate a potential that takes into account the interaction of the drift gas neutral with the molecular ion in its entirety. The (12-4) potential seems well suited for this approach.

#### 4.2.4.5 Application of calculation to amines

As a means of evaluating the methods developed in the previous chapter, the procedures described were also performed on mobility data of molecular ions reported in the literature. In order to highlight the advantage of using quantum chemically calculated geometries and trajectory simulation based collision cross sections over correlations based solely on mass, ions of similar  $m/z$  but different mobility values were chosen. The alkyl nitrates are relatively compact molecules. Consequently, the molecular, adduct and fragment ions are spread over a relatively large range of  $m/z$  values and exhibit mobility trends already well estimated by simple correlations (chapter 4.2.4.1). Additionally, the trajectory simulations were optimized for cations. The literature examples chosen were a number of amines reported by Karpas.<sup>109</sup> It is well established that these substances are ionized by PTR yielding protonated molecules in conventional IM spectrometry. Therefore, the structures of these protonated molecules were calculated by DFT at the B3LYP/6-31G(d,p) level. The optimized structures were used for trajectory simulations in the original and both modified versions of Mobcal (see chapter 4.2.4.3). Additionally, both  $m/z$  correlation procedures employing the (12-4) potential described in chapter 4.2.4.2 using (32) and (33), respectively, were performed. The combined procedure, using the PA'(N<sub>2</sub>) method for obtaining the  $r_m$  and subsequent fitting of  $a$  in the (12-4) potential approach was also carried out. Finally the approach using both simulated  $r_m$  from PA(N<sub>2</sub>) as well as the DFT structures and (49) and (50) to obtain the values of  $a$  was performed. The collision cross sections and mobilities obtained with the various procedures are compiled in tables 10 and 11, respectively (the fitting parameters are given in chapter 7, table 17). As expected, the mobility values obtained in He are systematically too large. They were only included for reference.

The shortcomings of the fitting procedure relying only on a correlation to  $m/z$  can be seen in figure 77. While the experimental mobilities of the compounds with similar mass vary, the mobilities calculated according to the fit represent average values. While the fitting procedure is useful for predicting mobilities of similar compounds, such as those of homologous series, it fails as a tool of calculating mobilities of unknown compounds.

The mobility values obtained in the calculations of  $a$  from the center of mass and the center of the Mulliken charges exhibit large deviations from the experimental values. While some of the mobility trends, especially for the compounds of similar  $m/z$  are reproduced, the overall quantitative agreement of the mobilities is poor. Comparing the values of  $a$  obtained for this method with the values calculated by the correlations (Table 17) reveals that the former are mostly much smaller, except in the cases of *n*-octylamine and 2,4-dinitroaniline, in which they are too large. The discrepancy between the experimental mobilities and those calculated via distance between the centers of mass and of Mulliken charges follow the same trend. Where the values of  $a$  differ from those of the correlations the most, the mobility differences are also the largest. This proposed calculation of the  $a$  values therefore seems inadequate for the mobility predictions of the amines, too. This could either be due to the fact that the centers of the Mulliken charges are generally not in good agreement with the actual centers of charge of the ions, or that the core model does not represent the actual interactions well enough. In the latter case, this shortcoming would be compensated in the correlations due to the fitting procedure but not here. The mobility values thus obtained will therefore be excluded from the further discussion.

Table 10: Collision cross sections of several amines: experimental values calculated from reference<sup>109</sup>, results obtained by TM, PA' and EHS in He; PA' in N<sub>2</sub> and TM in N<sub>2</sub>; results of calculations based on (12-4) potential; the fitted parameters are given in square brackets, except PA':  $r_m$  obtained from PA'(N<sub>2</sub>), DFT:  $a$  obtained from the distance between center of mass and center of Mulliken charges; the optimized parameters are: (12-4) [ $r_m, a$ ]:  $a^* = 0.1796$  and  $r_0 = 2.969$  Å, (12-4) [ $r_m, a, z$ ]:  $a^* = 0.2122$ ,  $r_0 = 2.571$  Å and  $z = 1.842 \times 10^{-3}$  Å/u, (12-4) [PA',  $a$ ]:  $a^* = 0.2505$ ; abbreviations used: dimethylformamide (DMF), dimethylaniline (DMA)

Compound	$m/z^a$		$\Omega_D / \text{Å}$								
	Exp.		TM(He)	PA'(He)	EHS(He)	PA'(N <sub>2</sub> )	TM(N <sub>2</sub> )	(12-4) [ $r_m, a$ ]	(12-4) [ $r_m, a, z$ ]	(12-4) [PA', $a$ ]	(12-4) [PA', DFT]
Methylamine	32.1	110	33.7	35.2	35.8	<b>82.7</b>	<b>100</b>	106	112	<b>124</b>	78.8
Ethylamine	46.1	114	39.5	42.1	43.4	<b>92.9</b>	<b>100</b>	110	112	<b>123</b>	90.8
DMF <sup>b</sup>	74.1	113	44.4	49.4	50.8	<b>107</b>	<b>108</b>	120	117	<b>123</b>	84.6
DMF <sup>c</sup>	74.1	113	44.6	49.5	51.1	<b>107</b>	<b>108</b>	120	117	<b>123</b>	101
<i>n</i> -Butylamine	74.1	126	51.9	55.6	57.9	<b>113</b>	<b>111</b>	120	117	<b>124</b>	135
Pyridine	80.1	111	46.2	48.8	49.9	<b>105</b>	<b>102</b>	122	119	<b>123</b>	78.5
Pyridazine	81.1	119	46.9	47.6	48.5	<b>104</b>	<b>106</b>	122	119	<b>123</b>	90.4
Triazine	82.1	126	47.7	46.2	46.7	<b>103</b>	<b>111</b>	122	119	<b>123</b>	97.4
2-Acetylpyridine	122.1	123	57.3	62.9	64.7	<b>127</b>	<b>119</b>	134	132	<b>126</b>	111
2,4-DMA	122.2	130	62.7	66.7	69.0	<b>130</b>	<b>122</b>	134	132	<b>127</b>	120
<i>N,N</i> -DMA	122.2	137	61.7	66.1	69.1	<b>130</b>	<b>118</b>	134	132	<b>127</b>	104
Isoquinoline	130.2	141	60.1	63.7	65.3	<b>127</b>	<b>119</b>	136	134	<b>126</b>	93.9
Diisobutylamine	130.3	126	71.9	77.5	82.2	<b>154</b>	<b>125</b>	136	134	<b>134</b>	94.1
<i>n</i> -Octylamine	130.3	155	76.8	82.6	87.1	<b>145</b>	<b>140</b>	136	134	<b>131</b>	269
Acridine	180.2	143	73.6	78.3	80.6	<b>148</b>	<b>134</b>	149	152	<b>132</b>	90.0
Dicyclohexylamine	182.3	158	82.3	87.7	94.0	<b>158</b>	<b>140</b>	149	152	<b>136</b>	95.3
2,4-Dinitroaniline	184.1	141	67.3	73.6	76.0	<b>148</b>	<b>145</b>	150	153	<b>132</b>	194
Tri- <i>n</i> -butylamine	186.4	165	95.8	102	110	<b>182</b>	<b>152</b>	150	154	<b>145</b>	106
Dibenzylamine	198.3	161	88.7	93.0	98.6	<b>171</b>	<b>152</b>	153	158	<b>140</b>	101
Tribenzylamine	288.4	185	111	113	121	<b>198</b>	<b>179</b>	172	192	<b>152</b>	109

<sup>a</sup>values given for protonated species, <sup>b</sup>proton attached to O, <sup>c</sup>proton attached to N

## 4 Results and discussion

Table 11: Ion mobilities of several amines: experimental values from reference<sup>109</sup>, results obtained by TM, PA' and EHS in He; PA' in N<sub>2</sub> and TM in N<sub>2</sub>; results of calculations based on (12-4) potential; the fitted parameters are given in square brackets, except PA':  $r_m$  obtained from PA'(N<sub>2</sub>), DFT:  $a$  obtained from the distance between center of mass and center of Mulliken charges; the optimized parameters are: (12-4) [ $r_m, a$ ]:  $a^* = 0.1796$  and  $r_0 = 2.969 \text{ \AA}$ , (12-4) [ $r_m, a, z$ ]:  $a^* = 0.2122$ ,  $r_0 = 2.571 \text{ \AA}$  and  $z = 1.842 \times 10^{-3} \text{ \AA/u}$ , (12-4) [PA',  $a$ ]:  $a^* = 0.2505$ ; abbreviations used: dimethylformamide (DMF), dimethylaniline (DMA)

Compound	$m/z^a$		$K / \text{cm}^2\text{V}^{-1}\text{s}^{-1}$									
	Exp.	TM(He)	PA'(He)	EHS(He)	PA'(N <sub>2</sub> )	TM(N <sub>2</sub> )	(12-4) [ $r_m, a$ ]	(12-4) [ $r_m, a, z$ ]	(12-4) [PA', $a$ ]	(12-4) [PA', DFT]		
Methylamine	32.1	2.65	8.60	8.25	8.10	<b>3.51</b>	<b>2.89</b>	2.73	2.59	<b>2.33</b>	3.68	
Ethylamine	46.1	2.36	6.80	6.38	6.20	<b>2.89</b>	<b>2.69</b>	2.43	2.39	<b>2.18</b>	2.95	
DMF <sup>b</sup>	74.1	2.21	5.60	5.04	4.90	<b>2.33</b>	<b>2.31</b>	2.08	2.12	<b>2.01</b>	2.94	
DMF <sup>c</sup>	74.1	2.21	5.58	5.03	4.87	<b>2.33</b>	<b>2.31</b>	2.08	2.12	<b>2.01</b>	2.46	
<i>n</i> -Butylamine	74.1	1.98	4.80	4.48	4.30	<b>2.20</b>	<b>2.25</b>	2.08	2.12	<b>2.00</b>	1.84	
Pyridine	80.1	2.21	5.34	5.05	4.94	<b>2.35</b>	<b>2.41</b>	2.02	2.07	<b>1.99</b>	3.13	
Pyridazine	81.1	2.07	5.25	5.17	5.07	<b>2.37</b>	<b>2.33</b>	2.02	2.06	<b>1.99</b>	2.72	
Triazine	82.1	1.95	5.15	5.31	5.25	<b>2.38</b>	<b>2.21</b>	2.01	2.05	<b>1.99</b>	2.52	
2-Acetylpyridine	122.1	1.91	4.10	3.74	3.63	<b>1.85</b>	<b>1.98</b>	1.75	1.78	<b>1.86</b>	2.12	
2,4-DMA	122.2	1.81	3.75	3.52	3.41	<b>1.81</b>	<b>1.93</b>	1.75	1.78	<b>1.85</b>	1.95	
<i>N,N</i> -DMA	122.2	1.72	3.81	3.56	3.40	<b>1.80</b>	<b>1.99</b>	1.75	1.78	<b>1.84</b>	2.25	
Isoquinoline	130.2	1.66	3.89	3.67	3.58	<b>1.84</b>	<b>1.97</b>	1.71	1.74	<b>1.85</b>	2.48	
Diisobutylamine	130.3	1.85	3.25	3.02	2.85	<b>1.52</b>	<b>1.87</b>	1.71	1.74	<b>1.74</b>	2.48	
<i>n</i> -Octylamine	130.3	1.51	3.05	2.83	2.68	<b>1.61</b>	<b>1.66</b>	1.71	1.74	<b>1.78</b>	0.868	
Acridine	180.2	1.59	3.10	2.91	2.83	<b>1.54</b>	<b>1.70</b>	1.53	1.50	<b>1.72</b>	2.53	
Dicyclohexylamine	182.3	1.44	2.77	2.60	2.42	<b>1.44</b>	<b>1.63</b>	1.52	1.49	<b>1.67</b>	2.39	
2,4-Dinitroaniline	184.1	1.61	3.38	3.09	3.00	<b>1.54</b>	<b>1.57</b>	1.52	1.49	<b>1.72</b>	1.17	
Tri- <i>n</i> -butylamine	186.4	1.38	2.37	2.23	2.07	<b>1.25</b>	<b>1.50</b>	1.51	1.48	<b>1.56</b>	2.14	
Dibenzylamine	198.3	1.41	2.55	2.44	2.30	<b>1.33</b>	<b>1.49</b>	1.48	1.43	<b>1.61</b>	2.24	
Tribenzylamine	288.4	1.20	2.00	1.96	1.83	<b>1.12</b>	<b>1.24</b>	1.29	1.16	<b>1.46</b>	2.04	

<sup>a</sup>values given for protonated species, <sup>b</sup>proton attached to O, <sup>c</sup>proton attached to N

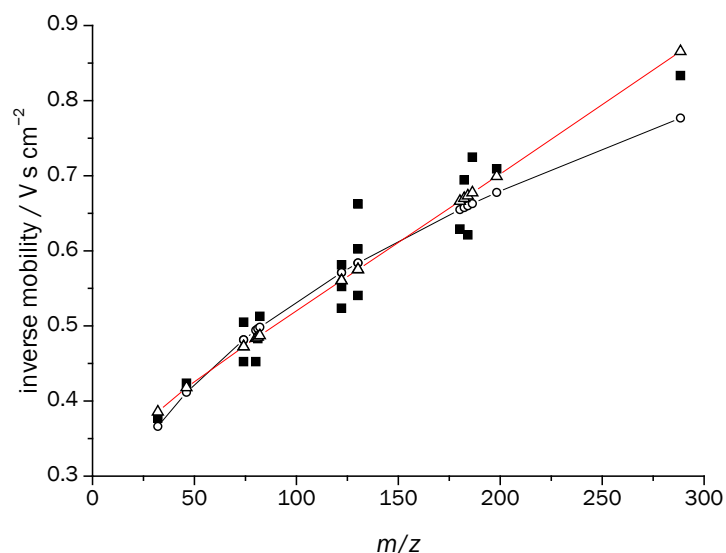


Figure 77: Fit to (12-4) potential, inverse mobility as a function of  $m/z$ , experimental values (■), fit optimizing  $a$  and  $r_m$  (○),  $a^* = 0.1796$  and  $r_0 = 2.969 \text{ \AA}$ ; fit optimizing  $a$ ,  $r_m$  and  $z$  (△),  $a^* = 0.2122$ ,  $r_0 = 2.571 \text{ \AA}$  and  $z = 1.842 \times 10^{-3} \text{ \AA/u}$

Due to the reasons stated above, the discussion in the remainder of this chapter will focus on the mobility values obtained by the TM(N<sub>2</sub>) and PA'(N<sub>2</sub>) trajectory simulations and the correlation to the (12,4) potential using the  $r_m$  values from the PA'(N<sub>2</sub>) method (bold in tables 10 and 11). A quick glance at tables 10 and 11 shows that the mobilities calculated by all three methods are within about 10 % deviation from the experimental values. A correlation between the calculated values and the experimental data yields more insights (Fig. 78, top). The values calculated from the PA'(N<sub>2</sub>) trajectories show a relatively good agreement for the larger compounds with low mobilities while the disagreement strongly increases towards higher mobility values. In general, the correlation to the experimental values is the lowest among the three methods compared. The values calculated from the TM(N<sub>2</sub>) trajectories are in relatively good agreement to the experimental value over the entire mobility range. However, they are systematically too large. The agreement of the (12-4) fit based on the  $r_m$  values from the PA'(N<sub>2</sub>) method with the experimental mobilities is comparable to that of the TM(N<sub>2</sub>) method. The values are too large for small mobilities while they are too small for large mobilities.

As mentioned above, the literature examples were specifically chosen to exhibit differing mobilities for compounds of similar  $m/z$ . These differences arise because ions possess different shapes and thus different collision cross sections. If the trajectory simulations are able to account for these effects, the differences of the calculated from the experimental mobilities should be relatively constant, even though the absolute values might deviate systematically. From the figure it can already be seen that this is not the general case for any of the methods described. The relative deviation of the calculated mobilities from the experimental values is shown for each compound at the bottom of figure 78. In this presentation, it becomes apparent that the variations of the calculated mobilities are quite inhomogeneous. The relative differences vary, especially in the groups of compounds possessing the same  $m/z$ . A possible conclusion is that the trajectory simulations still do not incorporate all effects that lead to the different mobilities of the compounds of the same  $m/z$ .

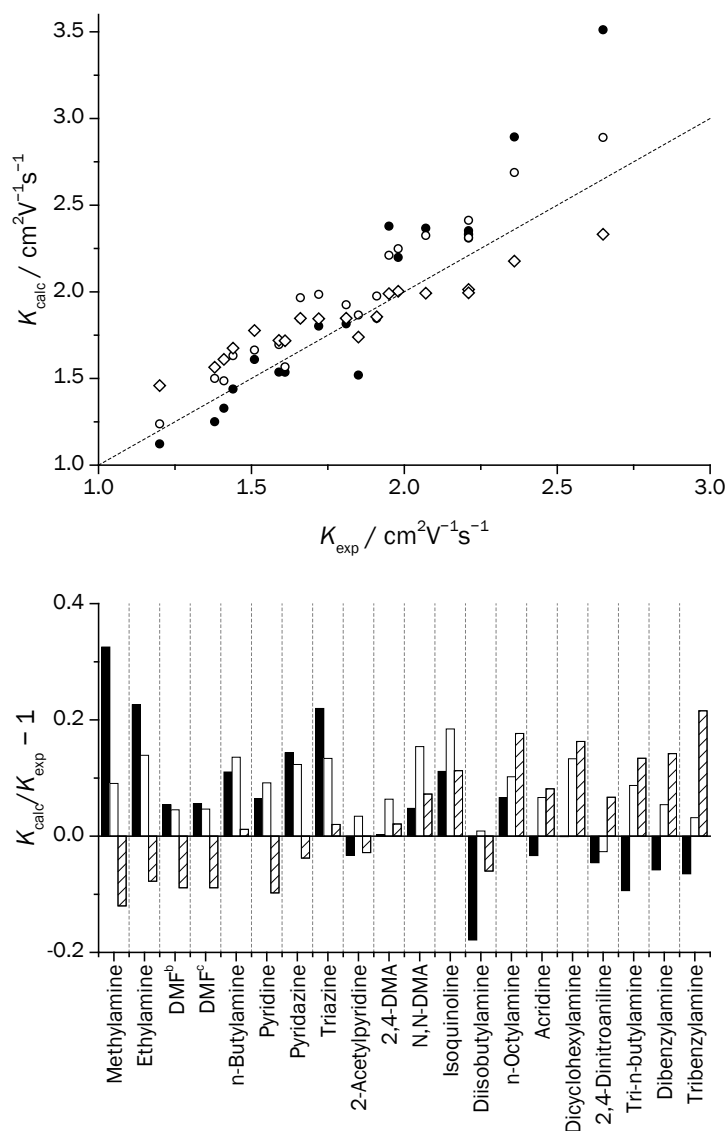


Figure 78: Comparison of experimental and calculated mobilities, top: correlation of calculated with experimental mobilities, TM adapted to  $\text{N}_2$  (○); PA' method in  $\text{N}_2$  (●),  $r_m$  from PA' in  $\text{N}_2$  and  $a^*$  fitted ( $a^* = 0.2505$ ) (◇); bottom: relative deviation of calculated mobilities from experimental values, TM adapted to  $\text{N}_2$  (solid bars); PA' method in  $\text{N}_2$  (open bars),  $r_m$  from PA' in  $\text{N}_2$  and  $a^*$  fitted (hatched bars)

To test this conclusion, it is useful to examine the correlation of the experimental and calculated values with the mobilities. It is advantageous to use the collision cross sections, as the differences are larger and the resulting plot is easier to interpret (Fig. 79, top). Similar to the correlation shown in chapter 4.2.4.1 of  $K^{-1}$  with  $m/z$ , due to (20) the collision cross section can be directly (empirically) correlated to the  $m/z$ . Put another way, the size of an ion will generally increase with its mass. As the literature values were specifically chosen to represent cases where the mobility, and therefore also the collision cross section, is not a direct function of  $m/z$ , the deviation of the experimental values from the correlation is large. However, the general trend can still be seen. The difference of each experimental value from the correlation can be considered a measure of the differences in shapes of the ions, if the line of the correlation is thought of as a mean cross section averaged all the different ion shapes.



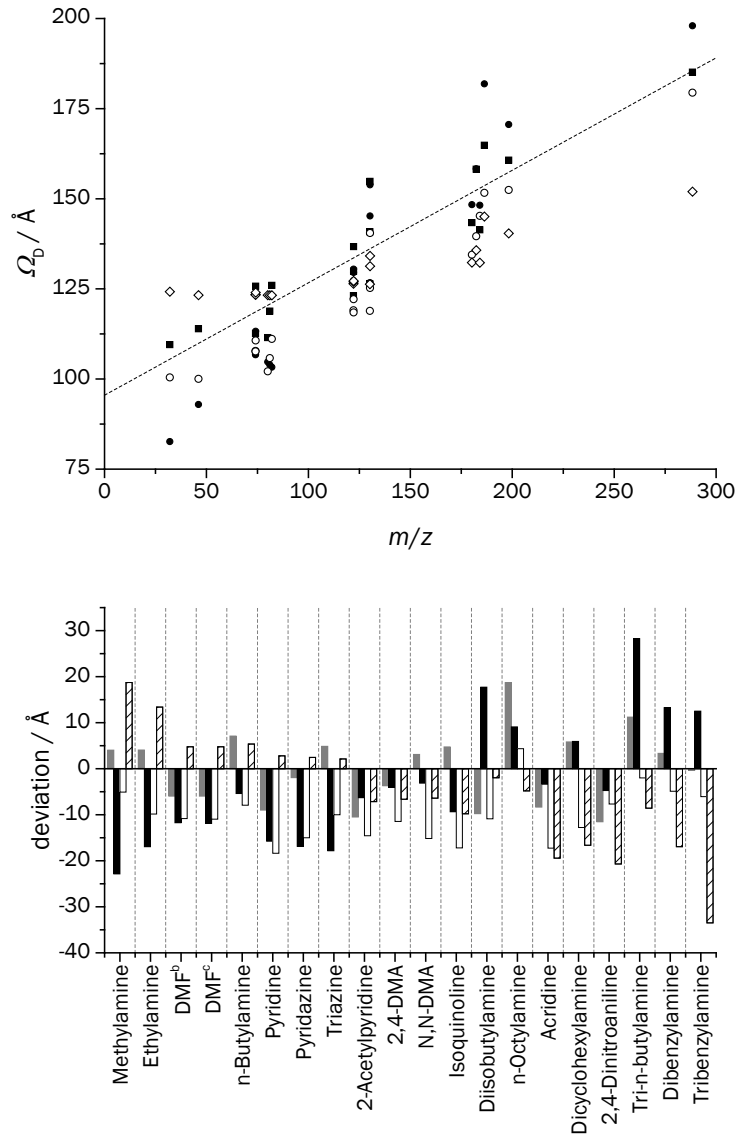


Figure 79: Top: correlation of experimental and calculated mobility values to  $m/z$ , experimental values (■), TM adapted to  $N_2$  (○), PA' method in  $N_2$  (●),  $r_m$  from PA' in  $N_2$  and  $a^*$  fitted ( $a^* = 0.2505$ ) (◇); bottom: deviation from the correlation of experimental and calculated mobility values, experimental values (grey solid bars), TM adapted to  $N_2$  (black solid bars); PA' method in  $N_2$  (open bars),  $r_m$  from PA' in  $N_2$  and  $a^*$  fitted (hatched bars)

In the plot, the calculated values are also shown. The simulations should reproduce the deviations from the correlation, if the influence of the different shapes is well accounted for. At the bottom of figure 79, the deviation of the experimental and the calculated collision cross sections from the correlation at the respective  $m/z$  value is shown for each ion. The closer the calculated value is to the experimental value, the more faithfully the simulation reproduces the different ion shapes. It is clear that no simulation successfully predicts all deviations. Generally, the simulations are more precise when the difference of the experimental cross section from the correlation is small. For the compounds of similar  $m/z$ , where the deviation of the experimental values changes considerably, the changes in the deviations of the calculated values are not as pronounced. For all correlations, some values can be found where the differences seem to be accounted for reasonably well, while there are other values where this is not the case.

Therefore, none of the methods can be said to be satisfactorily able to predict the changes in cross section that are independent of  $m/z$ . While the dataset chosen was an extreme case, the results showcase that more work has to be done in the field of mobility simulations if absolute value predictions of mobilities of chemically different compounds are to be achieved.

### 4.2.4.6 Conclusions

For compounds of similar shapes, such as those of homologous series, a reasonable prediction of mobilities for the identification of compounds from that series can be achieved by using simple empirical mobility-mass correlations. These correlations can be improved by physically more meaningful approaches, such as the calculation of collision cross sections as a function of  $m/z$  from interaction potentials. However, the parameters of these potentials also have to be obtained by fitting to experimental data. An interaction potential that can produce good fits is the (12-4) potential. Alternatively, mobilities can be calculated ab initio by performing trajectory simulations on ion structures obtained in quantum chemical calculations. In the past, the trajectory simulations have mostly been performed using He as the drift gas neutral. In those cases, the agreement to experiments was reasonably well. In the simulations, the position of the molecular ion is usually fixed and only the trajectories of the monoatomic He atom has to be considered. However, the diatomic nature of  $N_2$  results in an additional degree of freedom, namely the rotation of the  $N_2$  molecule, that has to be considered in the calculation. Additionally, the interaction of ion and neutral is more complex since ion-induced dipole interactions are potentially stronger. Therefore, trajectory simulations in  $N_2$  are much more challenging. Yet, as in most applications of IM spectrometry,  $N_2$  or air is used as the drift gas, these simulations are desirable.

It is possible to use a combination of the (12-4) potential based fitting approach and the values obtained in trajectory simulations. In cases where the simulated mobilities deviate systematically from experimental values, this combination can be used for compensation. The advantage of this approach over the procedure relying purely on fits to  $m/z$  is that the mobilities of different ion are not always a function of  $m/z$ . Conversely, adding the (12-4) potential, or a similar potential representing the interaction of the buffer gas neutral with the entire ion, directly to the trajectory simulations which generally take into account each atom in the molecular ion iteratively, could prove advantageous, especially considering the increased importance of the interaction potential in the case of  $N_2$ .

As could be seen, anions pose specific challenges to any such approach, as the additional electron apparently increases the collision cross sections compared to the case of cations. Deliberately using compounds of similar  $m/z$  but different mobilities reveals deficiencies in all approaches chosen. The methods reported only work well for ions of roughly similar shape and nature. A method for the universal accurate prediction of mobilities has yet to be devised.

## 5 OUTLOOK

Most of the topics covered in this thesis are subjects of ongoing research in our group.

The spectroscopic investigations of the ESI process have been continued, focusing on information obtained from the scattered light. The technique has been specifically applied to a novel design of orthogonal ESI source for the use in IM spectrometry. Recording images of the light scattered by the electrospray source operated in a tubular mesh counter electrode, it could be shown that the electrospray operated in a multijet mode inside the tubular counter electrode.<sup>65</sup>

The etalon spectrometer is currently applied in a real world application of LIBS. In the research project consortium I4S of the BonaRes program of the German Federal Ministry of Education and Research (BMBF), the instrument will be used for the cartography of nutrients in soils by LIBS. The advantages of the high resolution at a compact size of the spectrometer will be useful for the incorporation into an integrated vehicular system. Several improvements of the design are already being implemented. The single lenses will be replaced by photographic lens assemblies. Besides simplifying focusing the spectra, these lens assemblies also have the advantage of reducing spherical and chromatic aberrations. Light will be collected by a fiber assembly that terminates in a slit arrangement of the single fibers. Additionally, the spectrometer will be housed in a rugged casing, reducing maintenance requirements, such as calibration. The casing will also have the advantage of minimizing diffuse light on the detector. Finally, the instrument will be equipped with an ICCD, greatly improving its sensitivity.

The combination of the X-ray ionization chamber with the LTQ mass spectrometer is currently in use in different projects for the detection of the analytes in breath samples and in the headspace above biological samples such as bacteria and fungi. The results obtained with the instrument facilitate the identification of target analytes for specific analytical problems and the subsequent establishment of a detection scheme based on stand-alone IM spectrometry. Additionally, the results obtained in these measurements will allow further insights into the ionization chemistry of APCI.

The different approaches of predicting IM will be further pursued and refined. The range of ions investigated will be expanded by using mobility data obtained by IM spectrometers equipped with different ionization sources. Sources for the ionization of liquid samples, namely ESI and IR-MALDI, would dramatically expand the mass range of these investigations. Furthermore, these ionization sources are particularly suited for the ionization of biological molecules. The calculation of IM is of interest in this field as novel insights into processes such as protein folding and unfolding could be gained. There is also some work underway dedicated to finding all conformations a specific peptide can take at the temperatures encountered in IM spectrometry along with the probabilities the peptide will be in this conformation by molecular dynamics calculations. Mobility predictions, especially of large molecules, should benefit from that kind of approach.



## 6 REFERENCES

- (1) Atkins, P.; de Paula, J. *Atkins' Physical Chemistry*, 8th ed.; Oxford University Press: New York, 2006.
- (2) Forbes, M. W.; Jockusch, R. A. Gas-Phase Fluorescence Excitation and Emission Spectroscopy of Three Xanthene Dyes (Rhodamine 575, Rhodamine 590 and Rhodamine 6G) in a Quadrupole Ion Trap Mass Spectrometer. *J. Am. Soc. Mass Spectrom.* **2011**, 22 (1), 93–109.
- (3) Dashtiev, M.; Zenobi, R. Effect of buffer gas on the fluorescence yield of trapped gas-phase ions. *J. Am. Soc. Mass Spectrom.* **2006**, 17 (6), 855–858.
- (4) Bondybey, V. E.; Miller, T. A. Laser induced fluorescence from fluorobenzene radical cations in the gas phase. *J. Chem. Phys.* **1979**, 70 (1), 138.
- (5) Tsee, J. J.; Wampler, F. B.; Rice, W. W. Laser-induced fluorescence excitation spectra of CCl<sub>2</sub> and CFCI radicals in the gas phase. *Chem. Phys. Lett.* **1979**, 65 (3), 425–428.
- (6) Puretzy, A. A.; Geohegan, D. B. LIF imaging and gas-phase diagnostics of laser desorbed MALDI-matrix plumes. *Appl. Surf. Sci.* **1998**, 127–129, 248–254.
- (7) Grossmann, F.; Monkhouse, P. B.; Ridder, M.; Sick, V.; Wolfrum, J. Temperature and pressure dependences of the laser-induced fluorescence of gas-phase acetone and 3-pentanone. *Appl. Phys. B Laser Opt.* **1996**, 62 (3), 249–253.
- (8) Wang, Y.; Hendrickson, C. L.; Marshall, A. G. Direct optical spectroscopy of gas-phase molecular ions trapped and mass-selected by ion cyclotron resonance: laser-induced fluorescence excitation spectrum of hexafluorobenzene (C<sub>6</sub>F<sub>6</sub><sup>+</sup>). *Chem. Phys. Lett.* **2001**, 334 (1-3), 69–75.
- (9) Kordel, M. Fluoreszenzmessungen an gespeicherten Farbstoffmolekülen in der Gasphase, Universität Karlsruhe (TH), 2007.
- (10) Demtröder, W. *Laserspektroskopie 1*, 6th ed.; Springer-Verlag: Berlin, Heidelberg, 2011.
- (11) Demtröder, W. *Laserspektroskopie 2*, 6th ed.; Springer-Verlag: Berlin, Heidelberg, 2013.
- (12) *Laser-Induced Breakdown Spectroscopy*; Musazzi, S., Perini, U., Eds.; Springer Series in Optical Sciences; Springer-Verlag: Berlin, Heidelberg, 2014; Vol. 182.
- (13) Lee, W.-B.; Wu, J.; Lee, Y.; Sneddon, J. Recent Applications of Laser-Induced Breakdown Spectrometry: A Review of Material Approaches. *Appl. Spectrosc. Rev.* **2004**, 39 (1), 27–97.
- (14) Mason, E. A.; McDaniel, E. W. *Transport Properties of Ions in Gases*; American Society for Mass Spectrometry: Santa Fe, NM, USA, 1988.
- (15) Revercomb, H. E.; Mason, E. A. Theory of Plasma Chromatography/Gaseous Electrophoresis - A Review. *Anal. Chem.* **1975**, 47 (7), 970–983.
- (16) Mason, E. A.; O'Hara, H.; Smith, F. J. Mobilities of polyatomic ions in gases: core model. *J. Phys. B At. Mol. Phys.* **1972**, 5 (2), 169–176.
- (17) Berant, Z.; Karpas, Z. Mass-mobility Correlation of Ions in View of New Mobility Data. *J. Am. Chem. Soc.* **1989**, 111 (11), 3819–3824.
- (18) Steiner, W. E.; English, W. A.; Hill, H. H. Ion–Neutral Potential Models in Atmospheric Pressure Ion Mobility Time-of-Flight Mass Spectrometry IM(tof)MS. *J. Phys. Chem. A* **2006**, 110 (5), 1836–1844.

- (19) von Helden, G.; Hsu, M. T.; Gotts, N.; Bowers, M. T. Carbon cluster cations with up to 84 atoms: structures, formation mechanism, and reactivity. *J. Phys. Chem.* **1993**, *97* (31), 8182–8192.
- (20) Shvartsburg, A. A.; Mashkevich, S. V.; Siu, K. W. M. Incorporation of Thermal Rotation of Drifting Ions into Mobility Calculations: Drastic Effect for Heavier Buffer Gases. *J. Phys. Chem. A* **2000**, *104* (42), 9448–9453.
- (21) Wyttenbach, T.; Helden, G.; Batka, J. J.; Carlat, D.; Bowers, M. T. Effect of the long-range potential on ion mobility measurements. *J. Am. Soc. Mass Spectrom.* **1997**, *8* (3), 275–282.
- (22) Shvartsburg, A. A.; Jarrold, M. F. An exact hard-spheres scattering model for the mobilities of polyatomic ions. *Chem. Phys. Lett.* **1996**, *261* (1-2), 86–91.
- (23) Shvartsburg, A. A.; Liu, B.; Jarrold, M. F.; Ho, K.-M. Modeling ionic mobilities by scattering on electronic density isosurfaces: Application to silicon cluster anions. *J. Chem. Phys.* **2000**, *112* (10), 4517.
- (24) Alexeev, Y.; Fedorov, D. G.; Shvartsburg, A. A. Effective Ion Mobility Calculations for Macromolecules by Scattering on Electron Clouds. *J. Phys. Chem. A* **2014**, *118* (34), 6763–6772.
- (25) Shvartsburg, A. A.; Liu, B.; Siu, K. W. M.; Ho, K. Evaluation of Ionic Mobilities by Coupling the Scattering on Atoms and on Electron Density. *J. Phys. Chem. A* **2000**, *104* (26), 6152–6157.
- (26) Mesleh, M. F.; Hunter, J. M.; Shvartsburg, A. A.; Schatz, G. C.; Jarrold, M. F. Structural Information from Ion Mobility Measurements: Effects of the Long-Range Potential. *J. Phys. Chem.* **1996**, *100* (40), 16082–16086.
- (27) Kim, H.; Kim, H. I.; Johnson, P. V.; Beegle, L. W.; Beauchamp, J. L.; Goddard, W. a.; Kanik, I. Experimental and Theoretical Investigation into the Correlation between Mass and Ion Mobility for Choline and Other Ammonium Cations in N<sub>2</sub>. *Anal. Chem.* **2008**, *80* (6), 1928–1936.
- (28) Campuzano, I.; Bush, M. F.; Robinson, C. V.; Beaumont, C.; Richardson, K.; Kim, H.; Kim, H. I. Structural Characterization of Drug-like Compounds by Ion Mobility Mass Spectrometry: Comparison of Theoretical and Experimentally Derived Nitrogen Collision Cross Sections. *Anal. Chem.* **2012**, *84* (2), 1026–1033.
- (29) Gross, J. H. *Massenspektrometrie*; Springer Berlin Heidelberg: Berlin, Heidelberg, 2013.
- (30) *Gerthsen Physik*; Meschede, D., Ed.; Springer-Lehrbuch; Springer Berlin Heidelberg: Berlin, Heidelberg, 2010.
- (31) Schwartz, J. C.; Senko, M. W.; Syka, J. E. P. A two-dimensional quadrupole ion trap mass spectrometer. *J. Am. Soc. Mass Spectrom.* **2002**, *13* (6), 659–669.
- (32) *LTQ XL Hardware Manual*, Revision A.; Thermo Electron Corporation, 2006.
- (33) Rienstra-Kiracofe, J. C.; Tschumper, G. S.; Schaefer, H. F.; Nandi, S.; Ellison, G. B. Atomic and Molecular Electron Affinities: Photoelectron Experiments and Theoretical Computations. *Chem. Rev.* **2002**, *102* (1), 231–282.
- (34) *IUPAC Compendium of Chemical Terminology. XML on-line corrected version: <http://goldbook.iupac.org> (2006-), 2nd ed.*; McNaught, A. D., Wilkinson, A., Nič, M., Jiráť, J., Košata, B., Jenkins, A., McNaught, A., Eds.; Blackwell Scientific Publications: Oxford, 1997.

- (35) Kebarle, P.; Verkerk, U. H. Electrospray: From Ions in solution to Ions in the gas phase, what we know now. *Mass Spectrom. Rev.* **2009**, *28* (6), 898–917.
- (36) Fernández De La Mora, J.; Loscertales, I. G. The current emitted by highly conducting Taylor cones. *J. Fluid Mech.* **1994**, *260* (-1), 155.
- (37) Kebarle, P. A brief overview of the present status of the mechanisms involved in electrospray mass spectrometry. *J. Mass Spectrom.* **2000**, *35* (7), 804–817.
- (38) *CRC Handbook of Chemistry and Physics*, 10th ed.; Lide, D. R., Ed.; CRC Press/Taylor and Francis: Boca Raton, FL, 2010.
- (39) Iribarne, J. V.; Thomson, B. A. On the evaporation of small ions from charged droplets. *J. Chem. Phys.* **1976**, *64* (6), 2287–2294.
- (40) Boesl, U.; Zimmerman, R.; Weickhardt, C.; Lenoir, D.; Schramm, K. W.; Kettrup, A.; Schlag, E. W. Resonance-enhanced multi-photon ionization: a species-selective ion source for analytical time-of-flight mass spectroscopy. *Chemosphere* **1994**, *29* (7), 1429–1440.
- (41) Boesl, U.; Neusser, H. J.; Schlag, E. W. Two-Photon Ionization of Polyatomic Molecules in a Mass Spectrometer. *Z. Naturforsch. A* **1978**, *33* (12), 1546–1548.
- (42) Seki, K. Ionization Energies of Free Molecules and Molecular Solids. *Mol. Cryst. Liq. Cryst. Inc. Nonlinear Opt.* **1989**, *171* (1), 255–270.
- (43) Boesl, U. Multiphoton excitation and mass-selective ion detection for neutral and ion spectroscopy. *J. Phys. Chem.* **1991**, *95* (8), 2949–2962.
- (44) Lubman, D. M.; Kronick, M. N. Multiwavelength-selective ionization of organic compounds in an ion mobility spectrometer. *Anal. Chem.* **1983**, *55* (6), 867–873.
- (45) Löhmannsroeben, H.-G.; Beitz, T.; Laudien, R.; Schultze, R. Laser-based ion mobility spectrometry for sensing of aromatic compounds. In *Optical Science and Technology, the SPIE 49th Annual Meeting*; Chu, A., Szykman, J., Eds.; Denver, CO, USA, 2004; Vol. 5547, pp 16–24.
- (46) Laudien, R.; Riebe, D.; Beitz, T.; Löhmannsroeben, H.-G. Detection of explosive related nitroaromatic compounds (ERNC) by laser-based ion mobility spectrometry. In *Optically Based Biological and Chemical Detection for Defence IV*; Carrano, J. C., Zukauskas, A., Eds.; SPIE Europe Security and Defence. International Society for Optics and Photonics, 2008; Vol. 7116, p 71160T.
- (47) Brendler, C.; Riebe, D.; Ritschel, T.; Beitz, T.; Löhmannsroeben, H. G. Investigation of neuroleptics and other aromatic compounds by laser-based ion mobility mass spectrometry. *Anal. Bioanal. Chem.* **2013**, *405* (22), 7019–7029.
- (48) Brendler, C.; Riebe, D.; Zenichowski, K.; Beitz, T.; Löhmannsroeben, H.-G. Laser-based ion mobility spectrometer for the direct analysis of aromatic compounds in liquids. *Int. J. Ion Mobil. Spectrom.* **2014**, *17* (3-4), 105–115.
- (49) Oster, T.; Kühn, A.; Illenberger, E. Gas phase negative ion chemistry. *Int. J. Mass Spectrom. Ion Process.* **1989**, *89* (1), 1–72.
- (50) Edtbauer, A.; Sulzer, P.; Mauracher, A.; Mitterdorfer, C.; Ferreira da Silva, F.; Denifl, S.; Märk, T. D.; Probst, M.; Nunes, Y.; Limão-Vieira, P.; Scheier, P. Dissociative electron attachment to pentaerythritol tetranitrate: Significant fragmentation near 0 eV. *J. Chem. Phys.* **2010**, *132* (13), 134305.
- (51) Rutherford, E.; Kling, R. K. M. The energy of the becquerel-and x-rays and the necessary energy for the production of ions in gases. *Phys. Z.* **1900**, *2*, 53–55.

- (52) Döring, H.-R. Ion mobility spectrometer with mechanically stabilized vacuum-tight x-ray window. US6740874 B2, May 25, 2004.
- (53) Matsuoka, S. Ion-molecule reactions of  $N_3^+$ ,  $N_4^+$ ,  $O_2^+$ , and  $NO_2^+$  in nitrogen containing traces of oxygen. *J. Chem. Phys.* **1981**, 75 (2), 681.
- (54) Pershenkov, V. S.; Tremasov, A. D.; Belyakov, V. V.; Razvalyaev, A. U.; Mochkin, V. S. X-ray ion mobility spectrometer. *Microelectron. Reliab.* **2006**, 46 (2-4), 641–644.
- (55) Mitchell, K. B. Fluorescence Efficiencies and Collisional Deactivation Rates for  $N_2$  and  $N_2^+$  Bands Excited by Soft X Rays. *J. Chem. Phys.* **1970**, 53 (5), 1795.
- (56) Moddeman, W. E. Determination of the K–LL Auger Spectra of  $N_2$ ,  $O_2$ , CO, NO,  $H_2O$ , and  $CO_2$ . *J. Chem. Phys.* **1971**, 55 (5), 2317.
- (57) Stolte, W. C.; He, Z. X.; Cutler, J. N.; Lu, Y.; Samson, J. A. R. Dissociative photoionization cross sections of  $N_2$  and  $O_2$  from 100 to 800 eV. *At. Data Nucl. Data Tables* **1998**, 69 (1), 171–179.
- (58) *NIST Chemistry WebBook, NIST Standard Reference Database Number 69*; Linstrom, P. J., Mallard, W. G., Eds.; National Institute of Standards and Technology: Gaithersburg MD.
- (59) Celotta, R. J.; Bennett, R. A.; Hall, J. L.; Siegel, M. W.; Levine, J. Molecular Photodetachment Spectrometry. II. The Electron Affinity of  $O_2$ . *Phys. Rev. A* **1972**, 6 (2), 631–642.
- (60) Appelhans, A. D.; Dahl, D. A. SIMION ion optics simulations at atmospheric pressure. *Int. J. Mass Spectrom.* **2005**, 244 (1), 1–14.
- (61) Frisch, M. J.; Trucks, G. W.; Schlegel, H. B.; Scuseria, G. E.; Robb, M. A.; Cheeseman, J. R.; Scalmani, G.; Barone, V.; Mennucci, B.; Petersson, G. A.; Nakatsuji, H.; Caricato, M.; Li, X.; Hratchian, H. P.; Izmaylov, A. F.; Bloino, J.; Zheng, G.; Sonnenberg, J. L.; Hada, M.; Ehara, M.; Toyota, K.; Fukuda, R.; Hasegawa, J.; Ishida, M.; Nakajima, T.; Honda, Y.; Kitao, O.; Nakai, H.; Vreven, T.; Montgomery Jr., J. A.; Peralta, J. E.; Ogliaro, F.; Bearpark, M.; Heyd, J. J.; Brothers, E.; Kudin, K. N.; Staroverov, V. N.; Kobayashi, R.; Normand, J.; Raghavachari, K.; Rendell, A.; Burant, J. C.; Iyengar, S. S.; Tomasi, J.; Cossi, M.; Rega, N.; Millam, J. M.; Klene, M.; Knox, J. E.; Cross, J. B.; Bakken, V.; Adamo, C.; Jaramillo, J.; Gomperts, R.; Stratmann, R. E.; Yazyev, O.; Austin, A. J.; Cammi, R.; Pomelli, C.; Ochterski, J. W.; Martin, R. L.; Morokuma, K.; Zakrzewski, V. G.; Voth, G. A.; Salvador, P.; Dannenberg, J. J.; Dapprich, S.; Daniels, A. D.; Farkas, Ö.; Foresman, J. B.; Ortiz, J. V.; Cioslowski, J.; Fox, D. J. Gaussian 09 Revision A.02. Gaussian, Inc.: Wallingford CT 2009.
- (62) Östmark, H.; Wallin, S.; Ang, H. G. Vapor Pressure of Explosives: A Critical Review. *Propellants, Explos. Pyrotech.* **2012**, 37 (1), 12–23.
- (63) Oxley, J. C.; Smith, J. L.; Brady, J. E.; Brown, A. C. Characterization and Analysis of Tetranitrate Esters. *Propellants, Explos. Pyrotech.* **2012**, 37 (1), 24–39.
- (64) Riebe, D.; Zühlke, M.; Zenichowski, K.; Beitz, T.; Dosche, C.; Löhmannsröben, H.-G. Characterization of Rhodamine 6G Release in Electrospray Ionization by Means of Spatially Resolved Fluorescence Spectroscopy. *Z. Phys. Chem.* **2011**, 225 (9-10), 1055–1072.
- (65) Zühlke, M.; Riebe, D.; Beitz, T.; Löhmannsröben, H.-G.; Zenichowski, K.; Diener, M.; Linscheid, M. An electrospray ionization-ion mobility spectrometer as detector for high-performance liquid chromatography. *Eur. J. Mass Spectrom.* **2015**, 21 (3), 391.



- (66) Chingin, K.; Frankevich, V.; Balabin, R. M.; Barylyuk, K.; Chen, H.; Wang, R.; Zenobi, R. Direct access to isolated biomolecules under ambient conditions. *Angew. Chem., Int. Ed.* **2010**, *49* (13), 2358–2361.
- (67) Penzkofer, a.; Leupacher, W. Fluorescence behaviour of highly concentrated rhodamine 6G solutions. *J. Lumin.* **1987**, *37* (2), 61–72.
- (68) Riebe, D.; Beitz, T.; Dosche, C.; Löhmannsröben, H.-G.; Raab, V.; Raab, C.; Unverzagt, M. High-Resolution Spectrometer Using Combined Dispersive and Interferometric Wavelength Separation for Raman and Laser-Induced Breakdown Spectroscopy (LIBS). *Appl. Spectrosc.* **2014**, *68* (9), 1030–1038.
- (69) LOT-QuantumDesign GmbH. Pen-Ray line sources for wavelength calibration [http://lot-qd.com/fileadmin/Mediapool/products/lightsources/en/LQ\\_Pen-Ray\\_Line\\_sources\\_for\\_wavelength\\_calibration\\_en.pdf](http://lot-qd.com/fileadmin/Mediapool/products/lightsources/en/LQ_Pen-Ray_Line_sources_for_wavelength_calibration_en.pdf) (accessed Sep 2, 2015).
- (70) Srivastava, A.; Singh, V. B. Theoretical and experimental studies of vibrational spectra of naphthalene and its cation. *Indian J. Pure Appl. Phys.* **2007**, *45* (9), 714–720.
- (71) Krishnakumar, V.; Mathammal, R. Density functional and experimental studies on the FT-IR and FT-Raman spectra and structure of benzoic acid and 3,5-dichloro salicylic acid. *J. Raman Spectrosc.* **2009**, *40* (3), 264–271.
- (72) Kramida, A.; Ralchenko, Y.; Reader, J. *NIST Atomic Spectra Database (version 5.2)*, [Online]; National Institute of Standards and Technology: Gaithersburg, MD, 2014.
- (73) Riebe, D.; Laudien, R.; Brendler, C.; Beitz, T.; Löhmannsröben, H.-G. Laser ionization of H<sub>2</sub>S and ion-molecule reactions of H<sub>3</sub>S<sup>+</sup> in laser-based ion mobility spectrometry and drift cell time-of-flight mass spectrometry. *Anal. Bioanal. Chem.* **2013**, *405* (22), 7031–7039.
- (74) Wróblewski, T.; Ziemczonek, L.; Karwasz, G. P. Proton transfer reactions for ionized water clusters. *Czechoslov. J. Phys.* **2004**, *54* (SUPPL. 3), 747–752.
- (75) Eiceman, G. A.; Karpas, Z.; Hill, H. H. *Ion Mobility Spectrometry*, 2nd ed.; CRC Press: Boca Raton, 2014.
- (76) Steadman, J.; Cole, S. K.; Baer, T. Visible and ultraviolet resonance enhance multiphoton ionization photoelectron spectroscopy of H<sub>2</sub>S in the one-photon wavelength region 143–158 nm. *J. Chem. Phys.* **1988**, *89* (9), 5498.
- (77) Dibeler, V. H.; Rosenstock, H. M. Mass Spectra and Metastable Transitions of H<sub>2</sub>S, HDS, and D<sub>2</sub>S. *J. Chem. Phys.* **1963**, *39* (11), 3106.
- (78) Weishäupl, R. Prüfstandtaugliche Lasermassenspektrometrie von Abgasinhaltsstoffen an Otto- und Dieselmotoren: Quantitativer Spurennachweis von Stickoxiden, Ammoniak, Kohlenmonoxid und Aromaten, Technische Universität München, 2003.
- (79) Wójcik, L.; Markowski, A. Ion-molecule reaction in pure H<sub>2</sub>S. *Vacuum* **2005**, *78* (2-4), 193–197.
- (80) Wójcik, L.; Markowski, A. High-pressure investigations of positive ion-molecule reactions in a mixture of H<sub>2</sub>S and CH<sub>4</sub>. *Vacuum* **2009**, *83*, S173–S177.
- (81) Brendler, C. Untersuchung von Pharmaka und Umweltchemikalien in der Laser-Ionenmobilitäts- und Massenspektrometrie, Universität Potsdam, 2014.
- (82) Arshadi, M.; Kebarle, P. Hydration of OH<sup>-</sup> and O<sub>2</sub><sup>-</sup> in the gas phase. Comparative solvation of OH<sup>-</sup> by water and the hydrogen halides. Effects of acidity. *J. Phys. Chem.* **1970**, *74* (7), 1483–1485.

- (83) Spangler, G. E.; Carrico, J. P. Membrane inlet for ion mobility spectrometry (plasma chromatography). *Int. J. Mass Spectrom. Ion Phys.* **1983**, *52* (2-3), 267–287.
- (84) Crawford, C. L.; Hill, H. H. Comparison of reactant and analyte ions for <sup>63</sup>Nickel, corona discharge, and secondary electrospray ionization sources with ion mobility-mass spectrometry. *Talanta* **2013**, *107*, 225–232.
- (85) Compton, R. N.; Reinhardt, P. W.; Cooper, C. D. Collisional ionization of Na, K, and Cs by CO<sub>2</sub>, COS, and CS<sub>2</sub>: Molecular electron affinities. *J. Chem. Phys.* **1975**, *63* (9), 3821.
- (86) Knapp, M.; Echt, O.; Kreisler, D.; Märk, T. D.; Recknagel, E. Formation of long-lived CO<sub>2</sub><sup>-</sup>, N<sub>2</sub>O<sup>-</sup>, and their dimer anions, by electron attachment to van der waals clusters. *Chem. Phys. Lett.* **1986**, *126* (3-4), 225–231.
- (87) Denifl, S.; Vizcaino, V.; Märk, T. D.; Illenberger, E.; Scheier, P. High resolution electron attachment to CO<sub>2</sub> clusters. *Phys. Chem. Chem. Phys.* **2010**, *12* (20), 5219.
- (88) Skalny, J. D.; Stoica, A.; Orszagh, J.; Vladoiu, R.; Mason, N. J. Positive and negative corona discharges in flowing carbon dioxide. *J. Phys. D. Appl. Phys.* **2008**, *41* (17), 175211.
- (89) Rokushika, S.; Hatano, H.; Hill, H. H. Ion mobility spectrometry in carbon dioxide. *Anal. Chem.* **1986**, *58* (2), 361–365.
- (90) Ellis, H. W.; Pai, R. Y.; Gatland, I. R.; McDaniel, E. W.; Wernlund, R.; Cohen, M. J. Ion identity and transport properties in CO<sub>2</sub> over a wide pressure range. *J. Chem. Phys.* **1976**, *64* (10), 3935–3941.
- (91) Tans, P.; Keeling, R. Trends in Atmospheric Carbon Dioxide <http://www.esrl.noaa.gov/gmd/ccgg/trends/> (accessed Oct 23, 2015).
- (92) McCarthy, M. C.; Allington, J. W. R.; Sullivan, K. O. A quadratic configuration interaction study of N<sub>2</sub>O and N<sub>2</sub>O<sup>-</sup>. *Mol. Phys.* **1999**, *96* (12), 1735–1737.
- (93) Krishnakumar, E.; Srivastava, S. K. Dissociative attachment of electrons to N<sub>2</sub>O. *Phys. Rev. A* **1990**, *41* (5), 2445–2452.
- (94) Pinnaduwege, L. A.; Tav, C.; McCorkle, D. L.; Ding, W. X. Temperature dependence of electron attachment to methylene chloride. *J. Chem. Phys.* **1999**, *110* (18), 9011.
- (95) Rajapakse, M. Y.; Stone, J. A.; Eiceman, G. A. Decomposition Kinetics of Nitroglycerine·Cl-(g) in Air at Ambient Pressure with a Tandem Ion Mobility Spectrometer. *J. Phys. Chem. A* **2014**, *118* (15), 2683–2692.
- (96) Kozole, J.; Tomlinson-Phillips, J.; Stairs, J. R.; Harper, J. D.; Lukow, S. R.; Lareau, R. T.; Boudries, H.; Lai, H.; Brauer, C. S. Characterizing the gas phase ion chemistry of an ion trap mobility spectrometry based explosive trace detector using a tandem mass spectrometer. *Talanta* **2012**, *99*, 799–810.
- (97) Alge, E.; Adams, N. G.; Smith, D. Rate coefficients for the attachment reactions of electrons with *c*-C<sub>7</sub>F<sub>14</sub>, CH<sub>3</sub>Br, CF<sub>3</sub>Br, CH<sub>2</sub>Br<sub>2</sub> and CH<sub>3</sub>I determined between 200 and 600 K using the FALP technique. *J. Phys. B At. Mol. Phys.* **1984**, *17* (18), 3827–3833.
- (98) Wang, W. C.; Lee, L. C. Electron attachment rate constants of HBr, CH<sub>3</sub>Br, and C<sub>2</sub>H<sub>5</sub>Br in N<sub>2</sub> and Ar. *J. Appl. Phys.* **1988**, *63* (10), 4905.
- (99) Daum, K. A.; Atkinson, D. A.; Ewing, R. G. The role of oxygen in the formation of TNT product ions in ion mobility spectrometry. *Int. J. Mass Spectrom.* **2002**, *214* (2), 257–267.

- (100) Sulzer, P.; Rondino, F.; Ptasinska, S.; Illenberger, E.; Märk, T. D.; Scheier, P. Probing trinitrotoluene (TNT) by low-energy electrons: Strong fragmentation following attachment of electrons near 0eV. *Int. J. Mass Spectrom.* **2008**, *272* (2-3), 149-153.
- (101) Ewing, R. G.; Atkinson, D. A.; Eiceman, G. A.; Ewing, G. J. A critical review of ion mobility spectrometry for the detection of explosives and explosive related compounds. *Talanta* **2001**, *54* (3), 515-529.
- (102) Sulzer, P.; Mauracher, A.; Ferreira da Silva, F.; Denifl, S.; Märk, T. D.; Probst, M.; Limão-Vieira, P.; Scheier, P. Probing royal demolition explosive (1,3,5-trinitro-1,3,5-triazocyclohexane) by low-energy electrons: Strong dissociative electron attachment near 0 eV. *J. Chem. Phys.* **2009**, *131* (14), 144304.
- (103) Kanu, A. B.; Hill Jr., H. H. Identity confirmation of drugs and explosives in ion mobility spectrometry using a secondary drift gas. *Talanta* **2007**, *73* (4), 692-699.
- (104) Asbury, G. R.; Klasmeier, J.; Hill Jr., H. H. Analysis of explosives using electrospray ionization/ion mobility spectrometry (ESI/IMS). *Talanta* **2000**, *50* (6), 1291-1298.
- (105) Tam, M.; Hill, H. H. Secondary Electrospray Ionization-Ion Mobility Spectrometry for Explosive Vapor Detection. *Anal. Chem.* **2004**, *76* (10), 2741-2747.
- (106) Karpas, Z. The structure and mobility in air of protonated ketones. *Int. J. Mass Spectrom. Ion Process.* **1991**, *107* (3), 435-440.
- (107) Borsdorf, H.; Schelhorn, H.; Flachowsky, J.; Döring, H.-R.; Stach, J. Corona discharge ion mobility spectrometry of aliphatic and aromatic hydrocarbons. *Anal. Chim. Acta* **2000**, *403* (1-2), 235-242.
- (108) Cline, A. K.; Renka, R. L. A storage-efficient method for construction of a Thiessen triangulation. *Rocky Mt. J. Math.* **1984**, *14* (1), 119-140.
- (109) Karpas, Z. Ion mobility spectrometry of aliphatic and aromatic amines. *Anal. Chem.* **1989**, *61* (7), 684-689.



## 7 APPENDIX

Table 12: Results of fitting the (12-4) core potential model with correction factor  $z$  to the data of the explosives compounds,  $a^* = 0.2122$ ,  $r_0 = 2.265 \text{ \AA}$  and  $z = 7.895 \times 10^{-4} \text{ \AA/u}$

Species	$m/z$	$K_{\text{exp}} / \text{cm}^2\text{V}^{-1}\text{s}^{-1}$	$K_{\text{calc}} / \text{cm}^2\text{V}^{-1}\text{s}^{-1}$	$r_m / \text{Å}$	$a / \text{Å}$	$\epsilon_c / \text{meV}$	$\Omega_{\text{D, calc}} / \text{Å}^2$
$\text{NO}_2^-$	46	2.424	2.397	5.017	1.065	33.64	85.11
$\text{NO}_3^-$	62	2.223	2.234	5.330	1.131	26.41	86.73
$\text{N}_2\text{O}_5^-$	108	1.987	1.917	6.036	1.281	16.05	94.11
$\text{N}_2\text{O}_6^-$	124	1.915	1.833	6.243	1.325	14.03	97.14
$[\text{EGDN}+\text{NO}_3]^-$	214	1.446	1.488	7.228	1.534	7.807	115.0
$[\text{RDX}-\text{H}]^-$	221	1.447	1.467	7.297	1.549	7.519	116.4
$[\text{TNT}-\text{H}]^-$	226	1.449	1.453	7.345	1.559	7.324	117.4
$\text{NG}^-$	227	1.429	1.450	7.354	1.561	7.285	117.6
$[\text{Tetryl}-\text{NO}_2]^-$	241	1.371	1.411	7.487	1.589	6.783	120.4
$[\text{ETN}-\text{NO}_2]^-$	256	1.422	1.373	7.626	1.619	6.302	123.4
$[\text{NG}+\text{Cl}]^-$	262	1.352	1.358	7.681	1.630	6.124	124.6
$[(\text{RDX}-\text{H})+\text{NO}_2]^-$	267	1.361	1.346	7.726	1.640	5.982	125.6
$[\text{NG}+\text{NO}_3]^-$	289	1.283	1.296	7.922	1.681	5.413	130.0
$[\text{ETN}+\text{H}]^-$	303	1.271	1.266	8.043	1.707	5.092	132.8
$[\text{PETN}]^-$	316	1.229	1.239	8.155	1.731	4.820	135.4
$[\text{ETN}+\text{OH}]^-$	319	1.230	1.234	8.180	1.736	4.760	136.0
$[\text{PETN}+\text{Cl}]^-$	351	1.164	1.174	8.447	1.793	4.186	142.3
$[(\text{PETN}-\text{H})+\text{NO}_2]^-$	361	1.152	1.157	8.529	1.810	4.027	144.3
$[\text{ETN}+\text{NO}_3]^-$	364	1.164	1.151	8.554	1.816	3.981	144.9
$[\text{PETN}+\text{NO}_3]^-$	378	1.114	1.128	8.667	1.840	3.777	147.7
$[2(\text{RDX}-\text{H})+\text{NO}_2]^-$	488	0.9553	0.9747	9.522	2.021	2.593	169.6
$[2(\text{ETN}-\text{H})+\text{NO}_3]^-$	664	0.8330	0.8003	10.802	2.293	1.565	205.1
$[(2\text{PETN}-\text{H})+\text{Cl}]^-$	666	0.7870	0.7987	10.817	2.296	1.557	205.5
$[2(\text{PETN}-\text{H})+\text{NO}_3]^-$	692	0.7896	0.7780	11.000	2.335	1.456	210.8

Table 13: Values of the collision cross sections of the explosive compound ions obtained experimentally and by simulations with the various versions of Mobcal

Species	$m/z$	Exp.	$\Omega_D / \text{\AA}^2$				
			TM(He)	PA'(He)	EHS(He)	TM(N <sub>2</sub> )	PA'(N <sub>2</sub> )
NO <sub>2</sub> <sup>-</sup>	46	111.0	29.75	33.02	33.21	98.03	87.72
NO <sub>3</sub> <sup>-</sup>	62	114.9	30.82	37.50	37.85	97.94	95.24
N <sub>2</sub> O <sub>5</sub> <sup>-</sup>	108	119.8	44.42	54.26	56.09	110.5	123.0
N <sub>2</sub> O <sub>6</sub> <sup>-</sup>	124	122.6	46.51	57.58	59.67	110.6	127.9
[EGDN+NO <sub>3</sub> ] <sup>-</sup>	214	156.0	71.60	83.73	88.45	141.0	169.0
[RDX-H] <sup>-</sup>	221	155.5	73.17	81.77	86.46	143.8	164.2
NG <sup>-</sup>	227	157.4	76.42	88.50	94.14	146.8	176.6
[ETN-NO <sub>2</sub> ] <sup>-a</sup>	256	157.1	79.54	91.80	97.40	146.4	180.4
[ETN-NO <sub>2</sub> ] <sup>-b</sup>	256	157.1	80.25	93.73	99.50	145.7	183.8
[NG+Cl] <sup>-</sup>	262	165.0	84.91	93.90	101.4	159.6	172.9
[(RDX-H)+NO <sub>2</sub> ] <sup>-</sup>	267	163.8	81.11	89.21	95.36	148.7	174.4
[NG+NO <sub>3</sub> ] <sup>-</sup>	289	173.1	86.89	98.79	106.4	163.0	191.1
[ETN+H] <sup>-</sup>	303	174.4	93.46	103.6	111.4	159.6	197.6
[PETN] <sup>-</sup>	316	180.1	93.98	106.6	115.8	162.5	203.1
[ETN+OH] <sup>-</sup>	319	179.9	93.36	105.7	114.5	163.1	201.1
[ETN+NO <sub>3</sub> ] <sup>-</sup>	364	189.1	102.2	113.1	124.3	174.9	211.1

<sup>a</sup>dissociation of CO-NO<sub>2</sub> bond at C1 or C4, <sup>b</sup>dissociation of CO-NO<sub>2</sub> bond at C2 or C3

Table 14: Results of fitting the (12-4) core potential model to the data of the explosives compounds based on  $r_m$  obtained by the PA'(He) method,  $a^* = 0.3313$

Species	$m/z$	$K_{\text{exp}} / \text{cm}^2\text{V}^{-1}\text{s}^{-1}$	$K_{\text{calc}} / \text{cm}^2\text{V}^{-1}\text{s}^{-1}$	$\Omega_{\text{PA}'(\text{He})} / \text{\AA}^2$	$r_m / \text{\AA}$	$a / \text{\AA}$	$\varepsilon_c / \text{meV}$	$\Omega_{\text{D, calc}} / \text{\AA}^2$
$\text{NO}_2^-$	46	2.424	1.932	33.02	3.242	1.074	371.6	105.6
$\text{NO}_3^-$	62	2.223	1.797	37.50	3.455	1.145	288.1	107.8
$\text{N}_2\text{O}_5^-$	108	1.987	1.591	54.26	4.156	1.377	137.6	113.4
$\text{N}_2\text{O}_6^-$	124	1.915	1.562	57.58	4.281	1.418	122.2	114.0
$[\text{EGDN}+\text{NO}_3]^-$	214	1.446	1.478	83.73	5.162	1.710	57.80	115.7
$[\text{RDX}-\text{H}]^-$	221	1.447	1.476	81.77	5.102	1.690	60.60	115.6
$\text{NG}^-$	227	1.429	1.469	88.50	5.308	1.758	51.73	116.0
$[\text{ETN}-\text{NO}_2]^-^{\text{a}}$	256	1.422	1.455	91.80	5.406	1.791	48.08	116.4
$[\text{ETN}-\text{NO}_2]^-^{\text{b}}$	256	1.422	1.452	93.73	5.462	1.810	46.12	116.6
$[\text{NG}+\text{Cl}]^-$	262	1.352	1.450	93.90	5.467	1.811	45.95	116.7
$[(\text{RDX}-\text{H})+\text{NO}_2]^-$	267	1.361	1.456	89.21	5.329	1.765	50.91	116.1
$[\text{NG}+\text{NO}_3]^-$	289	1.283	1.436	98.79	5.608	1.858	41.52	117.3
$[\text{ETN}+\text{H}]^-$	303	1.271	1.423	103.6	5.743	1.903	37.75	118.1
$[\text{PETN}]^-$	316	1.229	1.413	106.6	5.826	1.930	35.64	118.7
$[\text{ETN}+\text{OH}]^-$	319	1.230	1.415	105.7	5.802	1.922	36.24	118.6
$[\text{ETN}+\text{NO}_3]^-$	364	1.164	1.389	113.1	6.001	1.988	31.65	120.1

Table 15: Results of fitting the (12-4) core potential model to the data of the explosives compounds based on  $r_m$  obtained by the PA'(N<sub>2</sub>) method,  $a^* = 0.2020$ 

Species	$m/z$	$K_{\text{exp}} / \text{cm}^2\text{V}^{-1}\text{s}^{-1}$	$K_{\text{calc}} / \text{cm}^2\text{V}^{-1}\text{s}^{-1}$	$\Omega_{\text{PA}'(\text{N}_2)} / \text{\AA}^2$	$r_m / \text{\AA}$	$a / \text{\AA}$	$\epsilon_c / \text{meV}$	$\Omega_{\text{D, calc}} / \text{\AA}^2$
NO <sub>2</sub> <sup>-</sup>	46	2.424	2.414	87.72	5.284	1.067	25.96	84.50
NO <sub>3</sub> <sup>-</sup>	62	2.223	2.247	95.24	5.506	1.112	22.03	86.21
N <sub>2</sub> O <sub>5</sub> <sup>-</sup>	108	1.987	1.886	123.0	6.257	1.264	13.21	95.70
N <sub>2</sub> O <sub>6</sub> <sup>-</sup>	124	1.915	1.823	127.9	6.380	1.289	12.22	97.64
[EGDN+NO <sub>3</sub> ] <sup>-</sup>	214	1.446	1.482	169.0	7.333	1.481	6.999	115.4
[RDX-H] <sup>-</sup>	221	1.447	1.507	164.2	7.230	1.461	7.409	113.3
NG <sup>-</sup>	227	1.429	1.434	176.6	7.497	1.514	6.409	118.8
[ETN-NO <sub>2</sub> ] <sup>-a</sup>	256	1.422	1.405	180.4	7.577	1.531	6.140	120.6
[ETN-NO <sub>2</sub> ] <sup>-b</sup>	256	1.422	1.387	183.8	7.648	1.545	5.916	122.1
[NG+Cl] <sup>-</sup>	262	1.352	1.444	172.9	7.419	1.499	6.682	117.2
[(RDX-H)+NO <sub>2</sub> ] <sup>-</sup>	267	1.361	1.434	174.4	7.451	1.505	6.566	117.9
[NG+NO <sub>3</sub> ] <sup>-</sup>	289	1.283	1.343	191.1	7.798	1.575	5.473	125.4
[ETN+H] <sup>-</sup>	303	1.271	1.309	197.6	7.931	1.602	5.115	128.4
[PETN] <sup>-</sup>	316	1.229	1.283	203.1	8.040	1.624	4.845	130.8
[ETN+OH] <sup>-</sup>	319	1.230	1.291	201.1	8.001	1.616	4.939	129.9
[ETN+NO <sub>3</sub> ] <sup>-</sup>	364	1.164	1.241	211.1	8.198	1.656	4.482	134.5



Table 16: Results of calculating mobilities of the explosive compounds from the (12-4) core potential model to using the  $r_m$  obtained by the PA'(N<sub>2</sub>) method and the  $a$  calculated from the DFT structures

Species	$m/z$	$K_{\text{exp}} / \text{cm}^2\text{V}^{-1}\text{s}^{-1}$	$K_{\text{calc}} / \text{cm}^2\text{V}^{-1}\text{s}^{-1}$	$\Omega_{\text{PA}}(\text{N}_2) / \text{\AA}^2$	$r_m / \text{\AA}$	$a / \text{\AA}$	$\epsilon_c / \text{meV}$	$\Omega_{\text{D, calc}} / \text{\AA}^2$
NO <sub>2</sub> <sup>-</sup>	46	2.424	3.321	87.72	5.284	0.158	11.88	61.421
NO <sub>3</sub> <sup>-</sup>	62	2.223	3.173	95.24	5.506	3×10 <sup>-7</sup>	8.931	61.063
N <sub>2</sub> O <sub>5</sub> <sup>-</sup>	108	1.987	2.052	123.0	6.257	0.933	10.21	87.923
N <sub>2</sub> O <sub>6</sub> <sup>-</sup>	124	1.915	2.241	127.9	6.380	0.415	6.483	79.443
[EGDN+NO <sub>3</sub> ] <sup>-</sup>	214	1.446	1.462	169.0	7.333	1.551	7.339	117.0
[RDX-H] <sup>-</sup>	221	1.447	1.475	164.2	7.230	1.566	7.974	115.7
NG <sup>-</sup>	227	1.429	1.661	176.6	7.497	0.733	3.921	102.6
[ETN-NO <sub>2</sub> ] <sup>-a</sup>	256	1.422	1.490	180.4	7.577	1.215	5.008	113.7
[ETN-NO <sub>2</sub> ] <sup>-b</sup>	256	1.422	1.654	183.8	7.648	0.592	3.312	102.4
[NG+Cl] <sup>-</sup>	262	1.352	1.467	172.9	7.419	1.415	6.318	115.3
[(RDX-H)+NO <sub>2</sub> ] <sup>-</sup>	267	1.361	1.483	174.4	7.451	1.327	5.834	114.0
[NG+NO <sub>3</sub> ] <sup>-</sup>	289	1.283	1.307	191.1	7.798	1.726	6.037	128.8
[ETN+H] <sup>-</sup>	303	1.271	1.303	197.6	7.931	1.628	5.200	128.9
[PETN] <sup>-</sup>	316	1.229	1.719	203.1	8.040	2×10 <sup>-5</sup>	1.965	97.60
[ETN+OH] <sup>-</sup>	319	1.230	1.335	201.1	8.001	1.424	4.386	125.7
[ETN+NO <sub>3</sub> ] <sup>-</sup>	364	1.164	1.240	211.1	8.198	1.662	4.497	134.6

Table 17: Parameters of (12-4) potential for various amines obtained in fitting procedure according to the different methods, the fitted parameters are given in square brackets, except PA':  $r_m$  obtained from PA'(N<sub>2</sub>), DFT:  $a$  obtained from the distance between center of mass and center of Mulliken charges; abbreviations used: dimethylformamide (DMF), dimethylaniline (DMA)

Compound	$r_m / \text{Å}$				$a / \text{Å}$				$\epsilon_c / \text{meV}$			
	(12-4) [ $r_m, a$ ]	(12-4) [ $r_m, a, z$ ]	(12-4) [PA', $a$ ]	(12-4) [PA', DFT]	(12-4) [ $r_m, a$ ]	(12-4) [ $r_m, a, z$ ]	(12-4) [PA', $a$ ]	(12-4) [PA', DFT]	(12-4) [ $r_m, a$ ]	(12-4) [ $r_m, a, z$ ]	(12-4) [PA', $a$ ]	(12-4) [PA', DFT]
Methylamine	6.08	5.38	5.13	5.13	1.09	1.14	1.28	0.34	13.3	25.4	37.6	15.6
Ethylamine	6.47	5.79	5.44	5.44	1.16	1.23	1.36	0.69	10.3	18.9	29.7	16.1
DMF <sup>a</sup>	7.08	6.45	5.83	5.83	1.27	1.37	1.46	0.44	7.23	12.3	22.5	9.68
DMF <sup>b</sup>	7.08	6.45	5.83	5.83	1.27	1.37	1.46	0.97	7.23	12.3	22.5	14.7
<i>n</i> -Butylamine	7.08	6.45	6.00	6.00	1.27	1.37	1.50	1.70	7.22	12.3	20.0	24.0
Pyridine	7.18	6.58	5.77	5.77	1.29	1.40	1.45	0.21	6.80	11.4	23.4	8.58
Pyridazine	7.20	6.60	5.75	5.75	1.29	1.40	1.44	0.66	6.74	11.2	23.8	12.2
Triazine	7.22	6.62	5.73	5.73	1.30	1.40	1.44	0.87	6.67	11.1	24.1	14.6
2-Acetylpyridine	7.82	7.36	6.37	6.37	1.40	1.56	1.59	1.19	4.84	7.24	15.8	11.5
2,4-DMA	7.82	7.37	6.42	6.42	1.40	1.56	1.61	1.44	4.84	7.24	15.3	13.4
<i>N,N</i> -DMA	7.82	7.37	6.44	6.44	1.40	1.56	1.61	0.96	4.84	7.24	15.1	9.08
Isoquinoline	7.92	7.50	6.35	6.35	1.42	1.59	1.59	0.61	4.59	6.73	16.0	7.54
Diisobutylamine	7.93	7.50	7.00	7.00	1.42	1.59	1.75	0.21	4.59	6.72	10.8	3.86
<i>n</i> -Octylamine	7.93	7.50	6.80	6.80	1.42	1.59	1.70	4.03	4.59	6.72	12.2	14.0
Acridine	8.49	8.30	6.87	6.87	1.53	1.76	1.72	0.09	3.48	4.48	11.7	3.88
Dicyclohexylamine	8.51	8.34	7.10	7.10	1.53	1.77	1.78	0.19	3.45	4.42	10.2	3.60
2,4-Dinitroaniline	8.53	8.36	6.87	6.87	1.53	1.77	1.72	2.83	3.42	4.36	11.7	31.0
Tri- <i>n</i> -butylamine	8.55	8.40	7.61	7.61	1.54	1.78	1.91	0.31	3.38	4.29	7.76	2.90
Dibenzylamine	8.67	8.58	7.37	7.37	1.56	1.82	1.85	0.26	3.21	3.94	8.82	3.21
Tribenzylamine	9.43	9.85	7.94	7.94	1.69	2.09	1.99	0.17	2.29	2.26	6.55	2.25

<sup>a</sup>proton attached to O, <sup>b</sup>proton attached to N

## 8 TABLE OF SYMBOLS AND ABBREVIATIONS

Sorted alphabetically, Latin letters first, Greek letters below.

Abbreviation	Meaning
$a$	Rigid core diameter
$a^*$	Reduced core diameter
APCI	Atmospheric pressure chemical ionization
API	Atmospheric pressure ionization
APLI	Atmospheric pressure laser ionization
$a_x$	Acceleration
$b$	Impact parameter
BTEX	Benzene, toluene, ethylbenzene and xylenes
$c$	Speed of light
CAD	Computer-aided design
CARS	Coherent anti-Stokes Raman scattering
$c_c$	(Vector pointing to) center of charge
CCD	Charge-coupled device
CD	Corona discharge
$c_m$	(Vector pointing to) center of mass
CRM	Charged residue model
$D$	Diffusion coefficient
$D_0$	bond dissociation enthalpy
DEA	Dissociative electron attachment
DMA	Dimethylaniline
DMF	Dimethylformamide
$e$	Elementary charge
$E/E$	Electric field strength (/scalar magnitude)
EA	Electron affinity
EGDN	Ethylene glycol dinitrate
EHS	Exact hard sphere scattering
$E_{hv}$	Photon energy
EI	Electron ionization
EMCCD	Electron-multiplying charge-coupled device

Abbreviation	Meaning
$E_{\text{pulse}}$	Laser pulse energy
ESI	Electrospray ionization
ETN	Erythritol tetranitrate
$F$	Force
$\mathcal{F}$	Finesse
FKM	Fluoropolymer elastomer
FWHM	Full width at half maximum
GC	Gas chromatograph(y)
ICCD	Intensified charge-coupled device
ID	Inner diameter
IE	Ionization energy
IEM	Ion evaporation model
IM	Ion Mobility
IMR	Ion-molecule reaction
$I_x$	Peak intensity (area)
$J$	Ionic flux
$K_0$	Reduced mobility
$k_B$	Boltzmann constant ( $k_B \approx 1.381 \text{ J K}^{-1}$ )
LIB(S)	Laser-induced breakdown (spectroscopy)
LIF	Laser-induced fluorescence
LTQ	Linear trap quadrupole
$m/z$	Mass-to-charge ratio
MALDI	Matrix-assisted laser desorption and ionization
MCP	Micro-channel plate
MFC	Mass flow controller
$m_x$	Mass
$n$	Refractive index
Nd:YAG	Neodymium-doped yttrium aluminium garnet
NG	Nitroglycerin
$n_x$	Number density
OD	Outer diameter

Abbreviation	Meaning
$p$	Pressure
$p(x)$	Partial pressure
PA	Proton affinity
PA'	Projection approximation
PAH	Polycyclic aromatic hydrocarbons
PEEK	Polyether ether ketone
PETN	Pentaerythritol tetranitrate
$p_i$	Vapor pressure
PTR	Proton-transfer reaction
$q$	Electric charge
$Q$	Volumetric flow rate
$q_M$	Mulliken charge
$r$	Ion-neutral distance
$R$	Gas constant
R6G	Rhodamine 6G
$R_{COD}^2$	Coefficient of determination
RDX	Royal demolition explosive (1,3,5-Trinitroperhydro-1,3,5-triazine)
REMPI	Resonance-enhanced multiphoton ionization
$R_{et}$	Reflectivity
RF	Radio frequency
$s$	Length
SPI	Single photon ionization
$T$	Temperature
Tetryl	2,4,6-Trinitrophenyl-methylnitramine
$t_f$	Time of flight
TIC	Total ion count
TM	Trajectory method
TNT	2,4,6-Trinitrotoluene
ToF	Time-of-flight
$U$	Electric potential
$V(r)$	Ion-neutral interaction potential

Abbreviation	Meaning
$v_d$	Average drift velocity
$V_m$	Molar volume
$v_x$	Average (root mean square) velocity
$z$	Correction factor used in (12-4) potential
$\alpha_d$	Dipole polarizability
$\gamma$	Surface tension
$\Delta_B H$	Adduct binding enthalpy
$\Delta_r G$	Free reaction enthalpy
$\Delta_r H$	Reaction enthalpy
$\Delta\omega$	Raman shift
$\delta\nu$	Free spectral range
$\Delta\nu$	Peak width
$\varepsilon$	(Kinetic) particle energy
$\varepsilon_x$	Permittivity of medium x
$\varepsilon_0$	Vacuum permittivity
$\varepsilon_x$	Potential well depth
$\theta$	Angle of deflection
$\kappa$	Conductivity
$\lambda_{MFP}$	Mean free path
$\lambda_x, \lambda_{ex}, \lambda_{max}$	Wavelength, excitation wavelength, wavelength of peak maximum
$\nu$	Frequency
$\sigma$	Differential cross section
$\sigma_{DEA}$	Cross section of dissociative electron attachment
$\sigma_{PI}$	Photoionization cross section
$\tau_c$	Mean time between collision
$\chi_x$	(Mole) fraction
$\Omega_x$	(Integral) cross section

## ACKNOWLEDGEMENTS

There are many people that I'm grateful to, without whom this work could never have been accomplished. First, I want to thank my family and friends for their support and faith in me. I couldn't have made it without you guys.

A very big thank you goes to my *Doktorvater*, Prof Dr Hans-Gerd Löhmannsröben. I deeply appreciate the opportunity of preparing my thesis in his labs just as much as I enjoyed all the things I learned in all the projects I was allowed to work in. Beyond that, there are many things about scientific thinking and practices that I learned from him. It goes without saying that I am also thankful to him for reviewing my thesis.

I would also like to express my gratitude to Prof Dr Kevin Pagel and Prof Dr Bernd Abel for taking the time to prepare reviews of my thesis.

A very special thank you goes to Dr Toralf Beitz, who I consider a mentor. From the proper planning, carrying out and documentation of experiments to the writing of papers and reports, he taught me a great many things. The interpretation of results greatly benefitted from a sheer endless number of discussions. His input on this thesis was also greatly appreciated.

I am also thankful to Stefan Kleinschmidt and Gennadiy Ronis, without whom many of the instruments described in this thesis would simply not exist.

Another person I want to thank is Dr Thomas Ritschel, who helped me a lot with the quantum chemical calculations.

Further thank yous go to my sister Jennifer Riebe and Christian Brendler for error checking this thesis and for many more things.

Our 'inner circle' of the ion mobility group, I also want to thank for great fellowship that made it feel like working with friends rather than 'mere' colleagues. I want to particularly mention Martin Zühlke, Karl Zenichowski, Alexander Erlar and José Villatoro.

The gratitude for the great atmosphere can be extended to include the entire physical chemistry group. Seldom in my life have I met such a large group of people open to discussion of a great many different topics. Our parties are legendary. My stay with you has been a very enjoyable time indeed.

# ERKLÄRUNG

Hiermit versichere ich, die vorliegende Dissertation an keiner anderen Hochschule eingereicht zu haben und sie selbständig verfasst sowie keine anderen Quellen und Hilfsmittel als die angegebenen verwendet zu haben.

25. April 2016

Daniel Riebe